AD-A226 022

RADC-TR-90-42, Vol II (of two)
In-House Report
March 1990

PROCEEDINGS OF THE 1989 ANTENNA APPLICATIONS SYMPOSIUM

Paul Mayes, et al

Sponsored by
Directorate of Electromagnetics
Rome Air Development Center
Hanscom Air Force Base
Air Force Systems Command

and

Electromagnetics Laboratory
Department of Electrical and Computer Engineering
College of Engineering
University of Illinois
Urbana-Champaign, Illinois 61801

APPROVED FOR PUBLIC RELEASE; DISTRIBUTION UNLIMITED.

Rome Air Develoment Center
Air Force Systems Command
Griffiss Air Force Base, NY 13441-5700

This report has been reviewed by the RADC Public Affairs Division (PA) and is releasable to the National Technical Information Service (NTIS). At NTIS it will be releasable to the general public, including foreign nations.

RADC-TR-90-42, Volume II (of two) has been reviewed and is approved for publication.

APPROVED: Robert J. Mailloux

ROBERT J. MAILLOUX
Chief, Antennas and Components Division
Directorate of Electromagnetics

APPROVED: John K. Schindler

JOHN K. SCHINDLER
Director of Electromagnetics

FOR THE COMMANDER: John A. Ritz

JOHN A. RITZ
Directorate of Plans and Programs

If your address has changed or if you wish to be removed from the RADC mailing list, or if the addressee is no longer employed by your organization, please notify RADC (EEAS) Hanscom AFB MA 01731-5000. This will assist us in maintaining a current mailing list.

Do not return copies of this report unless contractual obligations or notices on a specific document require that it be returned.

REPORT DOCUMENTATION PAGE

Form Approved
OMB No 0704-0188

1. AGENCY USE ONLY (Leave blank)	2. REPORT DATE	3. REPORT TYPE AND DATES COVERED
	March 1990	In-house

4. TITLE AND SUBTITLE
Proceedings of the 1989 Antenna Applications Symposium

5. FUNDING NUMBERS
PE 62702F
PR 4600 TA 14 WU PD

6. AUTHOR(S)
Paul Mayes et al

7. PERFORMING ORGANIZATION NAME(S) AND ADDRESS(ES)
Rome Air Development Center
Hanscom AFB, MA 01731-5000

Responsible Individual: John Antonucci (EEAS)

8. PERFORMING ORGANIZATION REPORT NUMBER
RADC-TR-90-42
Volume II

9. SPONSORING/MONITORING AGENCY NAME(S) AND ADDRESS(ES)

10. SPONSORING/MONITORING AGENCY REPORT NUMBER

11. SUPPLEMENTARY NOTES
Volume I consists of pages 1 through 342; Volume II consists of pages 343 through 611

12a. DISTRIBUTION/AVAILABILITY STATEMENT
Approved for public release; distribution unlimited

12b. DISTRIBUTION CODE

13. ABSTRACT *(Maximum 200 words)*

The Proceedings of the 1989 Antenna Applications Symposium is a collection of state-of-the-art papers relating to phased array antennas, multibeam antennas, satellite antennas, microstrip antennas, reflector antennas, HF, VHF, UHF and various other antennas.

14. SUBJECT TERMS
Antennas
Satellite antennas
Broadband antennas
Microstrip
Reflector
HF
VHF
UHF
Multibeam antennas
Array antennas

15. NUMBER OF PAGES
276

16. PRICE CODE
RH

17. SECURITY CLASSIFICATION OF REPORT	18. SECURITY CLASSIFICATION OF THIS PAGE	19. SECURITY CLASSIFICATION OF ABSTRACT	20. LIMITATION OF ABSTRACT
Unclassified	Unclassified	Unclassified	SAR

CONTENTS

* NOT INCLUDED IN THIS VOLUME

Contents

THURSDAY, 21 SEPTEMBER 1989

ARRAYS

Contents

ARRAYS AND NUMERICAL TECHNIQUES

FRIDAY, 22 SEPTEMBER 1989

EXPERIMENT AND THEORY

* NOT INCLUDED IN THIS VOLUME

Contents

EHF ACTIVE ARRAY

JOE KOBUS

SEPTEMBER 1989

MOTOROLA INC.
Government Electronics Group
Mail Drop R1216
8220 E. Roosevelt
Scottsdale, AZ 85251

UNCLASSIFIED ABSTRACT

This paper describes a circularly polarized, minimum volume, solid-state active aperture for tactical applications at Q-band. The design consists of 32 waveguide modules arrayed into four groups, each group fed from an active source. Broadwall Clavin compensated slots are used to maximize gain and reduce mutual coupling. Five Impatt modules (one driver and four output) are incorporated utilizing spatial combining. Circular polarization is accomplished via a meander-line polarizer suspended in front of the aperture. The array has 50% minimum efficiency over a 4.5% band.

1.0 SUMMARY OF OBJECTIVES

Primary objectives of the transmit antenna design are:

- Integrated Radio/Antenna Assembly
- Compatibility with receive array in a single assembly
- Capable of integration with four active sources
- Maximum gain
- Minimum volume
- Minimum cost

The goal was a 440 cubic inch rectangular box containing all electronics and antennas. Although other antenna types were considered, the most convenient and volume efficient are planar arrays permanently attached to a face of the box. In addition to attitude positioning, setting-up a terminal then only requires removal of a protective cover. No connections need be made or complex mechanical structures assembled. An integrated array, furthermore, is obviously compatible with a rectangular packaging form factor appropriate for minimum volume. To realize the program objectives, Motorola thus developed the Q-band active array modular concept shown in Figure 1; a photograph of the feasibility demonstration hardware is presented in Figure 2.

The transmit array occupies nearly half of approximately a one-foot square area; a K-band receive array occupies the other half of the same surface. To achieve maximum aperture efficiency, a waveguide slot array was chosen for the Q-band antenna. Minimum overall thickness results using broadwall slots grouped into 32 identical modules "window-fed" from a waveguide distribution network. Each group of 8 is excited from one quadrant of the antenna distribution network, and 4 active sources deliver

UNCLASSIFIED

ANTENNA/TRANSMITTER MODULAR CONCEPT(U)

FIGURE 1.

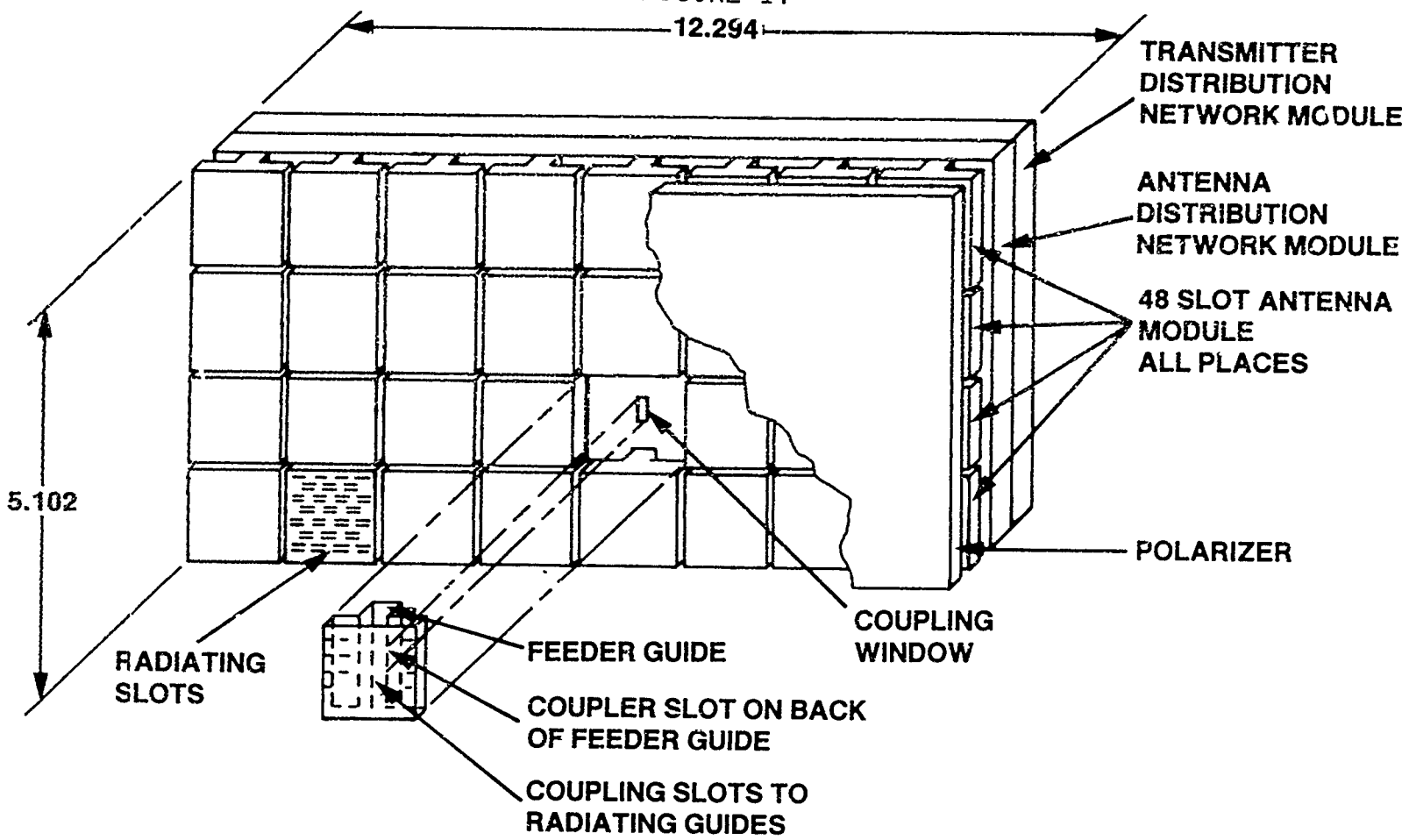

346

61217 1

UNCLASSIFIED

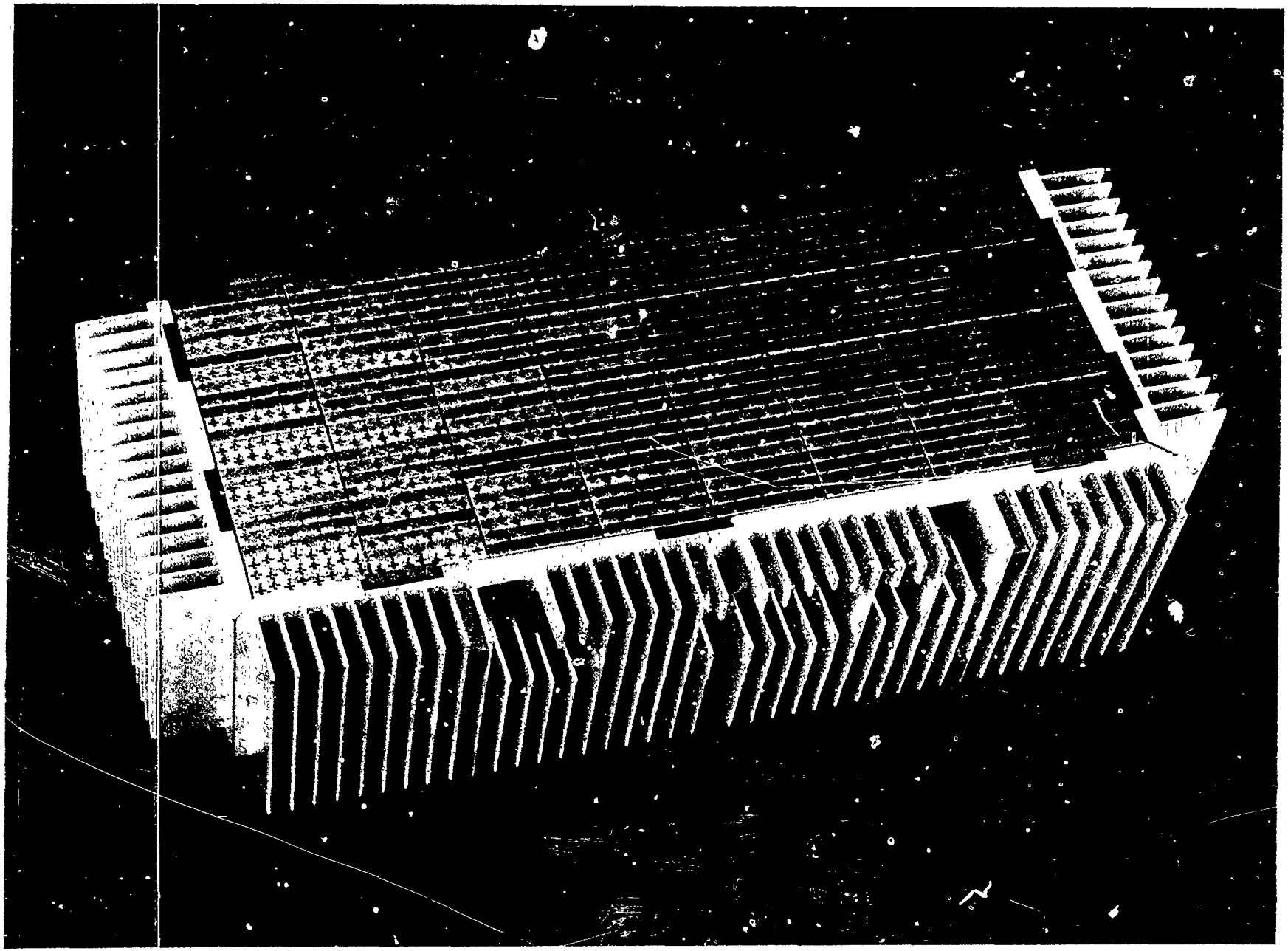

Figure 2. (U) Q-Band Array Feasibility Demonstration Model with Polarizer Removed

power to the quadrants. Circular polarization of the radiated fields is produced by a rectangular sandwich [1,2] located in front of the array.

Regarding the Q-band transmit array, a 50 percent overall aperture efficiency (including all feed network and polarizer losses) was achieved by Motorola's feasibility model. This is at least as good as electrical efficiencies commonly obtained with reflector antennas.

Motorola's plan for realizing the objectives in a modular design was devised to:

- Establish radiation module and feed network fabrication techniques early in the program
- Optimize all components during development
- Utilize computer modeling
- Scale radiation module including polarizer to X-band to establish design parameters
- Integrate antenna and transmitter modules in levels

These goals were all realized.

2.0 BASIC DESIGN CONSIDERATIONS

The SATCOMA transmit array gain goal is 37.5 dBI, including all losses. Fifty per cent minimum efficiency is also a design goal. Thus the required uniformly weighted aperture gain is 40.5 dBI. A Clavin-compensated [3,4,5] waveguide slot was selected for minimum element-to-element coupling and maximum radiator gain (7.8 dBI). Under these assumptions the number of array elements required becomes

$$N = 10^{\left(\frac{40.5 - 7.8}{10}\right)} = 1862 \qquad (1)$$

Analysis reveals, however, waveguide slot-array technology limits the maximum number of elements to 1536, resulting in a thinning loss

$$L_T = -10 \log_{10} \left(\frac{1536}{1862} \right) = .84 \text{ dB} \qquad (2)$$

Finally, the aperture area yielding 40.5 dBI is

$$A = \left(\frac{\lambda^2}{4\pi} \right) 10^{40.5/10} = 62.81 \text{ in}^2 \qquad (3)$$

at 44.5 GHz.

Minimum depth is realized from an array of slots formed in the broadwalls of a number of waveguide sections or "sticks". The size of each module, or group of sticks, depends, as is well-known, on the bandwidth demanded from it. Figures 3 and 4 show, respectively, a Q-band module and its scaled X-band counterpart.

Refer to Figures 1 and 5. Each quadrant of the array consists of 8 modules fed from a waveguide distribution network containing 7 magic-tee power dividers. An active signal source input is provided to each quadrant. These active sources are driven from a single input to another waveguide distribution network.

In order to demonstrate effective radiated power (ERP), it is first desirable to ascertain array gain. Invoking the reciprocity principle, this is accomplished through operation of the Q-band transmit array as a receive antenna. Active sources in the transmit routing network are removed and replaced with waveguide sections. Received power collected

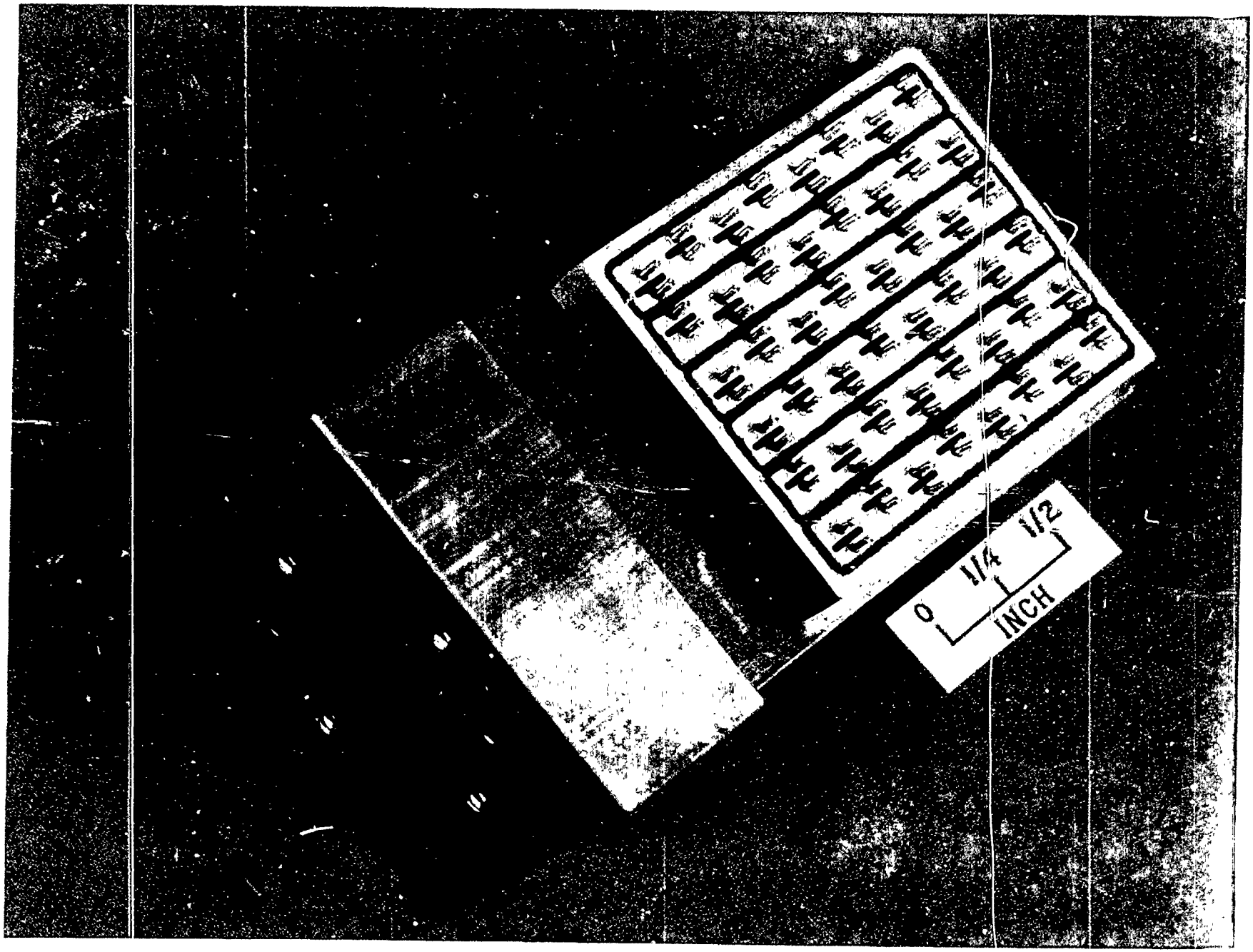

Figure 3. (U) First Q-Band Motorola Fabricated Brassboard Module

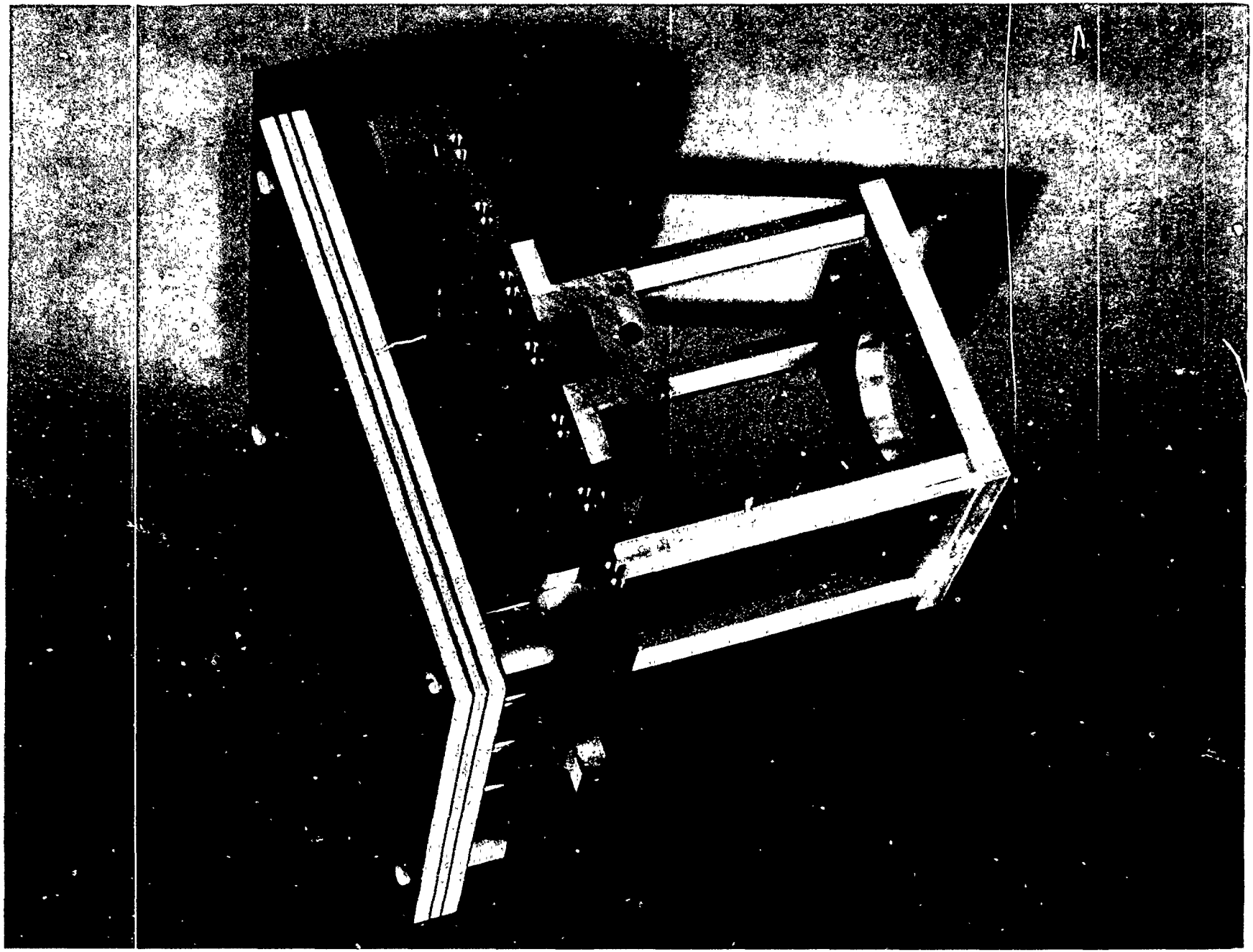

Figure 4. (U) Final X-Band Scaled Radiation Module

Q-BAND ARRAY CORPORATE FEED CONCEPT(U)

FIGURE 5.

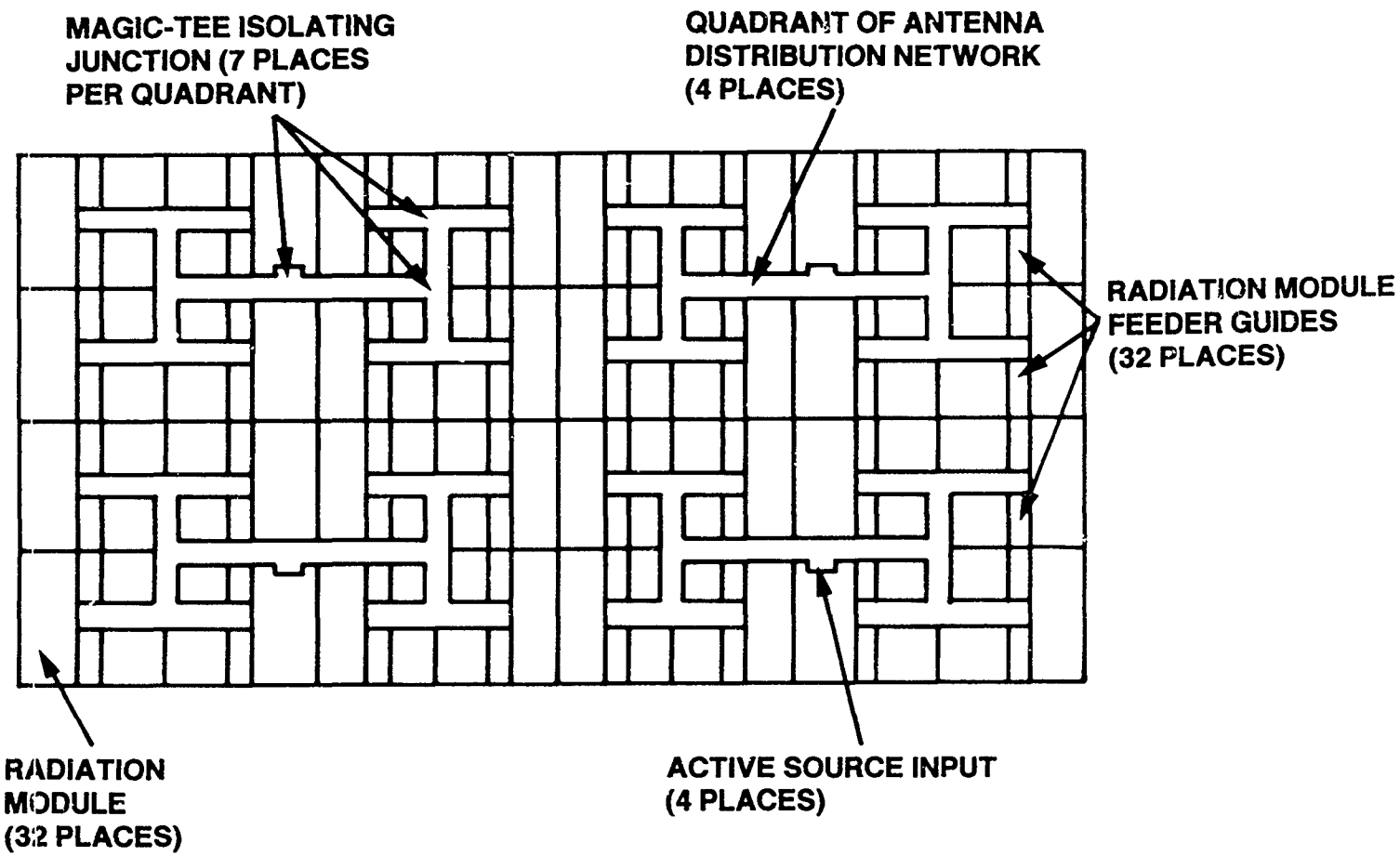

61217-2

by each of the four quadrant distribution networks is combined using the transmitter routing network (in reverse) sans active sources.

Calculation of ERP requires knowledge of all module gain and insertion phase variations, as well as the quadrant network insertion loss and phase variations, together with the power and phase of the four active sources. This information was determined and subsequently compared with recorded ERP. As component data accumulated during the engineering development effort budgets were prepared and updated. The last of these is presented in Table I.

Our approach taken to size the aperture is based on 40.5 dBLI ideal gain, together with a 50 percent minimum aperture efficiency. Thinning loss of .84 dB was found to result for a practical waveguide slot array design consisting of 32 modules of 48 slots each. Thus at 44.5 GHz, at least, individual module gains should be nominally

$$40.5 - .84 - 10 \log_{10} (32) = 24.6 \text{ dBI}, \qquad (4)$$

excluding impedance mismatch loss. Recorded module gain values listed in Table I include mismatch loss. Consequently we may conclude radiation module gain is consistent with our overall array design goal of 37.5 dBI.

3.0 FINAL TEST DATA

Input-to-output amplitude and phase measurements were performed for each of the quadrant distribution networks of Figure 5, as well as for the transmitter routing network with active sources removed. These data indicate channel line losses in excess of those expected for ideal waveguides; in addition to magic tees nearly 1 dB of quadrant network loss appears. Transmitter routing network loss is not relevant to array

Table I. (U)Final Transmit Array Gain Budget

GAIN OR LOSS PARAMETER (dB)	FREQUENCY F(GHz)		
	43.5	44.5	45.5
Average Module Gain G_o(dBLI) Including Impedance Mismatch Loss	24.08	24.35	24.38
Array Factor Gain $10 \log_{10}$ (32)	15.05	15.05	15.05
Module Uniformity Loss for ±.25 dB Amplitude and ±10 Degree Peak Phase Deviations $-10 \log_{10} (\eta_M)$	.06	.06	.06
Combined Loss of Four Quadrant Networks $-10 \log_{10} (\eta_{QN})$	1.30	1.36	1.50
Polarizer Loss	.35	.35	.35
Axial Ratio Loss Relative to Perfect Circular Polarization	.037	.024	.021
Expected Gain of Active Aperture (dBCPI)	37.38	37.61	37.50
Recorded Passive Array Gain (dBCPI)	37.6	37.6	37.6

performance because only the final outputs of the four active sources affect ERP. It is nevertheless necessary to know the transmitter network loss since it is used as a passive combiner to establish array gain. Quadrant network ohmic losses, on the other hand, do impact our budget.

Recorded amplitude and phase data obtained for the quadrant networks yield the composite efficiency of the antenna distribution network (line 4 of Table I). Loss contributors include both magic tees and guide channels. Analysis reveals phase errors are so small as to produce an almost negligible contribution to network efficiency. This was confirmed from recorded array patterns (e.g. Figures 6 and 7) which generally exhibit deep nulls between sidelobes. Table II summarizes pattern performance. Thus it may be concluded:

- Magic tees produce well-balanced power divisions and adequate isolation of radiation module mismatches
- All waveguide channels are precision phased

Machining tolerances must therefore be on target.

In order to perform passive array tests, active sources were removed from the transmitter routing network and replaced with four waveguide feed-throughs directly to the quadrant network inputs. These are precision-phased using shims. Amplitude and phase data recorded for the transmit network are not given here, but were incorporated in calculation of passive array gain.

Waveguide covers in the demonstration model are attached with screw-type fasteners. Lower waveguide channel resistive losses can undoubtedly be obtained by laser welding, the technique proven for efficient radiation module fabrication. Lower waveguide loss can conceivably raise overall transmit array efficiency by .8 dB to 60 percent.

FIGURE 6. **PASSIVE MODE H-PLANE PATTERN FOR Q-BAND ARRAY INCLUDING POLARIZER, RECORDED AT 44.5 GHz**

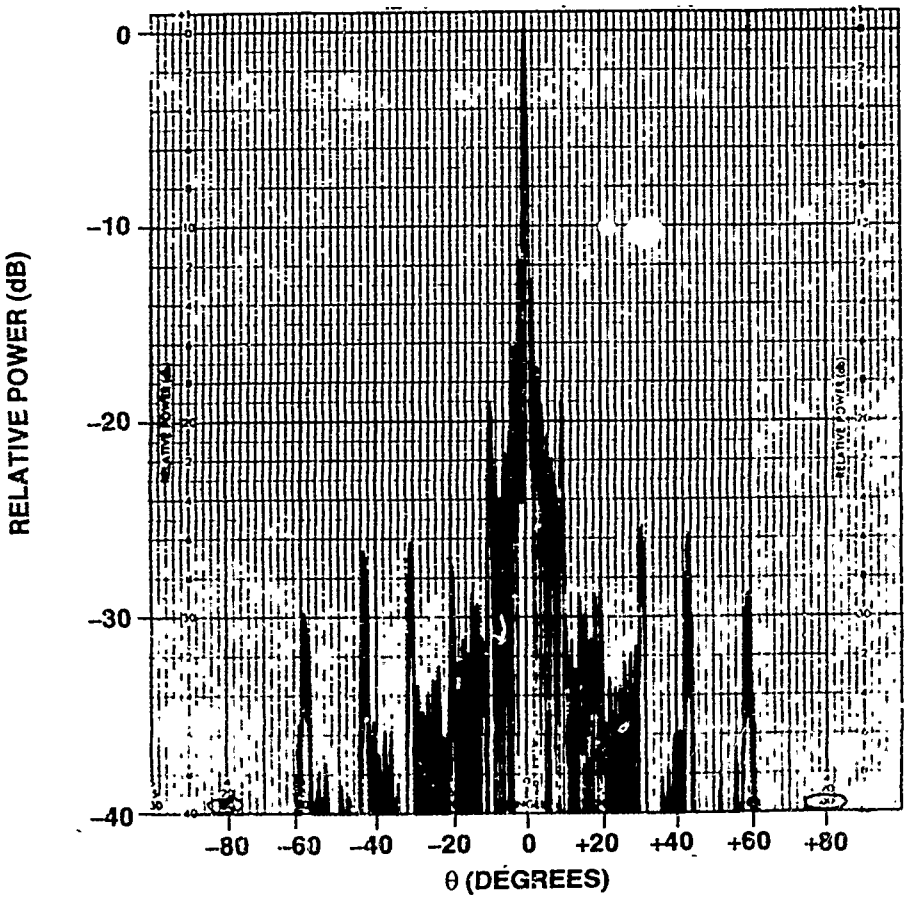

NOTE:
SOURCE ANTENNA IS A LINEARLY POLARIZED HORN ROTATING AT A SOMEWHAT FASTER RATE THAN THE ARRAY.

61846-6

FIGURE 7. **EXPANDED H-PLANE PATTERN FOR Q-BAND ARRAY WITH POLARIZER**

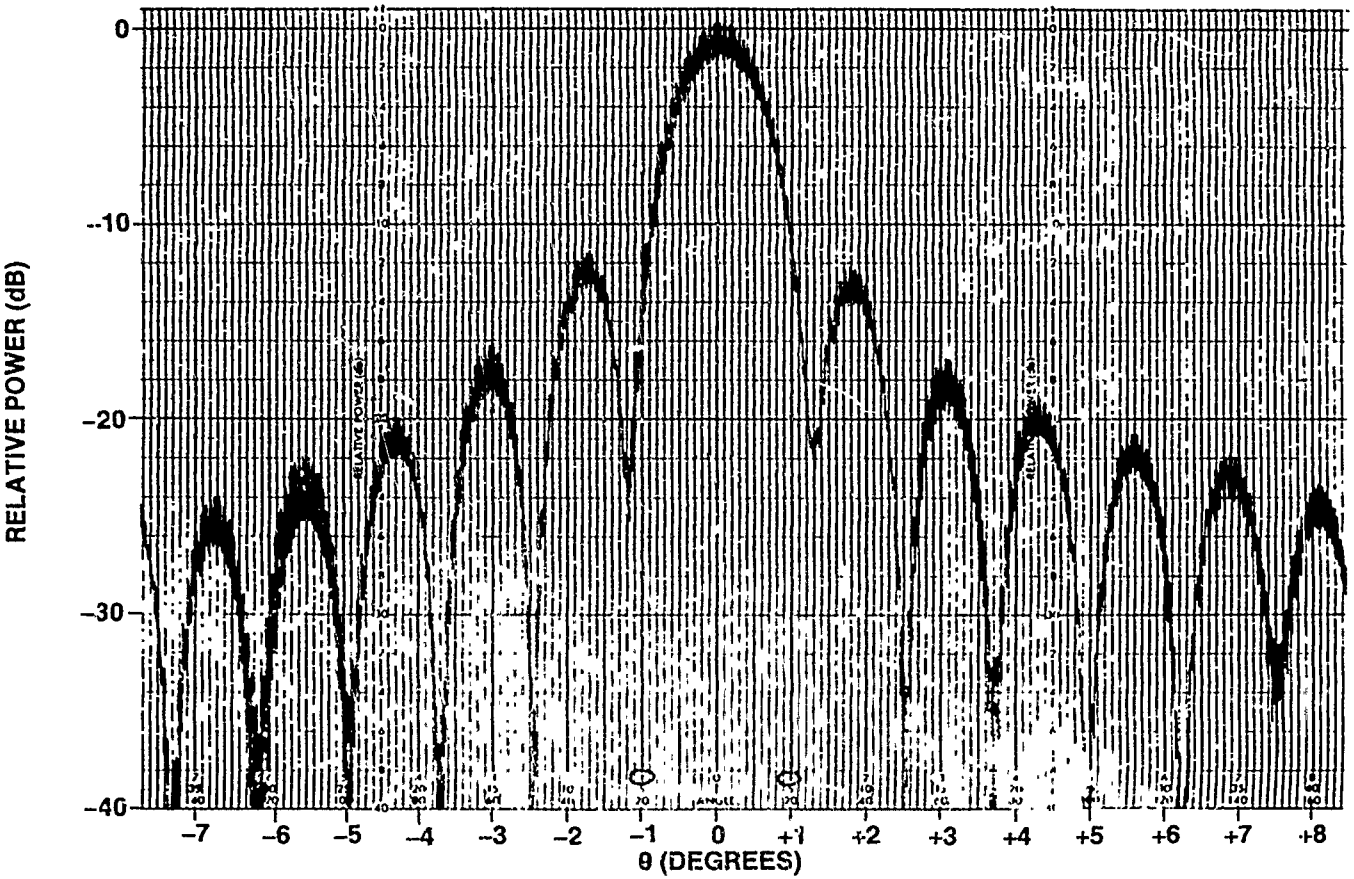

61846-5

Table II. (U) Radiation Pattern Summary for Q-Band Passive Array with Polarizer

Frequency F(GHz)	E-PLANE		45° - PLANE		H-PLANE	
	Boresight Axial Ratio (dB)	First Sidelobe Level (dB)	Boresight Axial Ratio (dB)	First Sidelobe Level (dB)	Boresight Axial Ratio (dB)	First Sidelobe Level (dB)
43.5	2	-13.9	1.6	-18.2	1.6	-13
44.5	2	-12.7	2	-17.5	2	-12.2
45.5	1.5	-13.1	1.5	-17.9	1.5	-12.6

ACKNOWLEDGMENTS

Supported by SATCOMA, Fort Monmouth, New Jersey
Contract No.DDAB07-84-C-J571

REFERENCES

1. Blakney, T.L., Burnett, J.R. and Cohn, S.B. (1972) A design method for meanderline circular polarizers. Paper presented at the 22nd Annual USAF Symposium on Antenna Applications, Allerton Park, Monticello Illinois.

2. Gysel, Ulrich H. and Robinson, Lloyd A. (1973) Investigation of Meanderline Polarizers for a Planar Antenna, SRI Project 2108-200. Final Report, Purchase Order No. 372669, Airborne Instruments Laboratory.

3. Clavin, Alvin (1974) An improved element for use in array antennas, IEEE Trans. Antennas Propogat. AP-22 (No.4): 521-526.

4. Papierz, A.B., Sanzgiri, S.M. and Laxpati, S.R. (1977) Analysis of antenna structure with equal E- and H- plane patterns, Proc. IEE 124 (No.1): 25-30.

5. Elliott, R.S. (1980) On the mutual admittance between Clavin elements. IEEE Trans. Antennas Propagat. AP-28 (No.6): 864-870.

UNIQUE
JOINT STARS PHASED-ARRAY ANTENNA

H. Shnitkin
Norden Systems, Inc.
Norwalk, CT 06856

1. ABSTRACT

The Joint STARS radar antenna is a 24-foot wide by 2-foot high planar X-band slotted array, scanned electronically via ferrite phase shifters to +/-60 degrees in azimuth and scanned mechanically to +/-100 degrees in elevation. (See Figures 1 and 2.) It is mounted inside a radome underneath the fuselage of an E-8A aircraft, (See Figure 3), and operates in a mapping as well as in a three-port interferometer azimuth target tracking mode.

Figure 1. Joint STARS Antenna on Pattern Range

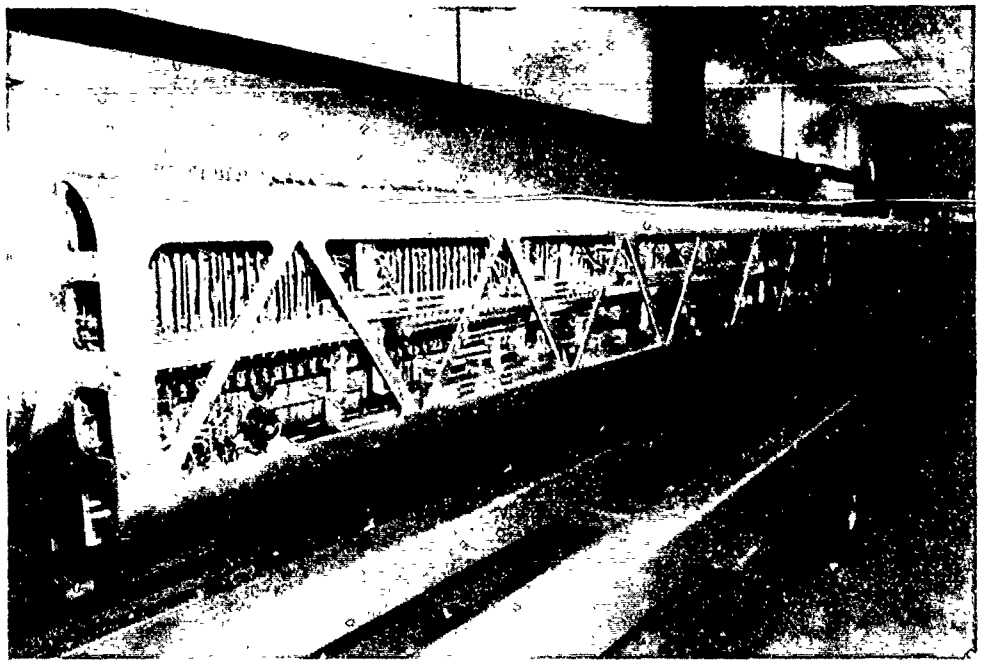

880109B-19

Figure 2. Rear View of Antenna

881203-1

Figure 3. Antenna Installed in EA-8 Aircraft

After a description of the antenna's architecture, performance, and construction, its five unique features are presented, namely:

1. Colinear slotted array aperture
2. Switchable dual-mode aperture
3. Multifunction electronic phasing
4. Automated phase alignment
5. Triple temperature compensation

2. ANTENNA DESCRIPTION

The Joint STARS antenna is a horizontally polarized, rectilinear lattice slot array, exhibiting extremely low azimuth and elevation sidelobes, and is capable of high precision azimuth tracking. Its aperture illumination is switchable via ferrite phase shifters so that it can generate a single, low sidelobe beam or three triple width low sidelobe beams from each one-third section of the aperture. The latter mode, called *interferometer tracking*, essentially divides the aperture into three parts and permits individual receive phase measurements to ascertain direction of arrival from differential time delay or phase measurements. In addition, a multichannel microwave receiver with Transmitter/Receiver limiters and RF down converters is part of the antenna.

2.1 Performance - Because of security restrictions, no detailed performance data can be devulged, except that the antenna operates over 3% in X-band, exhibits very low sidelobes in all modes, supports a

high power radar transmitter and possesses fractional milliradian boresight and beam pointing accuracies.

2.2 Antenna Architecture - The aperture consists of 456 vertical linear 28-slot array radiating elements, which are connected to twelve waveguide dual-mode feeds (DMF÷38) via ferrite phase shifters, compensating delay lines, and twist and match sections, as shown in Figure 4. Each vertical slotted array consists of a four-way divider (EL÷4) and four seven-slot resonant subarrays. The ferrite phase shifters are of the latching, nonreciprocal type, require 8-BIT digital phase commands, and can switch modes or scan angles within 7 μs at the PRF. The twist and match sections (quantity of 1824) are rectangular, horizontally polarized waveguide to double-ridge, vertically polarized, waveguide

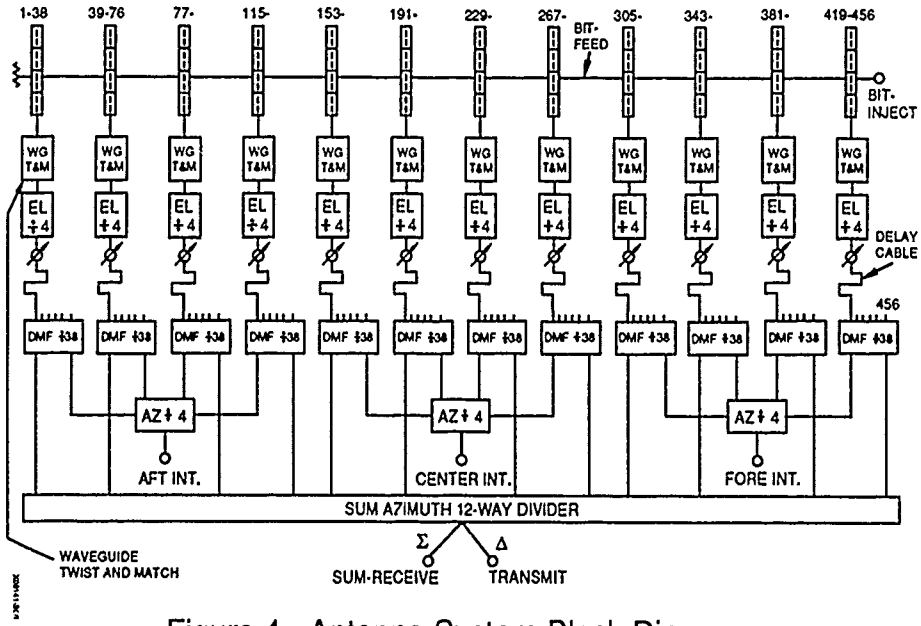

Figure 4. Antenna System Block Diagram

transitions with a high-Q resonant iris. These sections interconnect from the aperture's ridge waveguide to the four-way power divider's rectangular waveguide and provide optimum impedance match to the array at 42° of azimuth scan.

The compensating delay lines are semirigid, silicon dioxide coaxial cables whose group delay corrects for the differential phase delays of the waveguide dual mode feed to maintain accurate aperture phase over the instantaneous frequency band. Each dual-mode feed couples 38 radiators to either the sum corporate feed in the mapping mode or to one of three interferometer corporate feeds (AZ÷4) in the tracking mode. Both corporate feeds are time delay compensated waveguide directionalcoupler feeds and therefore achieve broadband phase and amplitude uniformity.

In addition, a loosely coupled traveling wave feed is added to the rear of the aperture with a -45 dB coupling path to each of the 456 elevation slot arrays. Its purpose is to simulate a received wave from about 47° in azimuth by injecting an RF test signal into the BIT INJECT port. This BIT feed is used for aperture phase alignment and in-flight pattern performance checks.

2.3 Construction - The mechanical construction is shown in Figure 5. A four-sided structural frame is formed by a three-sided aluminum trestle and the radiating aperture. The large triangular windows in the trestle surfaces allow easy access to install and service all electronic components while assuring structural rigidity and aperture

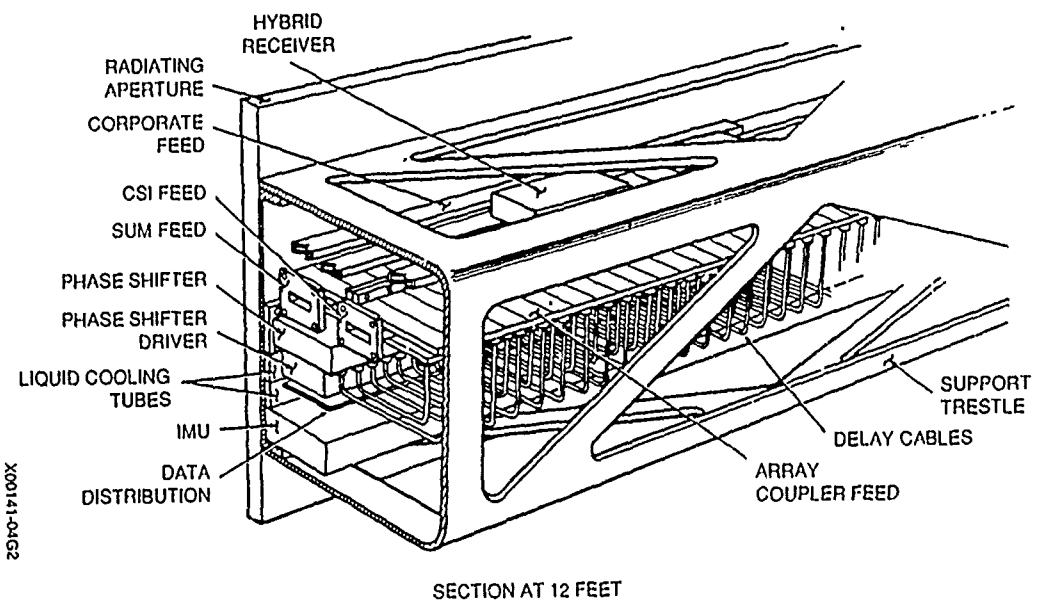

Figure 5. Mechanical Assembly of Antenna

flatness within .030 inch TIR. Semirigid cables were chosen to connect the phase shifters to the feed so as to allow for mechanical alignment tolerances and to facilitate phase shifter replacement.

3. COLLINEAR SLOTTED ARRAY APERTURE

The aperture consists of 456 vertical 28-slot arrays, each a single-ridge waveguide with broadwall shunt slots. Traditional broadwall slotted arrays require alternating slot displacement from the waveguide centerline, as shown in Figure 6. This configuration can be construed as the sum of an array comprising all "A" slots plus an array of all "B" slots. Both the "A" and the "B" array possess grating lobes due to their large

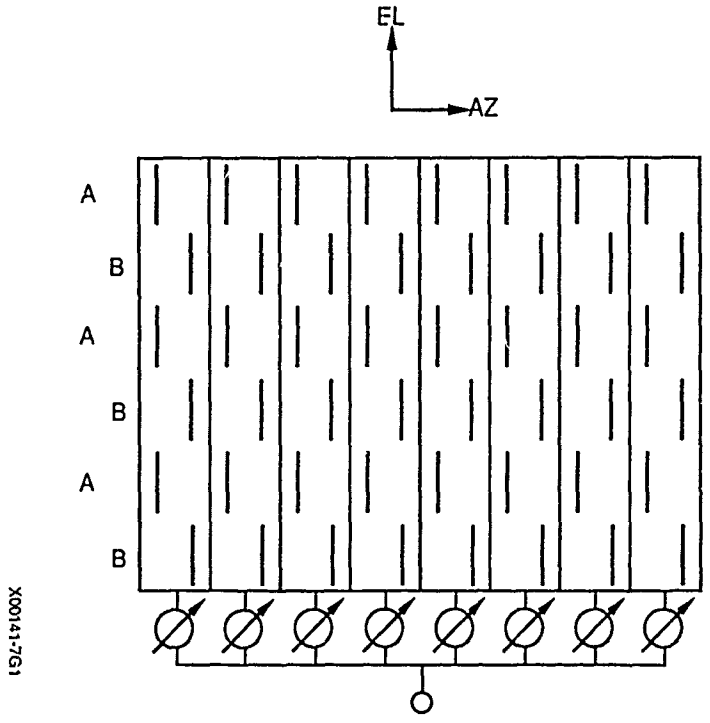

Figure 6. Conventional Waveguide Broadwall Slotted Array

vertical slot separation. But together at 0° azimuth the grating lobes are changed into ordinary sidelobes by the combination array factor. This is no longer true during azimuth scan causing a gradual transition from side lobes to intercardinal grating lobes as scan angle is increased. [Ref. 1] Since these secondary beams, or grating lobes, exceed the required sidelobe level, a truly collinear slotted array radiator was devised. [Ref. 2 and 3]

All slots are placed on a common centerline, while the trough depths of the ridge waveguide are altered periodically to achieve a waveguide field asymmetry, as illustrated in Figure 7. Thus, the electrical centerline, where the longitudinal H-field vanishes, can be displaced by

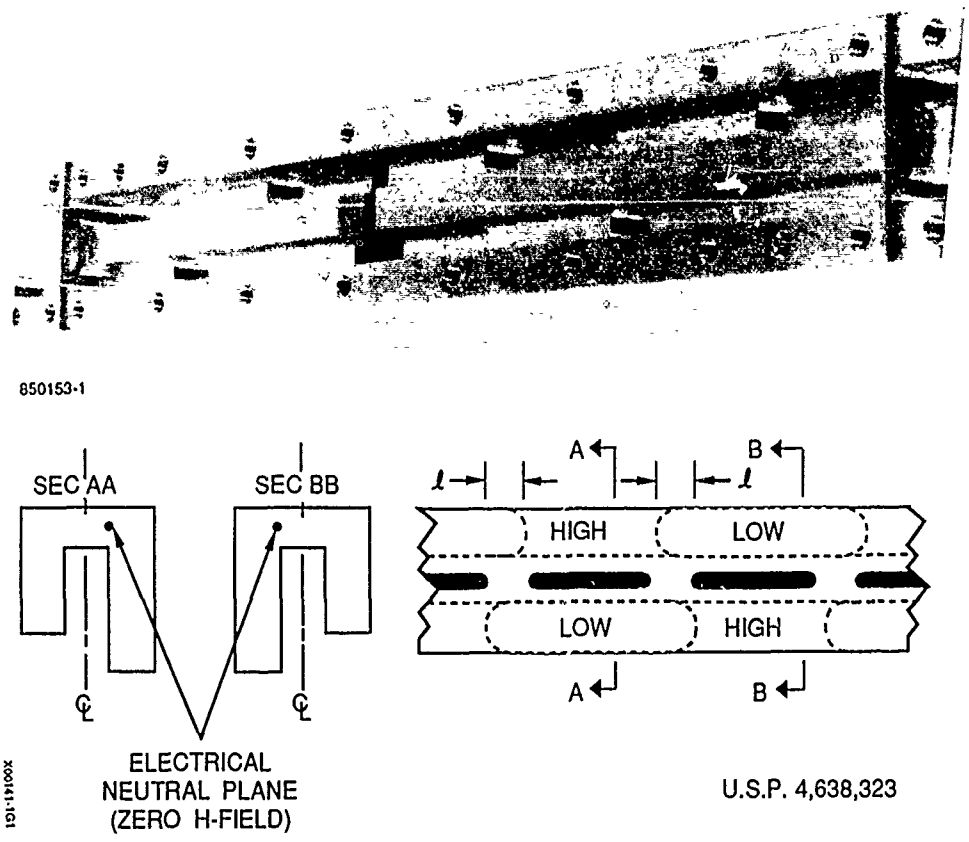

Figure 7. Collinear Slotted Array Configuration

varying amounts from the physical centerline. Slot conductance, guide wavelength, and 0°/180, phase can therefore be controlled by appropriate choice of the ridge waveguide trough asymmetry. This results in an easily manufacturable array design with all slots on a common centerline.

The success of the L slot collinear array was demonstrated by measured array elevation patterns, which achieved sidelobe levels to meet the specified maximum sidelobe envelope.

4. SWITCHABLE DUAL-MODE APERTURE

By appropriate commands to the ferrite phase shifters, the twelve dual-mode feeds convert one total low sidelobe aperture with tapered illumination for the mapping mode into three, one-third aperture, tapered illuminations for the tracking mode (see Figure 8). Each dual mode feed consists of two cascaded traveling wave directional coupler distribution feeds (Figure 9), similar to a two-beam Blass-type multibeam feed. [Ref. 4 and 5]. However, instead of the similar illumination and different linear phase tapers of the Blass feed, two different illuminations and two phase functions, specifically designed for maximum decoupling between the two traveling wave feeds, are produced. Mode switching via the phase shifters is accomplished by selectively adding one of two phase collimating functions to the scan angle phase taper. Each phase collimating function produces a linear aperture phase taper for only one mode and a decollimated, and thus decoupled, aperture phase for the other.

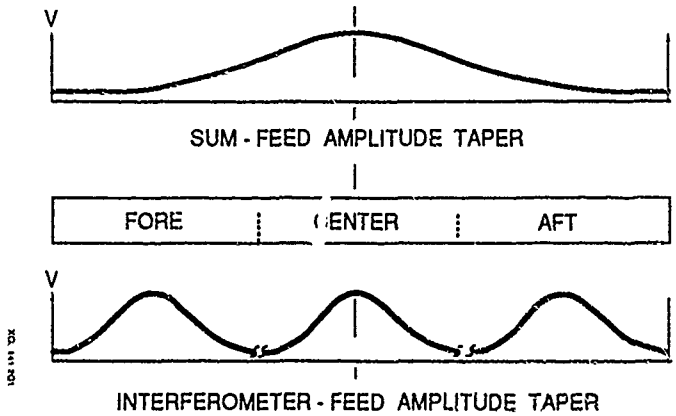

Figure 8. Aperture Illumination Function

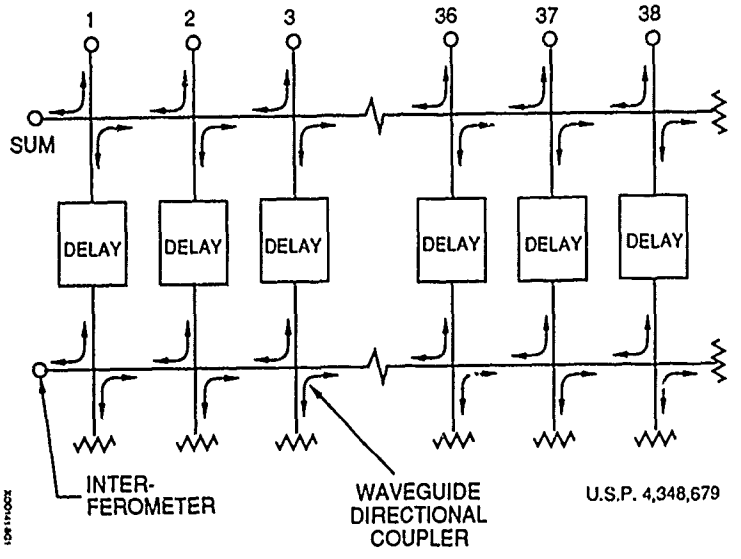

Figure 9. Dual-Mode Feed (DMF÷38)

The RF delays between the two rows of couplers have been adjusted at the factory to precisely yield the required output port power levels for the rear (interferometer) feed by controlling the phase difference between the voltage coupled from the rear feed and that from the front feed. The latter is produced by unavoidable coupling of the front feed directional couplers.

While the dual-mode feed produces the two prescribed aperture magnitudes, one for total aperture and one for one-third aperture, the transmission phases to each radiator are allowed to be arbitrary. This flexibility was purposely provided to allow the component manufacturers to concentrate on very accurate amplitude control. The arbitrary

transmission phases are subsequently compensated by the ferrite phase shifters, using a phase alignment table as described in Section 6.

5. MULTIFUNCTION ELECTRONIC PHASING

5.1 Description of the Ferrite Phase Shifters - The Joint STARS antenna utilizes 228 latching, nonreciprocal, dual ferrite phase shifter assemblies manufactured by Electro-Magnetic Sciences, Inc. (See Figure 10.) Nineteen of these are serially loaded at a 5-MHz clock rate with 8-Bit phase shift commands. A redundant set of data shift registers are provided to avoid catastrophic antenna failure should a single shift register in any chain of nineteen fail. Single saturated current reset is used to erase previous magnetic history. A 1.5-degree RMS differential

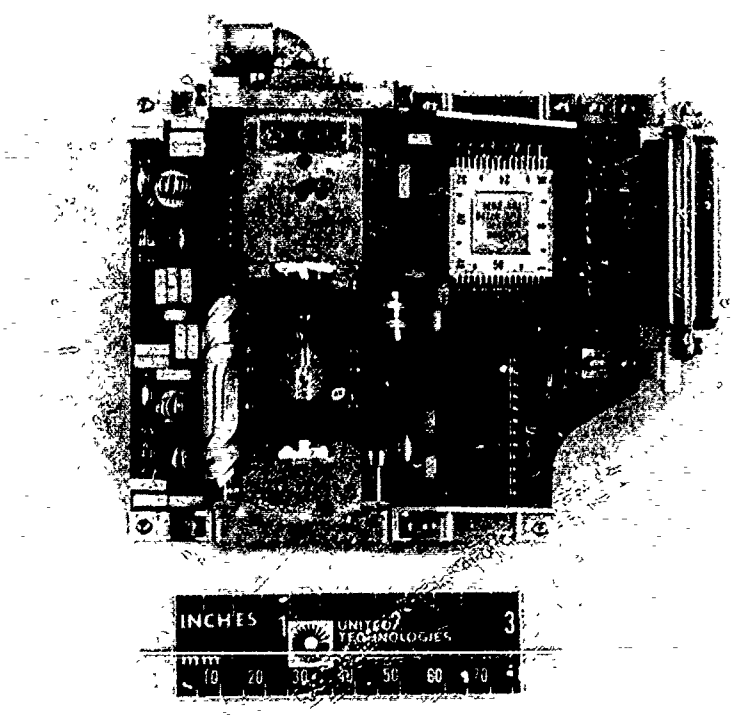

870322-1

Figure 10. Ferrite Phase Shifter Assembly

phase accuracy is mainly achieved via a magnetic flux sampling coil, a volt x time = flux integrator circuit, and an analog flux command comparator. The latter also performs a BIT function by confirming all successful ferrite flux drive sequences. Another important contributor to phase accuracy is an E-prom containing measured microwave phase data at specific frequencies and temperatures. This data is used to construct phase linearization tables needed to modify input phase commands to obtain the desired RF phase, as explained in Section 7.1.

5.2 Phase Shifter Tasks - Because of the high cost per ferrite phase shifter, six tasks have been assigned to it in addition to the obvious beam scanning function, as explained below.

1. *Mode Switching* - Either mapping beam or the three interferometer tracking beams are selected via the phase shifters. Specifically, the dual-mode feed (DMF÷38) phase delays are phase compensated for aperture collimation for either mapping or tracking mode, while randomly phased for the unwanted mode. Since mode switching can be accomplished within 7 μs, the radar can transmit a full aperture SUM beam while receiving on three, one-third aperture, INTERFEROMETER beams.

2. *Duplexing* - Adding 180° to the commands for phase shifters No. 1 through 228, switches the aperture collimation from the Sum-Receive port of the AZ-sum feed to the difference or Transmit port. (See Figure 4.) For Sum-

Receive the E-plane arm of the input magic tee is used and for Transmit, the H-plane arm. Thus a circulator/duplexer handling the full transmit power is avoided.

3. *Aperture Phase Alignment* - The combined feed assembly is permitted a 200° random phase tolerance for ease of manufacturing and for minimizing phase shifter quantization lobes. Every phase shifter command contains a phase compensation term to collimate the above random phase. This compensation phase is obtained by the automated phase alignment procedure described in Section 6 and is stored in eight alignment tables, for four frequencies and two modes.

4. *Thermal Compensation* - Aperture phase errors due to thermal distortion (bow and expansion) of either the aperture or the corporate feed are compensated for temperature via corrective phase shifter commands to maintain low sidelobes in flight. (For details see Section 7).

5. *Beam Broadening* - A quadratic or a cosine phase error is added to the phase shifter commands to broaden the main lobe for the rapid search radar mode without raising the random sidelobe level. The amount of quadratic or cosine phase error can be adjusted for as high as a hundred-fold increase in beamwidth.

6. *Self-Test* - Sequentially increasing the aperture phase taper commands to the ferrite phase shifters, while applying a test signal to the BIT-Inject port (Figure 4), produces an electrically scanned antenna pattern at the radar receiver. This pattern can be analyzed for conformance to the specification and for antenna trouble shooting.

Summary - The total resulting phase command to all ferrite phase shifters consists of the sum total of the following four 456-number arrays:

a. Ideal scan angle phase taper
b. Insertion phase alignment correction
c. Thermal compensation phase
d. Beam broadening phase

6. AUTOMATED PHASE ALIGNMENT

6.1 Description - The feed system exhibits up to 200° of random phase error due to manufacturing tolerances of the waveguide corporate feeds, dual-mode feeds, delay cables, ferrite phase shifters, four-way power dividers, and aperture. To maximize antenna gain, minimize sidelobes, and maintain boresight accuracy, phase compensation must be supplied through the ferrite phase shifters. This requires a measurement of aperture phase error from which an insertion phase alignment table is generated. Essentially, this phase alignment table is defined as the 456 negated measured aperture phase values of the

assembled antenna system. To achieve perfect aperture phase, i.e. perfectly linear phase taper, always add the above negated measured phase values to their respective scan phase commands.

The radar provides a computerized method for phase aligning the aperture in less than half a second, using either a received radiated RF signal or a test signal applied to the BIT-Inject port, shown in Figure 4. (for details see Ref. 6)

Three sequential phase alignments are generally performed; these are defined as follows:

1. *Range Alignment (RA)*: This is performed at the factory, using a far-field radiated signal from the zero azimuth direction, at temperature profile T1.
2. *First BIT Calibration (BC1)*: This is performed at the factory using an RF test signal applied to the BIT-Inject port at temperature profile T1.
3. *Second BIT Calibration (BC2)*: This is performed in-flight, using an RF test signal applied to the BIT-Inject port, but at ambient temperature profile T2.

Applying the negated RA values as phase shifter commands generates constant phase across the aperture at temperature T1 in the Transmit mode. Subtracting the two alignment tables, RA minus BC1, produces a *BIT-Feed Correction* table. This table provides for temperature insensitive phase conversion, allowing a BIT-Feed aligned antenna to be converted into an aperture-aligned antenna. Applying the

negated RA - BC1 + BC2 values as phase shifter commands produces constant aperture phase in-flight at temperature profile T2, by correcting RA, the alignment at temperature T1, by the change in alignment due to in-flight temperature change from T1 to T2.

The following procedure will align the antenna aperture:

1. Apply RF excitation (far-field or BIT-injection)
2. Set phase shifters to 456 sequential linear phase commands [456 linear phase differentials, from 0° to (455/456) x 360°]. This is equivalent to 456 progressive scan angles.
3. Measure received voltage vectors at the antenna's sum and three interferometer ports for each of the above 456 phase commands.
4. Perform a Fast Fourier Transform (FFT) computation on the 456 voltages measured in (3) to obtain complex aperture excitation voltages.
5. Negated phase of excitation voltages of (4) constitute an alignment table (RA, BC1, or BC2) for addition to the phase shifter scan commands.
6. To verify the above procedure repeat steps (1) through (4) after adding the alignment table of (5) to all phase commands. Examine the measured pattern in (3) and the phase and amplitude deviations in (4) to ascertain the alignment quality. A 3° rms phase error and a 0.34 dB rms

amplitude error will assure adequately low random sidelobe level.

6.2 Experimental Results - Simulated computer print-outs from the above alignment procedures are shown in Figure 11 to illustrate the precision of the aperture amplitude and phase alignment as well as theelectronically scanned antenna sidelobes. The upper plot starts at the left with the peak to the main beam, followed by all the right-side and then the left-side sidelobes, and ends at the right just short of the peak of the main beam. The other two plots are generated after performing an FFT and show amplitude and phase precision. Precision is highest near the array center and poorest at the array edges, where the array voltage is only about 9% that at the center.

The measured patterns of the five completed antenna systems illustrate the quality of the alignment. In all cases the specified maximum and 92% sidelobe limits were achieved for the 24-foot array. Furthermore, the measured patterns are consistent with sidelobe predictions based on aperture phase and amplitude tolerances as well as systematic sidelobes.

6.3 BIT-Feed Diagnostics - As a by-product of BIT-Calibration or Range Alignment, the quality of the antenna pattern, generated by measuring received signal strength while commanding the phase shifters to sequentially increasing aperture phase tapers, and the causes of pattern deficiencies can be diagnosed, as follows.

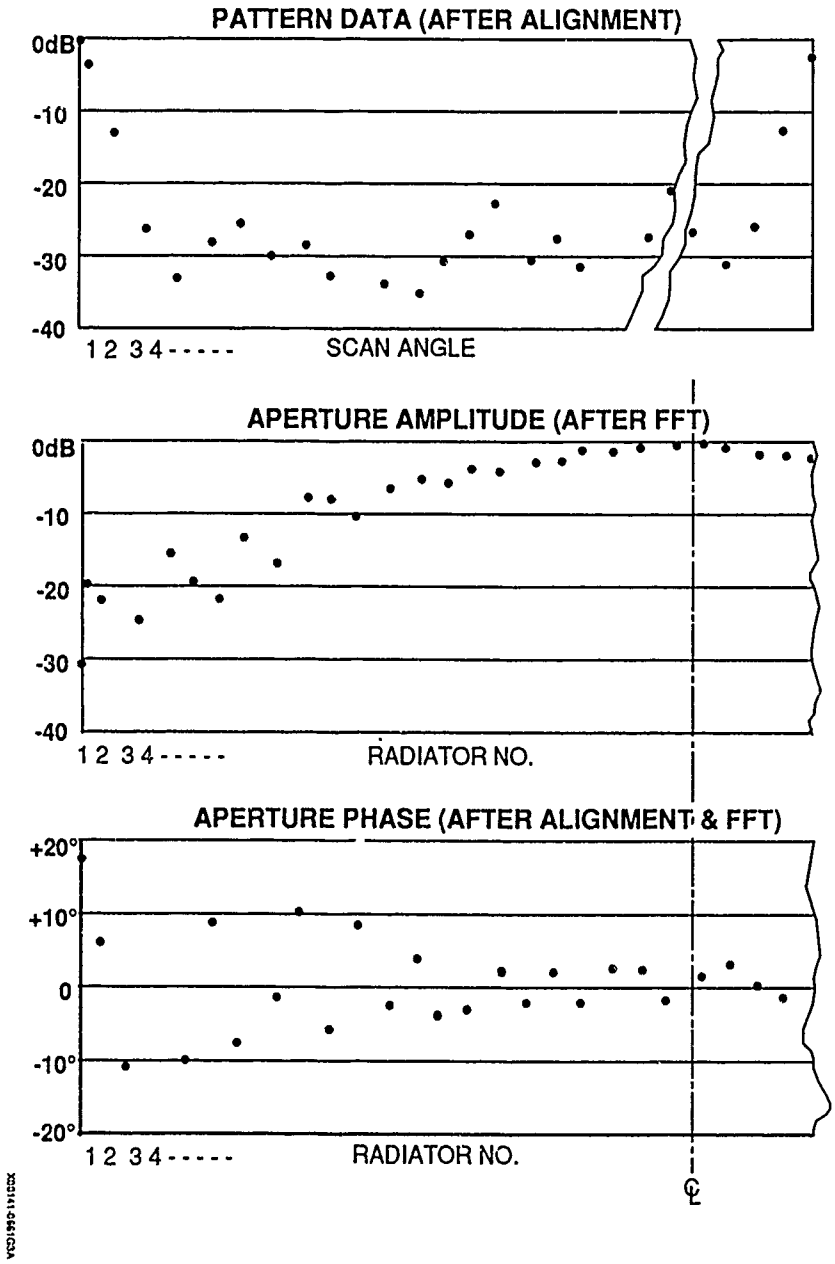

Figure 11. Simulated Range Alignment Computer Print-Outs

Examine the electronic scan pattern which was measured after applying alignment phase correction. If the sidelobes are excessive, look for:

1. Exceptionally low amplitude of an individual radiator, indicating a faulty RF connector, waveguide, or phase shifter.
2. Excessive random phase variation, indicating a faulty phase shifter or a noisy receiver.
3. Excessive random amplitude variation, indicating a faulty corporate feed, a faulty dual-mode feed, or a noisy receiver.

7. TRIPLE TEMPERATURE COMPENSATION

7.1 Phase Shifter Phase Linearity - Both, a temperature sensor and an E-prom containing a measured RF phase data table, are resident on every phase shifter for the purpose of instructing the beam steering computer how to calculate the appropriate phase linearization command table. This table is used to look up the compensated or linearized phase command to the phase shifter needed to achieve the desired RF phase shift at the current temperature and frequency.

7.2 Aperture Distortion - Data from temperature sensors at the aperture and at the rear of the antenna structure (trestle) allow computation of phase shifter command compensation to correct for a thermal aperture bow. This compensation is handled just like the beam broadening described in Section 5. In addition, thermal aperture growth

is computed and differential phase between adjacent radiating slots recalculated at the new temperature before scanning the beam electronically.

7.3 Feed Distortion - Ambient, phase shifter dissipation, and nonuniform transmitter power heating of the waveguide corporate feed cause severe aperture phase errors in flight. These are corrected by the three sequential phase alignment procedures described in Section 6, namely: Range Alignment, BIT Calibration at same temperature at the factory, and a second in-flight BIT Calibration. Every several minutes an updating in-flight BIT Calibration (BC2) is performed. Using the factory supplied tables of RA and BC1, an updated aperture alignment table of -(RA - BC1 + BC2) is computed and added to each phase shifter command every nine minutes. (See Section 6.)

8. CONCLUSION

The design, performance, and unique features of the Joint STARS phased array antenna were presented. These included:

1. A novel collinear slot array configuration
2. Switching between low sidelobe sum and low sidelobe interferometer modes via ferrite phase shifters
3. A rapid in-flight phase alignment technique
4. A method of maintaining phase alignment and low sidelobes over a wide temperature range.

9. ACKNOWLEDGEMENTS

Acknowledgement is hereby given to the program sponsor, ESD-JSPR, Hanscom Air Force Base, MA., and the prime contractor, Grumman Melbourne Systems Division.

10. REFERENCES

1. Kurtz, L.A., and Yee, J.S., *Second Order Beams of Two Dimensional Slot Arrays,* IRE Trans A-P, pp. 356-362, Oct. 1957.
2. U.S. Pat. 4,638,323, Jan 20, 1987: *Asymmetric Ridge Waveguide Collinear Slot Array Antenna*, by H. Shnitkin and J. Green.
3. Shnitkin, H., Green, J., Bertalan, P., Norden Systems, *Asymmetric Ridge Waveguide Radiating Element for a Scanned Planar Array,* 1988 IEEE APS International Symposium Digest, pp. 55 and Proceedings of the 1988 Antenna Applications Symposium, University of Illinois.
4. U.S. Pat. 4,348,679, Sept. 7, 1982: *Multimode Dual-Feed Array Radar Antenna*, by H. Shnitkin and P. Smith.
5. Hanson, R.C., *Microwave Scanning Antennas*, Vol. 3, pp. 247.
6. Shnitkin, H., *Rapid In-Flight Phase Alignment of an Electronically Phase Scanned Antenna Array*, Phased Arrays 1985 Symposium (Report RADC-TR-85-171, pp. 293)

AN OCTAVE BAND HIGH GAIN RECEIVE CYLINDRICAL ARRAY ANTENNA WITH FULL AZIMUTH COVER *

by J.C. Herper, A. M. Bucceri and J. J. Stangel

UNISYS CORPORATION

UNISYS S&GSG

GREAT NECK, NEW YORK

Abstract - An octave bandwith, compact high gain receive antenna providing multiple beams with 360-degree azimuth coverage has been developed. A test antenna has been fabricated consisting of a Luneburg lens collimator feeding a cylindrical array of 128 column networks.

Multiple simultaneous beams are realized in azimuth by focusing the received signals through the Luneburg lens to a focal aperture. A circulator at each lens port provides the isolation between the column networks and the receiver. Adjacent lens ports are combined after the circulators to provide the desired focal aperture to which a receiver is connected. The lens focal aperture design controls antenna beamwidth to be approximately constant with frequency for an octave bandwidth.

The column networks generate a CSC^2 fan beam in elevation. Each printed stripline circuit consists of a broadband 16 to 1 power combiner with baluns and dipoles incorporated into a com-

* This work was supported in part by the USAF, Air Force Systems Command, Hanscom AFB under contract number F19628-85-0018.

pact and lightweight design. Broadband Wilkenson tee type power combiners and transmission line lengths are configured to realize the appropriate amplitude and phase distribution. Schiffman type phase shifters constitute the balun design providing the transformation from unbalanced to balanced two wire line feed for the wideband dipole.

Full 360 degree azimuth coverage is demonstrated for simultaneous beams showing agreement with computer model predictions for both beamwidth and sidelobe level control. These patterns also confirm the relationship between the Luneburg lens focal aperture and antenna beamwidth invariance with frequency.

INTRODUCTION

This paper describes the design, development and experimental evaluation of an octave bandwidth cylindrical array for an advanced radar application. The application requires that the array efficiently receive signals simultaneously in a cluster of contiguous high gain beams which may be electronically scanned to any azimuth sector. The combined requirement for high efficiency, high cross-over, low sidelobes and octave bandwidth represents a challenging antenna design problem.

The design approach is illustrated by the functional diagram of Figure 1. N column networks with integrated radiating elements are arranged to form the cylindrical array. Signals incident on the array exit from the column networks through single pole, double throw (SPDT) switches to a two-dimensional Luneburg lens network. The Luneburg lens has a circular geometry with ports along its perimeter. Signals incident from a given azimuth are focused toward the opposite ports of the lens. The focused signals exit through the SPDT switches to the electronic switching matrix. The switching matrix accesses the M Luneburg lens ports associated with the azimuth sector designated for beam formation. The switching matrix contains single pole, multi-throw switches where the number of throws equals N/M and determines the angular width of the sector for simultaneous coverage.

The signals emanating from the switch ports are amplified and combined in a beam weighting network to produce K beams. To achieve low sidelobes and high cross-over between adjacent beams, a lossy beam weighting network is generally needed, and hence the low noise amplifiers (LNA's) preserve signal-to-noise ratio. With proper choice of beam weights, the antenna produces beams whose gain, beamwidth, sidelobes and pointing direction are substantially independent of frequency.

These design principles and performance characteristics are demonstrated by the experimental model antenna pictured in Figure 2. The model, which operates in S-through C-band, is a cylindrical array formed from 128 columns of vertically polarized dipoles. The unit is capable of simultaneously producing eight contiguous beams over any electronically selectable 45 degree angular sector. As illustrated in the block diagram of Figure 3, the configuration and operation of the demonstration antenna is similar to that of the baseline design approach except that (1) circulators are used in place of SPDT switches, (2) 3 dB power dividers are used after the circulators to simplify the switching matrix and eliminate the beam weighting network and (3) the LNA's are deleted. The design, construction and measured performance of the demonstration model are detailed in the following sub-sections of this paper.

DEMONSTRATION MODEL DESIGN

The cylindrical array/Luneburg lens antenna represents a

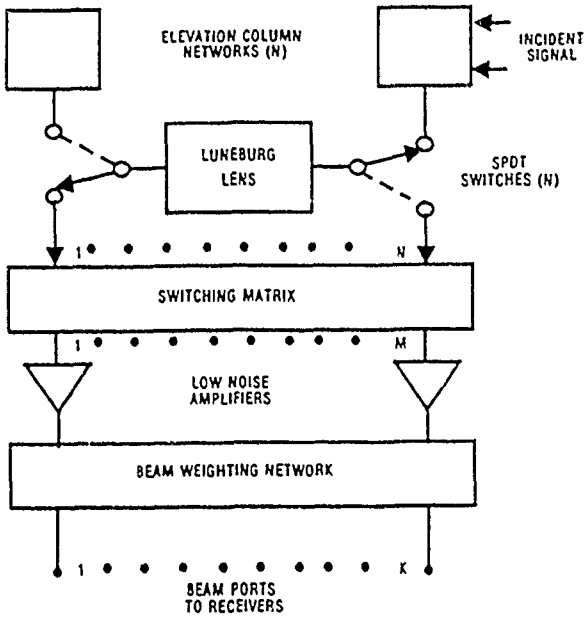

Figure 1 - CYLINDRICAL ARRAY DESIGN APPROACH - A two-dimensional Luneburg lens beamformer allows wideband simultaneous reception on a cluster of directive beams covering an electronically selectable azimuth sector.

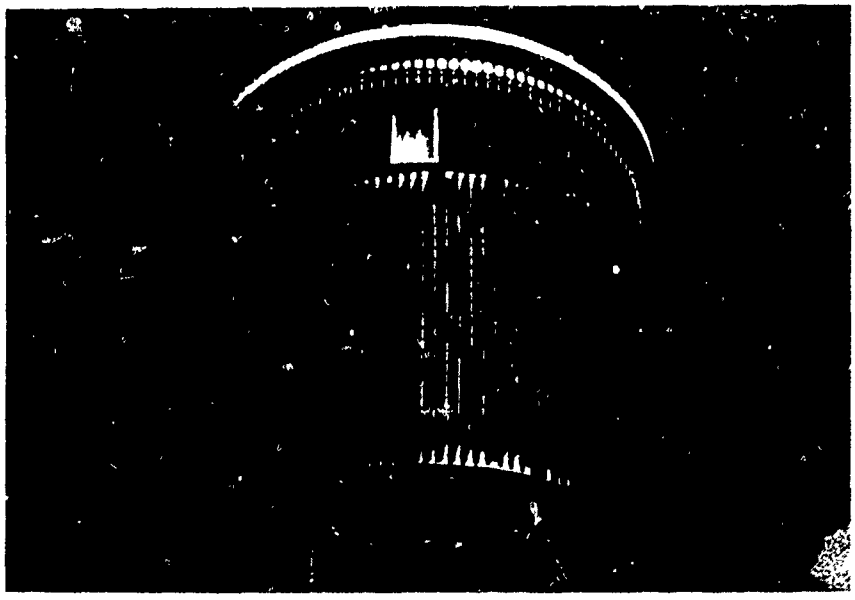

Figure 2 - DEMONSTRATION MODEL - The key principles of the approach are verified in an experimental model which operates over the octave band from 3.0 to 6.0 GHz.

near optimal design for an octave band, high gain receive antenna with 360 degree coverage in azimuth. This configuration requires 25 percent fewer elements, is more compact and utilizes a single lens beamformer compared to a multifaced planar array approach. The Luneburg lens coupled with a multiple beamforming switching network is a simpler and more reliable design than the complicated commutator transfer switch commonly used in cylindrical arrays.

The cylindrical array lattice design is based on the scan requirements determined by elevation coverage for the cosecant-squared fan beam and the projected illuminated aperture on the cylinder in azimuth. For octave bandwidth operation, the rectangular lattice inter-element spacing was calculated at the highest operating frequency to conform to a main beam elevation coverage of 25 degrees and an azimuthal scan of $\pm$60 degrees. The demonstration model antenna is comprised of a cylindrical array of 2,048 vertically polarized dipoles arranged in 128 columns. The array is 40 inches in diameter and 22-1/2 inches high. Dipoles are integrated with a stripline elevation distribution network to comprise a single column network assembly. A corporate power divider with wideband Wilkinson tee couplers generates a vertical illumination consistent with realizing cosecant squared elevation coverage to 25 degrees over the specified octave band (3.0 to 6.0 GHz).

Azimuth collimation of signals entering the antenna through

the column networks is implemented with a two-dimensional Luneburg lens[1], whose interconnection with the column networks is illustrated in Figure 3. The Luneburg lens shows superior performance characteristics over an octave bandwidth because of the continuity of its index of refraction. Simultaneous collimation in all azimuth directions is achieved by radially varying the propagation constant in the lens medium. This is accomplished by varying the effective dielectric constant to provide real time delay for wideband operation.

Signals entering the Luneburg lens along a given arc come to a focus at a point opposite to this arc. Thus, the same port of the Luneburg lens is an entry point of signals from the column network and an exit point for signals to the switch matrix where these signals impinge on the cylindrical array from substantially opposite azimuth directions. Adjacent focal ports may be weighted and combined to provide the appropriate lens excitation to meet antenna beamwidth and sidelobe requirements. In general, for beamwidth invariance control, focal aperture lengths greater than one wavelength will contract azimuth illumination with increasing frequency thereby reducing the variation in beamwidth. The insertion of wideband circulators between the column networks and Luneburg lens ports isolates exiting and entering signals by virtue of the circulators non-reciprocal properties. Use of the circulators enables the use of a single beamformer lens and

results in a more compact beam feed network for octave band operation.

LUNEBURG LENS

The design of the Luneburg lens is based on a radially symmetric lens whose dielectric constant is determined as a function of the radius to any point within the lens circumference. The relationship governing this principal was derived by R. K. Luneburg[2] using geometric optics:

$$n = \sqrt{\varepsilon_r} = \sqrt{2 - r^2/R^2} \qquad 0 \leq r \leq R$$

where n is the refractive index, R is the radius to the perimeter of the lens and r is the radius to any point within the lens region. The amount of dielectric fill in a region is directly analogous to the refractive index of that region. By varying the height of the dielectric as a function of the radius, radiation of a point source at the edge of the lens produces a linear phase front exiting on the diametrically opposite side of the lens as illustrated by the ray trace diagram of Figure 4. A computer program was implemented to provide lens design and milling machine data for the fabrication of a piece-wise linear, contoured lens.

The general function for this contour is derived from Snell's law and ray tracing methods[3] showing that at a point on a ray path:

$$\sqrt{\varepsilon_r}\,(r/R)\sin\delta = \sin\theta_o$$

where δ is the angle between the ray path and the radial line and

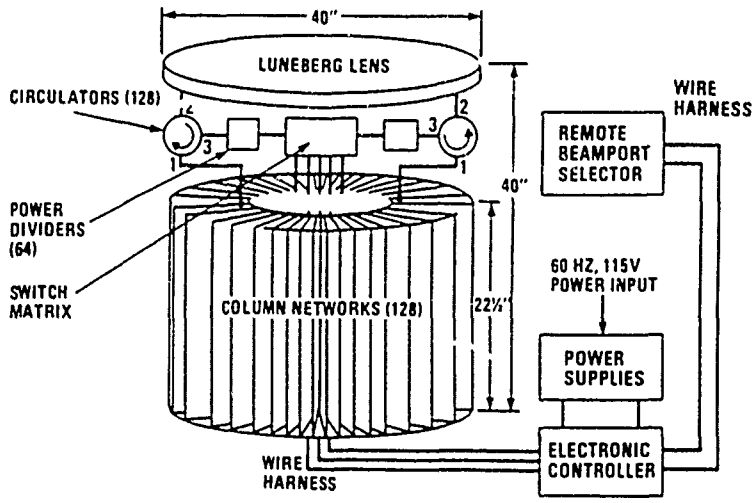

Figure 3 - **DEMONSTRATION MODEL BLOCK DIAGRAM** - The model is an electronic scanning cylindrical array incorporating all the key component hardware components inherent to the design approach.

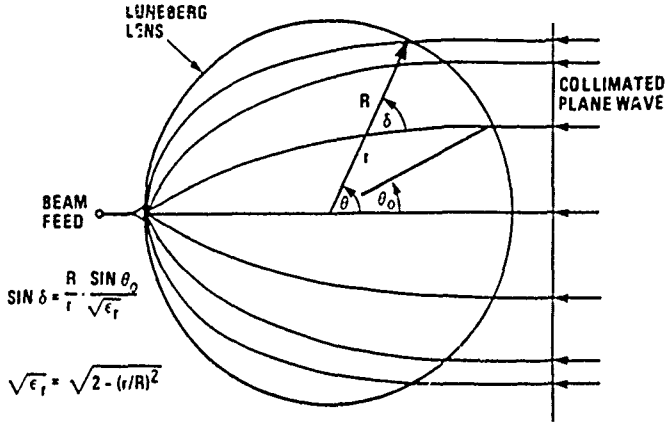

Figure 4 - **LUNEBURG LENS BEAMFORMER COLLIMATING PRINCIPLE** - The radially symmetric varying refractive medium in the two-dimensional lens focuses plane waves incident from any azimuth angle.

θ_o is the entering ray angle.

The demonstration Luneburg lens has a lid and a housing as shown in Figure 5. Together they form a cylindrical cavity, 41.16 inches in diameter and 0.50 inch high. This height is such that all but the dominant parallel plate waveguide mode are cut-off. Inside the cavity a Noryl lens is permanently bonded to the lid. This convex lens is 40.00 inches in diameter and 0.40 inch high at the center. The cavity formed by the lid and housing protects the dielectric lens. SMA connectors are mounted on the outside of the housing. The center conductor with Teflon insulation penetrates through the plate into the cavity where probe elements are affixed by means of a small setscrew. There are 128 probe elements mounted circumferentially along the outer perimeter of the cavity. The probes are equally spaced at one-half wavelength for the high frequency.

The design of the Luneburg lens probes employs a grating lobe series analysis for the determination of the input impedance. This assumes that the curvature of the lens is large enough for the probes to appear as though they are in a linear array. From this an initial probe configuration is obtained. Using a planar array simulator test fixture, the probe design is adjusted for a good match. Figure 6 shows the final probe match measured in the actual Luneburg lens environment and indicates better than a 1.6 VSWR over the octave band.

The excitation of the probes can be designed to produce far

Figure 5 - DEMONSTRATION MODEL LUNEBURG LENS - The Luneburg lens used in the demonstration model is a cylindrical cavity whose internal refractive index variation is determined by a contoured dielectric sheet.

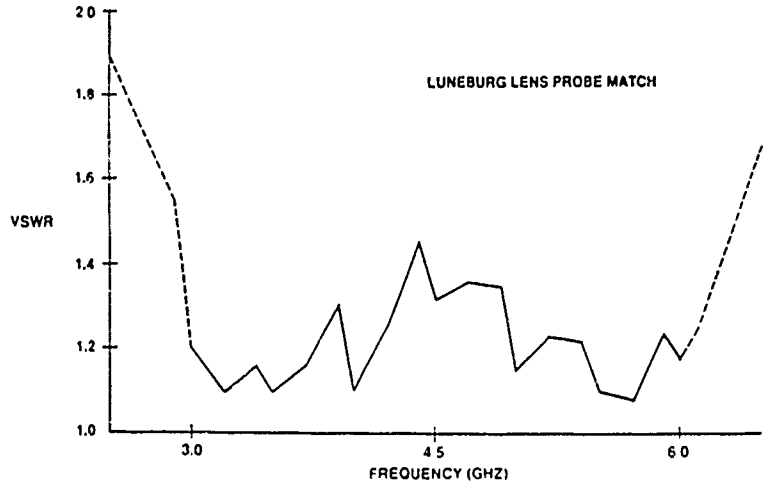

Figure 6 - LUNEBURG LENS PROBE MATCH - The input impedance of the Luneburg lens is matched over an octave bandwidth with a maximum VSWR less than 1.5.

field patterns whose azimuth beamwidths remain approximately constant over the octave bandwidth. The normal variation of beamwidth for a fixed aperture over an octave bandwidth is 2:1. Consequently, the effective aperture of the antenna must vary with frequency to maintain beamwidth invariance. As illustrated in Figure 7, the effective aperture produced by the Luneburg lens changes with frequency to minimize beamwidth variation. If the probes are excited to form a line source of length L, the width of the effective aperture, W, approximately equals 2R /L where

is the wavelength and R is the lens radius. This results in a far field half-power beamswidth of approximately L/2R, which is independent of frequency. If the probe excitation is such that L is greater than a wavelength at the lowest operating frequency, the far field beamwidth is substantially constant over the band.

CYLINDRICAL ARRAY ANALYSIS

The performance of the cylindrical array/Luneburg lens antenna is simulated using a computer program developed for this specific antenna configuration. The simulation computes the far field patterns via a diffraction calculation using the cylindrical array amplitude and phase distribution. The far field pattern can be calculated using Luneburg lens voltages obtained from a theoretical model or from experimental data.

The Luneburg lens is designed to give the desired far field pattern performance by optimizing the focal illumination. The appropriate output ports of the Luneburg lens are assigned volt-

age phases and amplitudes by superposing probe excitation on the opposite side of the lens. These probes are in the focal region and are spaced and electrically weighted to control the focal illumination. The focal illumination includes the effects of mutual coupling by employing element patterns for the probes computed using modal analysis. For this case a planar dipole array modal analysis program approximates the local region of the probes with the probe spacing used as the column spacing. The losses through the inhomogeneous lens cavity are included in the amplitude determinations.

Computed patterns for the demonstration antenna are presented in Figure 8. The antenna simulation is for 64 pairs of equally weighted focal probes forming 64 beam ports. From these results, the demonstration model Luneburg lens was designed, fabricated and tested. Far field patterns generated from measured lens port voltages are presented in Figure 9. There is good agreement between the theoretical and experimental patterns with regard to 3dB beamwidth and near-in sidelobes as shown over the entire octave frequency band. High backlobes present in the generated patterns for the measured lens result from inter-probe coupling[5] which causes energy to be reflected back through the circulators and to the array face. These backlobes can be eliminated by replacing the circulators with SPDT switches.

For a 20% beamwidth variation over an octave band, an optimum design utilizing three lens probes in the focal aperture with

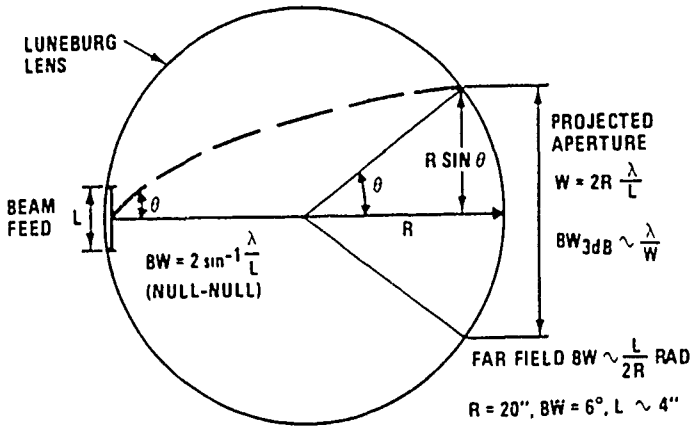

Figure 7 - **DESIGN FOR CONSTANT BEAMWIDTH** - The Luneburg lens facilitates an antenna design whose azimuth beamwidth remains substantially invariant with frequency.

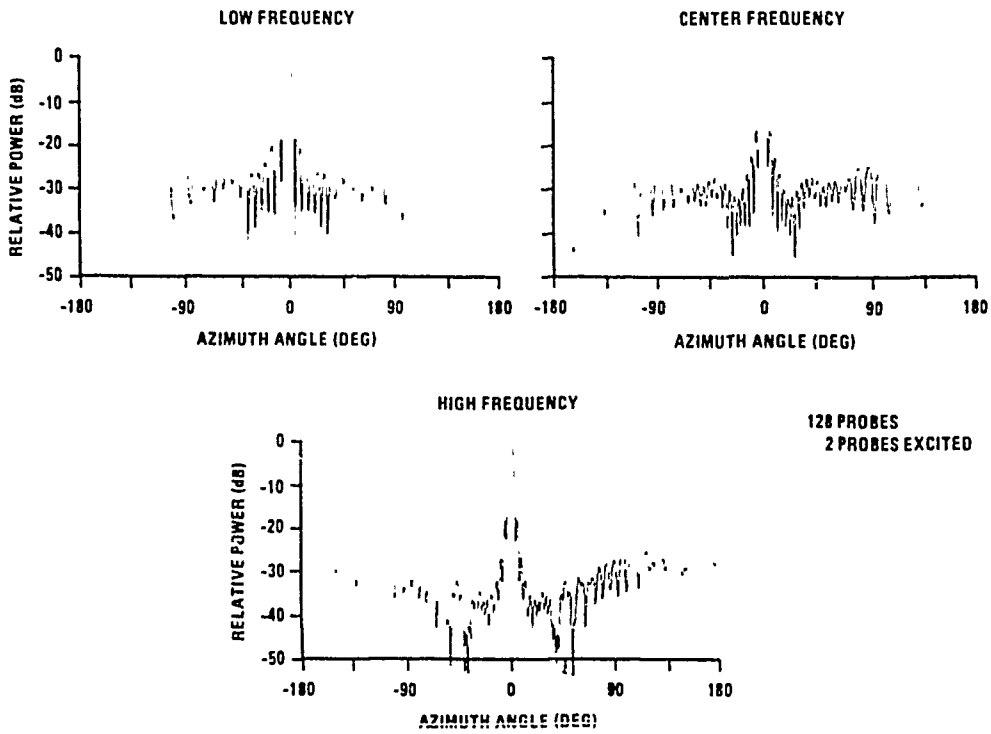

Figure 8 - **COMPUTED DEMONSTRATION MODEL PATTERNS** - The azimuth patterns of the cylindrical array are predicted using a computer model which incorporates analytically derived coupling coefficients for the Luneburg lens.

a power weighting of (0.5, 1.0, 0.5) is implemented as shown in Figure 10. This design requires low noise amplifiers in conjunction with these lossy feed networks since beam orthogonality requirements for all passive simultaneous beam antennas limit the efficiency for multiple probe feed networks. For this design receive signals pass through circulators to the switch matrix which selects a sector consisting of 16 contiguous lens ports and are amplified before being combined through the beamforming network resulting in 7 contiguous beamports.

A summary of the predicted performance generated from both computed and measured lens port voltages is given in Figure 11 which illustrates the 3 dB beamwidth control and the peak sidelobe level for various lens feed configurations over the octave band. These generated far field characteristics confirm the lens feed aperture relationship derived in Figure 7.

ELEVATION COLUMN NETWORK

A column network illumination is synthesized to realize a cosecant-squared fan beam to 25 degrees in elevation at the high frequency. The complex voltages at the elements are determined by Woodward synthesis using complex beam weights to match the desired elevation beam pattern. The voltage distribution transforms into a fan beam in the far field with the peak 2.5 degrees above the horizon and -3 dB or more energy on the horizon over the entire frequency band. The highest sidelobe is at 5 degrees below the horizon and 15 dB below the beam peak at the high

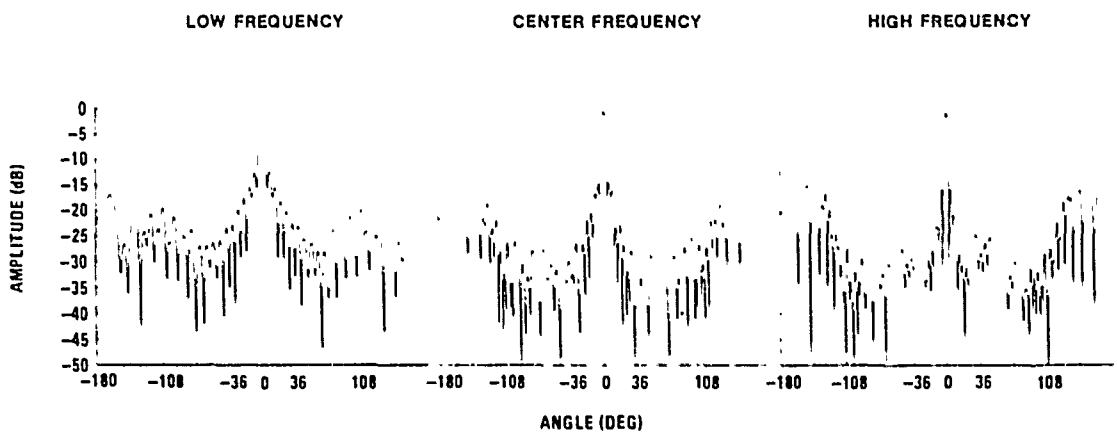

Figure 9 - **COMPUTED PATTERNS WITH MEASURED COUPLING DATA** - Mutual coupling in the Luneburg lens causes the backlobes of the demonstration model to increase by 5 to 12dB. This effect is virtually eliminated when SPDT switches, rather than circulators, interconnect the Luneburg lens and the column network.

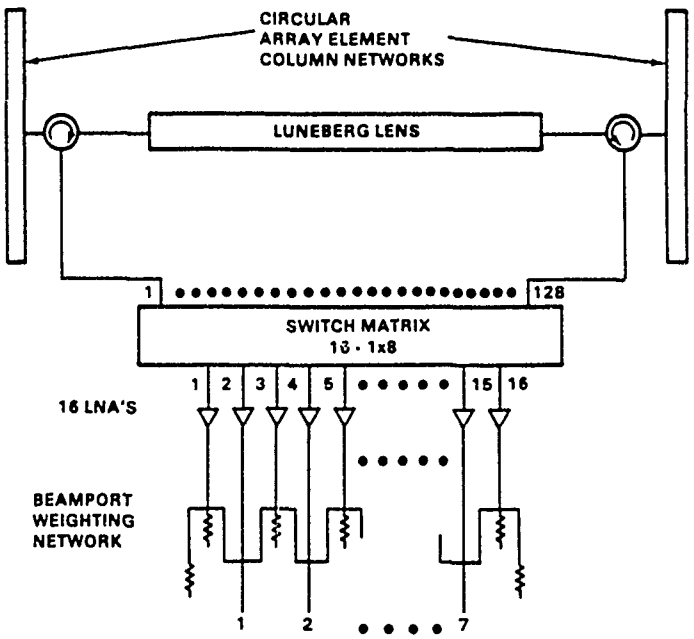

Figure 10 - **BASELINE FEED NETWORK SCHEMATIC** - A feed network which uses three Luneburg lens probes for each beam with a power weighting of (0.5,1.0,0.5) reduces sidelobes and improves frequency invariance.

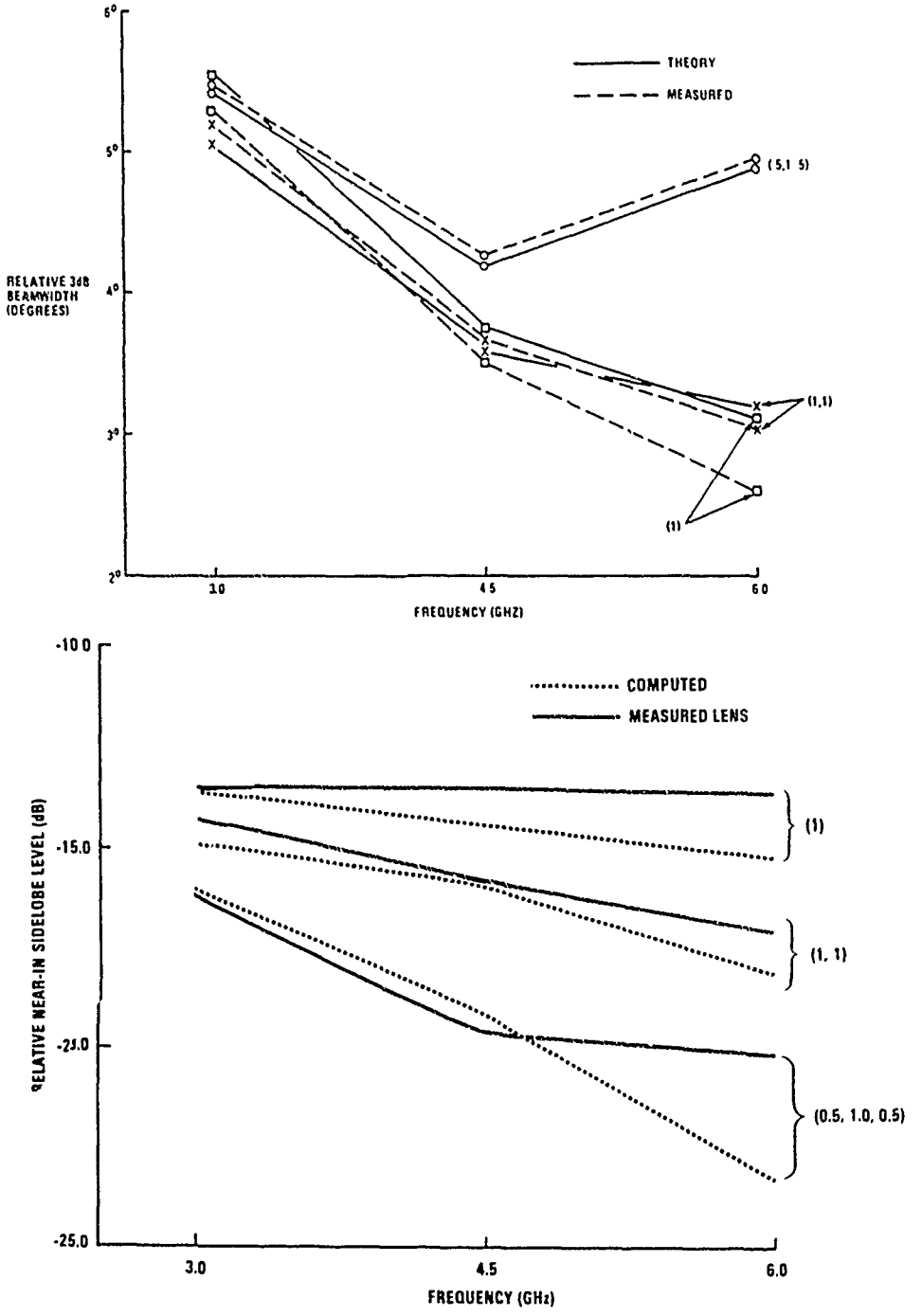

Figure 11 - LUNEBURG LENS EXCITATION TRADE-OFFS - Comparing the azimuth beamwidths and peak sidelobes produced when one, two or three Luneburg lens probes are excited for beam formation shows that three-probe excitation limits beamwidth changes to 20% with lower sidelobes over the octave band.

frequency. Figure 12 shows the cosecant-squared fan beam coverage to 25 degrees at the high frequency and 50 degrees at the low frequency. Ripple compared to the ideal cosecant squared power drop is better than 0.5 dB. Element amplitudes are modified slightly to simplify coupler design. Taper efficiency ranges from -1.8 dB at the high frequency to -1.1 dB at the low frequency.

The desired illumination taper is generated by a power divider network which feeds sixteen vertically polarized dipoles. The power divider, dipoles and wideband baluns are integrated into a single stripline assembly pictured in Figure 13.

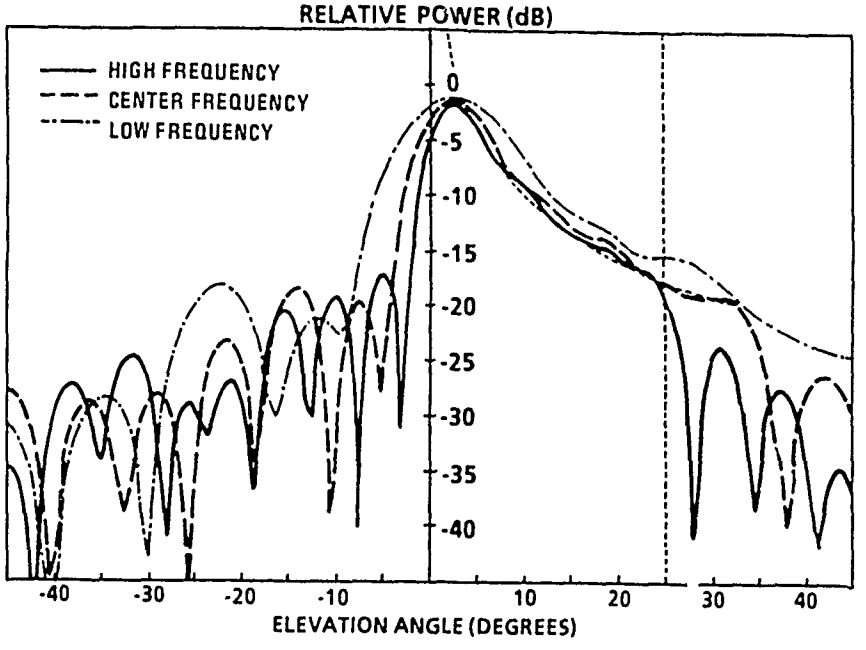

Figure 12 - CALCULATED ELEVATION PATTERNS - The antenna provides cosecant-squared elevation coverage to greater than 25 degrees over the octave band.

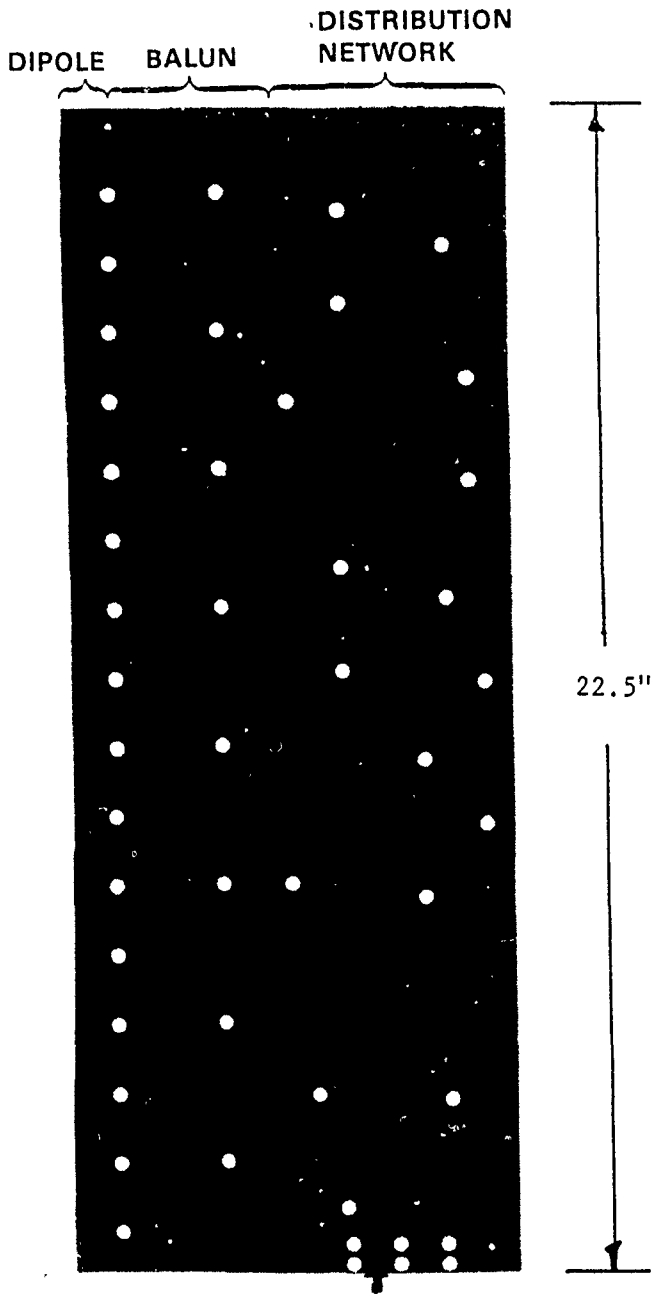

Figure 13 - **COLUMN NETWORK PRINTED CIRCUIT** - Sixteen dipoles and baluns, and a wide band distribution network are printed on a single layer simplifying the column network.

The power divider network consists of 15 compensated Wilkinson tees ranging in coupling values from 3.0 dB to 4.5 dB. The various coupling values are determined by a top-down power coupling technique from the element ports. The VSWR over most of the frequency band was measured to be better than 1.2 with 1.35 maximum at the band edges. These values are very close to the optimum theoretical values. The measured loss through the column network is then 1.8 dB over the frequency band.

The wideband balun is comprised of three cascaded 60^{o} Schiffman phase shifters and a transformer to 140 ohm balanced two wire line. This design allows for a planar topography whereby networks are printed on a single sheet resulting in a mechanically simple structure. The phase shift in the Schiffman phase shifter is obtained by a quarter-wave resonant coupled line. The measured phase error and VSWR for a single Schiffman stage are plotted in Figure 14 indicating a maximum balun phase imbalance of 10 degrees over an octave band.

The radiating element is a simple dipole with a reactive wedge. Starting from calculations of active dipole impedances obtained from a cylindrical array modal analysis[4] computer program, a design for the launching (two wire line) section was generated matching these load impedances into the balun section. A single element waveguide simulator was fabricated and the dipole design was validated and refined empirically to optimize the match over the octave band. An average VSWR of less than

1.4:1 was measured over the operating band of the simulator. With the dipole design optimized, element patterns for the single element were taken in both principal planes at sample frequencies over the octave band. These measurements show clean smooth patterns with no detected resonances.

The integrated stripline network is printed on a (KAPTON) sheet as previously shown in Figure 13, which is sandwiched between two foam spacer sheets. Aluminum spacers 0.125" in height are used to maintain a continuous spacing between the outer aluminum ground planes. The printed circuit has 50 to 70 ohm stepped transformers at the connectors to match into the 70 ohm system of the 16:1 power divider. This entire network provides a light weight compact design which measures 23.5 inches high by 9 inches wide by 0.25 inch thick.

ANTENNA TEST

Antenna pattern data on the composite cylindrical array assembly demonstrate key performance characteristics over an octave band. These include: 360^{o} azimuthal coverage, relative azimuthal beamwidth invariance and sidelobe level control, and an elevation fan beam with CSC^2 power drop-off.

The cylindrical array/Luneburg lens demonstration antenna is configured with 64 azimuthal beamports which can be accessed one at a time using the remote beam selector. In Figure 15, each main beam is recorded sequentially and referenced through 360 degrees of azimuth. The data shows less than $\pm$0.5dB varia-

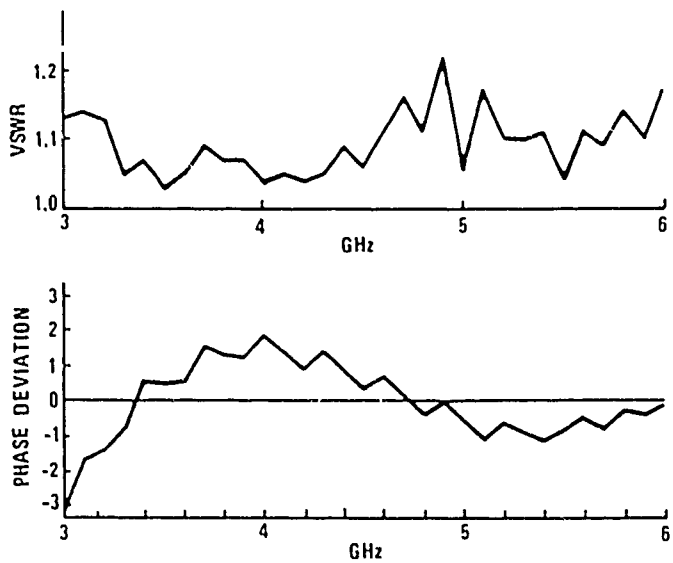

Figure 14 - 60-DEGREE SCHIFFMAN PHASE SHIFTER PERFORMANCE - Each balun contains three 60-degree Schiffman phase shifters to provide a balanced two-wire feed for the dipoles. Measured data shows that the VSWR is less than 1.2 and the phase error is less than 3 degrees for each Schiffman stage over the octave band.

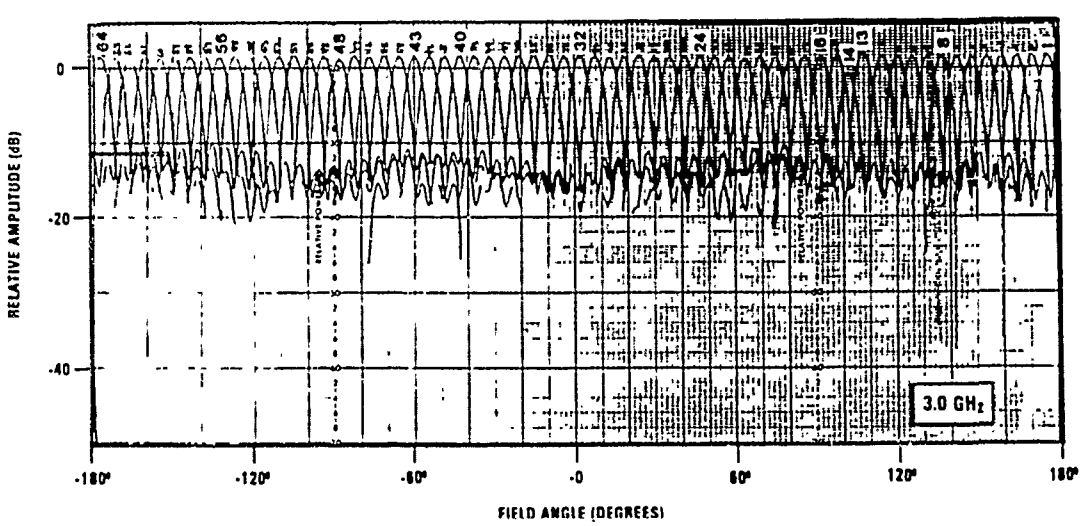

Figure 15 - DEMONSTRATION MODEL AZIMUTH COVERAGE - The measured beam patterns of the demonstration model verify uniform 360 degrees azimuth coverage within $\pm$0.5dB with 64 beams.

tion in gain over the full azimuth coverage.

To demonstrate beamwidth control, beamport No. 13 is configured for a triple probe excitation with (0.5, 1.0, 0.5) power weighting. As shown in Figure 16, 62 beamports are configured for a double probe excitation and beamport No. 14 provides single probe excitation. The 3 dB beamwidth variation with frequency for the measured and computed far field patterns for the demonstration antenna are plotted in Figure 17 for the various lens feed configurations. This plot shows that the 3 dB beamwidth for the measured and computed patterns correlate wel' over the octave band.

Since the 3 dB beamwidth is inversely proportional to frequency for a fixed antenna aperture, the beamwidth control can only be achieved by changes in antenna aperture distribution. For the cylindrical array/Luneburg lens this can only be effected by controlling the lens aperture distribution via a combination of the focal aperture length and element illumination. The probe element spacing in the Luneburg lens is one half wavelength at 6.0 GHz. When two lens probes are fed simultaneously, the focal aperture is increased and therefore some 3 dB beamwidth control is achieved near the high end of the band. When three lens probes are fed simultaneously, with a (0.5, 1.0, 0.5) power weighting, less than 20 percent variation in the 3 dB beamwidth is achieved over more than the octave band, demonstrating the desired control.

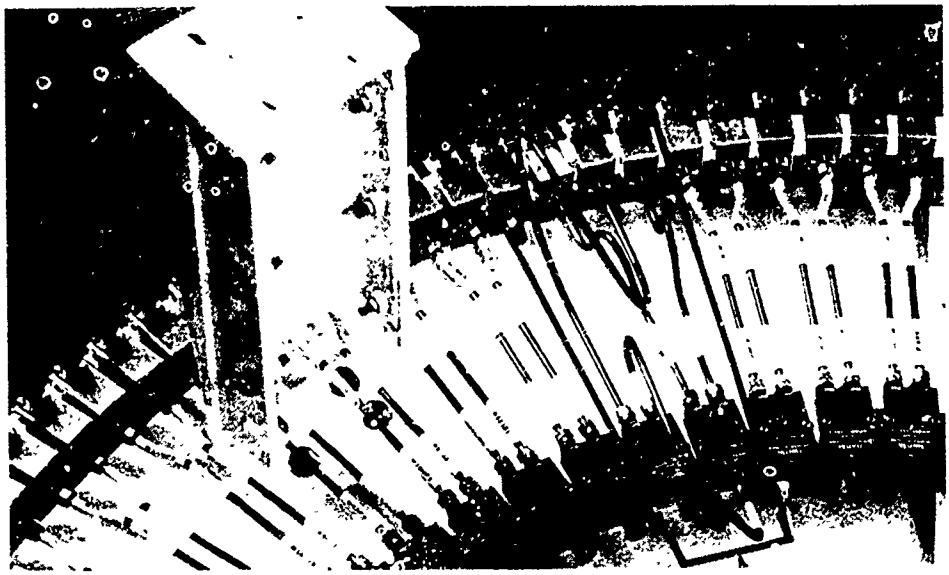

Figure 16 - **LENS PORT FEED MODIFICATION** - To experimentally verify trade-offs involving azimuth sidelobes and beamwidth invariance, the feeds for beams 13 and 14 on the demonstration model are modified to allow single-probe and weighted three-probe excitation of the Luneburg lens.

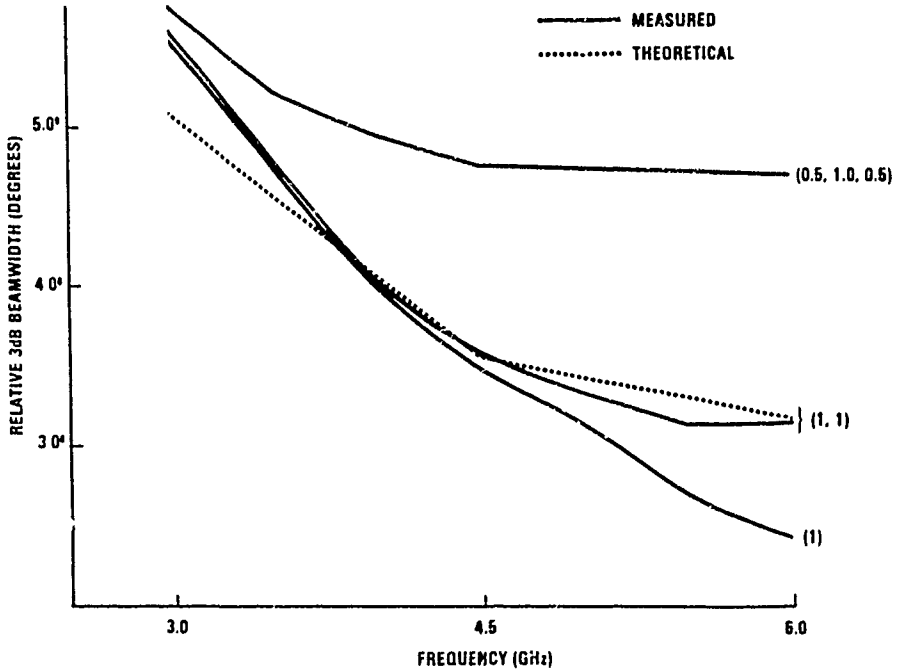

Figure 17 - **DEMONSTRATION MODEL BEAMWIDTHS** - The measured beamwidth for three different Luneburg lens probe excitations substantiates that beamwidth variations over the octave band are less for the weighted three-probe excitation as expected.

Recorded azimuthal and cross-polarized patterns are illustrated in Figure 18 for the beamport configured with the triple probe feed. Sidelobe levels are plotted over the octave band in Figure 19 for two lens feed configurations.

The predicted backlobes from inter-probe coupling in the Luneburg lens is also observed and can be easily improved by 20 dB with the replacement of the circulators with single pole double throw (SPDT) switches. Experiments were conducted to simulate this approach over a wide frequency band, and Figure 20 demonstrates the effectiveness of this design.

The superimposed cross-polarized patterns are normalized to the peak of the corresponding co-polarization patterns recorded on the same chart. The patterns shown are in the azimuth principal plane. In all cases, the cross-polarized levels are about 20 dB below the peak of the co-polarized pattern main beam. This result indicates that the demonstration model antenna wideband element achieves good element radiation characteristics while minimizing element cross-polarization level for more than an octave operating band. Measured elevation patterns are in good agreement with the computed patterns over the octave band. Both the computed and measured patterns are illustrated in Figure 21 for comparison at the design frequency of 6.0 GHz. The maximum deviation from a cosecant squared power drop off is approximately 1.0 dB for the measured elevation pattern at 6.0 GHz compared to 0.5 dB for the ideal case. These small deviations from the

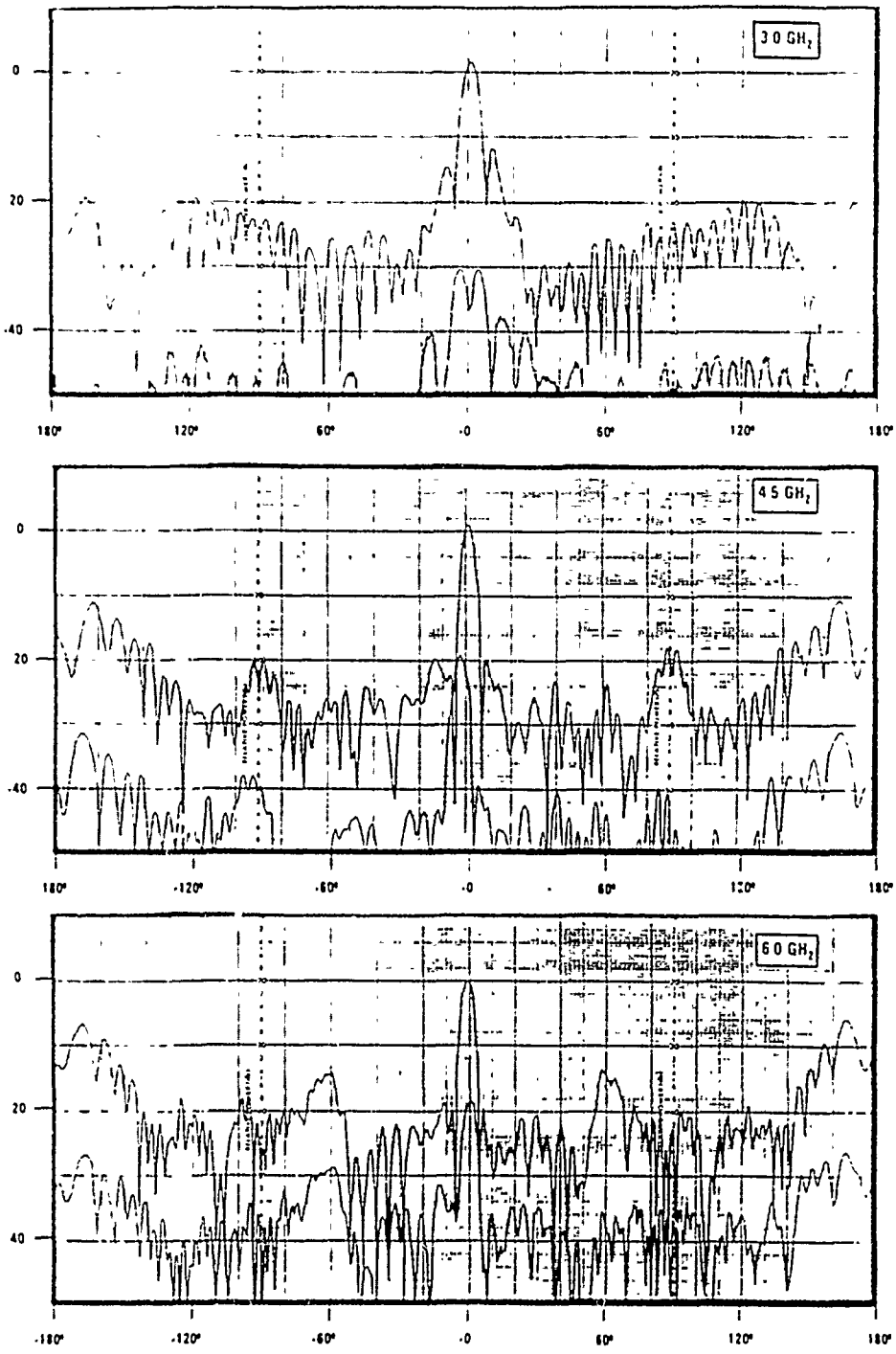

Figure 18 - **DEMONSTRATION MODEL AZIMUTH PATTERNS** - Measured co-polarized and cross-polarized patterns show good agreement with theory. The cross-polarized patterns are typically more than 20 dB below the co-polarized.

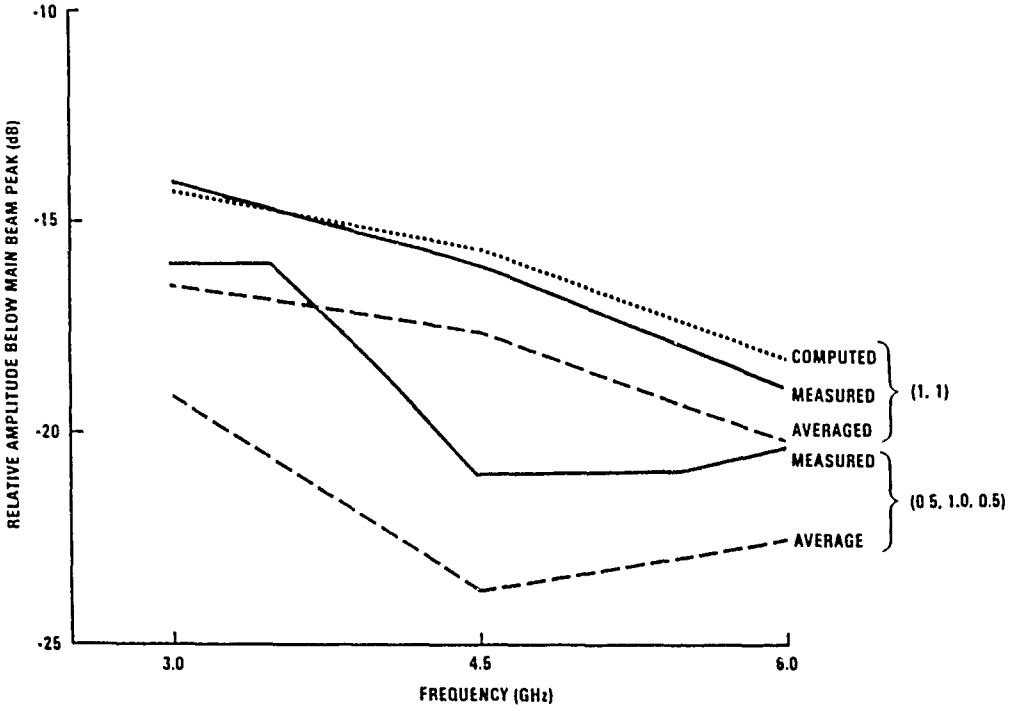

Figure 19 - **DEMONSTRATION MODEL SIDELOBES** - Measured peak and average azimuth sidelobes for two-probe and weighted three-probe Luneburg lens excitations indicates that the sidelobes for the three-probe excitation are about 4dB lower.

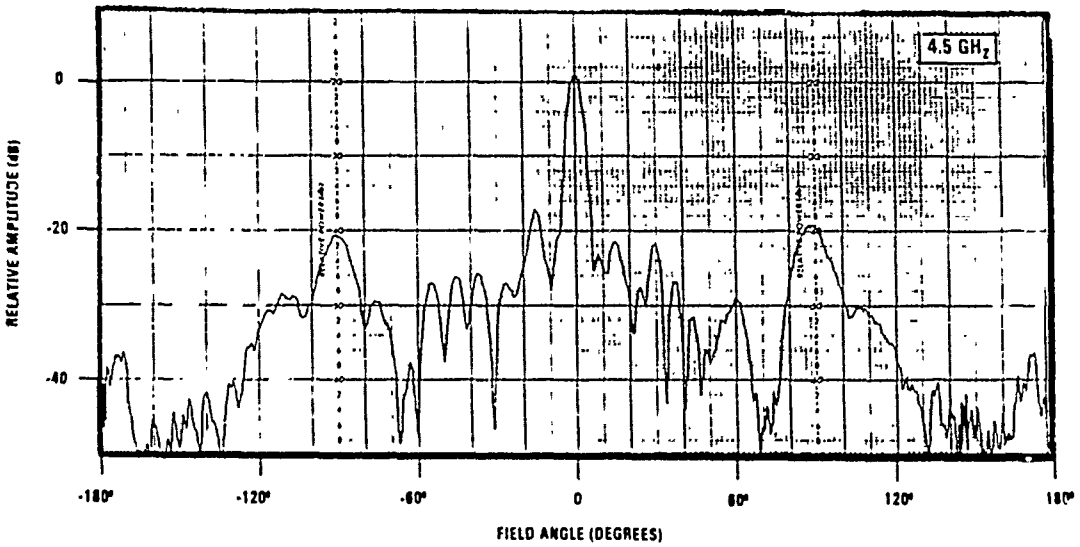

Figure 20 - **AZIMUTH PATTERN WITH SPDT SWITCHES** - The effect of using SPDT switches, rather than circulators, is evaluated on the demonstration model by terminating beam ports in the vicinity of the ports excited for the desired beam. Comparison of the resultant pattern at 4.5 GHz with that of Figure 18 shows that SPDT switches reduce backlobes by 25 to 30dB.

ideal patterns for this broadband network can be attributed to the fabrication tolerance errors and grating lobe incipience.

CONCLUSIONS AND SUMMARY

An octave bandwidth, electronic scanning cylindrical array has been designed, and a demonstration unit has been built and tested. The array receives signals simultaneously on a cluster of contiguous directive beams. Using a novel two-dimensional

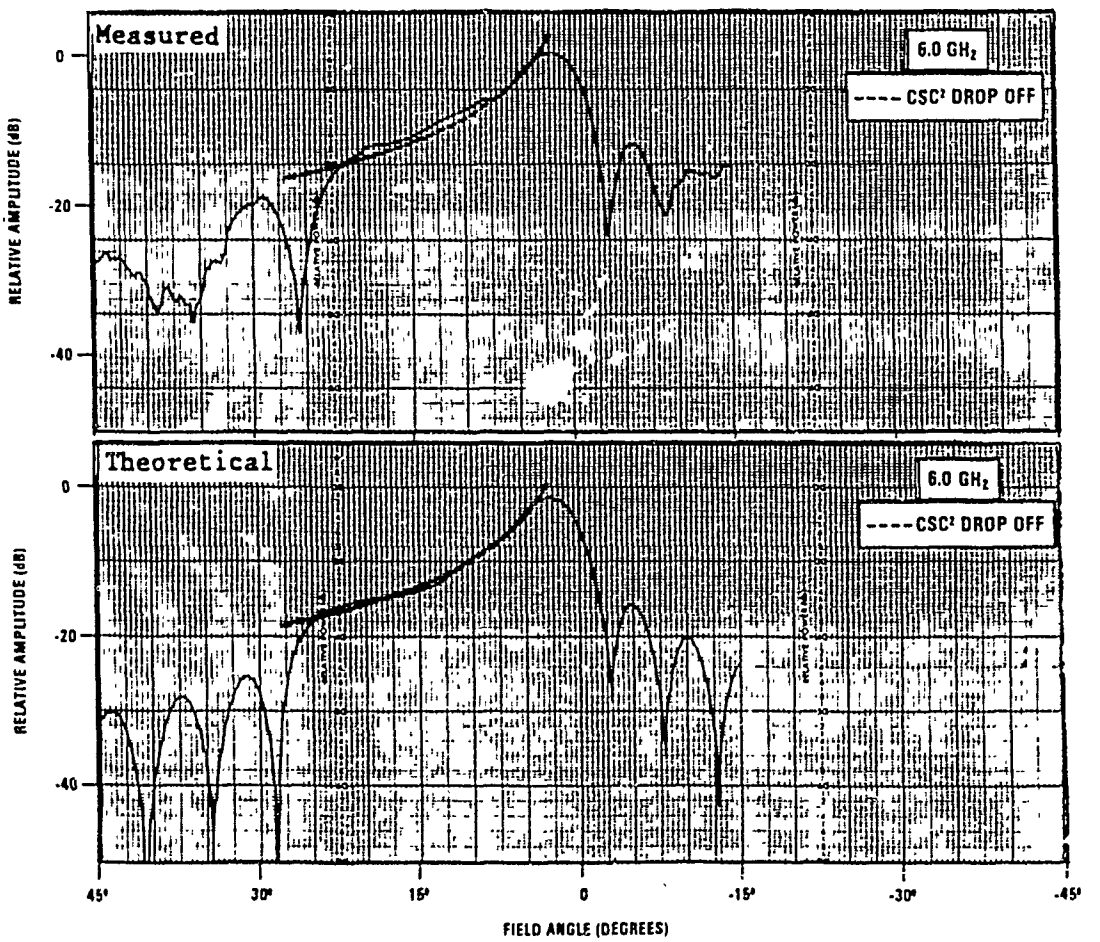

Figure 21 - DEMONSTRATION MODEL ELEVATION PATTERN - The measured elevation pattern at 6.0 GHz matches the desired cosecant-squared coverage to 25 degrees within ± 1 dB.

Luneburg lens beamformer with a simple switching network containing single pole, multi-throw switches, the beam cluster is positioned electronically to cover any azimuth sector. By properly weighting the Luneburg lens excitation, low azimuth sidelobes are obtained, and beam shapes and pointing angles remain substantially invariant over the octave frequency band. The radiating elements are axial dipoles which are integrated with wideband baluns and power distribution networks into single-layer stripline column networks. These column networks produce cosecant-squared shaped elevation coverage to 25 degrees or more in elevation. A versatile and comprehensive computer simulation addressing all critical aspects of the design has been generated and validated by experimental data on the demonstration model.

REFERENCES:

(1) PEELER, G.D.M. and ARCHER, D.H. (1953) A Two-Dimensional Microwave Luneburg Lens, I.R.E. Transactions Antennas and Propagation, July 1953, pp. 12-23.

(2) LUNEBURG, R.K. (1944) Mathematical Theory of Optics, Brown University Graduate School, Providence, R.I.

(3) MATHIS, H.F. (1960) Checking Design of Stepped Luneburg Lens, IRE Trans. Antennas and Prop., May 1960, pp. 342-343.

(4) JASIK, H. (1954) The Electromagnetic Theory of the Luneburg Lens, Report Number AF CRC-TR-54-121.

(5) HERPER, J.C., HESSEL, A. and TOMASIC, B. (1985) Element Patterns of an Axial Dipole in a Cylindrical Phased Array, Part I: Theory, IEEE Transactions Antennas and Propagation, AP-33, No. 3, pp. 259-272.

(6) HESSEL, A. and SHAPIRA, J. (1977) Mutual Coupling Coefficients in Collector Arrays on Circular Cylindrical Concave Surfaces, IEEE Transactions Antennas and Propagation, AP-25, No. 6, pp. 741-747.

CONFORMAL ACTIVE PHASED ARRAY DEMONSTRATION

Jerome D. Hanfling
Raytheon Company, Equipment Division
Wayland, MA

Abstract

The development and demonstration of a conformal active phased array has been sponsored by the Electromagnetics Directorate of Rome Air Development Center at Hanscom, AFB. The array has transmit/receive modules which utilize state-of-the-art gallium arsenide monolithic microwave integrated circuit technology for amplifiers and phase shifters.

The array aperture is linear with 64-microstrip patch radiators flush mounted conformal to a cylindrical surface. The patch radiators and T/R modules combine to provide a low profile, broadband phased-array element for low-noise reception and high-power transmit operation at S-band frequencies.

The control of the active devices is enabled by a unique beam steering controller VLSI gate array resident in each T/R module. This digital controller performs phase computations, controls the RF paths through the amplifiers and provides built-in test features for the array.

After integration and checkout of the array system indoors in the laboratory, the array receive and transmit performance was demonstrated by outdoor far-field antenna pattern measurements.

1.0 INTRODUCTION

A conformal antenna experiment called "Array/Module Integration and Test" (AMIT) has been developed for the Air Force Electronic Systems Division at Hanscom AFB, under Contract No. F19628-84-C-0137. The antenna is a linear array of 64-microstrip patch radiators flush mounted conformal to a cylindrical surface. This surface forms the front of a rectangular enclosure, as shown in the photograph of Figure 1. The array contains Transmit/Receive (T/R) modules furnished by the government out of the Conformal Array Module (CAM) program sponsored by The Signal Generation and Control Branch of the Surveillance Directorate of RADC at Griffiss, AFB [1]. The patch radiators and T/R modules combine to provide a low-profile, broadband phased-array element. For the AMIT program, the patch radiators are mounted external to the skin of the conformal array enclosure and the T/R modules are fastened on the inside, as shown in Figure 2. Much of the array system, as represented in the block diagram of Figure 3, is contained within this enclosure. The hardware in the enclosure is shown in Figure 4; here the array is undergoing bench-top tests prior to outdoor installation.

This paper first describes the array system, the hardware details and the command and control system. Then the low-profile microstrip-patch radiator is discussed. The remainder of the paper concentrates on some unique aspects of active array testing and corresponding test results.

2.0 ARRAY HARDWARE DESCRIPTION

2.1 Array System

A block diagram of the active array system is shown in Figure 3. The heart of the array system is the CAM T/R module, as shown in Figure 5, which consists of an RF assembly (containing a phase shifter, and a power amplifier and a low-noise amplifier, see Figure 6), and a Distributed Module Controller (DMC) gate array separated by a logic interface circuit. Several subsystems are necessary to operate the active array. Inside the conformal array enclosure is an RF feed network, an ethylene glycol/water cooling manifold, power supplies, energy storage capacitors and a junction box which contains the array interconnections. Outside the enclosure are the beam steering controller, HP-1000 computer, interlock chassis, and monitors. The data and DC connections to the modules are made by 64 separate cables and corresponding 15 pin D-sub connectors. The array system is powered by eight 10 volt power supplies (8 T/R modules per supply), one 5 volt supply and one -10 volt supply.

The RF feed network, as presented in Figure 7, is an equal power split 1:64 divider network. It is configured from commercial couplers and dividers. The sum and difference amplitude tapers, transmit uniform illumination, and compensation for different insertion losses , the network through the T/R modules are obtained by a variety of fixed attenuators. The pads are inserted between the dividers and the T/R modules. The physical

layout of the junction box, cables, power supplies and interconnections are pictured in Figure 4.

2.2 Patch Radiator

The patch radiator being used in the AMIT program is balanced fed providing good quality horizontal linear polarization (along roll axis of cylinder) over a wide bandwidth at S-band [2]. The element spacing has been selected to meet a $\pm$60 deg. azimuth and $\pm$40 deg. elevation scan coverage. The goal is to achieve a less than 2:1 VSWR over the band in a low profile, lightweight, and low loss implementation.

In accordance with the above objectives a high performance, compact microstrip patch radiator has been developed [3] [4]. A mechanical radiator design was formulated that placed the double-tuned matching network/balun structure underneath the patch and resulted in a low profile structure with a single coaxial input, as shown in Figure 8.

The basis of the development effort for this Duroid substrate patch radiator is a recently developed software design tool that provides a numerical code that accurately models patch radiators in an infinite array. The code models patch radiators mounted on a substrate of dielectric constant, ε, each patch being driven by up to four probe feeds. The effect of the matching network is not included in this code. However, the code allows a determination of the scattering matrix of the patch, each probe

being considered an input port. Using the methodology of references 5 and 6, this scattering matrix can be coupled to that of the matching network so as to arrive at the radiator's behavior at each scan angle selected [7].

The design was carried out using infinite array waveguide simulators. These measurements and the above code were combined to predict and verify performance. The results are summarized in the Smith chart plot of active impedance in Figure 9. Both the E, H, and diagonal (D) plane performance are close to ideal, with the exception of the E-plane performance for θ >50 deg. and for the upper end of the frequency band. This blind spot is due to the generation of a TM surface wave. It can be eliminated by reducing the element spacing in the array lattice. A better than 2:1 VSWR out to 45 deg. scan angle has been achieved. This is just beyond the required 40 deg. scan coverage.

Sixty-four patch radiators were built, tested, and installed on a 10 foot radius of curvature section representing the fuselage of the aircraft, as shown in Figure 1. The embedded element patterns were measured using this conformal array fixture for various element locations on the cylinder. The test results, as plotted in Figure 10, compare favorably to the $\cos^{3/2}\theta$ and $\cos\theta$ ideal gain fall-off curves.

3.0 ARRAY COMMAND/CONTROL SYSTEM

Each monolithic T/R module in the array requires a digital Beam Steering Unit (BSU) to perform such functions as phase computations and to set the proper mode of operation of the module. A distributed approach is used for AMIT, where serial data busses send to every DMC the same steering angle and frequency. These are then clocked into each T/R module corresponding to row and column intersections, as shown in Figure 11, where the phase shift setting are calculated in the VLSI DMC chip. The module controller accomplishes the steering function by computing the phase shift for each element and then commanding the phase shifter at the corresponding location to the computed value.

In addition to beam steering, the module controller must also control both the Power Amplifier (PA) and the Low-Noise Amplifier (LNA). For example, during the transmit mode, as shown by the switch positions in Figure 6, the power amplifier is energized and the T/R switch connects the PA input to the phase shifter and the output to the antenna. At this time, the LNA is isolated from the transmit amplifier.

3.1 Array Operation

Control of the array is achieved by sending serial message signals to the DMC chips in response to the commands from the host computer. The RP68000 single-board [illegible] in the beam

steering controller unit executes the software that generates the waveforms to program and control the DMC chips in response to the commands from the host computer, as described in the block diagram of Figure 12. The DMC interface card is a special purpose peripheral to the RP68000 board. It contains shift registers for transmitting MODE and DATA words and for receiving BITE messages. It performs clock generation both for the shift registers and the DMC CLOCK lines and it performs the array element addressing function, allowing control of a single element or simultaneous control of all the T/R modules in the array.

3.2 Steering Calculation

The module controller accomplishes the steering function by computing the phase shift for each element and then commanding the phase shifter located in each antennule to the computer value. The phase shift that must be applied to each element in order to properly form the radiated beam is (in radians) given by equations (1) and (2) as follows:

$$\phi = \frac{2\pi}{\lambda} Y_i \sin\beta + \frac{2\pi}{\lambda} Z_i \cos\beta + \Delta\phi_i - \frac{2\pi}{\lambda} Z_i \qquad (1)$$

$\Delta\phi_i$ = Determined from calibration

Z_i = Path length factor

$$Z_i = R\left[1 - \cos\left(\frac{(2n-1)\Delta s}{2R}\right)\right] \qquad (2)$$

where

R = radius of cylinder

Δs = element arc length spacing

n = element position from center of array

A digital adaption of these equations is used in the BSU software.

3.3 Self Test

The controller has a self test capability that can be used to check if it is correctly performing the beam steering computation as well as its other control functions. Steering data (with a known result) can be applied to the controller. After the controller's phase shift is computed, its value is returned to the command and control interface where a comparison is made of this result with the known result and a pass/fail determination is made. The pass/fail result is then sent to the main display computer in the form of a status word. Control data, such as T/R switching can also be sent to the controller and returned for comparison. The controller can be used to perform RF tests on any individual T/R module; and active bit-wiggle test of a specified T/R module can be performed by sending a test phase shift word from the command and control interface to the module controller. A horn external to the array is then used to verify the proper RF operation of the tested module.

The 68000 microprocessor assembly language program for controlling an array of elements containing DMCs contains subroutines for the various array modes and functions as follows: initialization, diagnostics, resets, clears, loads, phase compute, BITE, receive and transmit operation, pulse train protection and module test routines.

4.0 ARRAY CALIBRATION

4.1 Calibration Techniques

After the checkout of the array in the laboratory the radiators were installed on the surface of the conformal housing. The array was then hoisted onto an outdoor pattern test pedestal. The setup for operating the array is shown in Figure 13 and includes various equipments for mount control, array electronic control, DC power, air conditioning, heat exchange, RF excitation and reception, signal analysis, temperature and current monitoring, power interlocks, beam steering and host computer control.

The apriori knowledge, from bench-top tests, of the insertion amplitude and phase from the input of the feed to the output at each module was not adequate to form a beam. The addition of the radiators and the outdoor environment necessitated the use of a free-space calibration technique.

A calibration procedure was developed which involved receiving a wave front from a far field source and sampling the amplitude and phase at each element. The key to the technique is to be able to turn on one module at a time while all other modules are turned off and all radiators are switched into loads internal to the T/R module. This enables the insertion amplitude and phase to be determined in the mutual coupling environment of neighboring radiators, i.e. the actual embedded element pattern is present. Once this signal path is established the mount can be rotated producing an embedded element pattern. This will enable the transmission amplitude and phase to be observed for all angles of interest. Any irregularities in the element pattern may indicate a fault in the microstrip radiator or at the array surface. This would have to be corrected before the calibration can proceed. Typical good element patterns for radiators at locations are shown in Figure 10. This gain fall off approaches the $\cos^n \theta$ function where $3/2>n>1$ which indicates a well matched radiator.

For the receive case, the technique using an external remote source in the far field for measuring amplitude and phase is shown in Figure 14. Similar considerations exist for transmit, but with the turned-on element transmitting; the received signal is detected at the source location filtered and brought back to the receiver, as shown in Figure 15. To carry out receiving and transmitting calibrations, the 64 element positions were traversed and the digital phase shifters stepped through each bit setting with phase (ϕ_i) and amplitude (A_i) being recorded.

4.2 Phase Calibration

For phase calibration the objective is to have equal insertion phase from the input of the source to the output of the feed or vice versa when each element position is interrogated one at a time. This focuses the array to the far field. The geometry is then translated to the cylindrical surface of the array so that the beam steering alogrithm, equation (Eq. 1) stored in the discrete module controller (DMC) can be utilized. The geometric modification factor is the path lengths (Z_i) from the cylindrical surface to a plane, equation (Eq. 2).

In the process of phase calibration, both the monitoring of the component performance and the isolation and correction of faults can be exercised. For example, if a 39 degree phase shift is required the 6, 11 and 22 degree bits would be set; a failed 11 degree bit can be partially compensated for by choosing a 45 degree command reducing the error from 11 to 6 degrees. Here a fault has been located and partially corrected.

4.3 Amplitude Calibration

For amplitude, the objective would be to achieve the specified illumination functions such as Taylor for sum and Bayliss for difference. On AMIT, where only a one-step attenuator was implemented in the module, electronic control of amplitude to fine increments was not available; instead, fixed attenuators were inserted in series with the module to obtain the desired

illumination. The amplitude was measured and the results used to find faults in the element radiator-to-output port transmission paths. Corrections were made by attenuator substitution or insertion and T/R module replacement. Where electronic BITE or current monitoring indicated that the modules were probably good, the fault was isolated to the radiator. The end result was phase and amplitude calibration files to which future calibrations were referenced and appropriately adjusted. Using these measured phase and amplitude data files, antenna patterns were calculated.

4.4 Measured Results

An example of such a calibration for the receive sum port for a scanned beam was taken by rotating the pedestal by 40 degrees from the down range boresight. This resulted in a plane wave source at 40 degrees from the array broadside, as shown in Figure 16. The resultant amplitude illumination as compared to the ideal illumination for an $\bar{n}$ = 10, -50 dB Taylor is shown in Figure 17. Correction for errors was limited by the use of the fixed attenuators. Larger errors such as at position no. 42 may mean a low gain amplifier or other component deficiency.

The corresponding far field pattern as computed from the measured calibration file is compared to the actual measured far-field pattern, as shown in Figure 18.

During the test program, receive and transmit beams were formed and steered over a wide scan sector. The free space calibration

technique was used to derive the array illuminations and produce collimated sum, difference, and transmit beams. The performance characteristics associated with the beams were determined as follows: pattern sidelobes, aperture gain, amplifier gain, effective radiated power and power output. The measured values of these parameters were in agreement with performance expectations.

5.0 CONCLUSION

A conformal phased array containing state-of-the-art gallium arsenide MMIC T/R modules has been successfully operated in receive and transmit both in the laboratory and on the pattern test range. The array has been calibrated for CW receive and pulse transmit operation using free-space far-field range techniques. It is planned to add 12-bit digital attenuators to the array to permit more accurate amplitude illumination calibration and to provide the precision needed to compensate for amplitude illumination distortion as a function of beamsteering [8].

6.0 ACKNOWLEDGEMENTS

The key workers on the program at Raytheon included O. Bedigian (software), S. Hartel (test), P. Pears (beamsteering), C. Dahl (mechanical), J. Swartzel (interconnections), E. Gray (T/R module), J. Murray (controller), and J. Schuss on the radiator design and full-scale implementation. The program was managed at Raytheon by T. Mahoney and at RADC by D. Jacavanco.

7.0 REFERENCES

1. Jessen D.N., Bacher C.F. and Gray E.S. (1987), "Ten Watt Monolithic S-Band Transceiver Modules", paper presented at the Government Microcircuit Applications Conference (GOMAC) (Orlando, FL).

2. Hanfling J.D., and Schuss J.J. (1986), "Experimental Results Illustrating Performance Limitations and Design Tradeoffs in Probe Fed Microstrip Patch Element Phased Arrays", IEEE Antennas and Propagation Symposium Digest (Blacksburg, VA).

3. Hanfling J.D., Schuss J.J., and Morrow R.E. (1989), "A Dual Polarized Patch Radiator for Phased Arrays", IEEE Antennas and Propagation Symposium Digest (San Jose, CA).

4. Schuss J.J., Hanfling J.D. and Bauer R.L. (1989), "Design of Wideband Patch Radiator Phased Arrays", IEEE Antennas and Propagation Symposium Digest (San Jose, CA).

5. Schuss J.J., Hanfling J.D., Conti R.J., Herrick B.R. (1985), "Numerical Design of Millimeter Wave Patch Radiator Arrays", Proc. of the Phased Arrays '85 Symposium (Bedford, MA).

6. Liu C.C., Hessel A. and Shmoys J. (1988), "Performance of Probe Fed Microstrip-Patch Element Phased Arrays", IEEE Transactions on Antennas and Propagation, Vol. AP-36, #11.

7. Schuss J.J. and Hanfling J.D. (1987), "Nonreciprocity and Scan Blindness in Phased Arrays using Balanced Fed Radiators", IEEE Transactions on Antennas and Propagation, Vol. AP-35, #2.

8. Antonucci J. and Franchi P. (1985), "A Simple Technique to Correct for Curvature Effects on Conformal Phased Arrays", Antenna Applications Symposium (Urbana Champaign, IL).

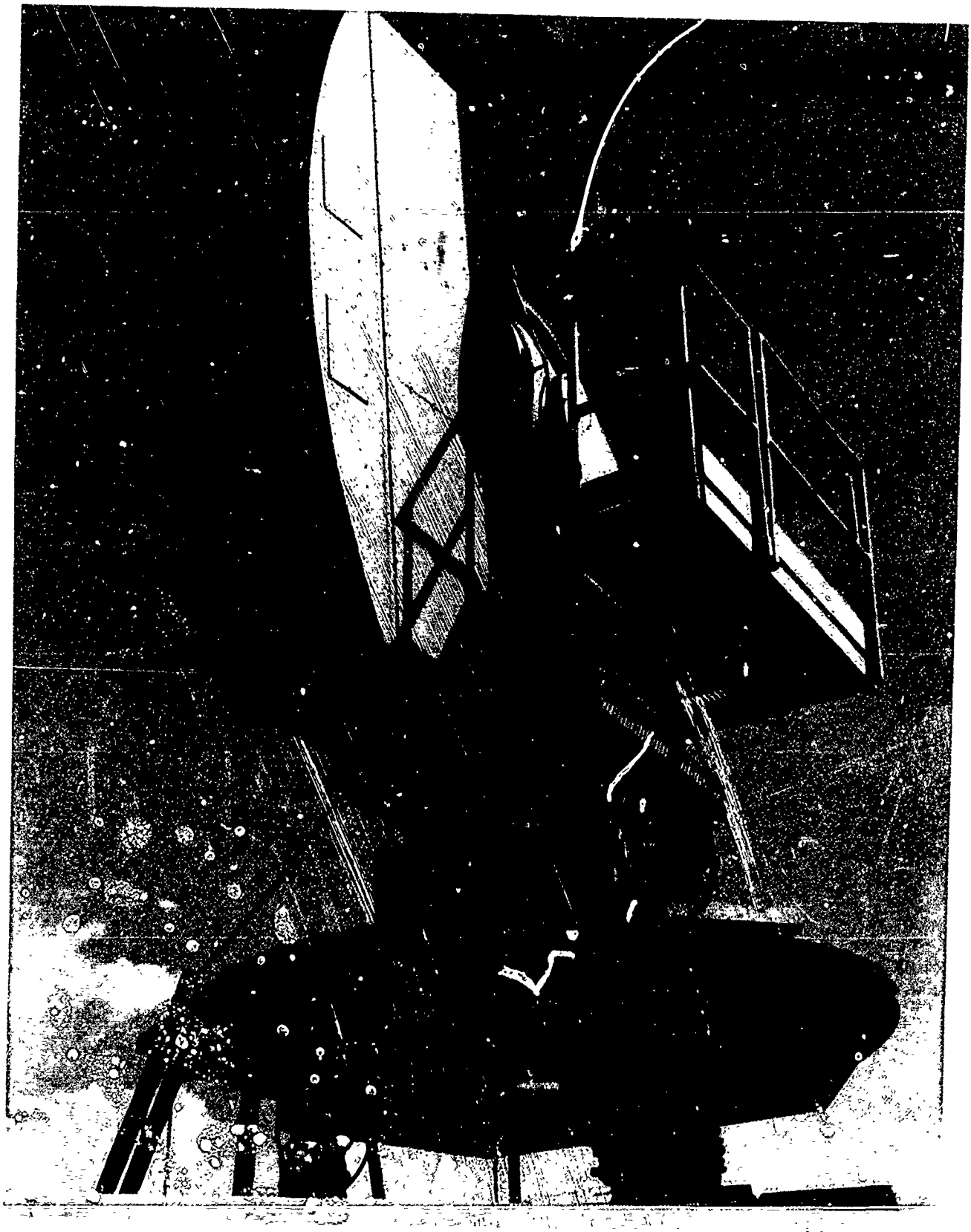

Figure 1. AMIT Conformal Array on Pattern Test Mount

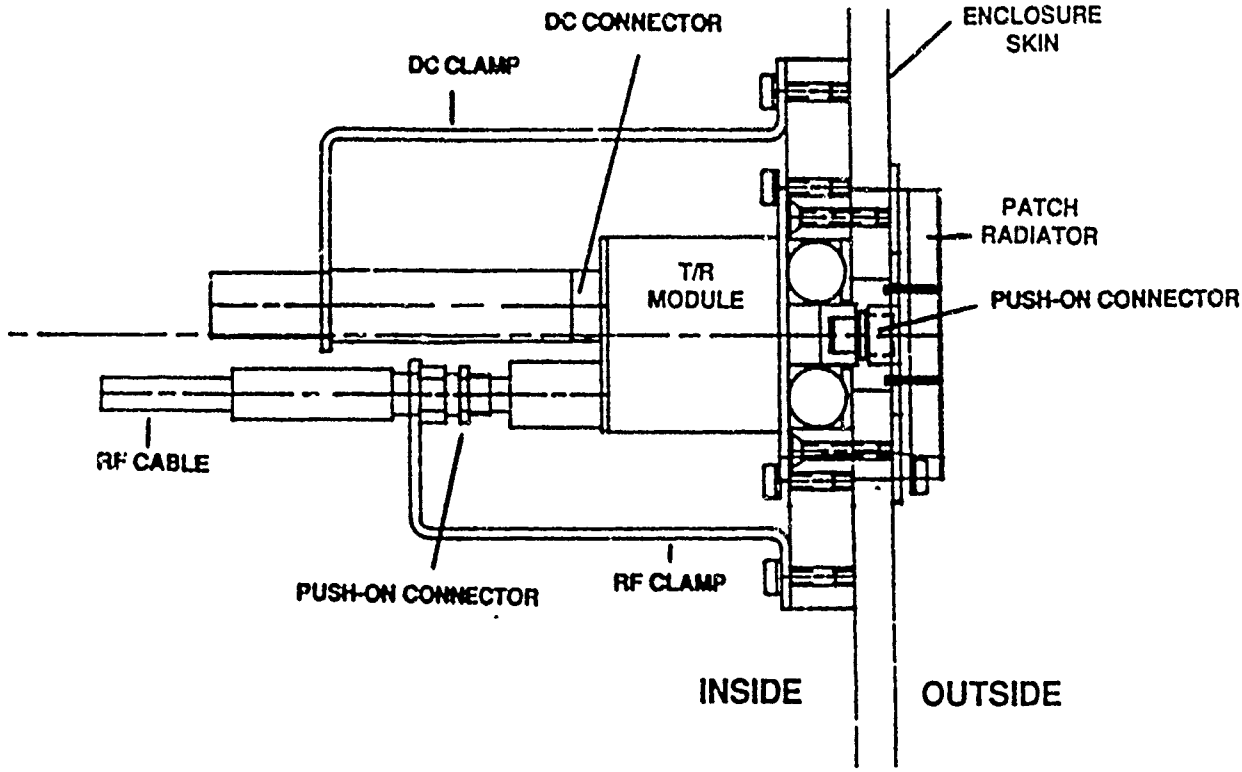

Figure 2. T/R Module and Radiator Mounting Arrangement

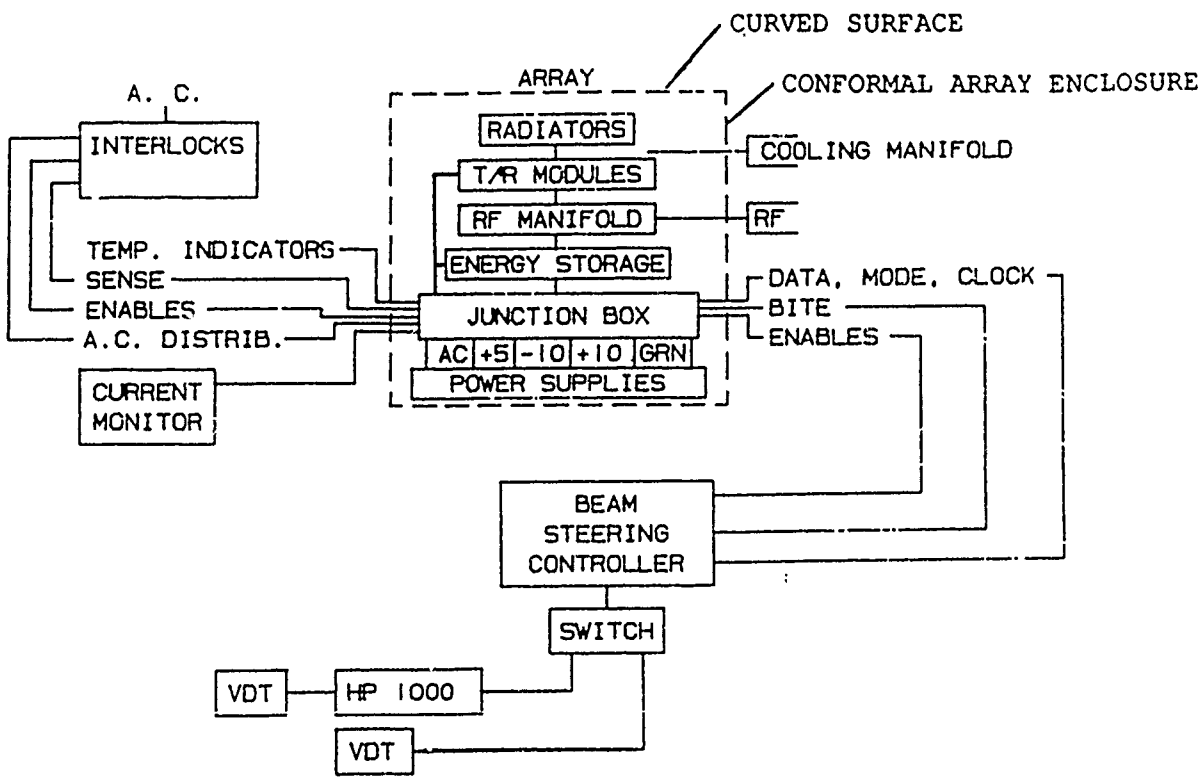

Figure 3. AMIT Array System Block Diagram

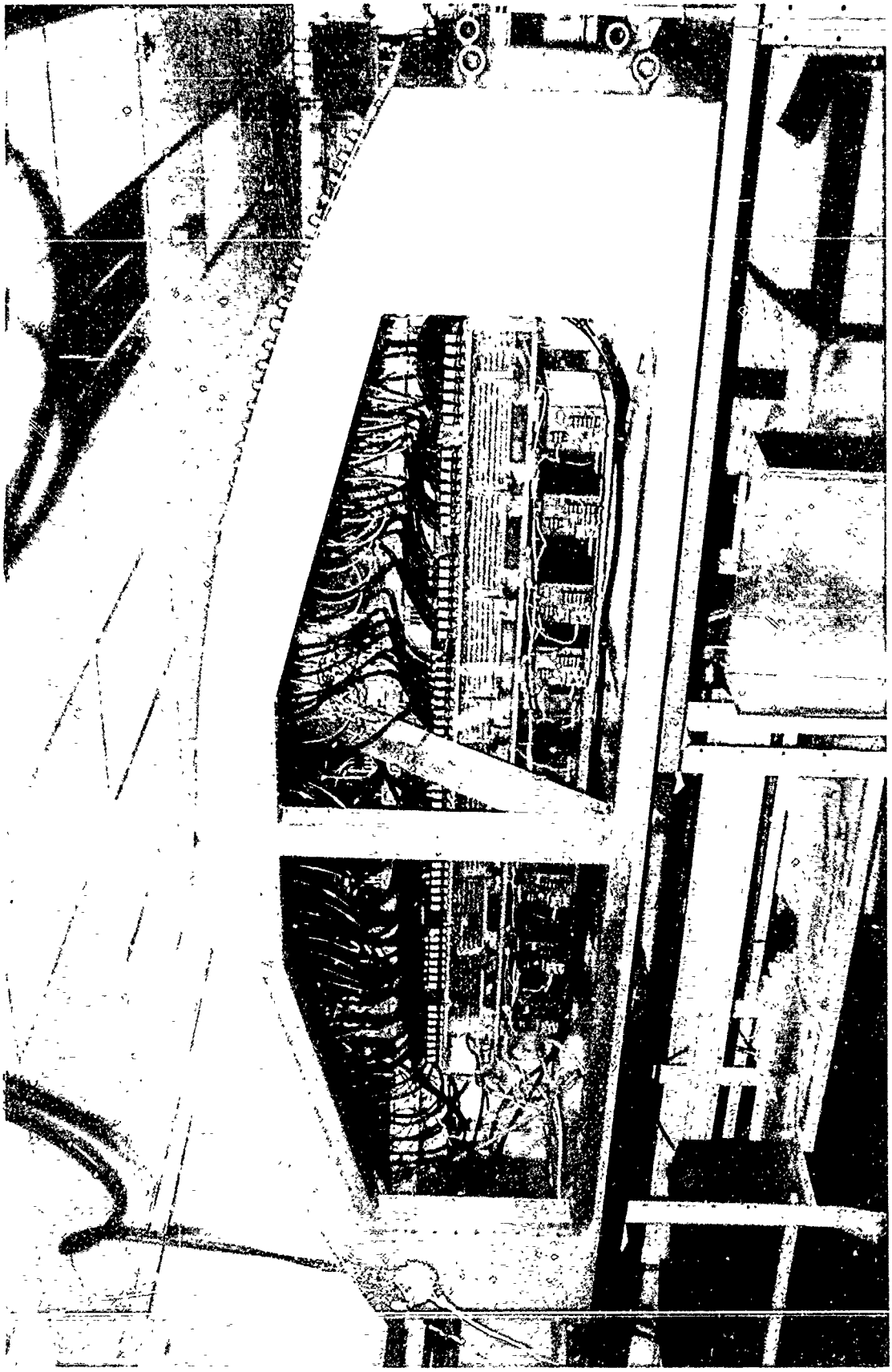

Figure 4. Hardware Inside Conformal Array Enclosure

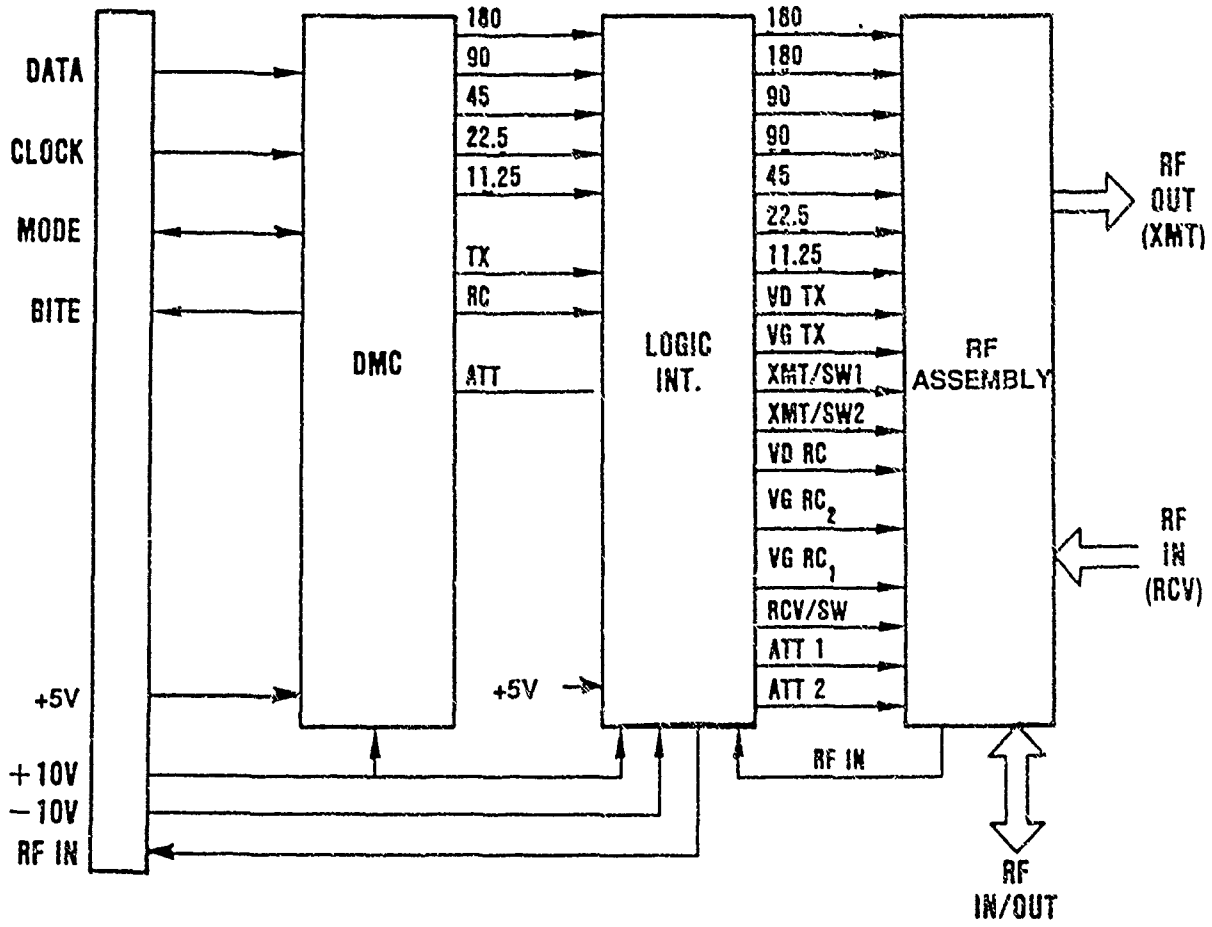

Figure 5. T/R Module Block Diagram with DMC

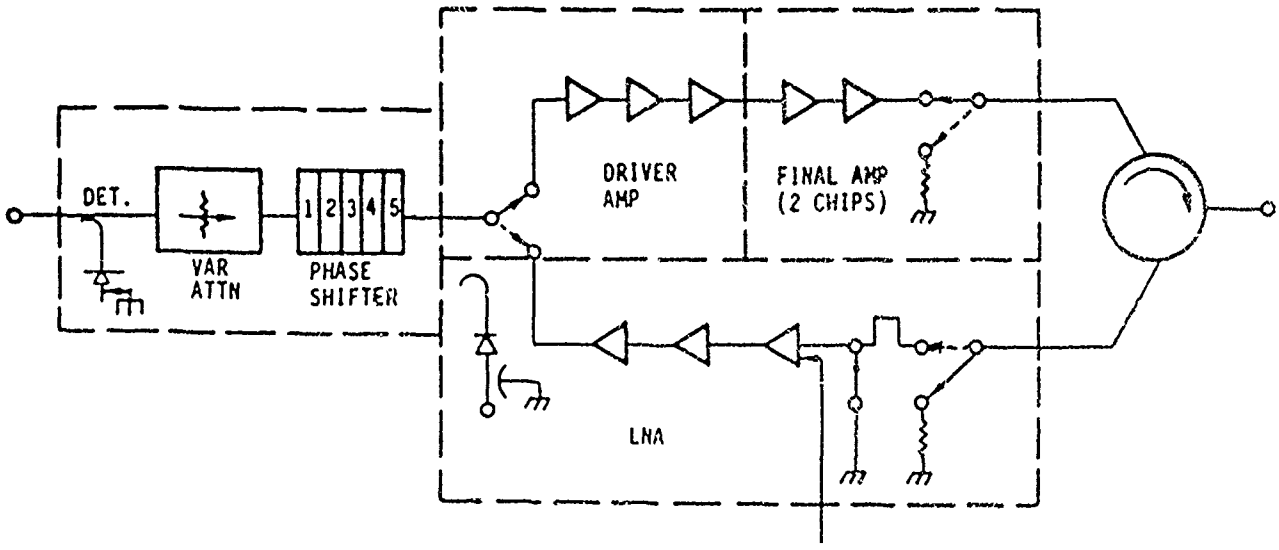

Figure 6. T/R Module RF Assembly Block Diagram

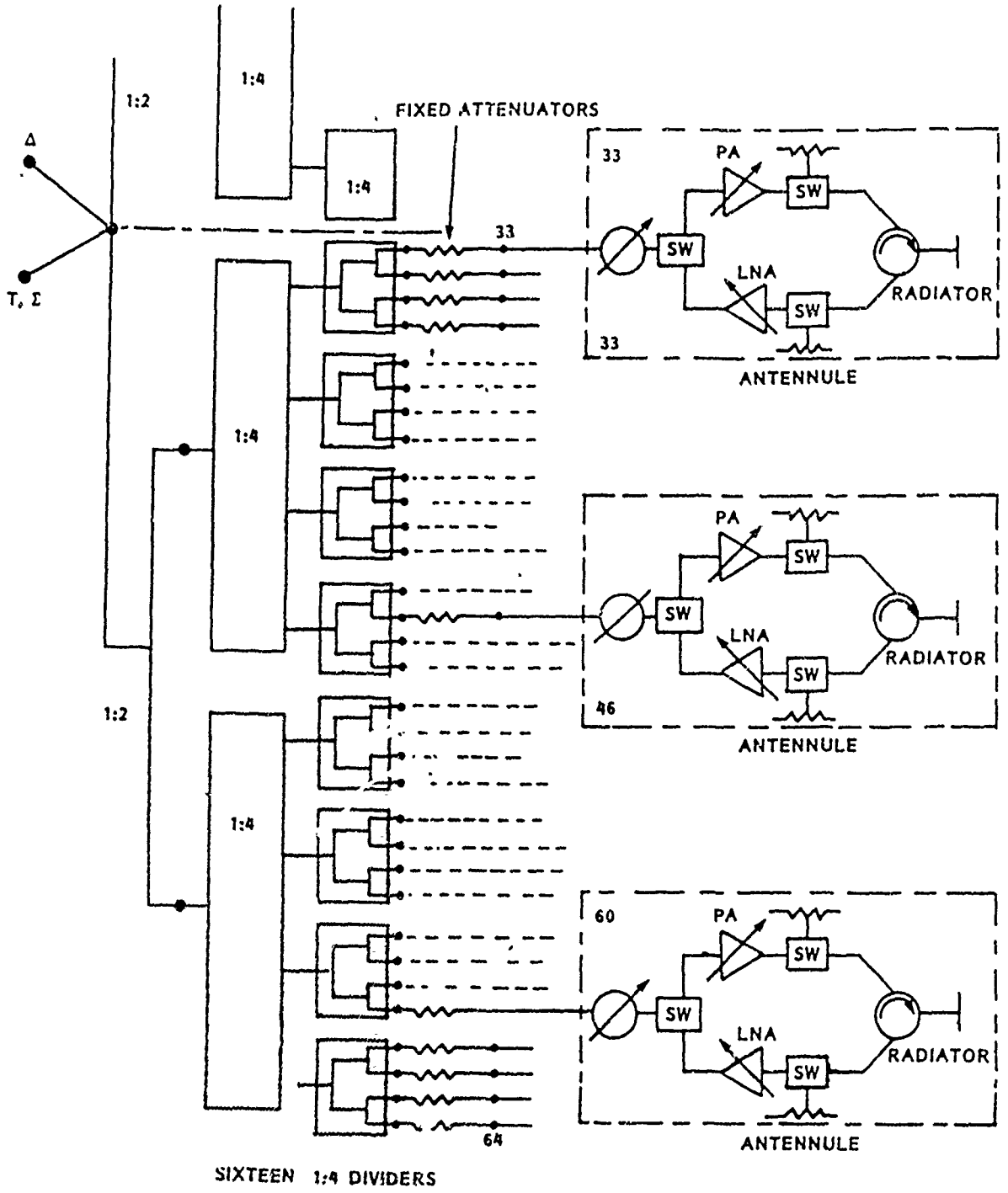

Figure 7. 1 x 64 RF Feed Network Schematic
430

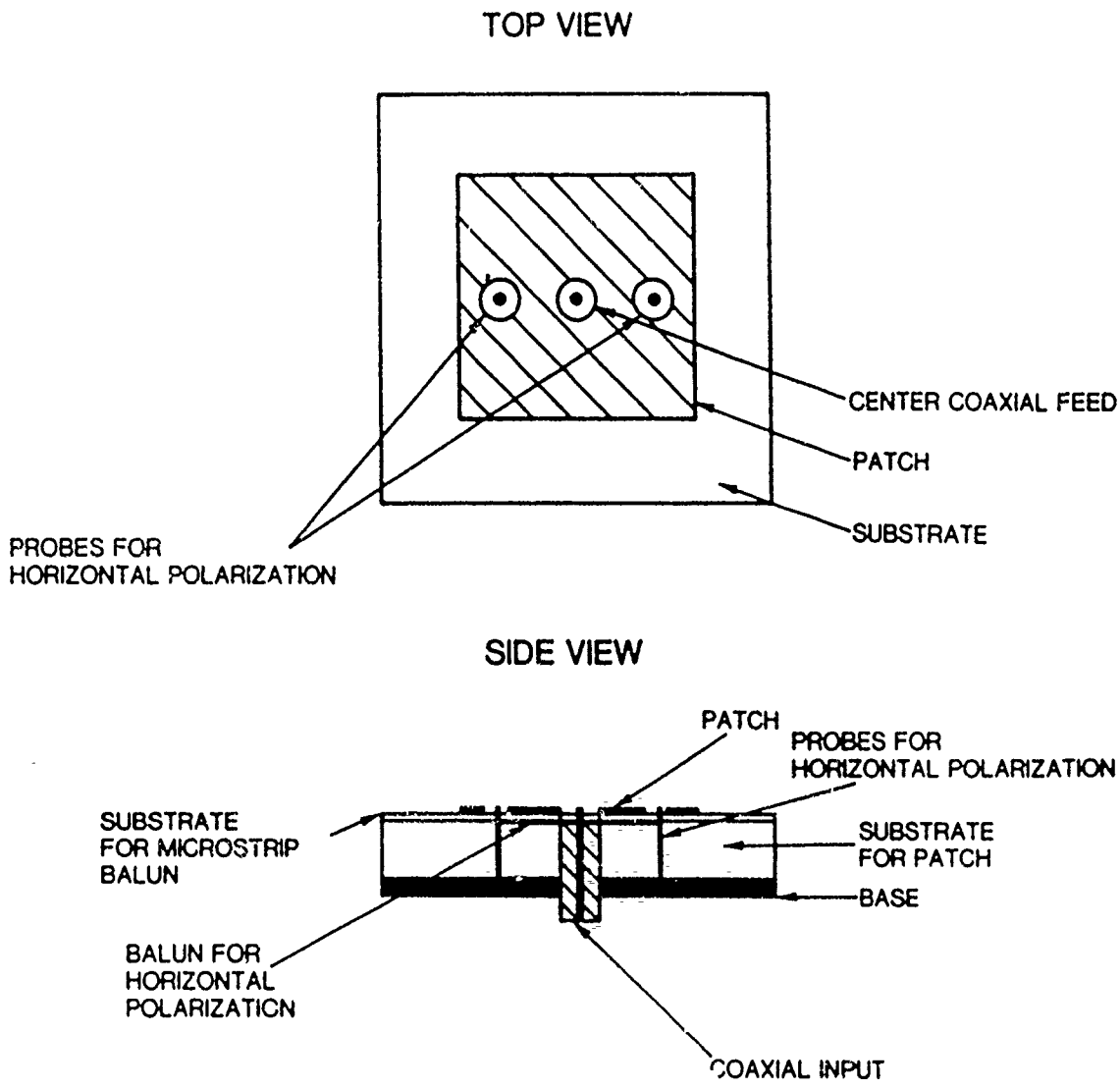

Figure 8. Linear Polarized Patch Radiator Configuration

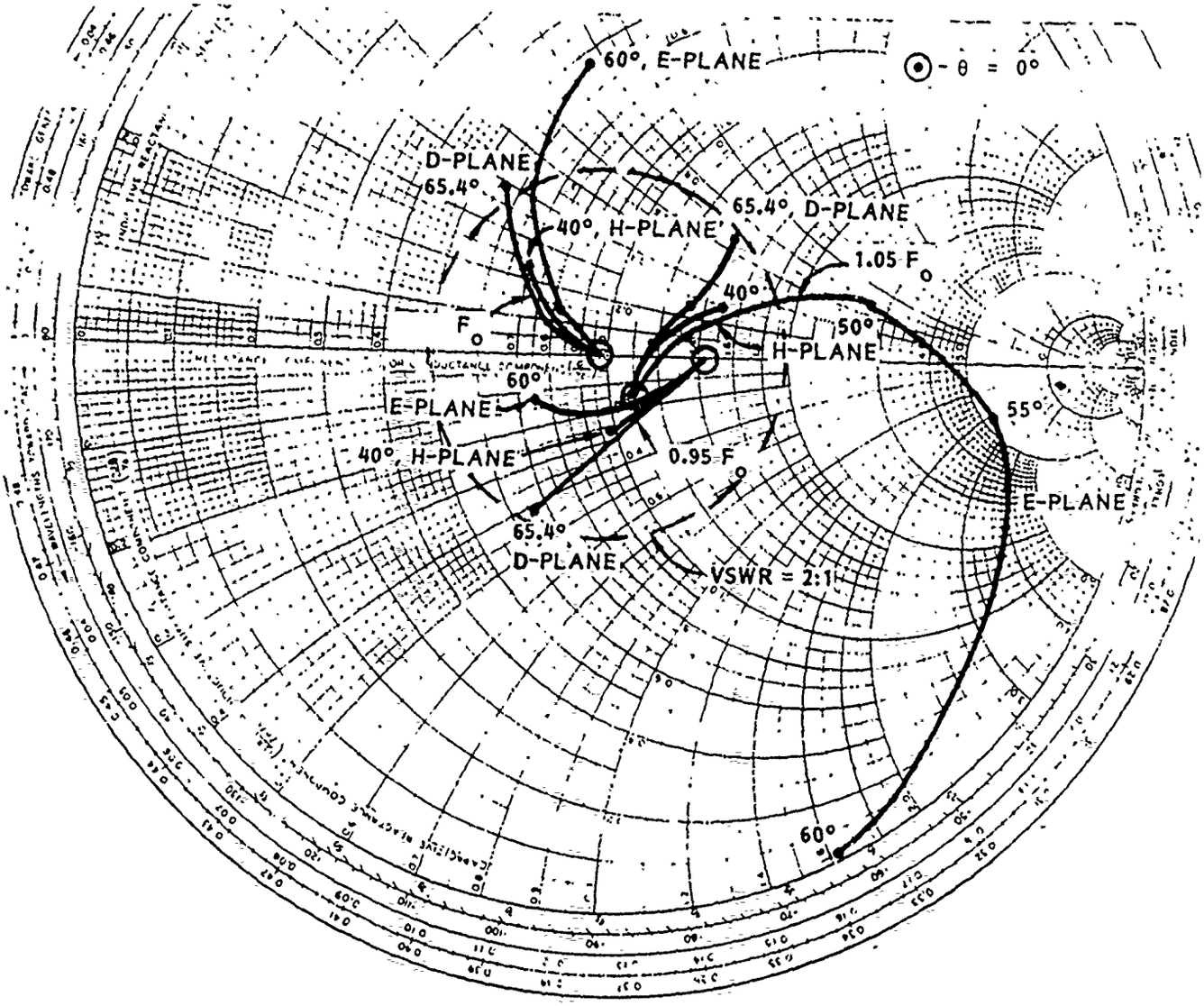

Figure 9. Impedance vs Scan Angle and Frequency for Required Coverage

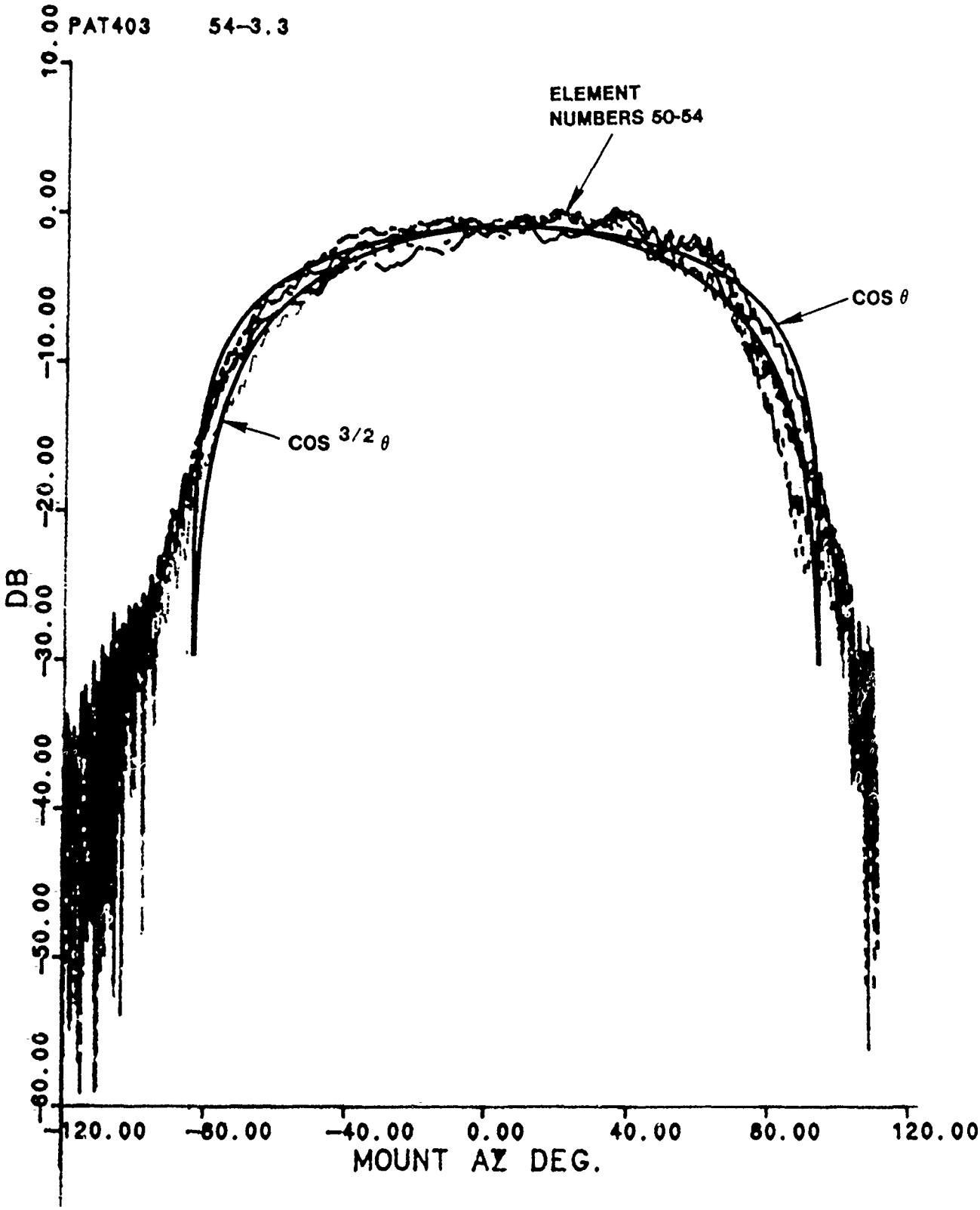

Figure 10. Measured Embedded Element Patterns on a Conformal Array

433

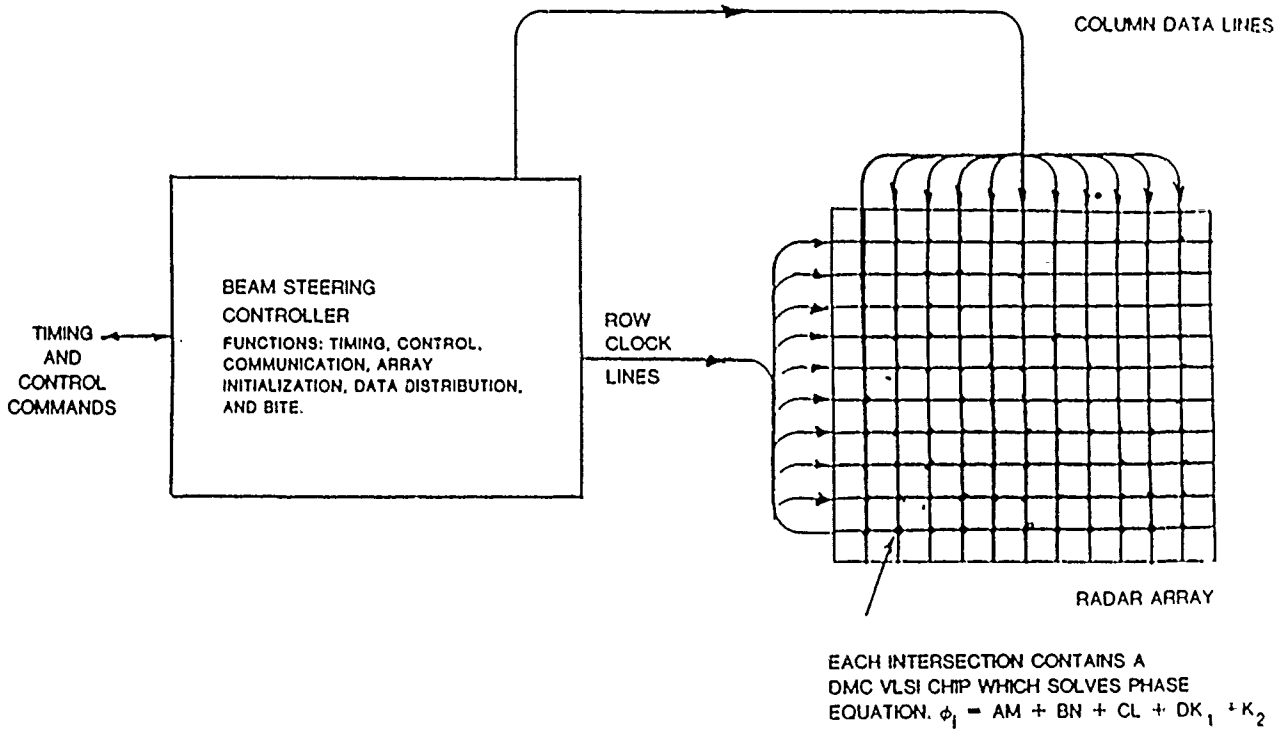

Figure 11. BSU Block Diagram of Distributed Computation Architecture

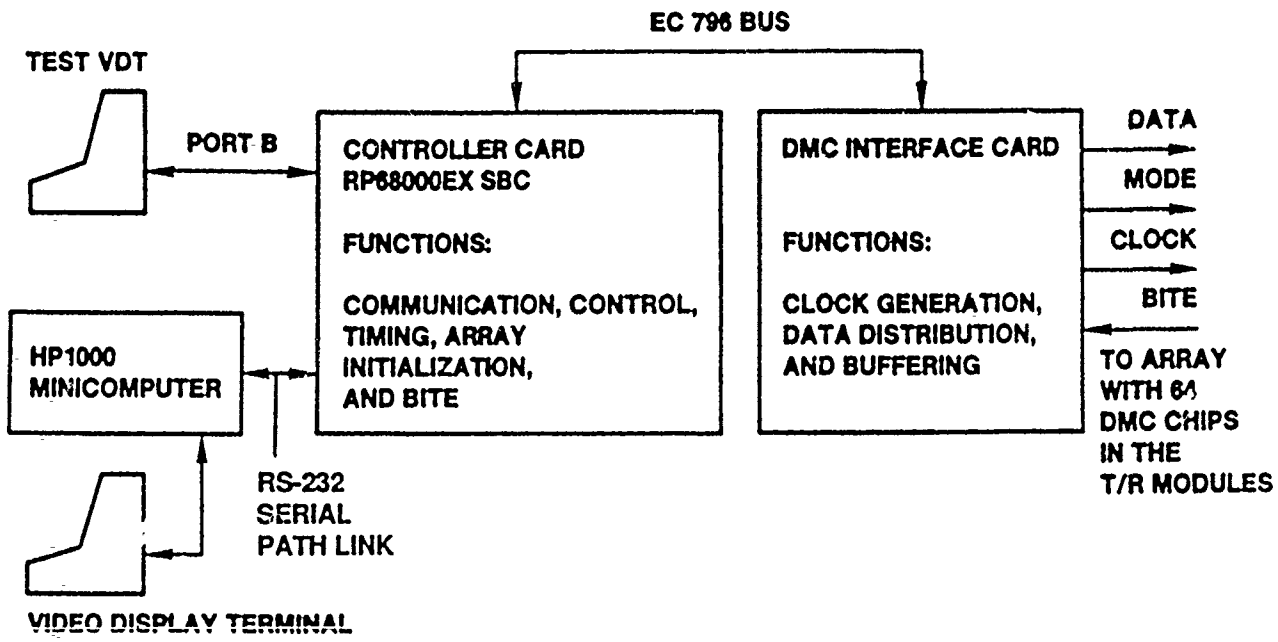

Figure 12. AMIT Beam Steering Controller Block Diagram

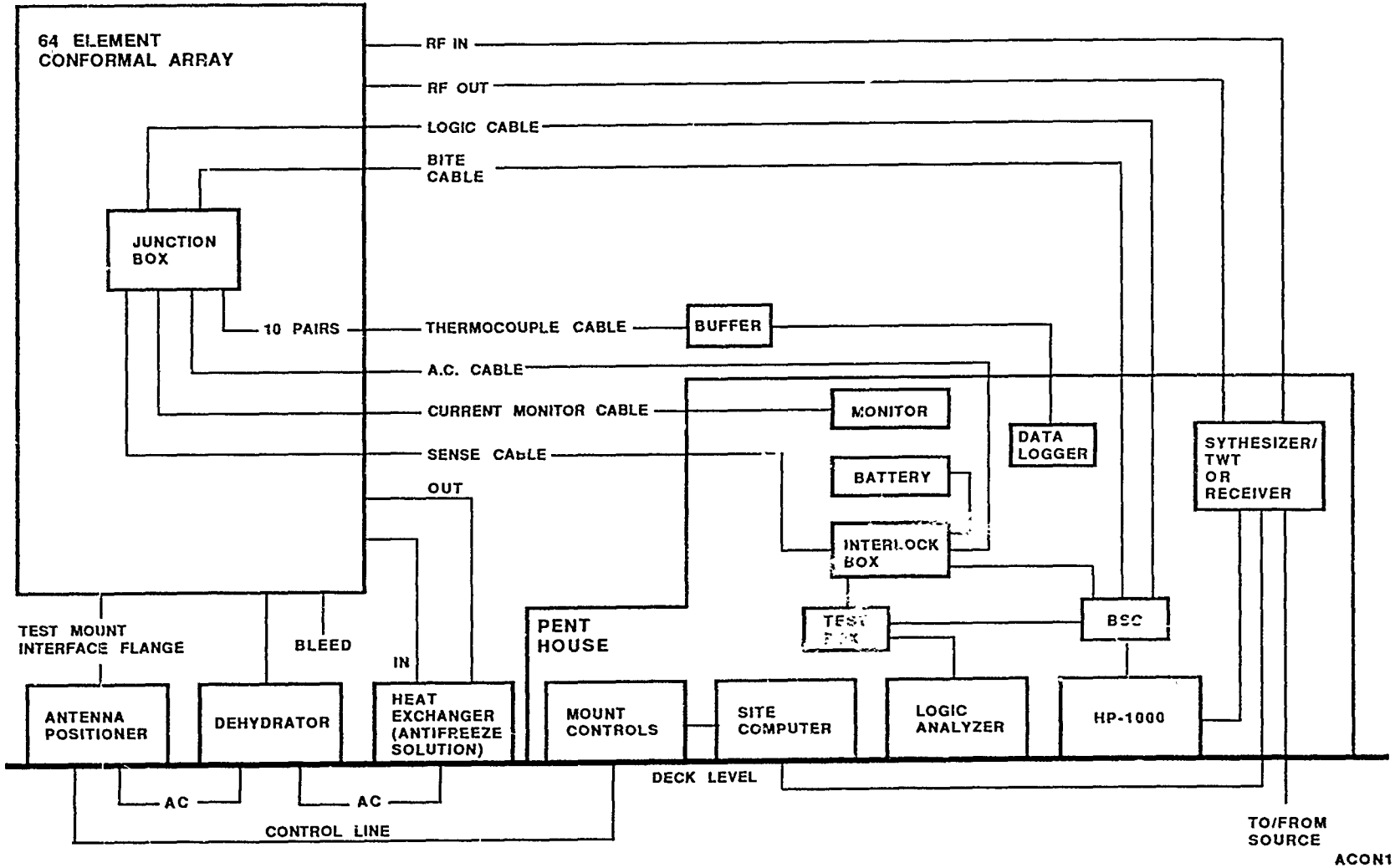

Figure 13. Interconnection of AMIT Array Equipment for Roof-Top Tests

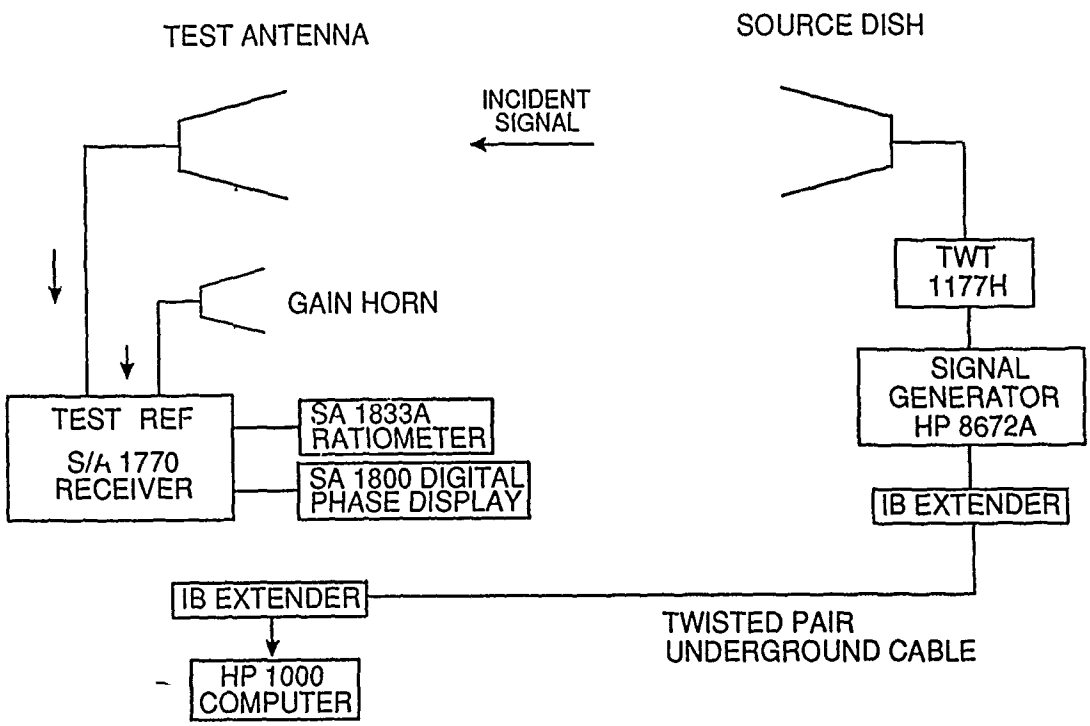

Figure 14. AMIT Receive Calibration Setup Using a Remote Source

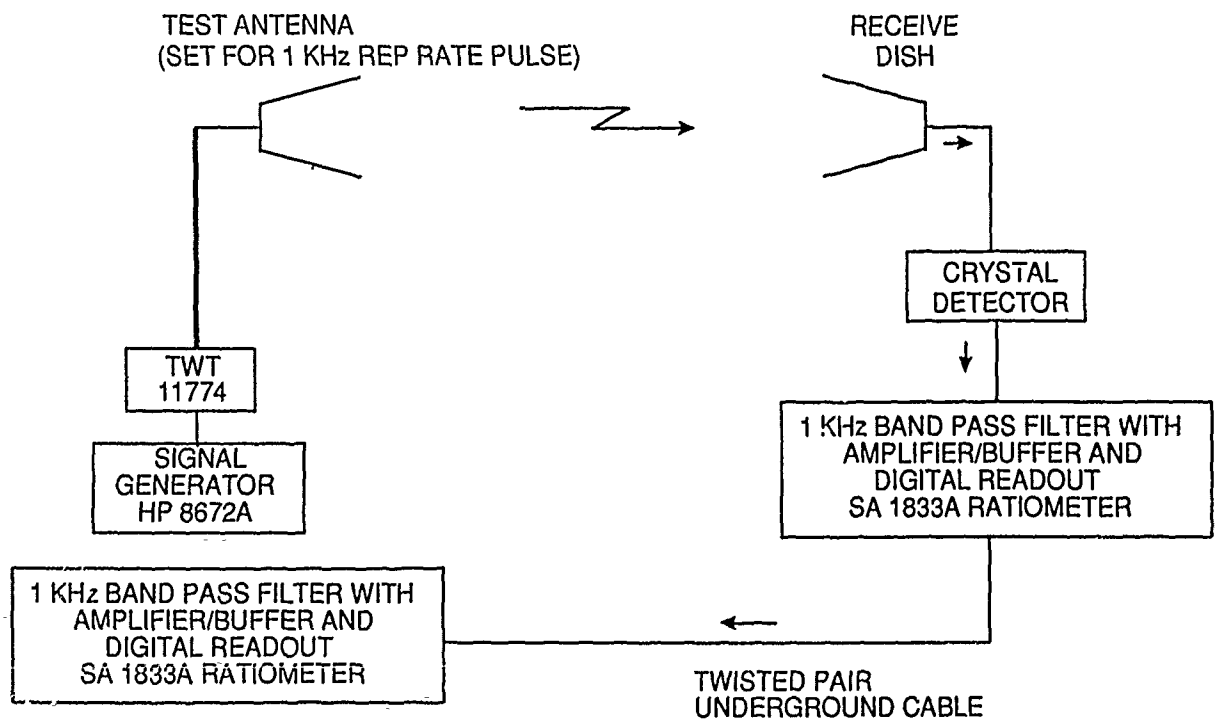

Figure 15. AMIT Transmit Calibration Setup Using a Filtered Signal Link

436

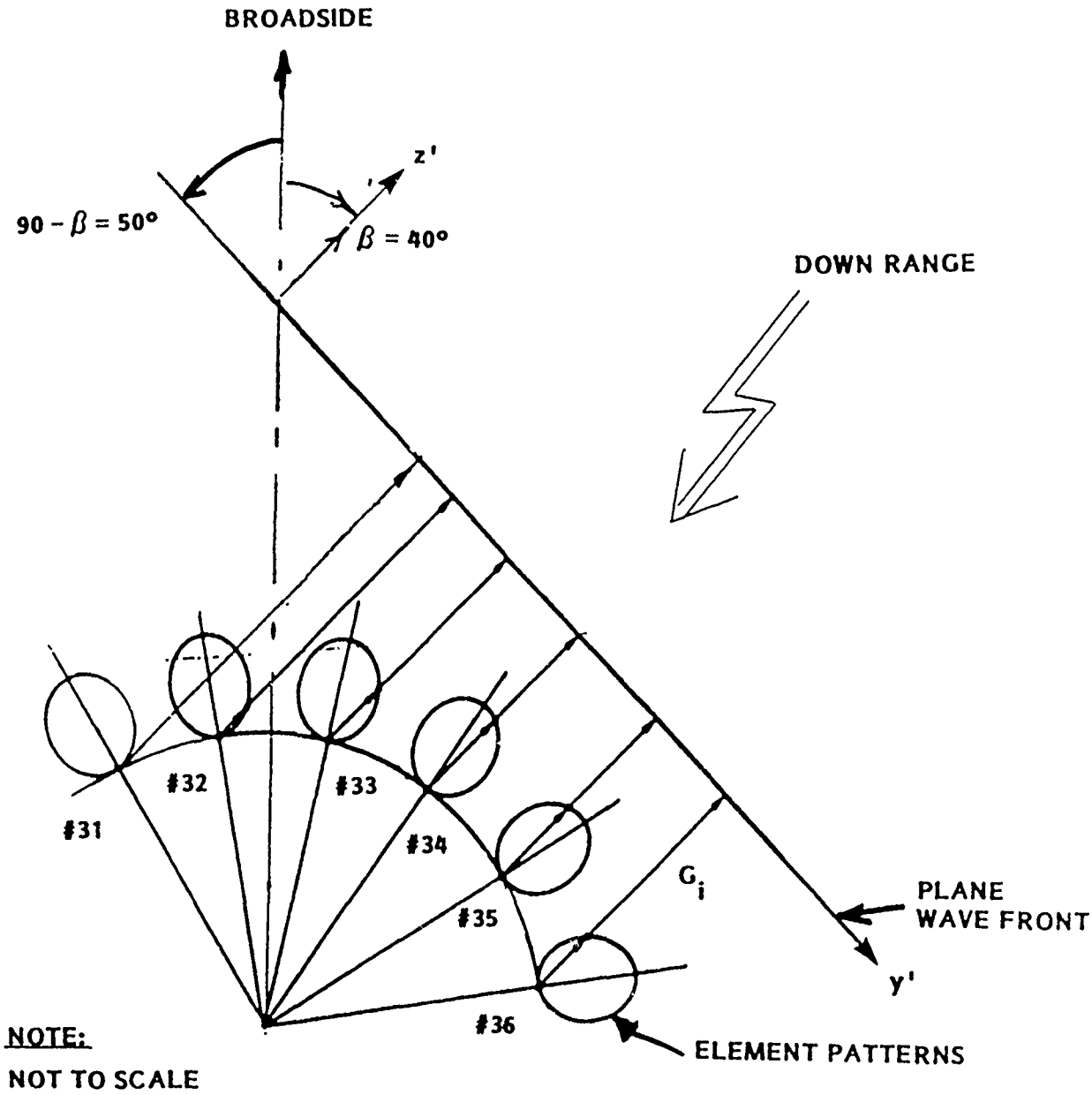

Figure 16. AMIT Array Plane Wave Calibration
for Steered Case
437

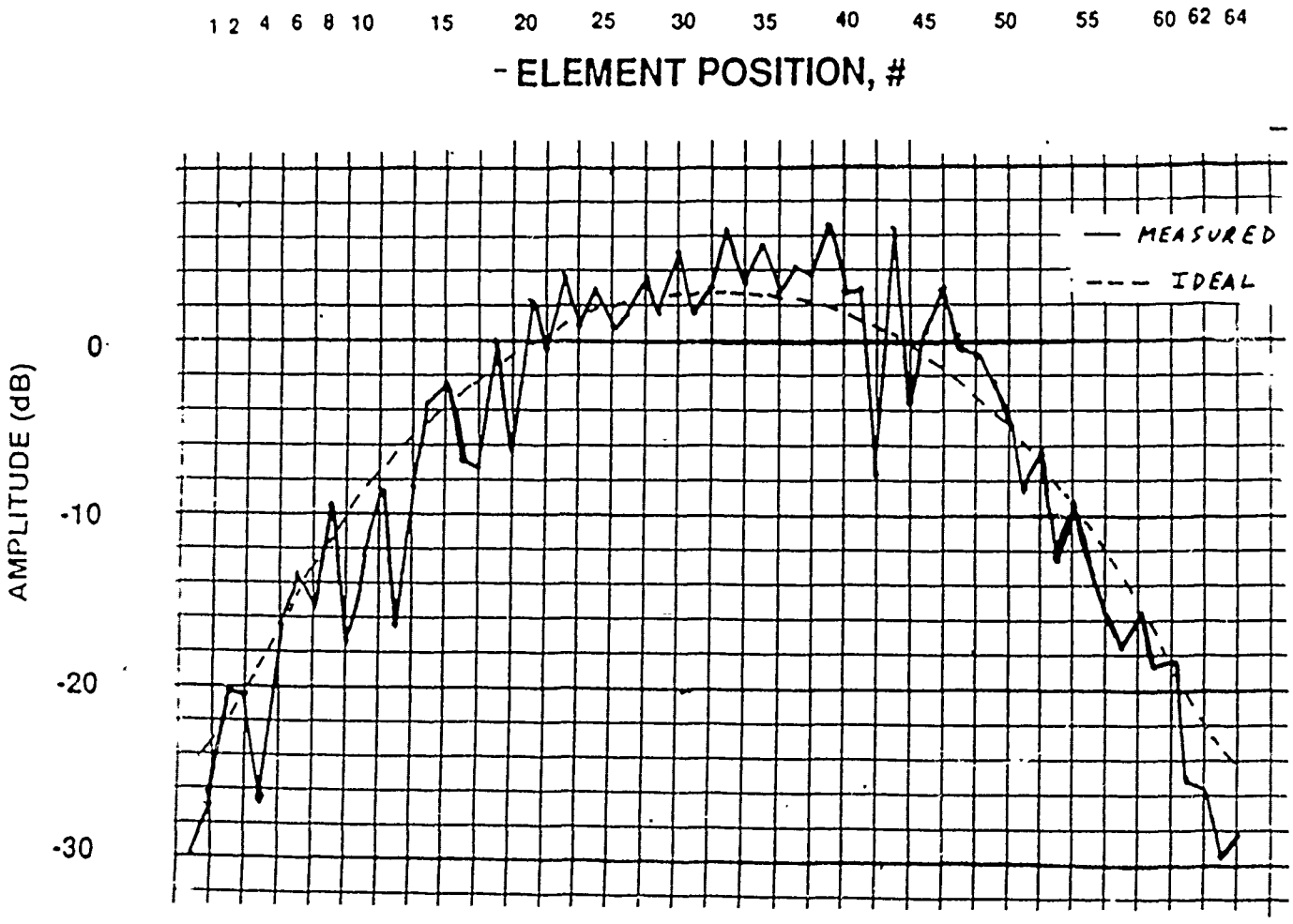

Figure 17. Measured Illumination for Free Space Calibration 40° Scan Angle (Compared to ideal $\bar{n}$ = 10, -50 dB Taylor)

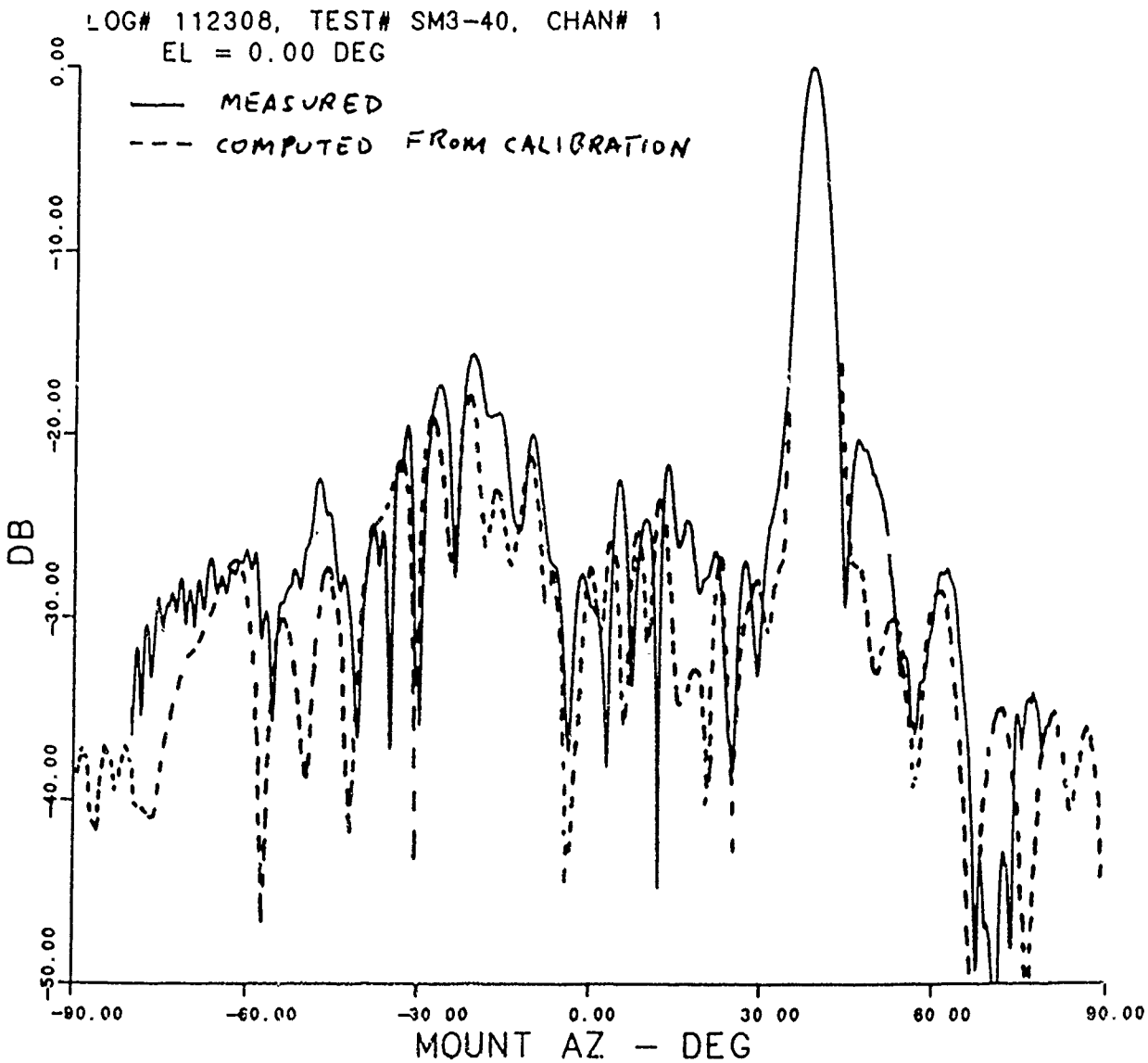

Figure 18. Comparison of Far-Field Patterns from Calibration File with Measured Results on Range

HIGH PRECISION FREQUENCY LOCKING TECHNIQUE FOR ACTIVE MICROSTRIP ANTENNA ARRAYS

Gabriel Colef, George Eichmann, Raymond L. Camisa*
and Aly E. Fathy*
Department of Electrical Engineering
The City College of New York
New York, N.Y. 10031
*SRI-David Sarnoff Research Center
Princeton, N.J.

ABSTRACT

In this paper, a new frequency locking approach for active microstrip antenna arrays is introduced. For better inter-injection locking, a two-dimensional mutual coupling arrangement of the individual elements is used. This spatial arrangement may be complemented with a phase-lock loop to provide a fine tuning of the frequency-lock. Experimental results obtained with Gunn oscillators mounted on the patch antennas are presented. The measured frequency spectrum of the received locked signals are also given.

1. INTRODUCTION

Recent developments in microwave and millimeter-wave integrated circuits and solid-state devices make it possible to incorporate oscillators on a microstrip patch antenna [1-3]. Active antenna

arrays, which can be obtained by properly combining individual active elements, can be used in applications where large power solid-state microwave and millimeter-wave sources are needed. The advantage of using microstrip technology is its low cost, and conformal configuration. The investigation of the possibilities of combining the power from such large arrays is an important task. Since each active array element contains an independent oscillator, the control of the coherence of the large power source becomes a major issue. Recently, several ways of frequency locking of individual oscillators were reported. Both spatial and mutual injection locking have been investigated [1-3]. However, the injection by mutual coupling has the advantage over injecting a signal from space in that it does not require an additional locking signal.

Hummer and Chang investigated both active patch antennas and two-element arrays [1]. Results, obtained at 10 GHz, using 10 mW Gunn diodes as active elements, have shown combining efficiencies of 80 percent. The two-element array had a much narrower pattern than a single patch pattern. For frequency locking of the active array elements results were reported using both spatial injection and mutual coupling as the machanisms. The spatial injection of a signal from space proved to produce a narrower bandwidth than the one obtained by mutual coupling injection locking. Later results [2], reported a combining efficiency of 90 percent for both aperture-coupled patch antenna arrays as well as directly connecting the active elements to the patches. For a certain bias on the Gunn diodes, the pattern exhibited a break of the boresight beam into two lobes. This break was explained as a loss of phase lock.

Camilleri and Bayraktoroglu [3] presented a monolithic active antenna using a millimeter-wave IMPATT oscillator operating at 43.3 GHz with a CW output power of 27 mW and a 7.2 percent conversion efficiency. Linear array radiating elements were combined and radiation patterns were measured as functions of the number of elements and the spacing between elements. An efficient power combining from independent sources eliminated the need for lossy power distribution networks. Inexpensive millimeter-wave power sources can be built by incorporating into the array a waveguide feed. Because the radiation pattern of a single element transmitter is similar to that of an open-ended waveguide, there was an efficient coupling of the source to the waveguide. The reported efficiencies (of the order of 10 percent, which is the efficiency of the same IMPATT structure without the radiating element) indicate that the structure worked well both as an oscillator and a radiator. The arrays of oscillators can be injection locked by two mechanisms; either injection locking by radiation coupling, or injection locking by means of coupling via transmission lines between elements. Here, the results reported were obtained using the second mechanism. An advantage of the transmission line coupling method is that the coupling strength could be adjusted by adjusting the characteristic impedance of the lines. The results showed that for two- and three-element arrays the injection locking mechanism worked very well and the radiation patterns sharpened.

Mutual coupling is one of the mechanisms of injection locking of adjacent elements in an active array. For the modeling of these effects, Benalla and Gupta [4] investigated a multiport network approach. The model was based on an equivalent mutual-coupling

admittance matrix network. To model the edge fields, the elements of these admittance matrices were found by using equivalent magnetic current line sources. Using this model, mutual coupling effects between radiating edges of the same patch antenna as well as neighboring element effects may be incorporated. The model results showed good agreement with the measurement data. For spacing of a quarter of free-space wavelength between patches, the coupling coefficient reached values of 20 dB. One of the important conclusions was that the coupling between nonradiating edges is much smaller than that from radiating edges. This effect is due to the cosine voltage distribution along the nonradiating edges, thus making it possible to partially cancel the positive portion by the negative portion of this voltage distribution.

This paper introduces a novel approach of frequency locking for active microstrip antenna array. It consists of two mechanisms. The dominant locking method is the interinjection locking by mutual coupling.

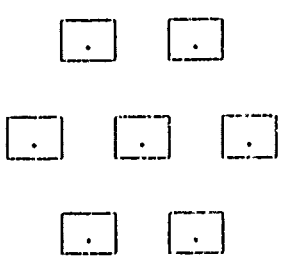

Figure 1. Proposed two-dimensional arrangement

The two-dimensional arrangement, shown in Fig. 1, provides for the spatial interaction between elements in a two-dimensional fashion. This mechanism is complemented with a phase-lock loop to provide additional frequency lock fine tuning.

2. TECHNICAL BACKGOUND

2.1 RECTANGULAR MICROSTRIP ANTENNAS

The rectangular microstrip antennas have been extensively studied and analyzed [5-6]. The various investigated models have proven useful for different applications and frequency ranges.

The rectangular patch antenna can be viewed as two radiating slots, whose admittances are then used to determine the radiation impedance and other parameters. The distance between the radiating slots is taken to be half of the guide wavelength. The physical distance L is adjusted to account for the fringing fields that occur at the radiating edges. These fields tend to increase the effective distance. It is L_{eff} that is to be half a wavelength. Expressions for the dimensions of the rectangular patch are given below:

$$W = \frac{c}{2f_r}\left(\frac{\epsilon_r + 1}{2}\right)^{-\frac{1}{2}} \tag{1}$$

$$L = \frac{c}{2f_r\sqrt{\epsilon_e}} - 2\Delta l \tag{2}$$

where W is the length of the slot and L is the spacing between slots.The correction factor Δl accounts for the fringing effects at the two radiating edges of the antenna, and is given as:

$$\frac{\Delta l}{h} = 0.412\frac{(\epsilon_e + 0.3)(W/h + 0.264)}{(\epsilon_e - 0.258)(W/h + 0.8)} \tag{3}$$

2.2 INPUT IMPEDANCE

To calculate the patch input impedance, a patch model must be established. One of the models which proved to be quite accurate and it is also easy to implement mathematically is the cavity modal-expansion model, where the patch is viewed as a thin cavity with magnetic walls [6-8]. A series of cavity resonant modes is then used to express the field between the patch and the ground plane. For the rectangular patch shown in Fig. 2,

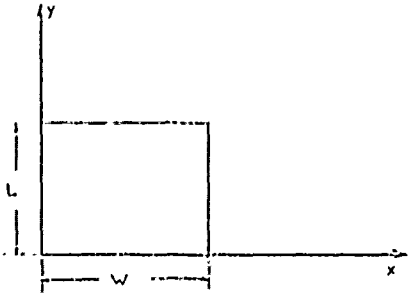

Figure 2. Rectangular patch antenna

the z-directed electric field is expanded as a series of TM_{mn} modes:

$$E_z(x,y) = \sum_m \sum_n A_{mn} e_{mn}(x,y) \tag{4}$$

These mode functions $e_{mn}(x,y)$ satisfy a two-dimensional wave-equation while the corresponding eigenvalues satisfy the equation:

$$k_{mn}^2 = \omega_{mn}^2 \mu\epsilon = k_n^2 + k_m^2 \tag{5}$$

For a nonradiating cavity

$$k_n = \frac{n\pi}{W}, \quad \text{and} \quad k_m = \frac{m\pi}{L}. \tag{6}$$

For the radiating cavity k_n and k_m are slightly different than the above values and hence k_{mn} becomes complex. The complex resonant frequency becomes $\omega_{mn} = \omega_r + j\omega_i$.

The input impedance becomes:

$$Z_{in} = \frac{V_{in}}{I_0} = -jZ_0 kh \sum_{m=0}^{\infty} \sum_{n=0}^{\infty} \frac{\psi_{mn}^2(x_0, y_0)}{k^2 - k_{mn}^2} G_{mn} \tag{7}$$

where h is the height of the dielectric, $k = \omega/c$. Also:

$$G_{mn} = \frac{\sin(n\pi d_x/2W)}{n\pi d_x/2W} \cdot \frac{\sin(m\pi d_y/2L)}{m\pi d_y/2L}$$

and

$$\psi_{mn} = \frac{\chi_{mn}}{\sqrt{WL}} \cos(k_n x) \cos(k_m y)$$

where χ_{mn} is a constant.

In Fig. 3, an equivalent electrical network is shown.

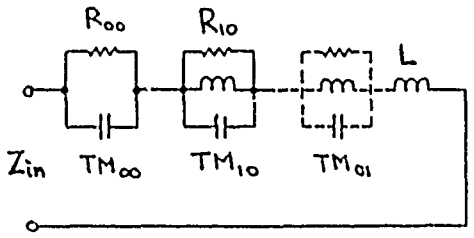

Figure 3. Equivalent circuit of patch antenna

If the operation of the patch antenna is confined to a small region around the TM_{10}, the network can be simplified and the input impedance becomes:

$$Z_{in} = jX_t - \frac{j(\omega/C_{10})}{\omega^2 - (\omega_r + j\omega_i)^2} \tag{8}$$

where $C_{10} = 0.5C_{dc}\cos(\pi y_0/L)$ and $C_{dc} = \epsilon_0 WL/h$. The term jX_t represents a net series inductance that accounts for the contributions from the other modes.

The complex eigenvalue k_{10} can be found through an iterative process which solves the equation:

$$\tan(k_{10}L) = \frac{2k_{10}\alpha_{10}}{k_{10}^2 - \alpha_{10}^2} \tag{9}$$

where :

$$\alpha_{10} = j\frac{2\pi Z_0 h}{\lambda_0 W} Y_{in} \tag{10}$$

and Y_{in} represents the radiating wall admittance and is

$$Y_{in} = (\pi/377)(W/\lambda_0) + j0.01668(\Delta l/h)(W/\lambda_0)\varepsilon_r \tag{11}$$

To account for different W/L ratios, the wall admittance may be modified by a factor:

$$F_y(W, L) = 0.7747 + 0.5977(W/L - 1) - 0.1638(W/L - 1)^2 \tag{12}$$

The solution for k_{10} is given by:

$$k_{10} = (\pi/L) - (\Delta_1/L) \tag{13}$$

where

$$\Delta_{p+1} = \frac{2(\alpha_{10}L)(\pi - \Delta_p)}{(\alpha_{10}L)^2 + 2\Delta_p\pi - \Delta_p^2 - \pi^2} - \frac{\Delta_p^3}{3} \tag{14}$$

For Δ_0, a starting value of zero is recommended.

Another microstrip patch model is the transmission line model which assumes that the two radiating edges are separated by a low impedance transmission line of length L. The expression of the input impedance of a microstrip patch with arbitrary feed point is:

$$Z_{in} = Z_c\left[\frac{Z_c\cos(\beta L_1)+jZ_w\sin(\beta L_1)}{Z_w\cos(\beta L_1)+jZ_c\sin(\beta L_1)}+\frac{Z_c\cos(\beta L_2)+jZ_w\sin(\beta L_2)}{Z_w\cos(\beta L_2)+jZ_c\sin(\beta L_2)}\right]^{-1}$$
$$+jX_t \tag{15}$$

The two input impedance expressions , Eqs. (7) and (15), are in good agreement.

2.3 MUTUAL CONDUCTANCE

The mutual conductance between two patch antennas is used to determine the array directivity and its input power. The expression of the mutual conductance is derived from the total radiated power. Since microstrip planar arrays radiate in half space, the mutual conductance between slots of length W placed in the X-Y plane and aligned in the Z direction is given by [9]:

$$C_{12} = \frac{1}{\pi}\sqrt{\frac{\epsilon}{\mu}}\int_0^{\pi}\frac{\sin^2\left(\frac{\pi W}{\lambda_0}\cos(\theta)\right)}{\cos^2(\theta)}\sin^3(\theta)J_0\left(\frac{X}{\lambda_0}2\pi\sin(\theta)\right)$$
$$\cdot\cos\left(\frac{Y}{\lambda_0}2\pi\cos(\theta)\right)d\theta \tag{16}$$

where J_0 is the Bessel function of first kind and zero order. Eq. (16) can be extended to patches with arbitrary position in the X-Y plane by considering contributions from both edges of each patch. A single expression for an odd mode excitation of the patch antennas can be shown to be:

$$C_{12} = \frac{1}{\pi}\sqrt{\frac{\epsilon}{\mu}}\int_0^{\pi}\frac{\sin^2\left(\frac{\pi W}{\lambda_0}\cos(\theta)\right)}{\cos^2(\theta)}\sin^3(\theta)\left[2J_0\left(\frac{X}{\lambda_0}2\pi\sin(\theta)\right)\right.$$
$$\left.+J_0\left(\frac{X+L}{\lambda_0}2\pi\sin(\theta)\right)+J_0\left(\frac{X-L}{\lambda_0}2\pi\sin(\theta)\right)\right]$$
$$\cdot\cos\left(\frac{Y}{\lambda_0}2\pi\cos(\theta)\right)d\theta \tag{17}$$

The terms in the sharp paranthesis represent mutual conductances from two slots spaced at distances of X, X-L, and X+L apart. Plots for the mutual conductance, obtained by numerical integration of Eq. (17), for various positioning of the two patches are shown in Fig 4 (a)-(c).

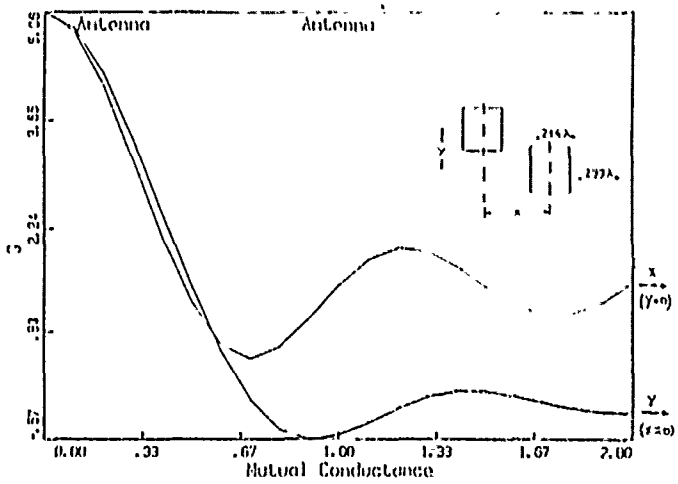

Figure 4(a). Mutual conductance of two rectangular patches when either X or Y are set to zero.

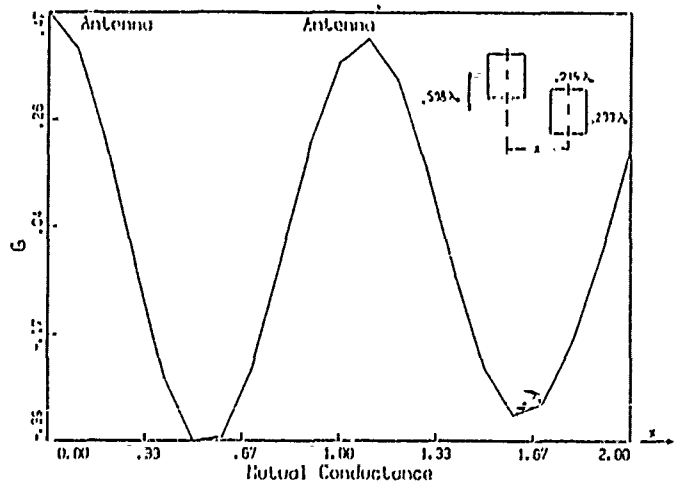

Figure 4(b). Mutual conductance of two rectangular patches when $Y = 0.598\lambda_0$.

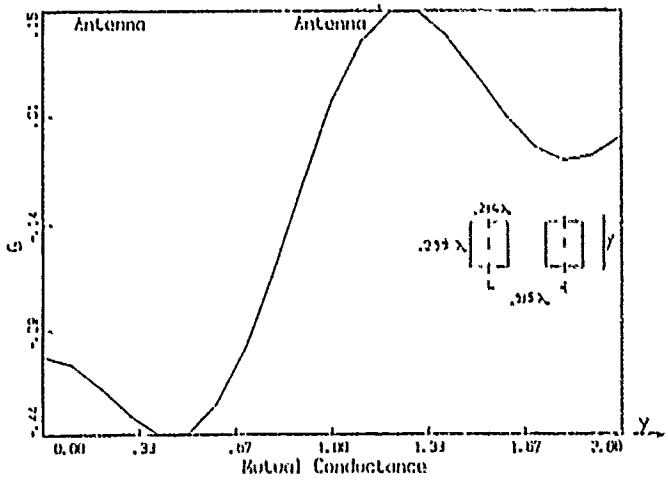

Figure 4(c). Mutual conductance of two rectangular patches when $Y = 0.515\lambda_0$.

The results in Fig. 4 (a) are similar to the ones shown in Ref. [9]. As the spacing between the elements increases (see Fig.4 (b)-(c)), the mutual conductance exhibits a slower decrease in magnitude with the relative position.

2.4 TWO-PORT PARAMETERS

The use of the moment method enables an elegant calculation of the two-port parameters of two microstrip patch antennas [10]. The expressions of the two-port impedance matrix are:

$$Z_{11} = -\sum_{n=1}^{N_1} I_n V_n^{(1)} \tag{18}$$

$$Z_{21} = Z_{12} = -\sum_{n=1}^{N} I_n V_n^{(2)} \tag{19}$$

where $V_n^{(i)}$ is the voltage due to source i, i = 1,2, and I_n represents the expansion mode currents.

3. EXPERIMENTAL RESULTS

Microstrip patches and arrays have been fabricated for the X-band frequencies. The Gunn diodes used operated around 8 GHz. The placement for the position of the Gunn diodes was such that oscillation condition occurred [2].

In Fig. 1, the geometrical positioning of the array elements is shown. The spacing between elements was a half of guide-wavelength in both directions. The performance of wider patche arrays, yielding better coupling between elements, was also investigated. In particular a W of 0.75 times the guide-wavelength was chosen.

In Fig. 5 (a)-(b), the measured patterns for a four element array excited from a single common source is shown. The half power beamwidths were less than 50 degrees for the H-plane pattern, and less than 35 degrees for the E-plane pattern. The spatial arrangement shows no main lobe break in the patterns. These results show that this arrangement is suitable for active arrays.

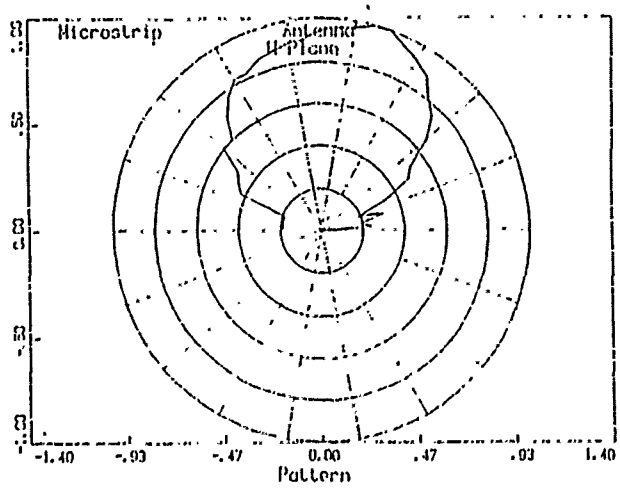

Figure 5(a). Relative power H-plane pattern for a four-element array.

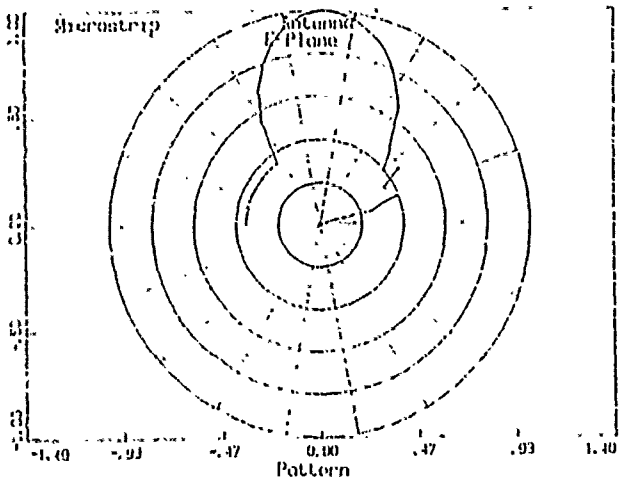

Figure 5(b). Relative power E-plane pattern for a four-element array.

In Fig. 6 (a) and (b), the measured coupling coefficient between patches of different positions is shown. The results show no significant difference in mutual coupling between elements regardless of their position with respect to the radiating edges. Uniform two-dimensional mutual coupling is made possible this way.

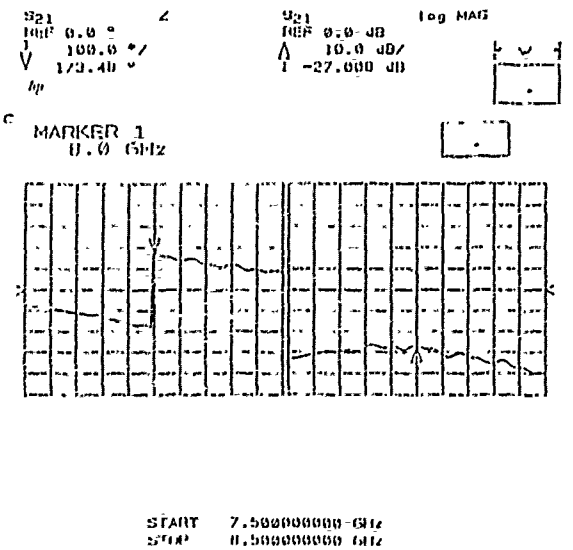

Figure 6(a). Coupling coefficient for two patches arranged as shown.

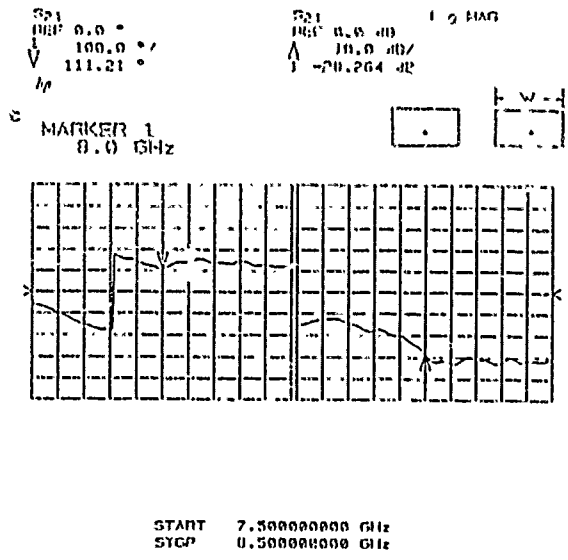

Figure 6(b). Coupling coefficient for two patches with adjacent non-radiating edges.

In Fig. 7, measured input impedance an array element where the feed-point is approximately .32L from one of the radiating edges is shown. The position of the feed point makes it possible that the resonant condition for the Gunn diode is achieved.

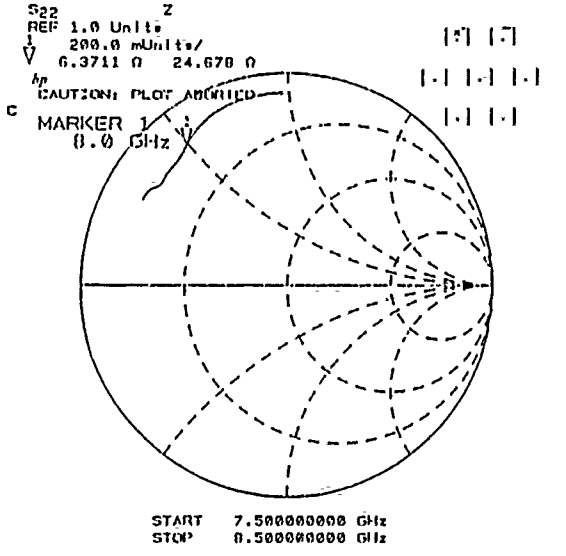

Figure 7. Measured input impedance of an array element in a seven-element array.

The results obtained for three active microstrip patches positioned, as shown in Fig. 8, are given in Fig. 9 - 12.

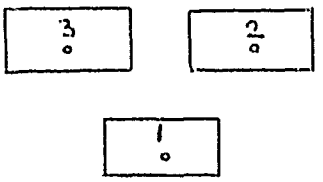

Figure 8. Two-dimensional arrangement of a three-element active array.

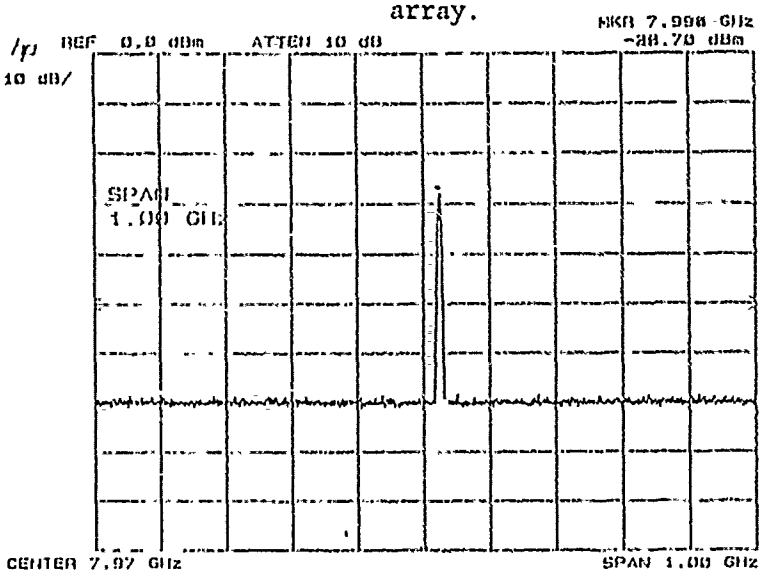

Figure 9. Frequency spectrum of element #1 in the array.

In Fig. 9, the frequency spectrum, obtained when only the Gunn diode of element #1 was biased, is shown. The radiation frequency is 7.996 GHz.

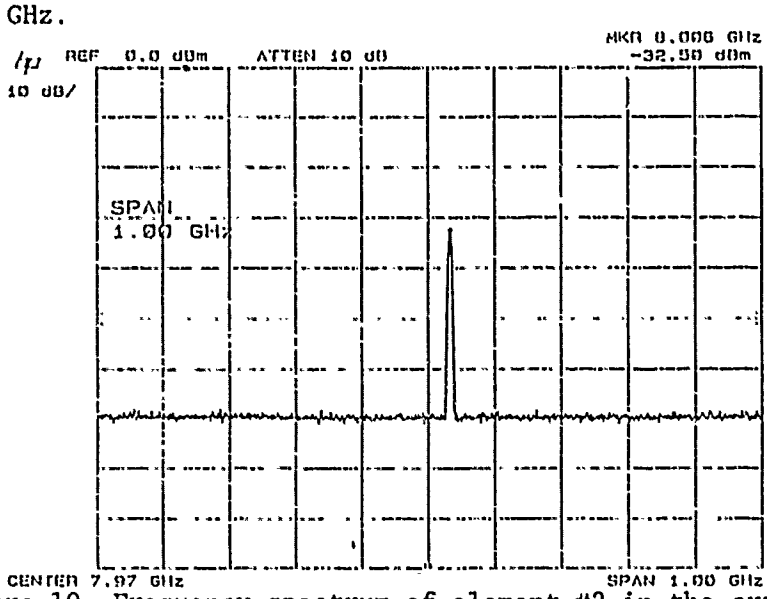

Figure 10. Frequency spectrum of element #2 in the array.

In Fig. 10, the frequency spectrum, obtained when the Gunn diode of element #2 was biased, is shown. The radiation frequency is 8.006 Glz.

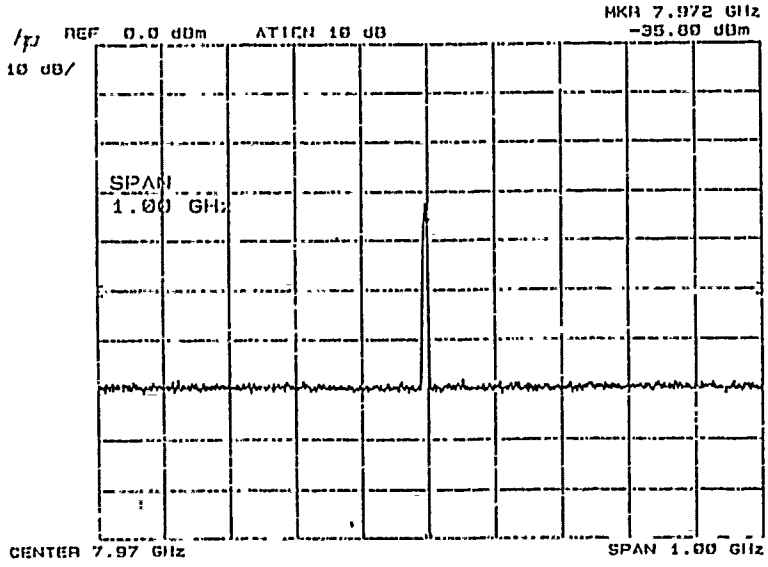

Figure 11. Frequency spectrum of elements #3 in the array.

In Fig. 11, the frequency spectrum for the biased Gunn diode of element 3 is shown. The radiation frequency is 7.972 Gllz. The differences in radiation frequencies are less than 34 Mllz.

When all the Gunn diodes were biased, the three oscillators injection locked to the frequency of 7.948 Gllz, as shown in Fig. 12.

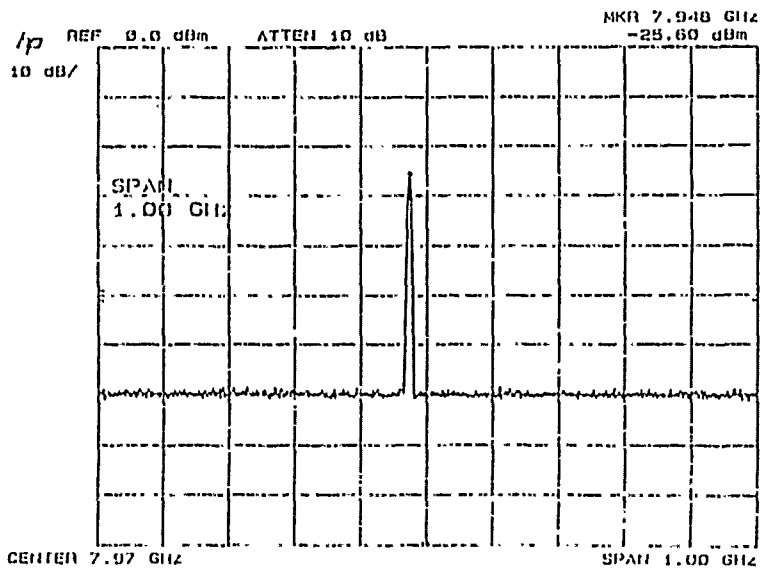

Figure 12. Frequency spectrum of injection-locked three-element array.

The calculated combining efficiency is around 87.5 percent. These results show that the new arrangement provides for efficient injection locking by mutual coupling. Additional measurements involving larger arrays are in progress.

4. SUMMARY AND CONCLUSIONS

In this paper, a new spatial arrangement for a two-dimensional microstrip active antenna array is introduced. The measurements of the array elements input impedance and coupling coefficient show that this arrangement is suitable for two-dimensional mutual-coupling injection-locked active array. This approach is superior to others for its two-dimensional array capabilities. A three-element active array was fabricated and tested. The active elements were Gunn diodes with oscillation frequencies around 8 GHz. The three active elements locked efficiently via mutual-coupling. The introduction in the array of an element provided with phase-lock loop will give a high precision frequency locked array. This additional element has to be coupled to only one of the elements of the array in order to injection lock all array elements. Therefore, the mutual-coupling injection-lock mechanism together with a phase-lock loop mechanism provide for a high precision frequency locking method. Results to support this statement are in progress.

5. REFERENCES

1. K. A. Hummer and K. Chang (1988), "Spatial Power Combining Using Active Microstrip Patch Antennas", Microwave and Optical Technology Letters, Vol. 1 , No. 1, pp. 8-9.

2. K. Chang, K. A. Hummer, and J. L. Klein (1989), "Experiments on Injection Locking of Active Antenna Elements for Active Phased Arrays and Spatial Power Combiners", IEEE Trans. on Microwave Theory and Tech., Vol. 37, No. 7, pp. 1078-1084.

3. N. Camilleri and B. Bayraktaroglu (1988), "Monolithic Millimeter-wave IMPATT Oscillator and Active Antenna", IEEE MTT-S Digest, Vol. 2, pp. 955-958

4. A. Benalla and K.C. Gupta (1989), "Multiport Network Approach for Modeling the Mutual Coupling Effects in Microstrip Patch Antennas and Arrays", IEEE Trans. on Antennas and Propag., Vol. 37, No. 2, pp.148-152.

5. I. J. Bahl and P. Bhartia (1980), "Microstrip Antennas", Artech House, Inc., Chapter 2.

6. K. R. Carver and J. W. Mink (1981), "Microstrip Antenna Technology", IEEE Trans. on Antennas and Propag., Vol. AP-29, No. 1, pp. 2-24

7. Y. T. Lo, D. Solomon, and W. F. Richards (1979), "Theory and Experiment on Microstrip Antennas", IEEE Trans. on Antennas and Propag., Vol. AP-27, No. 2, pp. 137-145

8. W. F. Richards, Y. T. Lo, and D. D. Harrison (1981), "An Improved Theory for Microstrip Antennas and Applications", IEEE Trans. on Antennas and Propag., Vol. AP-29. No. 1, pp. 38-46.

9. A. G. Derneryd (1978), "A Theoretical Investigation of the Rectangular Microstrip Antenna Element", IEEE Trans. on Antennas and Propag., Vol. AP-26, No. 4, pp. 532-535.

10. D. M. Pozar (1982), "Input Impedance and Mutual Coupling of Rectangular Microstrip Antennas", IEEE Trans on Antennas and Propag., Vol. AP-30, pp. 1191-1196.

PHEDRE : A COMPUTER PACKAGE FOR THE STUDY OF ELECTROMAGNETIC RADIATION

Christian RENARD

Fabrice CLERC

Louis BEAULIEU

MICROWAVE DEPARTMENT

ELECTRONIQUE SERGE DASSAULT

55, quai Marcel Dassault

92214 Saint-Cloud _ FRANCE

ABSTRACT 1

The constant demand for more sophisticated antennas requires the use of powerful simulation facilities .

By analogy with the circuit field, we have developped PHEDRE, a CAD-CAM software tool to design, characterize and optimize the behavior of single antennas, arrays and phased arrays with their radome and mounted on structures (eg. airborne antennas).

This paper describes the structure and possibilities of PHEDRE.

The close interconnection of 4 modules allows the user to choose the appropriate path to conceive and describe the antenna .
These modules have been devised with the idea of being adaptable and easy to use.

The computer software has been enlarged to facilitate exchanges :

- with other antenna computer programs (eg. wire antennas through the use of EFIE to define new radiators, antennas with plates,..)
- with automatic measurement and automatic manufacturing tools.

The oral presentation will be illustrated with the designs of:

- a very low sidelobe slot array antenna and its radome
- a phased-array antenna including the study of active elements .

1. INTRODUCTION 2

The study of the association of radiating elements with a radome requires the use of powerful simulation facilities.

By analogy with microwave circuits design softwares, we have developped a Computer-Aided Design software tool for antennas, taking into account the following features :

- modularity : to allow the adaptation of the softwares to the various antenna problems,
- possibility of updating in relation to future problems,
- possibility of linkage to other facilities through the exchange of data files .

The basic concept of this software lies in the computation of the response of a set of radiating elements to an arbitrarily polarized incident wave .

On the side of this main axis, specialized modules have been designed to master the influence of external and internal couplings, of the environment and of the radomes.

Figure 1 shows the general structure of the software and the associated "peripherals" described in the following sections.

2. CONNECTION TO EXTERNAL FACILITIES. 3

Connections to external facilities are :

- The exchange of datas with test facilities, in order :
  - . to facilitate the comparison of results,
  - . to use the power of the central computer when the local ones are not powerful enough,
  - . to easily obtain program inputs from measured datas .

  The test facilities can be :
  - . circuit test facilities, to characterize the feeding system,
  - . antenna test facilities, to get far-field or near-field (planar or cylindrical) measured data available.

- The use of computer results from circuit simulation programs (eg. SUPERCOMPACT) to analize the feeding of antennas

- The link with numerically controlled manufacturing machines, in order to facilitate the exchange of the mechanical dimensions (eg. the link to an automatic milling machine for a slot array antenna) and to collect the datas from the mechanical checking machines after the manufacturing of the antenna, as a feed-back to the programs .

3. MAIN FRAME OF THE PROGRAM. 4

The basic idea lies in the expression of the far field of an array as a function of the sum of fields originated from the various elementary radiators, identical or different in nature, placed in whatever manner in space, to which different complex weights are assigned, when the whole geometry is known.

In order to do this, two libraries have been established:

- a library of radiators defined by :
  - . analitical formulations,
  - . files created by the use of the Method of Moments to describe wire antennas or antennas made of plates
  - . files issued from measurements .
- a library of illuminating functions with :
  - ."standard" laws suitable for creating sum, difference patterns for rectangular or elliptical antennas, cosecant-squared,..)
  - ."advanced" laws, by the use of specific algorithms (eg. adaptive antennas).

From the previous datas, a certain amount of parameters can be be obtained, for example :

- the response of each radiator to an arbitrarily polarized incident wave,
- the global field radiated by the array (figure 2).

A specific module completes the previous results in order to give, besides the radiation pattern, informations about : 5

- the gain,
- the effects of errors on the amplitudes and the phases, by successive random samplings or by the use of a statistical model
- the ecartometry parameters for monopulse antennas.

4. COMPLEMENTS FOR THE PARASITIC PHENOMENA

The good working condition of an antenna requires the control of the following elements :

4.1. COUPLINGS.

- internal couplings associated with the feeding elements of the antenna. They are easily linked to the external couplings in a matrix form, in order to proceed to the analysis of the antenna;
- external couplings between the radiators, resulting in the modification of their weights or their active patterns.

In some cases, as for the slot array antennas, a process of synthesis can be carried out in order to determine the geometry of the antenna, to manufacture a mock-up and to execute an operation of Analysis with the real mechanical dimensions,

in order to validate the analitycal design. 6

An example of comparison between simulation and measurement for an antenna composed of five waveguides, each with 30 slots fed in progressive mode (figure 3) , with first sidelobes at 15 dB below the isotropic level, is shown on figure 4.

4.2. ENVIRONMENT.

The influence of a structure on the radiation pattern of an antenna is analyzed by the use of models based on the Uniform Theory of Diffraction (UTD) in the following steps (figure 5);

- definition of the exact geometry of the problem (through the use of appropriate software tools, eg. CATIA developped by DASSAULT SYSTEMES) or a geometry approximated by canonical surfaces ;
- definition of the different rays to take into account between a source and an observation point, according to the phenomenon (reflection, diffraction, multiple interaction)
- computation of the transfer functions along the different paths with the use of a library of electromagnetic models ;
- re-composition of the total field from the various components

4.3. RADOME.

The presence of a radome in front of an antenna can be studied by specific programs using :

- Geometrical Optics formulation for large antennas 7
- a near-field technique for medium-sized antennas
- the use of the reciprocity theorem for small or medium-sized antennas, to take into account the reaction antenna-radome.

The figure 6 (right) shows an example of the influence of a radome optimized for the antenna shown above.

5. CONCLUDING REMARKS

This paper has shown the possibility to extend the principles of Computer Aided Design in order to obtain a general treatment method for current and future array antennas.

6. REFERENCES.

1. Renard, C., Clerc, F., Bealieu, L. (1989) Progiciel d'étude du rayonnement électromagnétique. Paper presented at the Colloque Int'l sur le Radar meeting, Paris, France.
2. Tabbara,W., Clerc, F., Chety, L. (1989) SER d'objets ... Paper presented at the Colloque Int'l sur le Radar, Paris,France
3. Elliott, R.S.(1981) Antenna theory and design, Prentice-Hall,NY
4. Molinet, F., Beaulieu, L.(1984) Interaction of the electromagn. field with nearby structures, Ann. Telecom.39(n.1-2):44-51.

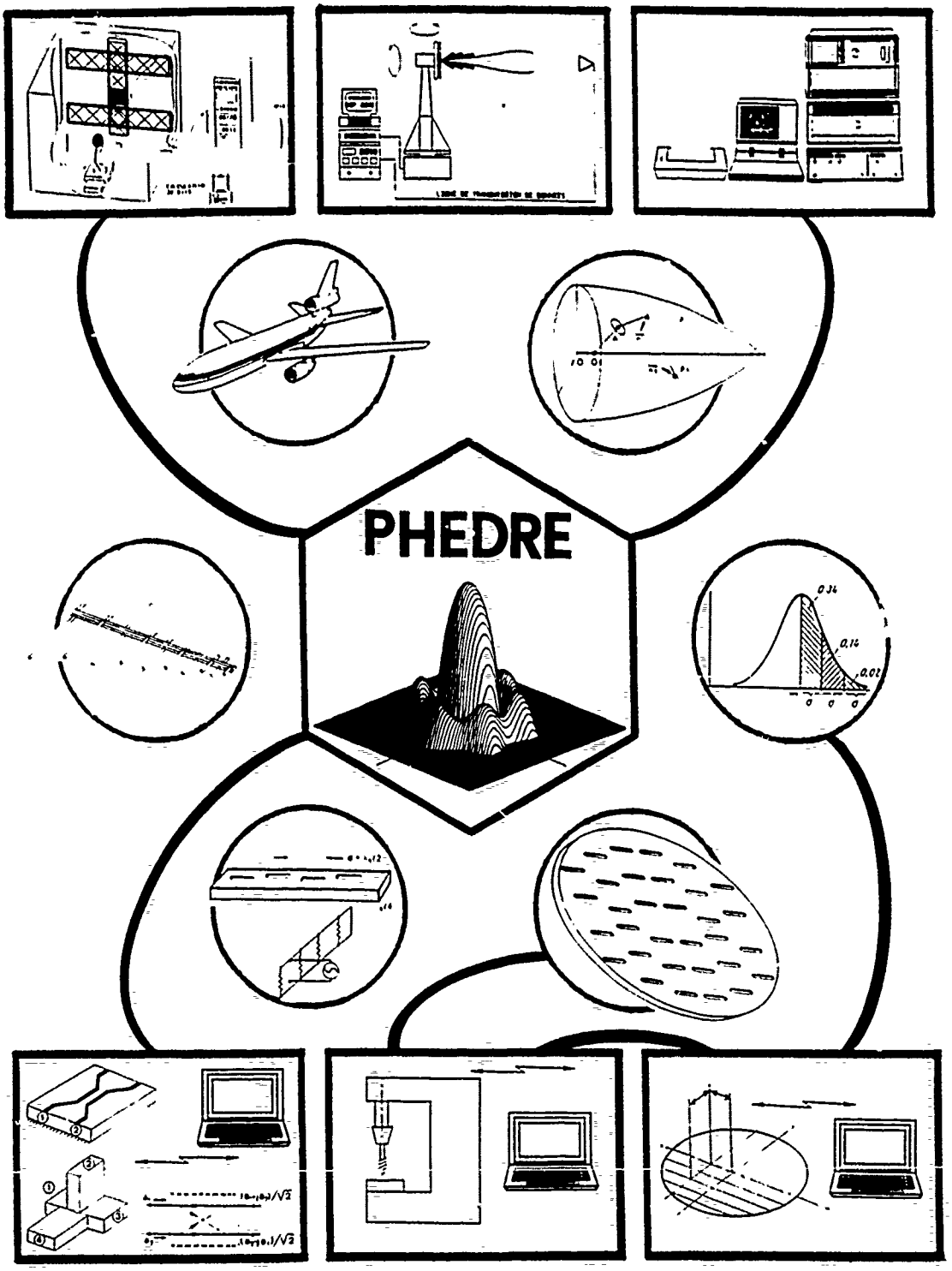

FIGURE 1

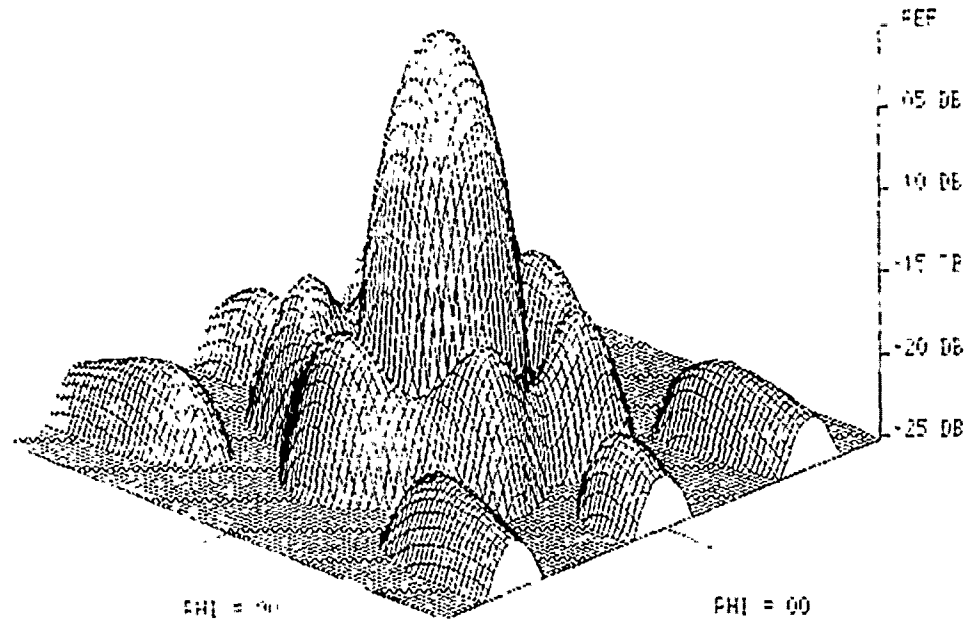

PHEDRE N1

(1) Array of 19 L-band elements on a disk

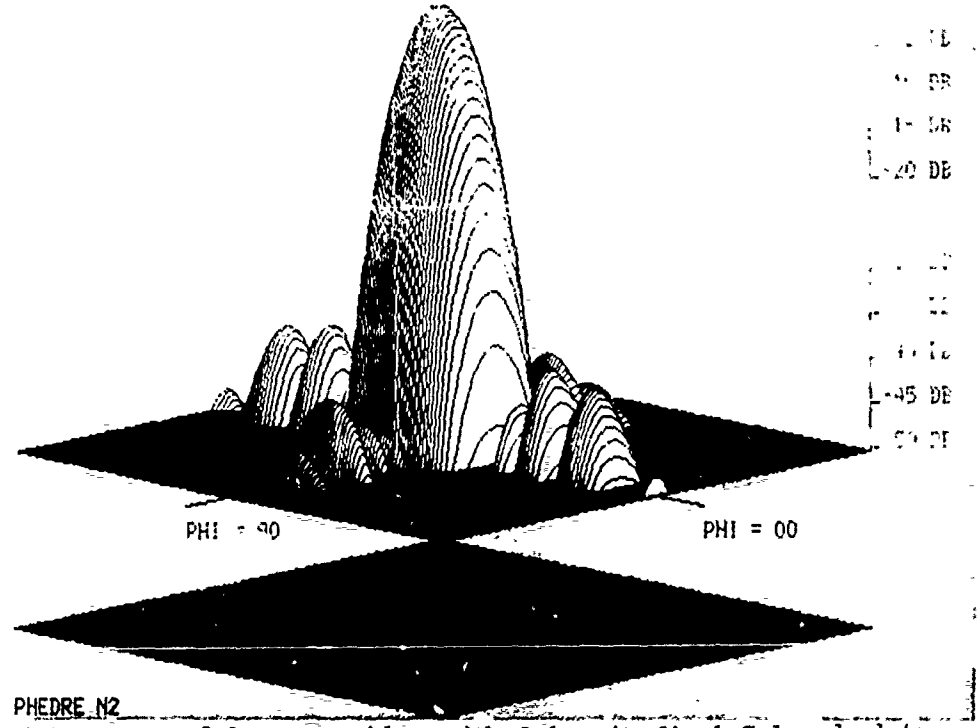

(2) Array of 8 waveguides with 8 longitudinal S-band slots

FIGURE 2

VERY LOW SIDE LOBE

TRAVELLING WAVE FED LONGITUDINAL SLOT ARRAY

KU - BAND

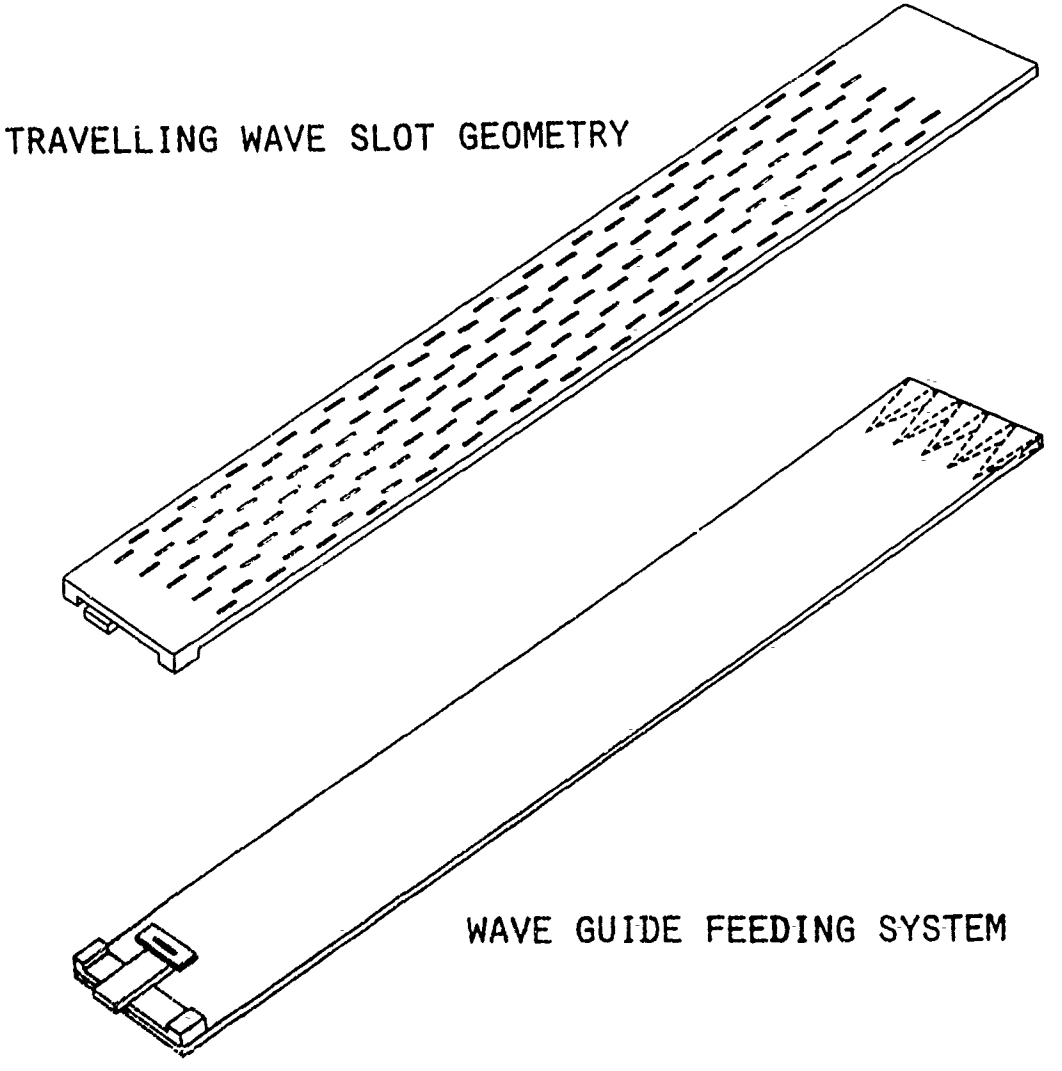

FIGURE 3

VERY LOW SIDE LOBE

TRAVELLING WAVE FED LONGITUDINAL SLOT ARRAY

Ku - band

simulation with manufacturing errors
waveguide and external mutual couplings

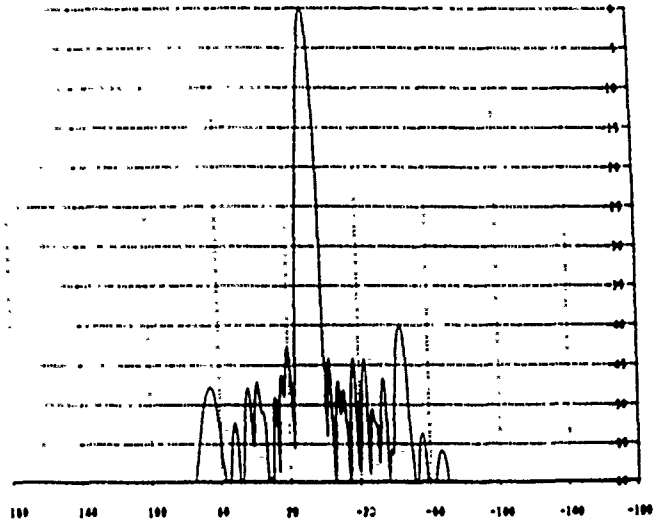

measurement of the array on far field range

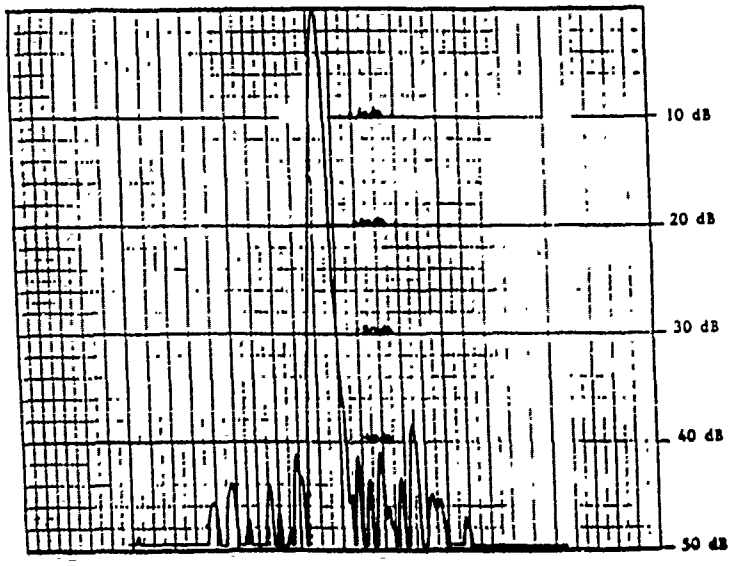

FIGURE 4

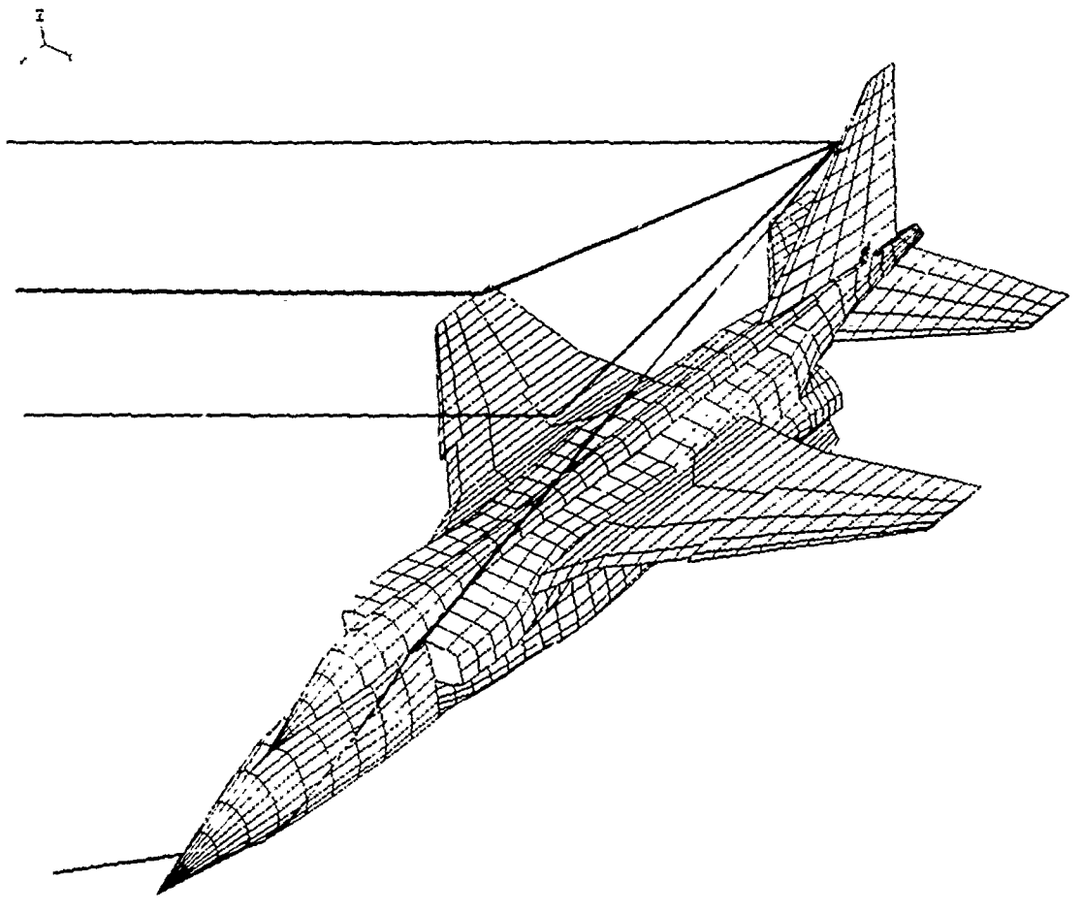

FIGURE 5

VERY LOW SIDELOBES ANTENNA
ANTENNA WITH RADOME MEASUREMENT

3-layer sandwich
non optimized radome

antenna
without radome

5-layer sandwich
optimized radome

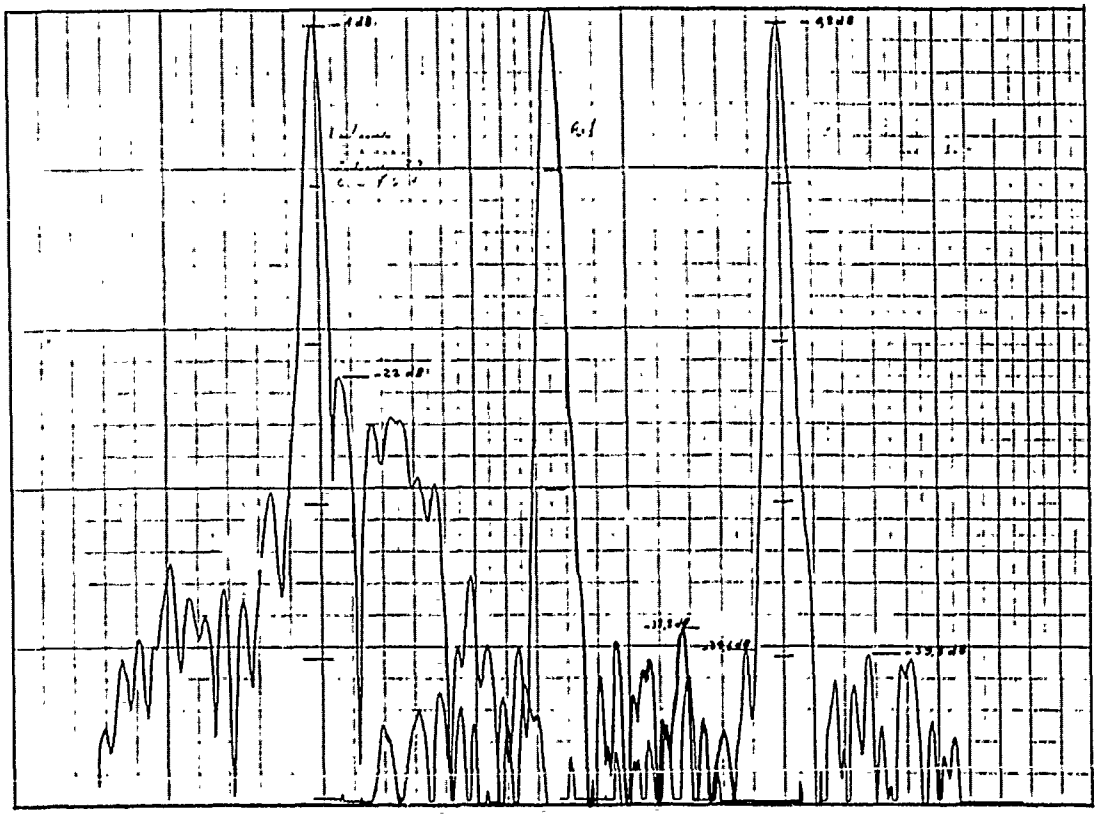

FIGURE 6

Moment Method Analysis of a Stripline-Fed Finite Slot Using Subdomain Basis Functions

Peter S. Simon, Kim McInturff
Deron L. Johnson, Joseph A. Troychak

Raytheon Electromagnetic Systems Division
Goleta, CA

1989 Antenna Applications Symposium
Monticello, IL, Sept. 20-22, 1989

Abstract

The input impedance of a finite slot in the groundplane of a stripline is numerically studied using the method of moments. The problem is cast so that the unknowns to be determined are the electric currents on the stripline center conductor and the equivalent magnetic currents in the slot. The cases where the slot is present in only one (the "unilateral" case) or both (the "bilateral" case) of the groundplanes are each included in the analysis.

The basis functions used in this study are the triangle subdomain functions introduced by Rao, Wilton and Glisson. The advantage of this choice is that the slot and strip geometries which can be analyzed include any shape whose boundary can be adequately approximated by a polygon. This class includes practically all shapes of engineering interest.

The accuracy of the method is verified by comparison to measured and theoretical results. The application of this analysis technique to the design of broad band stripline/slotline transitions is also discussed.

1 Introduction

Tapered notch antennas, otherwise known as Vivaldi or LTSA (Linearly Tapered Slotline Antennas), have been described by a number of workers[1]-[5]. The recent popularity of these elements for use in phased arrays is due to their wide impedance bandwidth, ease of manufacture, low cost, light weight, and small size. Current designs are mostly empirical due to the lack of an adequate theoretical model for notch elements. Due to the complexity of the elements, most analyses to date[6,7,8] have had to resort to rather crude approximations, which are not sufficiently accurate for many design purposes. Raytheon is engaged in an ambitious effort to rigorously analyze an array of single- or

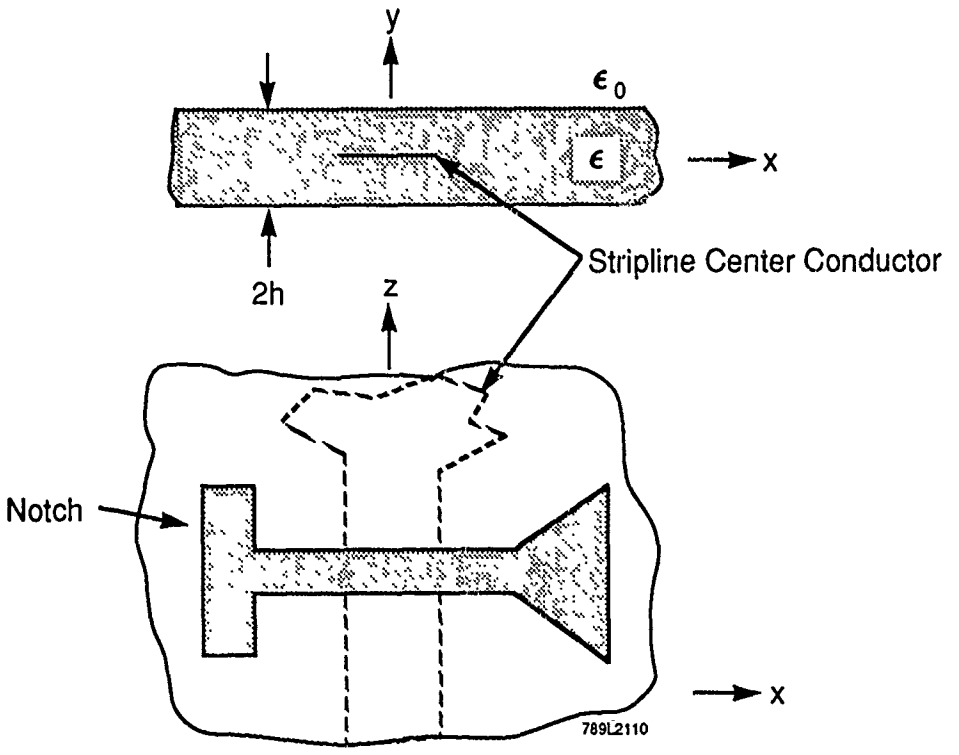

Figure 1: The geometry treated in this note consists of a stripline feeding a notch in one or both of its ground planes.

dual-polarized notch elements excited by stripline feeds. The analysis will be able to handle arbitrarily shaped stripline and notch regions.

This paper reports on some preliminary work which is the first step in the direction of the full notch array analysis. The geometry treated here consists of a stripline of arbitrary shape exciting an arbitrarily shaped, finite aperture in one or both of its groundplanes. The motivation for this work was to develop and demonstrate the capability to

1. model electric and magnetic currents using triangle subdomain basis functions on arbitrarily shaped domains.

2. treat the coupling between strip and aperture currents.

3. accurately compute the input impedance in the stripline feed.

These goals have been attained. In addition, we describe in Section 6 how a slight modification to the code results in a useful design tool for the stripline/slotline transition portion of the notch element.

The structure to be analyzed is shown in Figure 1. It consists of a balanced stripline with a finite aperture (or slot) cut in one (the "unilateral" case) or both (the "bilateral" case) of its ground planes. Both the stripline center

conductor and the slot may be of irregular polygonal shape, although the stripline assumes a uniform width at some distance from the slot. If slots are present in both ground planes then they must be identical in shape and location. Notice also that the stripline extends only a finite distance beyond the slot in the $+z$ direction.

2 Source Modeling and Input Impedance

An $e^{j\omega t}$ time convention is assumed and suppressed. RMS phasors are used for all fields and sources. The quantity of interest is the input reflection coefficient at $z = 0$ in the stripline, which is assumed to be far enough into the uniform width region and far enough from the slot so that the fields here in the stripline can be written as[1]

$$\mathbf{E}(x,y,z) = \left(ae^{-jkz} + be^{jkz}\right)\mathbf{e}(x,y) \tag{1}$$

$$\mathbf{H}(x,y,z) = \left(ae^{-jkz} - be^{jkz}\right)\mathbf{h}(x,y) \tag{2}$$

where $\mathbf{e}$ is the transverse electric field of the TEM stripline mode, $\mathbf{h} = \hat{\mathbf{z}}\times\mathbf{e}/\eta$, and η is the intrinsic impedance of the dielectric. a and b are the usual travelling wave variables whose ratio gives the input reflection coefficient, $\Gamma_{\text{in}} = b/a$. To determine Γ_{in} we first place a Perfect Magnetic Conducting (PMC) wall at $z = 0$ and impress on it at $z = 0^+$ an electric surface current

$$\mathbf{J}^i = \hat{\mathbf{z}}\times\mathbf{h}. \tag{3}$$

This current impressed on the PMC wall is the rigorous field theory realization of an open circuit current source which will ensure that the magnetic field at $z = 0^+$ is exactly $\mathbf{h}$. One could then, in principle, find the input impedance by computing the electric field in the source plane. However, knowledge of the stripline current $I(z)$ is also sufficient to determine the reflection coefficient since, in the vicinity of $z = 0$

$$I(z) = \left(I_0^+ e^{-jkz} - \Gamma_{\text{in}} I_0^+ e^{jkz}\right). \tag{4}$$

Once the current on the strip is computed using the moment method procedure described below, equation (4) is sampled at $N \geq 3$ locations in z. This results in an overdetermined set of linear equations in the unknowns I_0^+ and $\Gamma_{\text{in}} I_0^+$. A least squares solution then gives the input reflection coefficient.

[1] In equations (1) and (2) we have ignored the contribution of a propagating TEM parallel plate mode which would be excited in the unilateral case. Due to opposing symmetries this mode cannot couple with the stripline mode and thus its inclusion would have no effect on either the induced stripline currents or the input impedance, which is defined with respect to the stripline mode.

3 Equivalent Currents

First the center conductor (assumed to be infinitely thin) is removed and replaced with an equivalent electric surface current, $\mathbf{J}_s$.

If only one ground plane contains a slot, we assume that it is the one located at $y = h$. If both groundplanes contain slots (the bilateral case) then by symmetry we restrict consideration to the region $y > 0$ by enforcing a PMC boundary condition at $y = 0$. The induced electric surface current flows just above this PMC wall at $y = 0^+$. Therefore in both the unilateral and bilateral cases we deal with only a single slot.

As was done with the center conductor, the slot is removed (filled in with PEC or Perfect Electric Conductor) and the necessary magnetic surface currents are defined so that the total fields are unchanged. For fields in the region $|y| < h$ (interior) the required source is a magnetic surface current flowing at $y = h^-$ given by

$$\mathbf{M}_s^{\text{int}}(x, z) = \hat{\mathbf{y}} \times \mathbf{E}(x, h, z). \tag{5}$$

For fields in the region $y > h$ the equivalent source is a magnetic surface current flowing in the $y = h^+$ plane given by

$$\mathbf{M}_s^{\text{ext}}(x, z) = -\mathbf{M}_s^{\text{int}}(x, z). \tag{6}$$

The analysis now reduces to determining the induced electric and magnetic surface currents, $\mathbf{J}_s$ and $\mathbf{M}_s^{\text{int}}$, which is accomplished using the method of moments. The method of moments formulation involves solving integral equations whose kernels are Green's functions; the next section describes the required Green's functions and their efficient evaluation.

4 Green's Functions

Green's functions for three separate geometries are required. The first geometry is the PEC/PEC parallel-plate waveguide structure with a PMC wall at $z = 0$. Only the case where source and observation point are in the region $z > 0$ is of interest. This geometry will be needed to analyze the unilateral slot case. The second geometry is the PMC/PEC parallel-plate waveguide with a PMC wall at $z = 0$, needed for the case of a bilateral slot. The final geometry is the half-space $y > h$ with a PEC boundary condition at $y = h$.

4.1 PEC/PEC Parallel-Plate Green's Functions

We first treat the case of an infinite, dielectric loaded, PEC/PEC parallel-plate waveguide with plate separation $b = 2h$ which lacks the PMC wall at $z = 0$. The effect of the PMC wall is easily accommodated later using images.

The material between the plates is dielectric of permeability μ_0 and permittivity $\epsilon = \epsilon_r c_0$, with corresponding wavenumber $k = \omega\sqrt{\mu_0\epsilon}$ at the radian frequency ω. The electric and magnetic fields in the waveguide satisfy

$$\mathbf{E} = -j\omega\mathbf{A} - \nabla\Phi + \epsilon^{-1}\nabla\times\mathbf{F} \quad (7)$$

$$\mathbf{H} = j\omega\mathbf{F} - \nabla\Psi + \mu_0^{-1}\nabla\times\mathbf{A} \quad (8)$$

where $\mathbf{A}$ is the magnetic vector potential, Φ the electric scalar potential, $\mathbf{F}$ the electric vector potential, and Ψ the magnetic scalar potential. The potentials are taken to satisfy the Lorentz gauge, so

$$(\nabla^2 + k^2)\mathbf{A} = -\mu_0\mathbf{J} \quad (9)$$

$$(\nabla^2 + k^2)\Phi = -\sigma/\epsilon \quad (10)$$

$$(\nabla^2 + k^2)\mathbf{F} = \epsilon\mathbf{M} \quad (11)$$

$$(\nabla^2 + k^2)\Psi = -\sigma_m/\mu_0 \quad (12)$$

where $\mathbf{J}$ and σ are the electric current and charge densities, respectively, and $\mathbf{M}$ and σ_m are the corresponding magnetic quantities. The currents and charges are related via the equations of continuity

$$\nabla\cdot\mathbf{J} + j\omega\sigma = 0, \quad (13)$$

$$\nabla\cdot\mathbf{M} + j\omega\sigma_m = 0. \quad (14)$$

The boundary conditions on the potentials are stated in Table 1. A derivation can be found in [9].

PEC Wall	PMC Wall
$\Phi = 0$	$\Psi = 0$
$\frac{\partial\Psi}{\partial n} = 0$	$\frac{\partial\Phi}{\partial n} = 0$
$\hat{\mathbf{n}}\times\mathbf{A} = \mathbf{0}$	$\hat{\mathbf{n}}\times\mathbf{F} = \mathbf{0}$
$\nabla_n\cdot\mathbf{A} = 0$	$\nabla_n\cdot\mathbf{F} = 0$
$\hat{\mathbf{n}}\times(\nabla\times\mathbf{F}) = \mathbf{0}$	$\hat{\mathbf{n}}\times(\nabla\times\mathbf{A}) = \mathbf{0}$
$\hat{\mathbf{n}}\cdot\mathbf{F} = 0$	$\hat{\mathbf{n}}\cdot\mathbf{A} = 0$

Table 1: Boundary Conditions on Potentials

The potential Green's functions which are needed are those for A_x, A_z, Φ, F_x, F_z, and Ψ. Note from Table 1 that all these functions satisfy either Dirichlet ($U = 0$) or Neumann ($\frac{\partial U}{\partial n} = 0$) boundary conditions at the parallel plates. Therefore, we define Dirichlet (G_d) and Neumann (G_n) Green's

functions as the solutions to

$$(\nabla^2 + k^2)G(\mathrm{r};\mathrm{r}') = -\delta(\mathrm{r} - \mathrm{r}') \tag{15}$$

satisfying the radiation condition and the appropriate boundary condition on the parallel plates. In (15) $\mathrm{r} = (x, y, z)$ is the observation point and $\mathrm{r}' = (x', y', z')$ is the source point.

4.1.1 Dirichlet Boundary Condition

A modal series expansion for G_d is

$$G_d^{(m)}(\mathrm{r};\mathrm{r}') = \frac{1}{2\pi h}\sum_{n=1}^{\infty} \sin\left(\tfrac{n\pi}{2h}(y+h)\right)\sin\left(\tfrac{n\pi}{2h}(y'+h)\right) K_0(\alpha_n\sqrt{(x-x')^2+(z-z')^2}) \tag{16}$$

where K_0 is the modified Bessel function of order 0 and

$$\alpha_n = \sqrt{\left(\frac{n\pi}{2h}\right)^2 - k^2}. \tag{17}$$

Equation (16) is useful when the source and observation points are well separated. An alternative series can be obtained by imaging the source through the parallel-plate walls and summing the contributions of the images, which may now be considered to be radiating in a medium without boundaries. This method yields a second series expansion of G_d to be

$$G_d^{(i)}(\mathrm{r};\mathrm{r}') = \frac{1}{4\pi}\sum_{n=-\infty}^{\infty}\left(\frac{e^{-jkR_n^+}}{R_n^+} - \frac{e^{-jkR_n^-}}{R_n^-}\right) \tag{18}$$

where R_n^+ and R_n^- are distances between observation point and n^{th} order image points given by

$$R_n^+ = \sqrt{(x-x')^2+(z-z')^2+(y-y'-4nh)^2} \tag{19}$$

$$R_n^- = \sqrt{(x-x')^2+(z-z')^2+(y+y'-(2n+1)2h)^2}. \tag{20}$$

A technique due to Richards[10] for combining (16) and (18) to arrive at a single, numerically efficient formula valid for all r and r′ is described in [11] and used here. For $c \geq 0$, define ρ_c, P_n^+, and P_n^- as

$$\rho_c = \sqrt{(x-x')^2+(z-z')^2+c^2} \tag{21}$$

$$P_n^+ = \sqrt{\rho_c^2+(y-y'-4nh)^2} \tag{22}$$

$$P_n^- = \sqrt{\rho_c^2+(y+y'-(2n+1)2h)^2} \tag{23}$$

which amounts to replacing $(x-x')^2$ in (19) and (20) by $(x-x')^2+c^2$. Clearly, making this substitution in the series found in (16) and (18) preserves the equality of the two series. An additional benefit is that for any $c > 0$ the series

$$\mathcal{G}_d^{(m)}(\mathrm{r};\mathrm{r}') = \frac{1}{2\pi h}\sum_{n=1}^{\infty}\sin\left(\tfrac{n\pi}{2h}(y+h)\right)\sin\left(\tfrac{n\pi}{2h}(y'+h)\right)K_0(\alpha_n\rho_c) \qquad (24)$$

is convergent even when r and r′ coincide. Application of a Kummer transformation to (18) then results in the final formula

$$\begin{aligned} G_d(\mathrm{r};\mathrm{r}') &= \mathcal{G}_d^{(m)}(\mathrm{r};\mathrm{r}') + \\ &\frac{1}{4\pi}\sum_{n=-\infty}^{\infty}\left(\frac{e^{-jkR_n^+}}{R_n^+} - \frac{e^{-jkP_n^+}}{P_n^+} - \frac{e^{-jkR_n^-}}{R_n^-} + \frac{e^{-jkP_n^-}}{P_n^-}\right). \end{aligned} \qquad (25)$$

for the unbounded, parallel-plate, Dirichlet Green's function. The constant c is adjusted so that the series in (24) and (25) converge rapidly.

The derivative of G_d with respect to y is also required, and is given by

$$\begin{aligned} \frac{\partial G_d}{\partial y}(\mathrm{r};\mathrm{r}') &= \frac{\partial \mathcal{G}_d^{(m)}}{\partial y}(\mathrm{r};\mathrm{r}') + \\ &\frac{1}{4\pi}\sum_{n=-\infty}^{\infty}\left\{(y-y'-4nh)\left[e^{-jkP_n^+}\left(\frac{jk}{P_n^{+2}}+\frac{1}{P_n^{+3}}\right) - e^{-jkR_n^+}\left(\frac{jk}{R_n^{+2}}+\frac{1}{R_n^{+3}}\right)\right] + \right. \\ &\left.(y+y'-(2n+1)2h)\left[e^{-jkR_n^-}\left(\frac{jk}{R_n^{-2}}+\frac{1}{R_n^{-3}}\right) - e^{-jkP_n^-}\left(\frac{jk}{P_n^{-2}}+\frac{1}{P_n^{-3}}\right)\right]\right\} \end{aligned} \qquad (26)$$

where

$$\frac{\partial \mathcal{G}_d^{(m)}}{\partial y}(\mathrm{r};\mathrm{r}') = \frac{1}{4h^2}\sum_{n=1}^{\infty} n\cos\left(\tfrac{n\pi}{2h}(y+h)\right)\sin\left(\tfrac{n\pi}{2h}(y'+h)\right)K_0(\alpha_n\rho_c). \qquad (27)$$

The Dirichlet Green's function and its y derivative are then evaluated for source and observation points in the planes $y = 0$ and $y = h$. Note that of the special cases of interest only $G_d(x,0,z;x',0,z')$ and $\frac{\partial G_d}{\partial y}(x,h,z;x',0,z')$ are nonzero.

4.1.2 Neumann Boundary Condition

A similar procedure can be followed for the Neumann Green's function. The modal expansion is

$$\begin{aligned} G_n^{(m)}(\mathrm{r};\mathrm{r}') &= -\frac{j}{8h}H_0^{(2)}(k\rho_0) \\ &+ \frac{1}{2\pi h}\sum_{n=1}^{\infty}\cos\left(\tfrac{n\pi}{2h}(y+h)\right)\cos\left(\tfrac{n\pi}{2h}(y'+h)\right)K_0(\alpha_n\rho_0) \end{aligned} \tag{28}$$

where $H_0^{(2)}$ is the zero order Hankel function of the second kind. The multiple image expansion is

$$G_n^{(i)}(\mathrm{r};\mathrm{r}') = \frac{1}{4\pi}\sum_{n=-\infty}^{\infty}\left(\frac{e^{-jkR_n^+}}{R_n^+}+\frac{e^{-jkR_n^-}}{R_n^-}\right). \tag{29}$$

Combining these expressions as before we arrive at the accelerated formula for the Neumann Green's function

$$\begin{aligned} G_n(\mathrm{r};\mathrm{r}') &= \mathcal{G}_n^{(m)}(\mathrm{r};\mathrm{r}') + \\ &\frac{1}{4\pi}\sum_{n=-\infty}^{\infty}\left(\frac{e^{-jkR_n^+}}{R_n^+}-\frac{e^{-jkP_n^+}}{P_n^+}+\frac{e^{-jkR_n^-}}{R_n^-}-\frac{e^{-jkP_n^-}}{P_n^-}\right) \end{aligned} \tag{30}$$

where

$$\begin{aligned} \mathcal{G}_n^{(m)}(\mathrm{r};\mathrm{r}') &= -\frac{j}{8h}H_0^{(2)}(k\rho_c) \\ &+ \frac{1}{2\pi h}\sum_{n=1}^{\infty}\cos\left(\tfrac{n\pi}{2h}(y+h)\right)\cos\left(\tfrac{n\pi}{2h}(y'+h)\right)K_0(\alpha_n\rho_c). \end{aligned} \tag{31}$$

The derivative of G_n with respect to y is given by

$$\begin{aligned} \frac{\partial G_n}{\partial y}(\mathrm{r};\mathrm{r}') &= \frac{\partial \mathcal{G}_n^{(m)}}{\partial y}(\mathrm{r};\mathrm{r}') + \\ &\frac{1}{4\pi}\sum_{n=-\infty}^{\infty}\left\{(y-y'-4nh)\left[e^{-jkP_n^+}\left(\frac{jk}{P_n^{+2}}+\frac{1}{P_n^{+3}}\right)-e^{-jkR_n^+}\left(\frac{jk}{R_n^{+2}}+\frac{1}{R_n^{+3}}\right)\right]+\right. \\ &\left.(y+y'-(2n+1)2h)\left[e^{-jkP_n^-}\left(\frac{jk}{P_n^{-2}}+\frac{1}{P_n^{-3}}\right)-e^{-jkR_n^-}\left(\frac{jk}{R_n^{-2}}+\frac{1}{R_n^{-3}}\right)\right]\right\} \end{aligned} \tag{32}$$

where

$$\frac{\partial \mathcal{G}_n^{(m)}}{\partial y}(\mathbf{r};\mathbf{r}') = -\frac{1}{4h^2}\sum_{n=1}^{\infty} n \sin\left(\tfrac{n\pi}{2h}(y+h)\right)\cos\left(\tfrac{n\pi}{2h}(y'+h)\right) K_0(\alpha_n \rho_c). \tag{33}$$

Again we evaluate G_n and its y derivative for y and y' only at 0 or h. Among these special cases, those yielding nonzero values are $G_n(x,0,z;x',0,z')$, $G_n(x,0,z;x',h,z')$, $G_n(x,h,z;x',0,z')$, $G_n(x,h,z;x',h,z')$ and $\frac{\partial G_n}{\partial y}(x,0,z;x',h,z')$.

4.1.3 Potential Green's Functions with PMC wall at $z = 0$

We define the location of the image of the source point in the PMC wall at $z = 0$ as

$$\mathbf{r}'' = (x', y', -z'). \tag{34}$$

Then the various potential Green's functions for a PEC/PEC parallel plate waveguide with a PMC wall at $z = 0$ are given in terms of G_n and G_d by the following expressions.

$$G_\Phi(\mathbf{r};\mathbf{r}') = \epsilon^{-1}\left(G_d(\mathbf{r};\mathbf{r}') + G_d(\mathbf{r};\mathbf{r}'')\right) \tag{35}$$

$$G_{A_x}(\mathbf{r};\mathbf{r}') = \mu_0\left(G_d(\mathbf{r};\mathbf{r}') + G_d(\mathbf{r};\mathbf{r}'')\right) \tag{36}$$

$$G_{A_y}(\mathbf{r};\mathbf{r}') = \mu_0\left(G_n(\mathbf{r};\mathbf{r}') + G_n(\mathbf{r};\mathbf{r}'')\right) \tag{37}$$

$$G_{A_z}(\mathbf{r};\mathbf{r}') = \mu_0\left(G_d(\mathbf{r};\mathbf{r}') - G_d(\mathbf{r};\mathbf{r}'')\right) \tag{38}$$

$$G_\Psi^{\text{int}}(\mathbf{r};\mathbf{r}') = \mu_0^{-1}\left(G_n(\mathbf{r};\mathbf{r}') - G_n(\mathbf{r};\mathbf{r}'')\right) \tag{39}$$

$$G_{F_x}^{\text{int}}(\mathbf{r};\mathbf{r}') = -\epsilon\left(G_n(\mathbf{r};\mathbf{r}') - G_n(\mathbf{r};\mathbf{r}'')\right) \tag{40}$$

$$G_{F_y}^{\text{int}}(\mathbf{r};\mathbf{r}') = -\epsilon\left(G_d(\mathbf{r};\mathbf{r}') - G_d(\mathbf{r};\mathbf{r}'')\right) \tag{41}$$

$$G_{F_z}^{\text{int}}(\mathbf{r};\mathbf{r}') = -\epsilon\left(G_n(\mathbf{r};\mathbf{r}') + G_n(\mathbf{r};\mathbf{r}'')\right). \tag{42}$$

The superscript "int" used above distinguishes these interior magnetic source Green's functions from the exterior region Green's functions described in Section 4.3. The subscript describes which potential quantity the Green's function represents.

4.2 PEC/PMC Parallel-Plate Green's Functions

We now treat a parallel-plate waveguide consisting of the dielectric as before between a PMC wall at $y = 0$ and a PEC wall at $y = h$. One sees from examination of Table 1 that all the potentials satisfy either

(nd) Neumann boundary conditions at $y = 0$ and Dirichlet boundary conditions at $y = h$

or

(dn) Dirichlet boundary conditions at $y = 0$ and Neumann boundary conditions at $y = h$.

4.2.1 Neumann-Dirichlet Boundary Conditions

The Green's function satisfying Equation (15) with Neumann boundary conditions at $y = 0$ and Dirichlet boundary conditions at $y = h$ is denoted by $G_{nd}(\mathbf{r};\mathbf{r}')$. The following formulas give G_{nd} and its y derivative (when they are not identically zero) for the special cases of interest.

$$G_{nd}(x,0,z;x',0,z') = 2G_d(x,0,z;x',0,z') \quad (43)$$

$$\frac{\partial G_{nd}}{\partial y}(x,h,z;x',0,z') = 2\frac{\partial G_d}{\partial y}(x,h,z;x',0,z'). \quad (44)$$

4.2.2 Dirichlet-Neumann Boundary Conditions

The Green's function satisfying Equation (15) with Dirichlet boundary conditions at $y = 0$ and Neumann boundary conditions at $y = h$ is denoted by $G_{dn}(\mathbf{r};\mathbf{r}')$. G_{dn} and its y derivative (in the only special cases for which they are not identically zero) are

$$G_{dn}(x,h,z;x',h,z') = G_{nd}(x,0,z;x',0,z') \quad (45)$$

$$\frac{\partial G_{dn}}{\partial y}(x,0,z;x',h,z') = -\frac{\partial G_{nd}}{\partial y}(x,h,z;x',0,z'). \quad (46)$$

4.2.3 Potential Green's Functions with PMC wall at $z = 0$

The various potential Green's functions for a PMC/PEC parallel plate waveguide with a PMC wall at $z = 0$ are given by the following expressions.

$$G_\Phi(\mathbf{r};\mathbf{r}') = \epsilon^{-1}\left(G_{nd}(\mathbf{r};\mathbf{r}') + G_{nd}(\mathbf{r};\mathbf{r}'')\right) \quad (47)$$

$$G_{A_x}(\mathbf{r};\mathbf{r}') = \mu_0\left(G_{nd}(\mathbf{r};\mathbf{r}') + G_{nd}(\mathbf{r};\mathbf{r}'')\right) \quad (48)$$

$$G_{A_y}(\mathbf{r};\mathbf{r}') = \mu_0\left(G_{dn}(\mathbf{r};\mathbf{r}') + G_{dn}(\mathbf{r};\mathbf{r}'')\right) \quad (49)$$

$$G_{A_z}(\mathbf{r};\mathbf{r}') = \mu_0\left(G_{nd}(\mathbf{r};\mathbf{r}') - G_{nd}(\mathbf{r};\mathbf{r}'')\right) \quad (50)$$

$$G_\Psi^{\text{int}}(\mathbf{r};\mathbf{r}') = \mu_0^{-1}\left(G_{dn}(\mathbf{r};\mathbf{r}') - G_{dn}(\mathbf{r};\mathbf{r}'')\right) \quad (51)$$

$$G_{F_x}^{\text{int}}(\mathbf{r};\mathbf{r}') = -\epsilon\left(G_{dn}(\mathbf{r};\mathbf{r}') - G_{dn}(\mathbf{r};\mathbf{r}'')\right) \quad (52)$$

$$G_{F_y}^{\text{int}}(\mathbf{r};\mathbf{r}') = -\epsilon\left(G_{nd}(\mathbf{r};\mathbf{r}') - G_{nd}(\mathbf{r};\mathbf{r}'')\right) \quad (53)$$

$$G_{F_z}^{\text{int}}(\mathbf{r};\mathbf{r}') = -\epsilon\left(G_{dn}(\mathbf{r};\mathbf{r}') + G_{dn}(\mathbf{r};\mathbf{r}'')\right). \quad (54)$$

As before, superscript "int" used above distinguishes these interior magnetic source Green's functions from the exterior region Green's functions described in Section 4.3. The subscript describes which potential quantity the Green's function represents.

4.3 Exterior Region Green's Functions

The remaining set of Green's functions needed in this analysis gives the fields radiated into the half space $y > h$ by magnetic currents and charges impressed on a PEC ground plane at $y = h$. The partial differential equations satisfied by these potentials are identical to (11) and (12) if ϵ and k are replaced by their free-space values ϵ_0 and k_0, respectively. The effect of the PEC is easily accounted for by using image theory. The resulting equations for the exterior region Green's functions are

$$G_{\Psi}^{\text{ext}}(\mathbf{r}; x', h, z') = \frac{e^{-jk_0R}}{2\pi\mu_0 R} \tag{55}$$

$$G_{F_x}^{\text{ext}}(\mathbf{r}; x', h, z') = G_{F_z}^{\text{ext}}(\mathbf{r}; x', h, z') = \frac{-\epsilon_0 e^{-jk_0R}}{2\pi R} \tag{56}$$

where, as usual, R is the distance between source and observation points which in this case is

$$R = \sqrt{(x - x')^2 + (y - h)^2 + (z - z')^2}. \tag{57}$$

5 Moment Method Formulation

We now make a slight change of notation from the previous sections. Since the only currents to be treated are surface currents, we will dispense with the subscript "s" used to distinguish surface density functions from volume density functions. Thus, for example, the symbol "$\mathbf{J}$" will be used hereafter in place of "$\mathbf{J}_s$" and will be understood to represent an electric surface current with units of A/m. "σ" will be used henceforth to represent surface electric charge density with units C/m^2. Similar remarks hold for the magnetic sources.

Also, recall that $\mathbf{M}^{\text{ext}} = -\mathbf{M}^{\text{int}}$ and $\sigma_m^{\text{ext}} = -\sigma_m^{\text{int}}$. Therefore we formulate all our equations in terms of only $\mathbf{M}^{\text{int}}$ and σ_m^{int}, and the superscript "int" will be dropped from these quantities in the remainder of this note.

5.1 Integral Equations

The equations determining the electric and magnetic surface currents are

$$-(\hat{\mathbf{x}}\hat{\mathbf{x}} + \hat{\mathbf{z}}\hat{\mathbf{z}}) \cdot \mathbf{E}^s(\mathbf{r}) = (\hat{\mathbf{x}}\hat{\mathbf{x}} + \hat{\mathbf{z}}\hat{\mathbf{z}}) \cdot \mathbf{E}^i(\mathbf{r}), \qquad \mathbf{r} \in \text{support of } \mathbf{J} \tag{58}$$

$$(\hat{\mathbf{x}}\hat{\mathbf{x}} + \hat{\mathbf{z}}\hat{\mathbf{z}}) \cdot \left(\mathbf{H}^{\text{int}}(\mathbf{r}) - \mathbf{H}^{\text{ext}}(\mathbf{r})\right) = -(\hat{\mathbf{x}}\hat{\mathbf{x}} + \hat{\mathbf{z}}\hat{\mathbf{z}}) \cdot \mathbf{H}^{i}(\mathbf{r}), \qquad \mathbf{r} \in \text{support of M.} \tag{59}$$

In (58) $\mathbf{E}^i$ is the incident electric field radiated by the impressed electric current source at $z = 0^+$, and $\mathbf{E}^s$ is the scattered electric field between the plates given by

$$\mathbf{E}^s = -j\omega\mathbf{A} - \nabla\Phi + \epsilon^{-1}\nabla\times\mathbf{F}^{\text{int}}. \tag{60}$$

$\mathbf{A}$, Φ, and $\mathbf{F}^{\text{int}}$ in (60) are found by convolving the appropriate Green's functions and sources.

$$\mathbf{A}(\mathbf{r}) = \iint\limits_{y'=0} \{\hat{\mathbf{x}}J_x(\mathbf{r}')G_{A_x}(\mathbf{r};\mathbf{r}') + \hat{\mathbf{z}}J_z(\mathbf{r}')G_{A_z}(\mathbf{r};\mathbf{r}')\}\, dS' \tag{61}$$

$$\Phi(\mathbf{r}) = \iint\limits_{y'=0} \sigma(\mathbf{r}')G_\Phi(\mathbf{r};\mathbf{r}')\, dS' \tag{62}$$

$$\mathbf{F}^{\text{int}}(\mathbf{r}) = \iint\limits_{y'=h} \left\{\hat{\mathbf{x}}M_x(\mathbf{r}')G^{\text{int}}_{F_x}(\mathbf{r};\mathbf{r}') + \hat{\mathbf{z}}M_z(\mathbf{r}')G^{\text{int}}_{F_z}(\mathbf{r};\mathbf{r}')\right\} dS'. \tag{63}$$

The function $\mathbf{H}^i$ in Equation (59) is the incident magnetic field radiated by the impressed electric source at $z = 0^+$ with the notch area filled in by PEC. The remaining (scattered) magnetic fields in Equation (59) are expressed in terms of potential functions.

$$\mathbf{H}^{\text{int}} - \mathbf{H}^{\text{ext}} = j\omega\mathbf{F} - \nabla\Psi + \mu_0^{-1}\nabla\times\mathbf{A}. \tag{64}$$

The new functions used on the RHS of (64) are

$$\Psi(\mathbf{r}) = \Psi^{\text{int}}(\mathbf{r}) - \Psi^{\text{ext}}(\mathbf{r}) = \iint\limits_{y'=h} \sigma_m(\mathbf{r}')G_\Psi(\mathbf{r};\mathbf{r}')\, dS' \tag{65}$$

$$\begin{aligned}\mathbf{F}(\mathbf{r}) &= \mathbf{F}^{\text{int}}(\mathbf{r}) - \mathbf{F}^{\text{ext}}(\mathbf{r}) \\ &= \iint\limits_{y'=h} \{\hat{\mathbf{x}}M_x(\mathbf{r}')G_{F_x}(\mathbf{r};\mathbf{r}') + \hat{\mathbf{z}}M_z(\mathbf{r}')G_{F_z}(\mathbf{r};\mathbf{r}')\}\, dS'\end{aligned} \tag{66}$$

where

$$G_\Psi(\mathbf{r};\mathbf{r}') = G^{\text{int}}_\Psi(\mathbf{r};\mathbf{r}') + G^{\text{ext}}_\Psi(\mathbf{r};\mathbf{r}') \tag{67}$$

$$G_{F_x}(\mathbf{r};\mathbf{r}') = G^{\text{int}}_{F_x}(\mathbf{r};\mathbf{r}') + G^{\text{ext}}_{F_x}(\mathbf{r};\mathbf{r}') \tag{68}$$

$$G_{F_z}(\mathbf{r};\mathbf{r}') = G^{\text{int}}_{F_z}(\mathbf{r};\mathbf{r}') + G^{\text{ext}}_{F_z}(\mathbf{r};\mathbf{r}'). \tag{69}$$

5.2 Basis Functions

According to the method of moments, the unknown electric and magnetic currents are expanded in a set of known basis functions with unknown coefficients, which are then solved for by enforcing equations (58) and (59) in an approximate manner. We use the triangle subdomain basis functions of Rao *et al.*[12], which are particularly suitable for approximating arbitrarily shaped regions. We proceed by partitioning the support of **J** and the support of **M** into triangles. A basis function is then defined over each pair of triangles which share a common edge. Figure 2 shows two such triangles, T_n^+ and T_n^-, which share edge n of the triangulated surface. Points in T_n^+ may be designated either by the position vector $\mathbf{r}$, which locates them with respect to the global origin, or by $\boldsymbol{\rho}_n^+$, which is defined with respect to the free vertex of T_n^+. $\boldsymbol{\rho}_n^-$ is defined similarly for points in T_n^-, except that it is directed *toward* the free vertex of T_n^-. Which of the two triangles is designated "plus" and which is "minus" depends on the choice of positive current reference direction for the n^{th} edge. Positive reference current flows across the edge from T_n^+ to T_n^-. The basis function associated with the n^{th} edge is then defined as

$$\mathrm{f}_n(\mathrm{r}) = \begin{cases} \dfrac{l_n}{2A_n^+}\boldsymbol{\rho}_n^+ & \text{if } \mathrm{r} \in T_n^+ \\ \dfrac{l_n}{2A_n^-}\boldsymbol{\rho}_n^- & \text{if } \mathrm{r} \in T_n^- \\ \mathbf{0} & \text{otherwise} \end{cases} \tag{70}$$

where l_n is the length of the n^{th} edge, and $A_n^\pm$ is the area of triangle $T_n^\pm$. The properties of these basis functions are discussed in [12]. The unknown electric and magnetic currents are expanded in series of these basis functions.

$$\mathrm{M}(\mathrm{r}) = \sum_{n=1}^{N_M} \mathcal{M}_n \mathrm{f}_n^M(\mathrm{r}) \tag{71}$$

$$\mathrm{J}(\mathrm{r}) = \sum_{n=1}^{N_J} \mathcal{J}_n \mathrm{f}_n^J(\mathrm{r}). \tag{72}$$

The functions $\left\{\mathrm{f}_n^J\right\}$ and $\left\{\mathrm{f}_n^M\right\}$ are as defined in (70), but the former have their support in the plane $y = 0$ while the latter are nonzero only in the plane $y = h$. The number of electric current basis functions, N_J, is equal to the number of interior edges of the triangulated surface in the $y = 0$ plane (plus edges at $y = z = 0$). Similarly, the number of magnetic current basis functions, N_M, is equal to the number of interior edges in the triangulation of the notch area in the $y = h$ plane.

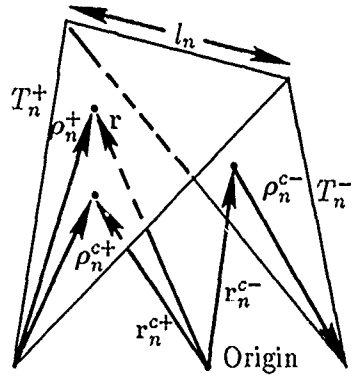

Figure 2: Triangular basis function geometry showing two triangles with a common edge (from [12]).

5.3 Reduction to Matrix Equation

We now define an inner product for use in testing equations (58) and (59) to be

$$\langle \mathrm{f}, \mathrm{g} \rangle = \iint \mathrm{f} \cdot \mathrm{g}\, dS. \tag{73}$$

We choose our testing functions to be the same as our basis functions (Galerkin's method). Then taking the inner product of (58) with each basis function in turn yields

$$j\omega \left\langle \mathrm{A}, \mathrm{f}_m^J \right\rangle + \left\langle \nabla\Phi, \mathrm{f}_m^J \right\rangle - \epsilon^{-1} \left\langle \hat{\mathrm{y}} \times \frac{\partial \mathrm{F}^{\mathrm{int}}}{\partial y}, \mathrm{f}_m^J \right\rangle = \left\langle \mathrm{E}^i, \mathrm{f}_m^J \right\rangle, \quad m = 1, 2, \ldots, N_J. \tag{74}$$

Following [12] we can approximate the second term on the LHS of (74) by

$$\left\langle \nabla\Phi, \mathrm{f}_m^J \right\rangle \approx -l_m \left[\Phi(\mathrm{r}_m^{c+}) - \Phi(\mathrm{r}_m^{c-}) \right] \tag{75}$$

where $\mathrm{r}_m^{c\pm}$ is the centroid of triangle $T_m^{\pm}$. The remaining terms are also approximated as in [12].

$$\left\langle \mathrm{A}, \mathrm{f}_m^J \right\rangle \approx \frac{l_m}{2} \left[\mathrm{A}(\mathrm{r}_m^{c+}) \cdot \rho_m^{c+} + \mathrm{A}(\mathrm{r}_m^{c-}) \cdot \rho_m^{c-} \right] \tag{76}$$

$$\left\langle \hat{\mathrm{y}} \times \frac{\partial \mathbf{F}^{\mathrm{int}}}{\partial y}, \mathrm{f}_m^J \right\rangle \approx \frac{l_m}{2} \left[\hat{\mathrm{y}} \times \frac{\partial \mathbf{F}^{\mathrm{int}}}{\partial y}(\mathrm{r}_m^{c+}) \cdot \rho_m^{c+} + \hat{\mathrm{y}} \times \frac{\partial \mathbf{F}^{\mathrm{int}}}{\partial y}(\mathrm{r}_m^{c-}) \cdot \rho_m^{c-} \right]. \quad (77)$$

$\rho_m^{c\pm}$ is the vector $\rho_m^{\pm}$ evaluated at the centroid of the corresponding triangle.

Returning now to Equation (59), we again compute the moment with each basis function in turn.

$$j\omega \left\langle \mathbf{F}, \mathrm{f}_m^M \right\rangle - \left\langle \nabla \Psi, \mathrm{f}_m^M \right\rangle + \mu_0^{-1} \left\langle \hat{\mathrm{y}} \times \frac{\partial \mathbf{A}}{\partial y}, \mathrm{f}_m^M \right\rangle = \left\langle -\mathbf{H}^i, \mathrm{f}_m^M \right\rangle, \quad m = 1, 2, \ldots, N_M. \quad (78)$$

We approximate these inner products in exactly the same way as before.

$$\left\langle \nabla \Psi, \mathrm{f}_m^M \right\rangle \approx -l_m \left[\Psi(\mathrm{r}_m^{c+}) - \Psi(\mathrm{r}_m^{c-}) \right] \quad (79)$$

$$\left\langle \mathbf{F}, \mathrm{f}_m^M \right\rangle \approx \frac{l_m}{2} \left[\mathbf{F}(\mathrm{r}_m^{c+}) \cdot \rho_m^{c+} + \mathbf{F}(\mathrm{r}_m^{c-}) \cdot \rho_m^{c-} \right] \quad (80)$$

$$\left\langle \hat{\mathrm{y}} \times \frac{\partial \mathbf{A}}{\partial y}, \mathrm{f}_m^M \right\rangle \approx \frac{l_m}{2} \left[\hat{\mathrm{y}} \times \frac{\partial \mathbf{A}}{\partial y}(\mathrm{r}_m^{c+}) \cdot \rho_m^{c+} + \hat{\mathrm{y}} \times \frac{\partial \mathbf{A}}{\partial y}(\mathrm{r}_m^{c-}) \cdot \rho_m^{c-} \right]. \quad (81)$$

Note that m in (75), (76), and (77) refers to the common edge of the triangles comprising the support of the m^{th} *electric current* basis function, while the same index was used in (79), (80), and (81) to designate an edge in the support of the m^{th} *magnetic current* basis function. This abuse of notation should cause no confusion since m will always be used consistently in any given expression, and the meaning should be clear from the context.

After substituting the expansions of the currents into (74) and (78) we obtain the desired matrix equation

$$\mathcal{A}\mathcal{X} = \mathcal{B}. \quad (82)$$

$\mathcal{A}$ is the so-called *interaction matrix*, a square matrix of order $N_J + N_M$. $\mathcal{X}$ is the column matrix of unknown current coefficients and $\mathcal{B}$ is the excitation matrix. It is illuminating to write these matrices in partitioned form, as follows.

$$\left[\begin{array}{c|c} \mathcal{Y} & \mathcal{U} \\ \hline \mathcal{W} & \mathcal{Z} \end{array}\right] \left[\begin{array}{c} \mathcal{M} \\ \hline \mathcal{J} \end{array}\right] = \left[\begin{array}{c} \mathcal{H} \\ \hline \mathcal{E} \end{array}\right] \quad (83)$$

where $\mathcal{E} = [\mathcal{E}_m]$ and $\mathcal{J} = [\mathcal{J}_m]$ are column matrices of length N_J, $\mathcal{H} = [\mathcal{H}_m]$ and $\mathcal{M} = [\mathcal{M}_m]$ are column matrices of length N_M, and $\mathcal{W} = [\mathcal{W}_{mn}]$, $\mathcal{U} = [\mathcal{U}_{mn}]$, $\mathcal{Y} = [\mathcal{Y}_{mn}]$, and $\mathcal{Z} = [\mathcal{Z}_{mn}]$ are matrices of dimensions $N_J \times N_M$, $N_M \times$

N_J, $N_M \times N_M$, and $N_J \times N_J$, respectively. The elements of the interaction matrix are given below.

$$\mathcal{W}_{mn} = -\frac{l_m}{\epsilon}\left[\hat{\mathbf{y}}\times\partial\mathbf{F}^{+}_{mn}\cdot\frac{\boldsymbol{\rho}^{c+}_{m}}{2} + \hat{\mathbf{y}}\times\partial\mathbf{F}^{-}_{mn}\cdot\frac{\boldsymbol{\rho}^{c-}_{m}}{2}\right] \tag{84}$$

where

$$\partial\mathbf{F}^{\pm}_{mn} = \iint \mathbf{f}^{M}_{n}(\mathbf{r}')\cdot\bar{\mathbf{G}}_{\partial F}(\mathbf{r}^{c\pm}_{m},\mathbf{r}')\,dS'$$

$$= \frac{l_n}{2}\left[\frac{1}{A^{+}_{n}}\iint_{T^{+}_{n}}\boldsymbol{\rho}^{+}_{n}\cdot\bar{\mathbf{G}}_{\partial F}(\mathbf{r}^{c\pm}_{m};\mathbf{r}')\,dS' + \frac{1}{A^{-}_{n}}\iint_{T^{-}_{n}}\boldsymbol{\rho}^{-}_{n}\cdot\bar{\mathbf{G}}_{\partial F}(\mathbf{r}^{c\pm}_{m};\mathbf{r}')\,dS'\right] \tag{85}$$

and the dyadic Green's function $\bar{\mathbf{G}}_{\partial F}$ is defined by

$$\bar{\mathbf{G}}_{\partial F}(\mathbf{r};\mathbf{r}') = \hat{\mathbf{x}}\hat{\mathbf{x}}\frac{\partial G^{\text{int}}_{F_x}}{\partial y}(\mathbf{r};\mathbf{r}') + \hat{\mathbf{z}}\hat{\mathbf{z}}\frac{\partial G^{\text{int}}_{F_z}}{\partial y}(\mathbf{r};\mathbf{r}'). \tag{86}$$

$$\mathcal{Z}_{mn} = l_m\left[j\omega\left(\mathbf{A}^{+}_{mn}\cdot\frac{\boldsymbol{\rho}^{c+}_{m}}{2} + \mathbf{A}^{-}_{mn}\cdot\frac{\boldsymbol{\rho}^{c-}_{m}}{2}\right) + \Phi^{-}_{mn} - \Phi^{+}_{mn}\right] \tag{87}$$

where

$$\mathbf{A}^{\pm}_{mn} = \iint \mathbf{f}^{J}_{n}(\mathbf{r}')\cdot\bar{\mathbf{G}}_{A}(\mathbf{r}^{c\pm}_{m},\mathbf{r}')\,dS'$$

$$= \frac{l_n}{2}\left[\frac{1}{A^{+}_{n}}\iint_{T^{+}_{n}}\boldsymbol{\rho}^{+}_{n}\cdot\bar{\mathbf{G}}_{A}(\mathbf{r}^{c\pm}_{m};\mathbf{r}')\,dS' + \frac{1}{A^{-}_{n}}\iint_{T^{-}_{n}}\boldsymbol{\rho}^{-}_{n}\cdot\bar{\mathbf{G}}_{A}(\mathbf{r}^{c\pm}_{m};\mathbf{r}')\,dS'\right] \tag{88}$$

$$\Phi^{\pm}_{mn} = \frac{j}{\omega}\iint \nabla'_{s}\cdot\mathbf{f}^{J}_{n}(\mathbf{r}')G_{\Phi}(\mathbf{r}^{c\pm}_{m},\mathbf{r}')\,dS'$$

$$= \frac{jl_n}{\omega}\left[\frac{1}{A^{+}_{n}}\iint_{T^{+}_{n}}G_{\Phi}(\mathbf{r}^{c\pm}_{m};\mathbf{r}')\,dS' - \frac{1}{A^{-}_{n}}\iint_{T^{-}_{n}}G_{\Phi}(\mathbf{r}^{c\pm}_{m};\mathbf{r}')\,dS'\right] \tag{89}$$

$$\bar{\mathrm{G}}_A(\mathrm{r};\mathrm{r}') = \hat{\mathrm{x}}\hat{\mathrm{x}}G_{A_x}(\mathrm{r};\mathrm{r}') + \hat{\mathrm{z}}\hat{\mathrm{z}}G_{A_z}(\mathrm{r};\mathrm{r}') \tag{90}$$

and we have used the fact that

$$\nabla_s \cdot \mathrm{f}_n(\mathrm{r}) = \begin{cases} \dfrac{l_n}{A_n^+} & \text{if } \mathrm{r} \in T_n^+ \\ -\dfrac{l_n}{A_n^-} & \text{if } \mathrm{r} \in T_n^- \\ 0 & \text{otherwise.} \end{cases} \tag{91}$$

$$\mathcal{Y}_{mn} = l_m \left[j\omega \left(\mathrm{F}_{mn}^+ \cdot \frac{\rho_m^{c+}}{2} + \mathrm{F}_{mn}^- \cdot \frac{\rho_m^{c-}}{2} \right) + \Psi_{mn}^+ - \Psi_{mn}^- \right] \tag{92}$$

where

$$\begin{aligned} \mathrm{F}_{mn}^{\pm} &= \iint \mathrm{f}_n^M(\mathrm{r}') \cdot \bar{\mathrm{G}}_F(\mathrm{r}_m^{c\pm}, \mathrm{r}')\, dS' \\ &= \frac{l_n}{2} \left[\frac{1}{A_n^+} \iint_{T_n^+} \rho_n^+ \cdot \bar{\mathrm{G}}_F(\mathrm{r}_m^{c\pm}; \mathrm{r}')\, dS' + \frac{1}{A_n^-} \iint_{T_n^-} \rho_n^- \cdot \bar{\mathrm{G}}_F(\mathrm{r}_m^{c\pm}; \mathrm{r}')\, dS' \right] \end{aligned} \tag{93}$$

$$\begin{aligned} \Psi_{mn}^{\pm} &= \frac{j}{\omega} \iint \nabla_s' \cdot \mathrm{f}_n^M(\mathrm{r}') G_\Psi(\mathrm{r}_m^{c\pm}, \mathrm{r}')\, dS' \\ &= \frac{jl_n}{\omega} \left[\frac{1}{A_n^+} \iint_{T_n^+} G_\Psi(\mathrm{r}_m^{c\pm}; \mathrm{r}')\, dS' - \frac{1}{A_n^-} \iint_{T_n^-} G_\Psi(\mathrm{r}_m^{c\pm}; \mathrm{r}')\, dS' \right] \end{aligned} \tag{94}$$

and

$$\bar{\mathrm{G}}_F(\mathrm{r};\mathrm{r}') = \hat{\mathrm{x}}\hat{\mathrm{x}}G_{F_x}(\mathrm{r};\mathrm{r}') + \hat{\mathrm{z}}\hat{\mathrm{z}}G_{F_z}(\mathrm{r};\mathrm{r}'). \tag{95}$$

$$\mathcal{U}_{mn} = \frac{l_m}{\mu_0} \left[\hat{\mathrm{y}} \times \partial \mathrm{A}_{mn}^+ \cdot \frac{\rho_m^{c+}}{2} + \hat{\mathrm{y}} \times \partial \mathrm{A}_{mn}^- \cdot \frac{\rho_m^{c-}}{2} \right] \tag{96}$$

where

$$\partial \mathrm{A}_{mn}^{\pm} = \iint \mathrm{f}_n^J(\mathrm{r}') \cdot \bar{\mathrm{G}}_{\partial A}(\mathrm{r}_m^{c\pm}, \mathrm{r}')\, dS'$$

$$= \frac{l_n}{2}\left[\frac{1}{A_n^+}\iint_{T_n^+}\rho_n^+\cdot\bar{\mathrm{G}}_{\partial A}(\mathrm{r}_m^{c\pm};\mathrm{r}')\,dS' + \frac{1}{A_n^-}\iint_{T_n^-}\rho_n^-\cdot\bar{\mathrm{G}}_{\partial A}(\mathrm{r}_m^{c\pm};\mathrm{r}')\,dS'\right] \tag{97}$$

and

$$\bar{\mathrm{G}}_{\partial A}(\mathrm{r};\mathrm{r}') = \hat{\mathrm{x}}\hat{\mathrm{x}}\frac{\partial G_{A_x}}{\partial y}(\mathrm{r};\mathrm{r}') + \hat{\mathrm{z}}\hat{\mathrm{z}}\frac{\partial G_{A_z}}{\partial y}(\mathrm{r};\mathrm{r}'). \tag{98}$$

5.4 Efficient Evaluation of Interaction Matrix Entries

As discussed in reference [12], efficient evaluation of interaction matrix entries requires consideration of face-pair contributions rather than edge-pair contributions. The face-pair integrals are of two basic types: vector and scalar. We describe here how to efficiently calculate the entries in $\mathcal{Z}$. Similar techniques are used for the other partitions. Consider first a typical vector integral needed to evaluate $\mathcal{Z}_{mn}$. The quantity

$$\mathrm{A}_i^{pq} = \frac{l_i}{2A^q}\iint_{T^q}\rho_i\cdot\bar{\mathrm{G}}_A(\mathrm{r}^{cp};\mathrm{r}')\,dS' \tag{99}$$

represents the magnetic vector potential at the centroid of triangle T^p due to the i^{th} basis function defined on triangle T^q. In (99) we have temporarily assumed a local numbering scheme on the source triangle, with vertices at r_1, r_2, and r_3, and where

$$\rho_i = \pm(\mathrm{r}' - \mathrm{r}_i), \qquad i = 1,2,3. \tag{100}$$

The plus sign above is selected if the associated basis function defines positive current to flow *out* of the i^{th} edge of the triangle, which lies opposite to the i^{th} vertex.

One problem in evaluating (99) is that the integrand is singular when triangles p and q are the same. The singularity, which occurs in $\bar{\mathrm{G}}_A$, is the same as that of the free-space Green's function (multiplied by 2 to account for the image in the PMC plane in the bilateral case)

$$\bar{\mathrm{G}}_A(\mathrm{r},\mathrm{r}') \to \frac{s\mu_0}{4\pi R}\bar{\mathrm{I}}, \qquad \text{as } \mathrm{r}' \to \mathrm{r} \tag{101}$$

where $\bar{\mathrm{I}}$ is the dyad $\hat{\mathrm{x}}\hat{\mathrm{x}} + \hat{\mathrm{z}}\hat{\mathrm{z}}$ and where $s = 1$ in the unilateral case and $s = 2$ in the bilateral case. There are several possible ways of handling this singularity. The first is to explicitly extract and integrate the contribution of the

singularity in closed form. The second is to use an adaptive cubature routine which is capable of accurately treating integrable singularities[13]. Although the latter method is simpler to implement, it is far more computationally expensive, requiring hundreds of integrand evaluations to achieve only about 0.1% relative accuracy. Therefore, we continue now with a description of the first method. It is convenient for the later numerical procedures to define the regular part of the dyadic Green's function as

$$\bar{\mathrm{G}}_A^r = \bar{\mathrm{G}}_A - \frac{s\mu_0}{4\pi R}\bar{\mathrm{I}}. \tag{102}$$

We can then write

$$\mathrm{A}_i^{pq} = \frac{l_i}{2A^q}\left\{ \iint_{T^q} \rho_i \cdot \bar{\mathrm{G}}_A^r(\mathrm{r}^{cp};\mathrm{r}')\, dS' + \frac{s\mu_0}{4\pi}\iint_{T^q}\frac{\rho_i}{R}\, dS' \right\}. \tag{103}$$

The first integral in (103) is well behaved in all cases and can be integrated numerically, using a low order Gaussian scheme designed especially for integration over triangular domains (see [14], Table 8.3). The second integral is singular, but can be integrated analytically in closed form[15]. These evaluations are examined in detail in the following paragraphs.

The dyadic in Equation (103) contains only two nonzero elements, $G_{A_x}^r$ and $G_{A_z}^r$, which are defined by

$$\bar{\mathrm{G}}_A^r = \hat{\mathrm{x}}\hat{\mathrm{x}}G_{A_x}^r + \hat{\mathrm{z}}\hat{\mathrm{z}}G_{A_z}^r. \tag{104}$$

The desired vector integral can thus be written as the sum of two scalar integrals.

$$\iint_{T^q} \rho_i \cdot \bar{\mathrm{G}}_A^r(\mathrm{r}^{cp};\mathrm{r}')\, dS' = \hat{\mathrm{x}}I_{ix} + \hat{\mathrm{z}}I_{iz} \tag{105}$$

where the scalar integrals are given by

$$I_{ix} = \iint_{T_q} (\hat{\mathrm{x}} \cdot \rho_i)\, G_{A_x}^r(\mathrm{r}^{cp};\mathrm{r}')\, dS' \tag{106}$$

$$I_{iz} = \iint_{T_q} (\hat{\mathrm{z}} \cdot \rho_i)\, G_{A_z}^r(\mathrm{r}^{cp};\mathrm{r}')\, dS'. \tag{107}$$

The integrals over the triangular regions are most efficiently accomplished by using normalized area coordinates[12,14] ξ and η. The source point can be written in terms of area coordinates as

$$\mathrm{r}' = \xi\mathrm{r}_2 + \eta\mathrm{r}_3 + (1-\xi-\eta)\mathrm{r}_1 \tag{108}$$

where it is recalled that the $\{\mathbf{r}_i\}$ are the vertices of the source triangle T^q. Similarly,

$$\rho_i = \pm(\mathbf{r}' - \mathbf{r}_i) = \pm\left(\xi\mathbf{r}_2 + \eta\mathbf{r}_3 + (1-\xi-\eta)\mathbf{r}_1 - \mathbf{r}_i\right). \tag{109}$$

The area element in normalized area coordinates is $dS' = 2A^q\, d\xi\, d\eta$.

Let t stand for either x or z. Then the integrals I_{it} can be expressed in terms of integrals which are independent of i in the following way.

$$I_{it} = \pm\hat{\mathbf{t}} \cdot [\mathbf{r}_2 I_{t\xi} + \mathbf{r}_3 I_{t\eta} + \mathbf{r}_1 I_{t\zeta} - \mathbf{r}_i I_t] \tag{110}$$

where

$$I_{t\xi} = 2A^q \int_0^1 \int_0^{1-\eta} \xi G^r_{A_t}(\mathbf{r}^{cp}; \xi\mathbf{r}_2 + \eta\mathbf{r}_3 + (1-\xi-\eta)\mathbf{r}_1)\; d\xi\, d\eta \tag{111}$$

$$I_{t\eta} = 2A^q \int_0^1 \int_0^{1-\eta} \eta G^r_{A_t}(\mathbf{r}^{cp}; \xi\mathbf{r}_2 + \eta\mathbf{r}_3 + (1-\xi-\eta)\mathbf{r}_1)\; d\xi\, d\eta \tag{112}$$

$$I_{t\zeta} = 2A^q \int_0^1 \int_0^{1-\eta} (1-\xi-\eta) G^r_{A_t}(\mathbf{r}^{cp}; \xi\mathbf{r}_2 + \eta\mathbf{r}_3 + (1-\xi-\eta)\mathbf{r}_1)\; d\xi\, d\eta \tag{113}$$

$$I_t = 2A^q \int_0^1 \int_0^{1-\eta} G^r_{A_t}(\mathbf{r}^{cp}; \xi\mathbf{r}_2 + \eta\mathbf{r}_3 + (1-\xi-\eta)\mathbf{r}_1)\; d\xi\, d\eta. \tag{114}$$

However, the above integrals are not all independent. We also have that

$$I_t = I_{t\xi} + I_{t\eta} + I_{t\zeta} \tag{115}$$

so that in general there are six integrals to be numerically evaluated for each observation point / source triangle pair. These integrals contribute to as many as nine entries of $\mathcal{Z}$, depending on the number of basis functions defined in each triangle. They are computed using the formula from [14],

$$2\int_0^1 \int_0^{1-\eta} f(\xi,\eta)\, d\xi\, d\eta \;\approx\; \sum_{k=1}^{7} w_k f(\xi_k, \eta_k). \tag{116}$$

The sample points and weights are given in Table 2. As mentioned previously, the second integral in (103) is evaluated using the formulas of [15].

In addition to the vector integrals that were just discussed, we also must calculate scalar integrals of the form

$$\Phi_i^{pq} = \pm\frac{jl_i}{\omega A^q} \iint_{T^q} G_\Phi(\mathbf{r}^{cp}; \mathbf{r}')\, dS'. \tag{117}$$

k	ξ_k	η_k	w_k
1	0.33333333	0.33333333	0.22500000
2	0.05971587	0.47014206	0.13239415
3	0.47014206	0.05971587	0.13239415
4	0.47014206	0.47014206	0.13239415
5	0.79742699	0.10128651	0.12593918
6	0.10128651	0.79742699	0.12593918
7	0.10128651	0.10128651	0.12593918

Table 2: Sample Points and Weights for Seven Point Triangular Cubature

Φ_i^{pq} is the electric scalar potential at the centroid of triangle T^p due to the surface electric charge density associated with the i^{th} basis function defined on triangle T^q. As before, the sign is taken to be positive if the basis function in question defines positive reference current to flow *out* of T^q through the i^{th} edge. Very little additional work is needed to compute this integral, since $G_{A_x} = \mu_0 c G_\Phi$. Using this fact, we can then write (117) as

$$\begin{aligned}\Phi_i^{pq} &= \pm\frac{jl_i}{\omega\mu_0 c A^q}\left\{\iint_{T^q} G_{A_x}^{r}(\mathrm{r}^{cp};\mathrm{r}')\,dS' + \frac{s\mu_0}{4\pi}\iint_{T^q}\frac{dS'}{R}\right\} \\ &= \pm\frac{j\omega l_i}{k^2 A^q}\left\{I_x + \frac{s\mu_0}{4\pi}\iint_{T^q}\frac{dS'}{R}\right\}. \qquad (118)\end{aligned}$$

Computation of I_x has already been described, and computation of the last integral above is accomplished using the formulas of [15]. We note again that the quantity Φ_i^{pq}/l_i is common to as many as nine entries of $\mathcal{Z}$.

5.5 The Effective Excitation Matrix

The excitation matrix entries are

$$\mathcal{E}_m = \left\langle \mathrm{E}^i, \mathrm{f}_m^J \right\rangle \qquad (119)$$

$$\mathcal{H}_m = \left\langle -\mathrm{H}^i, \mathrm{f}_m^M \right\rangle. \qquad (120)$$

First, since the impressed electric current radiates only evanescent waves into the parallel plate region, our assumption that the slot is far from the origin

implies that $\mathcal{H}_m = 0$ for all m. Second, the impressed currents are transverse to z, the direction of the induced currents near the origin. Thus, the incident magnetic vector potential makes no contribution to (119). The only remaining contributor to (119) is the incident electric scalar potential, whose source is impressed charge density. One can show that there is no impressed surface charge at $z = 0$, leaving only the impressed line charge at $z = y = 0$ which is due to the discontinuity in J_y^i there. Because the impressed and induced currents must be continuous at $z = 0$, it is also easy to show that there is an induced line charge at $z = y = 0$ which is exactly the negative of the impressed one. The sum of the scalar potentials due to these two sources is exactly zero. Therefore, we may choose not to compute either impressed or induced potentials due to these sources when filling our various matrices, as long as we force the induced currents near $z = 0$ to assume their prescribed values. We are then left with a homogeneous matrix equation where some of the unknowns (those corresponding to currents crossing the $z = 0$ plane) are actually known.

We now partition the "unknowns" in a different way than was done in the previous section. There, the partition was defined in a way convenient for filling the matrices. Here, we partition the unknowns according to the physical location of the corresponding basis function. We number the electric current basis functions so that those corresponding to triangle edges at $z = 0$ are numbered last. Then $\mathcal{X}_1$ is the column matrix of all magnetic current coefficients and all electric current coefficients for edges not at $z = 0$. $\mathcal{X}_2$ is the matrix of coefficients for electric current basis functions defined for edges at $z = 0$. If we partition the remaining matrices in a conformable fashion then the matrix Equation (82) becomes

$$\left[\begin{array}{c|c} \mathcal{A}_{11} & \mathcal{A}_{12} \\ \hline \mathcal{A}_{21} & \mathcal{A}_{22} \end{array}\right] \left[\begin{array}{c} \mathcal{X}_1 \\ \hline \mathcal{X}_2 \end{array}\right] = \left[\begin{array}{c} \mathbf{0} \\ \hline \mathbf{0} \end{array}\right]. \tag{121}$$

The matrix $\mathcal{X}_2$ is known. The set of remaining unknowns, $\mathcal{X}_1$, can be found by solving

$$\mathcal{A}_{11}\mathcal{X}_1 = -\mathcal{B}' \tag{122}$$

where $\mathcal{B}' = \mathcal{A}_{12}\mathcal{X}_2$.

5.6 Scaling and Matrix Condition Number

The matrix equation (122) exhibits very large condition numbers. This problem can be traced to the fact that the equations and unknowns are each expressed in two different sets of units. To insure that all unknowns have

units of A/m we define the auxiliary unknown

$$\mathcal{M}' = \frac{1}{\eta_0}\mathcal{M}. \tag{123}$$

Our set of matrix equations then becomes

$$\mathcal{Y}'\mathcal{M}' + \mathcal{U}'\mathcal{J} = \mathcal{H}' \tag{124}$$

$$\mathcal{W}'\mathcal{M}' + \mathcal{Z}\mathcal{J} = \mathcal{E} \tag{125}$$

where

$$\mathcal{Y}' = \eta_0^2\mathcal{Y},\ \mathcal{W}' = \eta_0\mathcal{W},\ \mathcal{U}' = \eta_0\mathcal{U},\ \mathcal{H}' = \eta_0\mathcal{H}. \tag{126}$$

In this way all matrix entries have units of Ω-m^2. These equations exhibit reasonable condition numbers and are amenable to accurate solution. After solving them, $\mathcal{M}$ is computed from $\mathcal{M}'$ using (123).

6 Stripline/Slotline Transition Design

A crucial element in the design of a notch radiator is the stripline/slotline transition. The transition performance can be the limiting factor in determining impedance bandwidth. Figure 3 shows a schematic diagram of a typical test fixture used for measuring transition performance. It consists of two transitions arranged back-to-back to facilitate easy measurement using stripline connectors. Swept frequency measurements of return loss and insertion loss for this symmetrical two-port provide information on the useful bandwidth of the transitions.

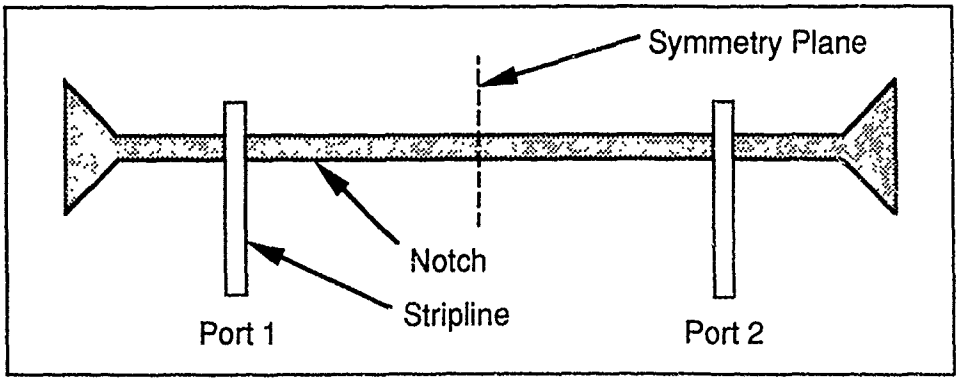

Figure 3: A stripline/slotline transition test fixture.

We use the usual technique of twice analyzing half the structure, placing first PMC and then PEC walls at the symmetry plane. If Γ_M and Γ_E are the

reflection coefficients calculated in the presence of the magnetic and electric wall, respectively, then the two-port scattering parameters are given by

$$S_{11} = S_{22} = \frac{1}{2}(\Gamma_M + \Gamma_E) \tag{127}$$

$$S_{12} = S_{21} = \frac{1}{2}(\Gamma_M - \Gamma_E). \tag{128}$$

The only changes needed to implement this capability are the addition of two more image points to the Green's functions and defining unknowns for edges along the symmetry plane in the notch triangulation. These unknowns are set to zero in the PEC case.

7 Results

In this section we compare program predictions with theoretical and measured results. All the cases reported here assume $\epsilon_r = 2.2$ and $h = 0.015$ inch. In all cases when a notch is present, it is bilateral.

7.1 Uniform Width Strip

The simplest test case is a uniform width stripline without any slot in its groundplane. The strip dimensions are 0.022 by 1.5 inches. The program was run using a coarse and a fine triangulation with $N_J = 30$ and 60, respectively. The program predictions were compared to simple transmission line theory assuming that the line was terminated in a perfect open circuit, neglecting any end effects. The magnitude and phase of the input reflection coefficient were computed at 0.2 GHz intervals between 1 and 20 GHz. The computed amplitude was equal to 1 (to 4 decimal places) for both triangulations at all frequencies. The difference between computed and theoretical phases was at most 56.0 and 8.1 degrees for the coarse and fine triangulations, respectively.

For the fine triangulation computing the entries in the fill matrix required 14.5 seconds per frequency and solving the matrix equation using double precision Gaussian elimination required 0.59 seconds per frequency. Since matrix fill time dominates the cost of the procedure, we implemented the interpolation technique of Newman[16]. Under this scheme the matrix is filled at some fixed number of logarithmically spaced frequencies (called knots) covering the band of interest. The matrix is reconstructed for intermediate frequencies by quadratically interpolating the matrix values at the closest three knots. Using this technique only 10 knots were required to cover the 20:1 frequency band.

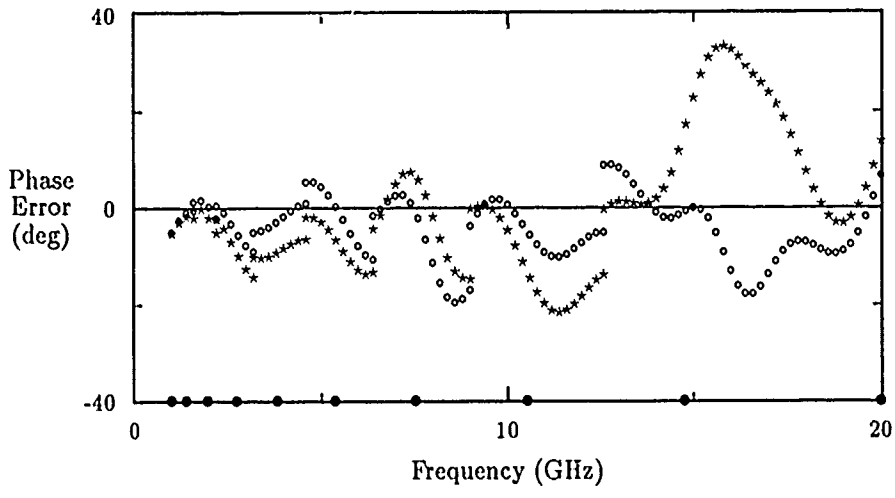

Figure 4: Reflection coefficient phase error for fine (o) and coarse ($\star$) triangulations of the stepped-width stripline. Knots are marked with bullets.

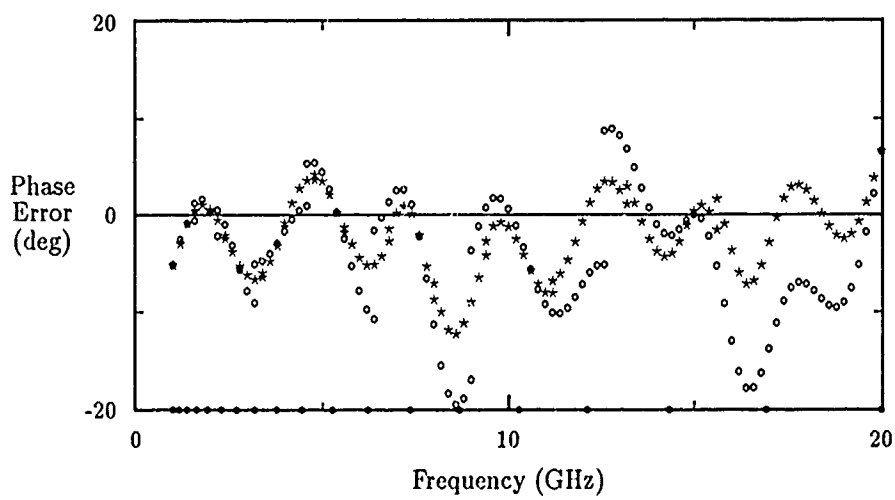

Figure 5: Reflection coefficient phase error for fine triangulation using 10 (o) and 19 ($\star$) knots. Knots used in the 19 point scheme are marked with bullets.

7.2 Stepped-width Strip

The next case consists of a stripline with a step in width. As in the previous case, there is no notch, and the main line width is 0.022 inch. At a point one inch from the feed port, the line increases in width to 0.044 inch. The length of the wide section is 0.5 inch. Again, two triangulations were examined, using 45 and 111 unknowns. Again the reflection coefficient magnitude was correctly computed to be unity over the band for both cases. The phase prediction was compared to a Touchstone circuit model and the error with respect to this model is plotted in Figure 4. Ten knots were used in the matrix fill interpolation procedure for both cases. It is seen that the error generally increases with frequency and the fine triangulation is superior to the coarse one. Jumps in the plotted values occur between knots where a change in frequencies used within the interpolation scheme occurs. By increasing the number of knots the magnitude of these jumps can be reduced. This can be seen in Figure 5 where 10 and 19 knot interpolation schemes are compared for the stepped-width strip.

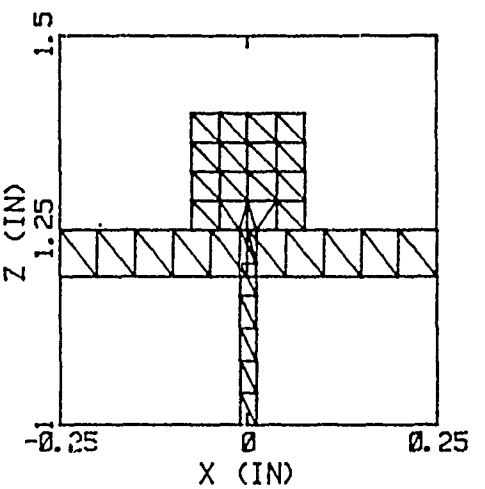

Figure 6: Detail of the triangulation used to model a stepped-width strip feeding a rectangular notch in it groundplanes. Uniform sized triangles are used on the portions of the structure not shown.

7.3 Stripline-fed Notch

Here a stepped-width stripline feeds a rectangular notch as shown in Figure 6. The notch measures 2 by 0.06 inches. The 0.022 by 1.25 inch uniform strip

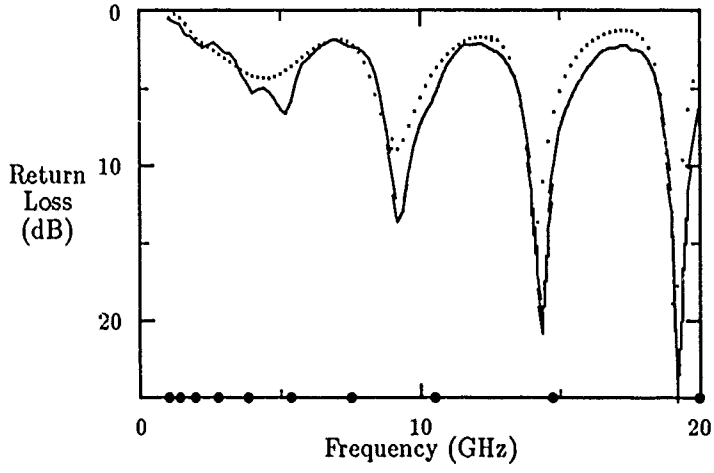

Figure 7: Comparison of measured (solid) and computed (dotted) return loss for the stripline-fed rectangular notch of Figure 6. Knots are marked with buliets.

is terminated with a 0.15 inch square stub. Notice that the width step occurs directly under one edge of the notch, adding to the difficulty in modeling this transition.

A test fixture was built and measured to provide a comparison with the numerical results of the program. Measured and computed return loss are displayed in Figure 7. For this case we had $N_J = 105$ and $N_M = 79$. Fill time and matrix equation solution time were 96 and 10.4 seconds per frequency, respectively. The good agreement between measured and computed results verifies the accuracy of the theory.

7.4 Two-port Transition Test Fixture

A two-port test fixture of the type shown in Figure 3 was constructed and measured. Good agreement was obtained for insertion loss measured and calculated between the two ports. These results will be presented at the symposium.

8 Conclusion

An efficient technique has been developed to analyze arbitrarily shaped, stripline-fed notches. Measurements verify the accuracy of the method. A simple extension of the analysis gives a useful tool for designing stripline/slotline transitions.

Acknowledgments

This work was supported by Raytheon corporate CAD funding. We wish to thank Raytheon management, especially M. Maybell, G. Hardie, and D. Holst for their support and encouragement.

We acknowledge many helpful discussions with Professors William F. Richards and Paul Klock. In fact, it was Professor Klock who suggested the sampling technique used for the input impedance calculation.

We thank Professor Don Wilton for providing us with a copy of his code EFIE which formed the basis for the triangulation scheme used by our codes.

Finally, we thank Professor Barry Joe of the University of Alberta for supplying us with a copy of his automatic triangular mesh generation program.

References

[1] L. R. Lewis, M. Fassett, and J. Hunt, "A broadband stripline array element," *IEEE AP-S Int. Symp. Dig.*, pp. 335–337, Atlanta, GA, 1974.

[2] P. J. Gibson, "The Vivaldi aerial," in *Proc.* 9th *European Microwave Conf.* (Brighton, UK), 1979, pp. 101–105.

[3] K. S. Yngvesson *et al.*, "Endfire tapered slot antennas on dielectric substrates," *IEEE Trans. Antennas Propagat.*, vol. AP-33, pp. 1392–1400, Dec. 1985.

[4] M. J. Povinelli and J. A. Johnson, "Design and performance of wideband, dual polarized stripline notch arrays," *IEEE AP-S Int. Symp. Dig.*, pp. 200–204, Syracuse, NY, June 6–10, 1988.

[5] U. Kotthaus and B. Vowinkel, "Investigation of Planar Antennas for Submillimeter Receivers," *IEEE Trans. Microwave Theory Tech.*, vol. 37, no. 2, pp. 375–380, Feb. 1989.

[6] R. Janaswamy and D. H. Schaubert, "Analysis of the tapered slot antenna," *IEEE Trans. Antennas Propagat.*, vol. AP-35, pp. 1058–1065, Sept. 1987.

[7] J. F. Johansson,"A moment method analysis of linearly tapered slot antennas," *IEEE AP-S Int. Symp. Dig.*, pp. 383–386, San Jose, CA, June 26–30, 1989.

[8] M. F. Catedra *et al.*, "Analysis of arrays of Vivaldi and LTSA Antennas," *IEEE AP-S Int. Symp. Dig.*, pp. 122–125, San Jose, CA, June 26–30, 1989.

[9] P. Simon, *Analysis of a Tapered Stripline Element in an Infinite Array Environment,* Appendix A, PhD Dissertation, University of California at Santa Barbara, in preparation.

[10] W. F. Richards *et al.*, "Acceleration of periodic Green's functions in free-space," in *Proc. USNC/URSI National Meeting* (Houston, TX), p. 81, May 23–26, 1983.

[11] R. Lampe, P. Klock, and P. Mayes, "Integral transforms useful for the accelerated summation of periodic, free-space Green's functions," *IEEE Trans. Microwave Theory Tech.*, vol. MTT-33, pp. 734–736, Aug. 1985.

[12] S. M. Rao, D. R. Wilton, and A. W. Glisson, "Electromagnetic scattering by surfaces of arbitrary shape," *IEEE Trans. Antennas Propagat.*, vol. AP-30, no. 3, pp. 409–418, May 1982.

[13] D. P. Laurie, "Algorithm 584, CUBTRI: Automatic cubature over a triangle," *ACM Trans. Math. Software*, Vol. 8, No. 2, pp. 210–218, June 1982.

[14] P. C. Zienkiewitz, *The Finite Element Method in Engineering Science*, New York: McGraw-Hill, 1971.

[15] D. R. Wilton *et al.*, "Potential integrals for uniform and linear source distributions on polygonal and polyhedral domains," *IEEE Trans. Antennas Propagat.*, vol. AP-32, no. 3, pp. 276–281, March 1984.

[16] E. H. Newman, "Generation of wide-band data from the method of moments by interpolating the impedance matrix," *IEEE Trans. Antennas Propagat.*, vol. AP-36, no. 12, pp. 1820–1824, Dec. 1988.

A TECHNIQUE TO MEASURE LARGE ANTENNA ARRAYS THAT CONTAIN RANDOM AMPLITUDE ERRORS.

Peter R. Franchi
Harvey Tobin
Hanscom Air Force Base, Massachusetts 01731

ABSTRACT:

The measurement of two dimensional planar arrays that are electrically long is currently a difficult task. The accurate measurement of the antenna pattern is limited by large antenna range requirements for far field ranges, the number of sample points that must be measured for near field characterization, and by the great size and very high tolerance of the reflector and feed in a compact range. At the 1988 Allerton Symposium we presented a paper[1] that described how to correct for the error level of the far field patterns using an ideal amplitude distribution. This paper is a follow on to the 1988 presentation. It describes how to measure and correct for error levels of a large aperture antenna that contains random errors in amplitude and phase by applying a quadratic and higher order phase correction to the phased array.

The errors that result from this approach are analyzed as a function of range, antenna electrical length, sidelobe level and degree of correction. Both computer simulations and analysis are used to examine the limitations of this approach.

INTRODUCTION:

In the future the United States Air Force will be mounting large lightweight phased arrays on the fuselages of long aircraft. The size of the antenna arrays considered are approximately 60λ to 300λ in length. Todays conventional antenna ranges are not

sufficient to measure accurately the performance of low sidelobe antennas in the far field. This is based on the accepted $2D^2/\lambda$ criterion. For example, the far field distance for a 10'x 100' aperture at C-band would be 23 miles away. If low sidelobes are required, then the distance would be even greater to prevent distortion within the far field patterns. To use compact ranges would require a massive high tolerance reflector, and the necessary near field ranges to house the reflectors would be extremely expensive.

This paper discusses a method to help overcome the limitations of conventional antenna ranges. For a typical two dimensional planar array shown in Fig.1, to measure the far field performance in the smaller dimension the antenna can be considered, to be in the far field. For the larger dimension the antenna can be considered to be in the region of the Fresnel field resulting in apparent far field pattern distortion. An accurate far field measurement of the antenna, however can be reclaimed from this Fresnel region measurement by putting in a phase correction over the aperture.

At the 1988 Allerton Symposium we presented a paper that considered a undisturbed 50db Taylor amplitude distribution, and explained how to approximate the far field pattern employing repeated phase corrections of quadratic and cubic terms.

This report is an extension of the 88 Allerton report considering how random amplitude errors added to the 50db Taylor distribution affect the validity of the quadratic phase correction. These errors have been inserted by perturbing the

amplitude distribution in a statistically random way with a zero mean and fixed variance. Random phase errors were not employed since the random amplitude errors cause typically the same pattern distortions. These amplitude errors would be typical of beamformer network errors or measurement errors but do not represent errors caused by coarsely quantized phase shifters. Basically the phase shifter setting errors here are considered much smaller than the beamformer network errors.

Finally, we must define sidelobe levels that are caused by different sources and which can be separated for low sidelobe arrays. The theoretical or ideal sidelobe were treated in the previous report. Error sidelobes result from amplitude(and/or phase) error in the aperture illumination function due to network errors. In this paper ideal sidelobes are considered to be set much lower than the error sidelobe levels, and do not affect the sidelobe considerations. The error sidelobes are the principle concern of our measurement technique. Measurement of the pattern in the Fresnel zone results in sidelobes that are incrementally higher than the error sidelobes. This incremental increase is called add-on error. In order to obtain an accurate representation of the far field pattern with a Fresnel zone measurement we must keep this add on error very small. The increase in sidelobe level can be held within an acceptable bound by applying the phase correction as many times as needed.

DISCUSSION:

In the 1988 Allerton report we studied how to measure large antenna arrays by applying a phase correction to the antenna.

The results showed that by applying a second order correction to the phase term the add-on error can be reduced significantly the sidelobe levels. We also showed that we can do even better by applying a third order term.The equations are:

$$\frac{k \cos^2\theta D^2}{8R_0} \quad \text{For the quadratic term} \quad (1)$$

$$\frac{k D^3 \sin\theta \cos^2\theta}{16R_0^2} \quad \text{For the cubic term} \quad (2$$

where,

$k=2\pi/\lambda$

λ=free space wavelength

D=aperture width

R_0=distance from tranmsit recieve (test) antenna.

θ_0=angle of scan for which correction is made.

The results are plotted as add on error versus R/λ for several D values, and the number of phase settings. This is shown in Figure

For this application in which the sidelobe level is primarily determined by aperture errors, we consider a low sidelobe antenna whose geometry is given by Figure 3. To find and expression of R w consider an arbitrary triangle and from the distance formula,

$$R=\{(b-x)^2+(h-0)^2\}^{1/2} \quad (3)$$

squaring this term we obtain

$$R^2=(b-x)^2+h^2 \quad (4)$$

$$R^2=b^2-2bx+x^2+h^2 \quad (5)$$

we note that;

$$R_0^2=b^2+h^2 \quad (6)$$

therefore substituting for b^2+h^2,

$$R^2=R_0^2+x^2-2bx \qquad (7)$$

but,

$$\cos\alpha=b/R_0 \qquad (8)$$

$$b=R_0\cos\alpha$$

therefore replacing this gives;

$$R^2=R_0^2+x^2-2R_0x\cos\alpha$$

then,

$$R=[R_0^2+x^2-2R_0x\cos\alpha]^{1/2} \qquad (9)$$

The expression for the field in the Fresnel region of a aperture antenna is given by,

$$E(u)=C_0\int f(x)\,\frac{e^{jkR}}{R}dx \qquad (10)$$

considering R much grater than D (10) can be expressed as,

$$E(u)=C_0\int f(x)\,\frac{e^{jkR}}{R_0}dx \qquad (11)$$

where,

C_o is arbitrary constant

$1/R_0$ is the amplitude term

e^{jkR} is the phase term

$f(x)$ is the aperture illumination functio:

Expanding out R (in Eq.9) in the phase term we obtain;

$$R=R_o-x\sin\theta+x^2/2R_o\cos^2\theta+.....H.O.T \qquad (12)$$

The term we are most concerned with is the quadratic term, therefore we want to express (10) as,

$$E(u)=\int f(x)e^{jk(ux-\beta x^2)}dx \qquad (13)$$

where,

$$C_1=\frac{C_o e^{jk}}{R_0}$$

$$u=kd\sin\theta$$

$$\beta=\frac{kd^2}{8R_0}\cos^2\theta$$

For amplitude and phase errors in f(x) (13) can be written as,

$$E(u)=C_1\int f(x)e^{-(\alpha(x)+j\delta(x))}e^{j\beta x^2}e^{jux}dx \qquad (14)$$

where,

$\alpha(x)$-random amplitude error in f(x)

$\delta(x)$-random phase error in $\dot{f}(x)$

for small error,

$$E(u)=\int f(x)[1-j\beta x^2]e^{jux}dx + \int f(x)(\alpha(x)-j\delta(x)+j\alpha(x)\beta x^2 -\delta(x))e^{jux}dx \qquad (15)$$

the first term is the ideal theoretical pattern.
We then assume that the deterministic sidelobes are low enough that they do not contribute to the overall pattern, then (15) can be expressed as,

$$E(u)=C_1\int f(x)[-\alpha(x)-j\delta(x)+j\alpha(x)\beta x^2-\delta(x)\beta x^2]e^{jux}d \qquad (16)$$

writing this expression as a sum;

$$g(u)=\Sigma f_n[-\alpha_n-j\delta_n+j\alpha_n\beta n\Delta x^2-\delta_n+j\alpha_n\beta n\Delta x^2-\delta_n\beta_n\Delta x^2]e^{jun\Delta x} \qquad (17)$$

converting this into power;

$$P(u)=|E(u)E^*(u)|\,C_1{}^2 \qquad (18)$$

$$=C_1{}^2\Sigma f_n[-\alpha_n(1-j\beta n\Delta x^2)-j\delta_n(1-j\beta n^2\Delta x^2)e^{jun\Delta x}$$

$$*\Sigma f_m{}'-\alpha_m(1+j\beta m^2\Delta x^2)+j\beta m^2\Delta x^2))e^{-jum\Delta x} \qquad (19)$$

multiplying this out we obtain;

multiplying this out we obtain;

$$=C_1^2\Sigma\Sigma[f_n f_m \alpha_n \alpha_m (1+\beta^2 n^2 m^2 \Delta x^4) f_n f_n \delta_n \delta_m 1+\beta^2 n^2 m^2 \Delta x^4)+j\delta_m f_n f_m - \alpha j\beta m^2 \Delta x^2 - j\delta_n$$

$$f_m f_n(-\alpha) - j\beta n^2 \Delta x^2] e^{ju\Delta x(n-m)} \qquad (20)$$

$$=C_1^2\Sigma[f^2 \delta^2 n(1+\beta^2 n^4 \Delta x^4) + f^2 \delta^2 n(\beta^2 n^4 \Delta x^4)] \qquad (21)$$

$$P(u)=C_1^2\Sigma f_n^2(\alpha^2 n+\delta^2 n)+f^2 n(\alpha^2 n+\delta_n^2)\beta^2 n^4 \Delta x^4 \qquad (22)$$

if $\alpha_n^2=\delta_n^2$ is independent of n

because the amplitude and phase errors do not contribute any type of different errors, then we can write the expression as

$$P(u)=(2\alpha_n^2\Sigma f_n^2+2\alpha_n^2\beta^2\Delta x^4\Sigma n^4 f_n^2)C_1^2 \qquad (23)$$

and this is equivalent to,

$$P(u)=2\alpha_n^2\int f^2(x)\,dx+2\alpha_n^2\beta^2\int x^4 f^2(x)\,dx \qquad (24)$$

therefore we can express the add on error as,

$$\Delta E=\frac{\varepsilon^2}{\varepsilon_0}=\frac{P(u)}{P_0(u)} \qquad (25)$$

$$=\frac{2\alpha_n^2\Sigma f_n^2+2\alpha_n^2\beta^2\Delta x^4\Sigma x^4 f_n^2}{2\alpha_n^2\Sigma f_n^2}$$

$$=\frac{1+\Delta x^4\beta^2\Sigma n^4 f_n^2}{\Sigma f_n^2} \qquad (26)$$

for a continuous aperture,

$$\frac{1+\beta^2\int x^4 f^2(x)\,dx}{\int f^2(x)\,dx} \qquad (27)$$

The add on error is now defined by equation (28) relating it

to the aperture illumination function f(x) and β which includes the scan angle, aperture size, wavelength and Fresnel range. This equation along with equations (10) and (11) allow the experimentalist to set acceptable error limits.

SIMULATION:

The theoretical results of the last section represent the average behavior of the add on error when an infinite set of antenna patterns are taken, corresponding to Gaussian distributed amplitude and phase errors. In an actual measurement only one pattern or a very small number of sample patterns will be taken (for one scan condition or frequency, etc.). This represents the basic problem of characterizing sidelobe behavior when phase/amplitude errors are dominant. In other words, the actual sidelobes over any particular angular region will not represent the average level or the RMS level. The simulation results are an average of eleven different patterns taken for the same statistical errors. While these patterns are statically the same they are different in specific sidelobe behavior.

Another unavoidable issue is what is the best method of characterizing the error sidelobe levels. In all cases the pattern with and without quadratic phase correction is compared with the ideal far field pattern. Three methods seem obvious. One is a comparison of the average sidelobe level (in power) over a finite angular region. The second is the RMS average of a point by point difference (both of these over the same angular region) and the third is a comparison of the changes on the peak sidelobes. Since this last approach seems to be the most commonly used by

experimentalists, it is used here. Peak sidelobes are defined by the experimentalist rule of thumb of 5db or more above the mean level of the far field pattern. Using this criterion the simulation gives an average of the number of sidelobes that are above the mean value of -47.5db within a sector of width eight degrees or about .14 in sinθ space.

Figure 4 is the far field pattern of the array with the first set of errors over 4° to 12°. Figure 5 is the pattern at R_o=150′ without correction. Figure 6 is the pattern with quadratic phase correction for $\theta_0=0^{\circ}$. It is quite clear that with the quadratic correction the near field pattern approximates the far field pattern well.

Looking at cumulative probability curves of sidelobes for the same cases (percentage of sidelobes above a given sidelobe level) there is a similar picture. Figure 7 represents the curve of the far field distribution for the pattern in Figure 4. Likewise Figures 8 and 9 represent the curves of the field distributions of Figures 5 and 6.

Taking all eleven data sets and averaging the absolute value of the add-on error gives the plots in Figure 10. The average of the eleven simulations follows the theoretical behavior for the three cases but it is clear more averaging would be needed for a better comparison.

CONCLUSION:

The pattern distortion error that results from the use of phase correction in measuring very large arrays in their near field or Fresnel field have been derived theoretically. These expressions have been compared to ideal pattern disto. from

simulations in the previous Allerton paper and there is a very close match and to error antenna patterns in this paper with a less accurate but quite good match. It should be possible to limit the add on measurement error by the applications of these equations and applying both quadratic and cubic phase correction as many times as the conditions, R_0,D,λ, the illumination taper and the expected phase and amplitude error call for.

REFERENCES:

1. P.R. Franchi, H.Tobin,"Technique to Measure Large Arrays",Proc 1988 Antennas and Applications Symposium, RADC TR-89-121 Vol II.

2. Silver, Samuel(1949) "Microwave Antenna Theory and Design" McGraw Hill, New York pp 188-189.

3. Jull, E.V. (1962) " An Investigation of Near Field Radiation Patterns Measured with Large Antennas" APS Vol#4, AP-10.

FIG. 1 TYPICAL PLANAR ARRAY

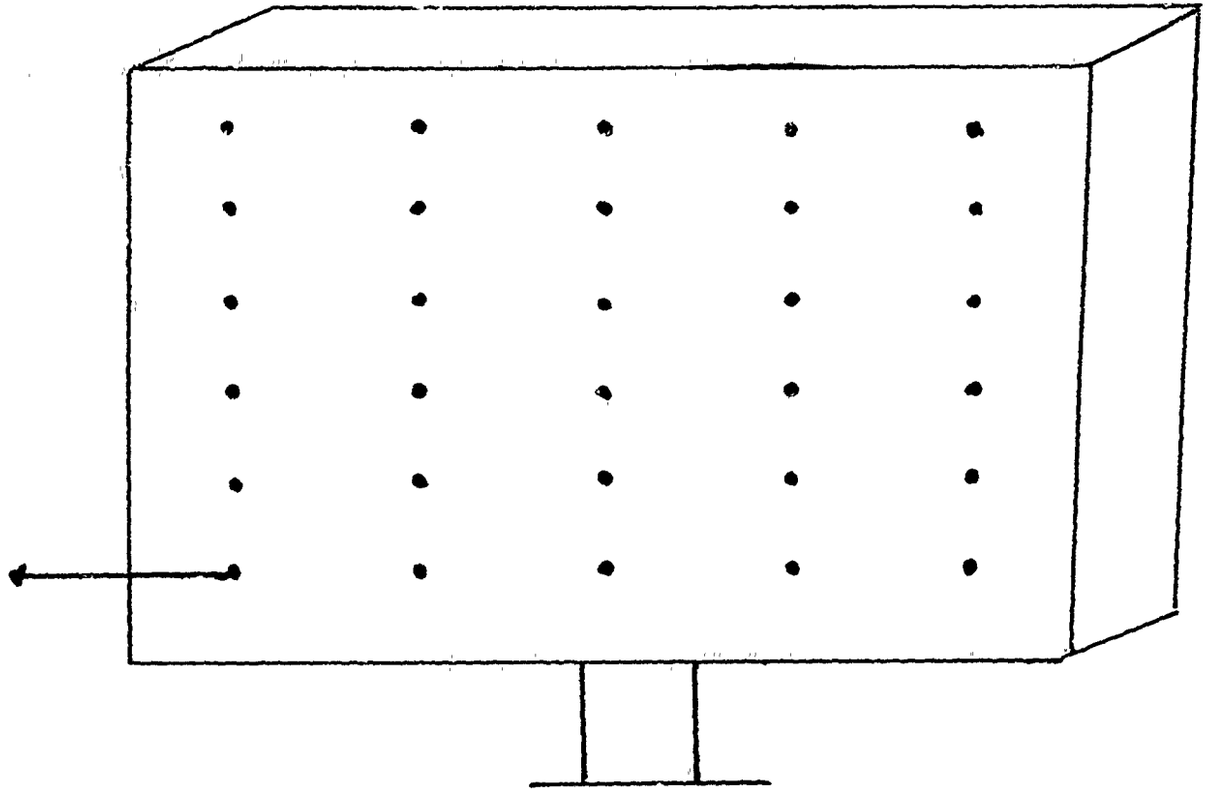

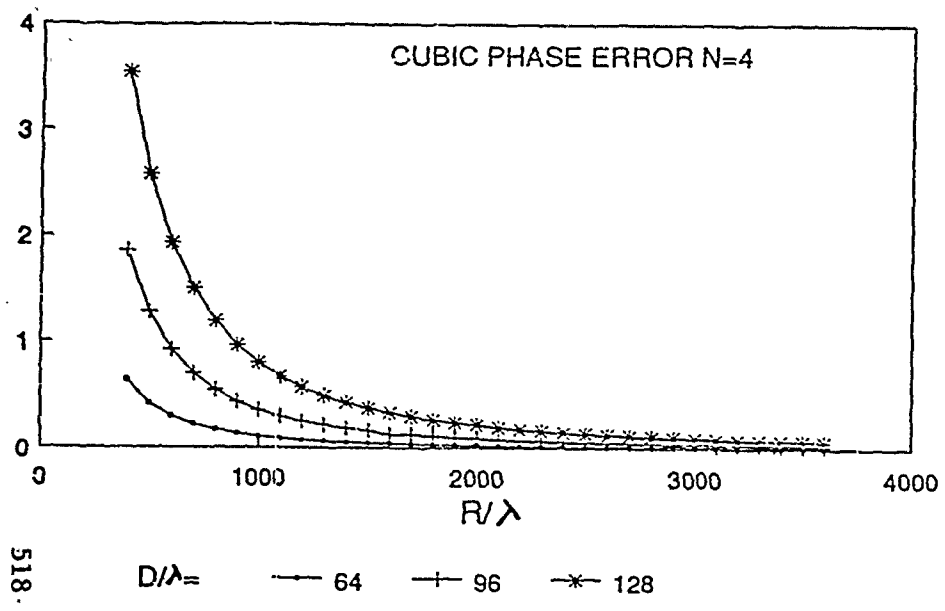

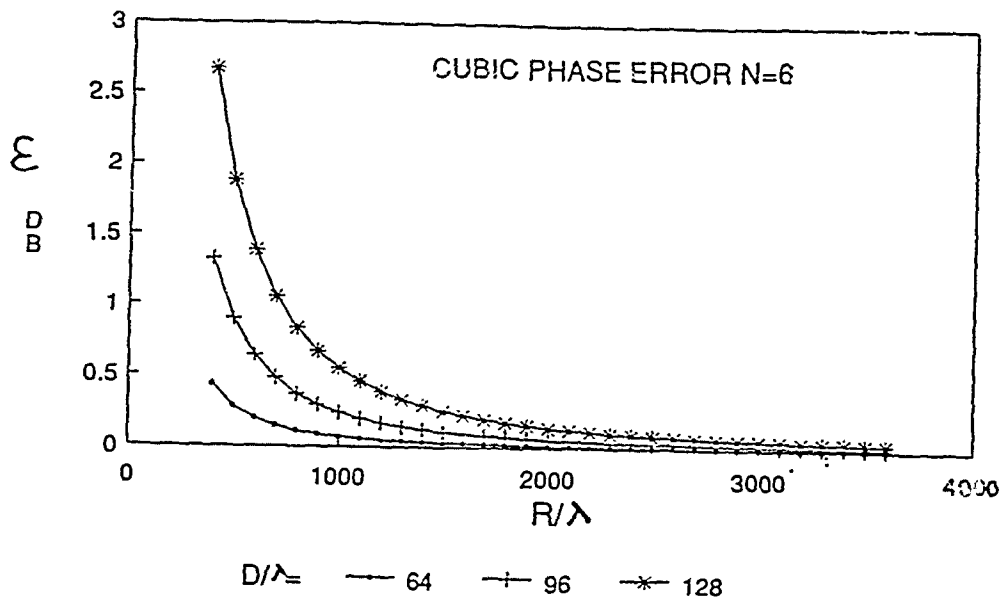

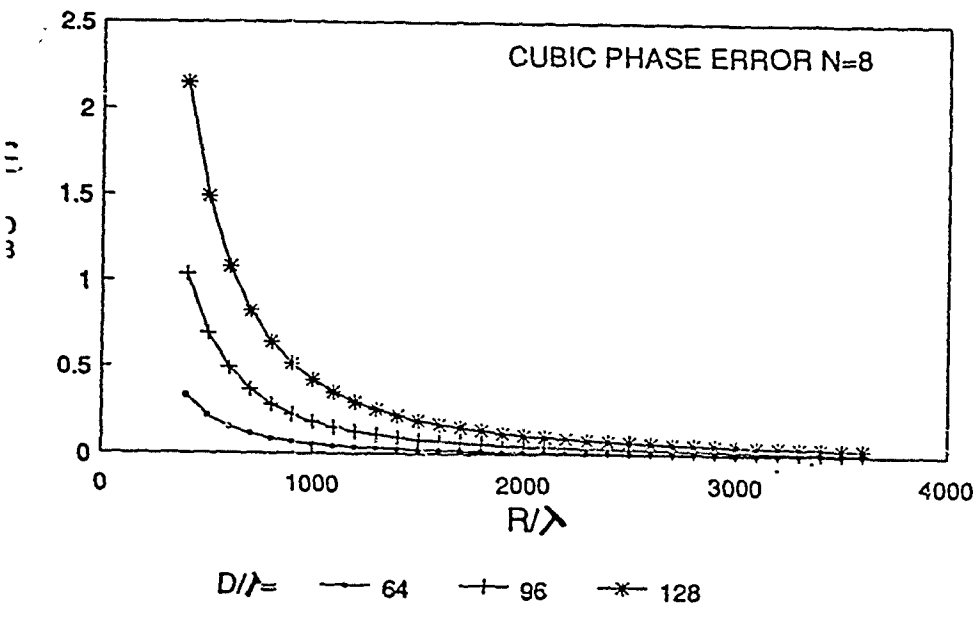

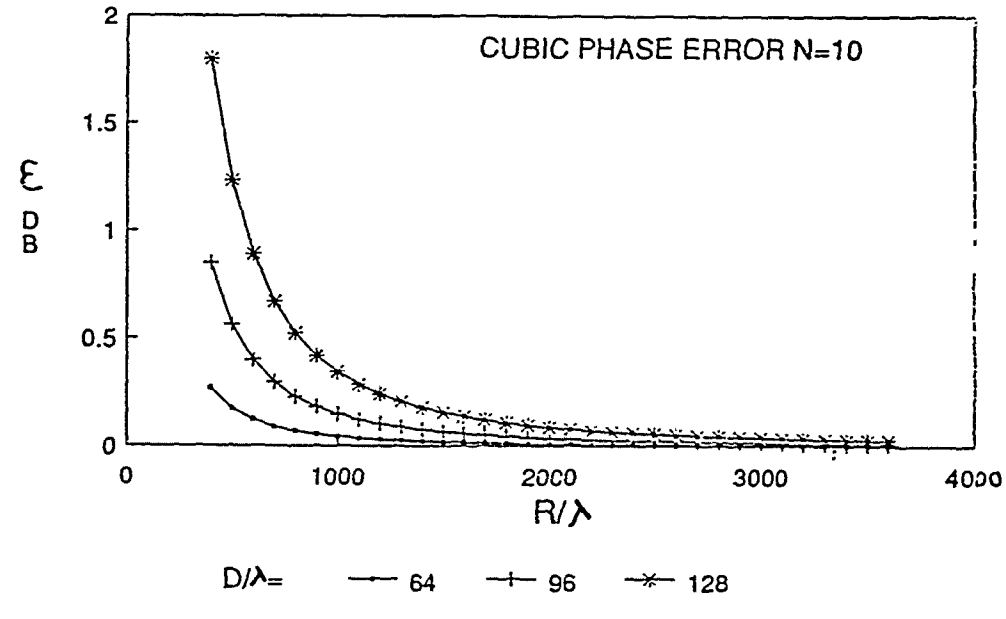

FIG.2 AMOUNT OF PHASE SHIFTER CHANGE
N-PHASE SHIFTER SETTINGS

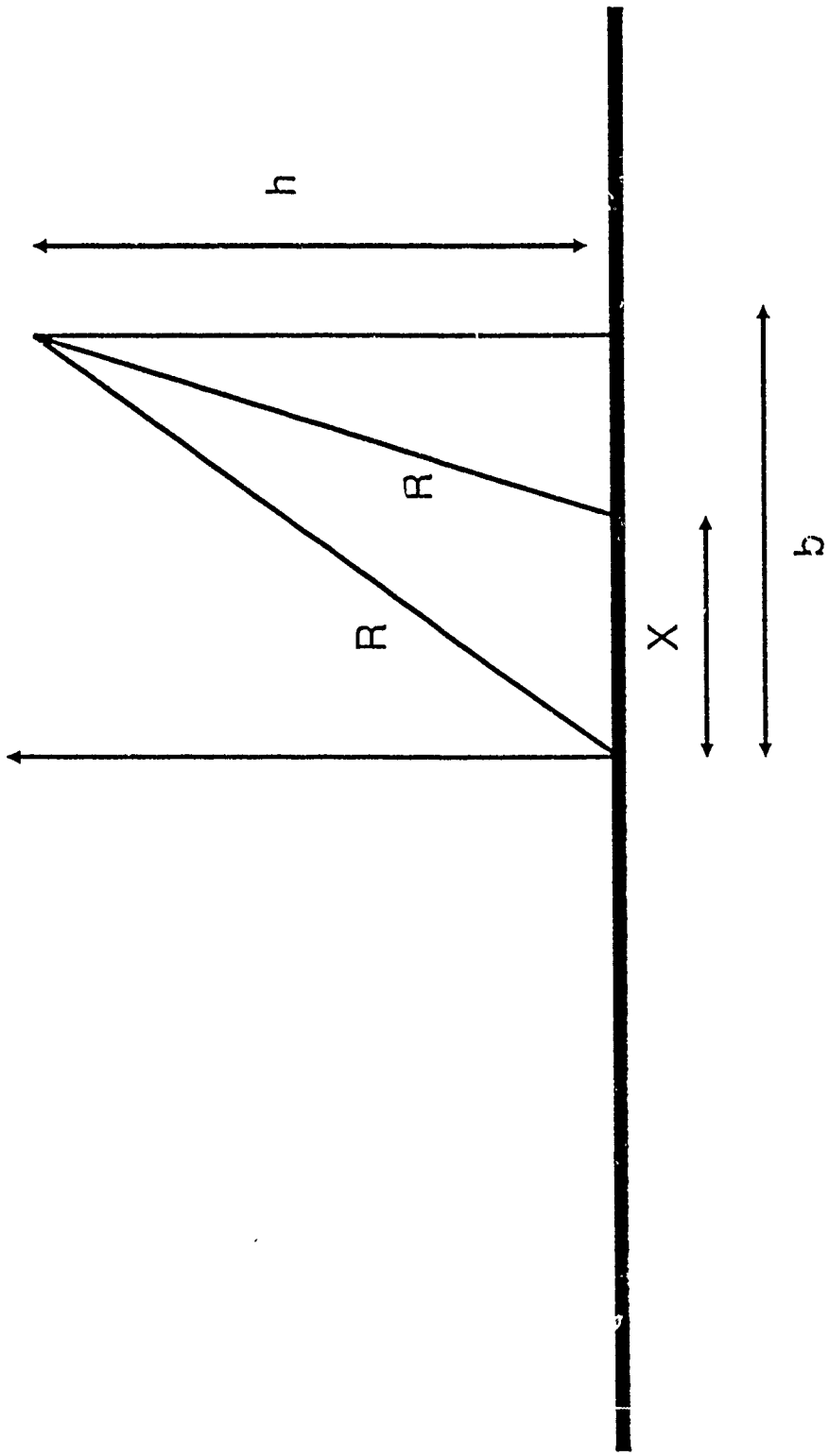

Fig. 3 Antenna Geometry

FIG.4 F.FIELD PATTERN 4-12(DEG)

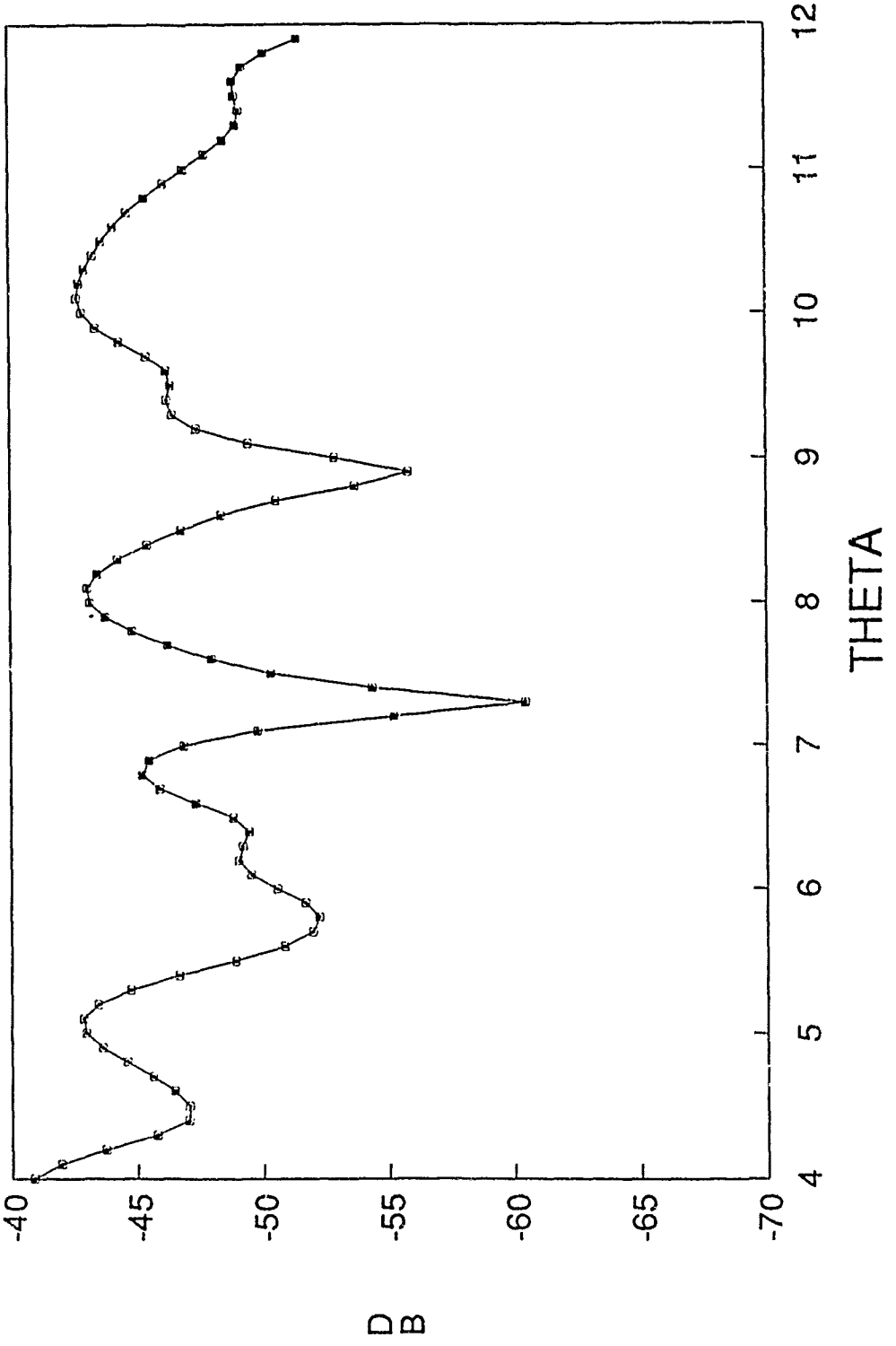

FIG.5 PATTERN W.OUT CORRECTION 4-12(DEG)

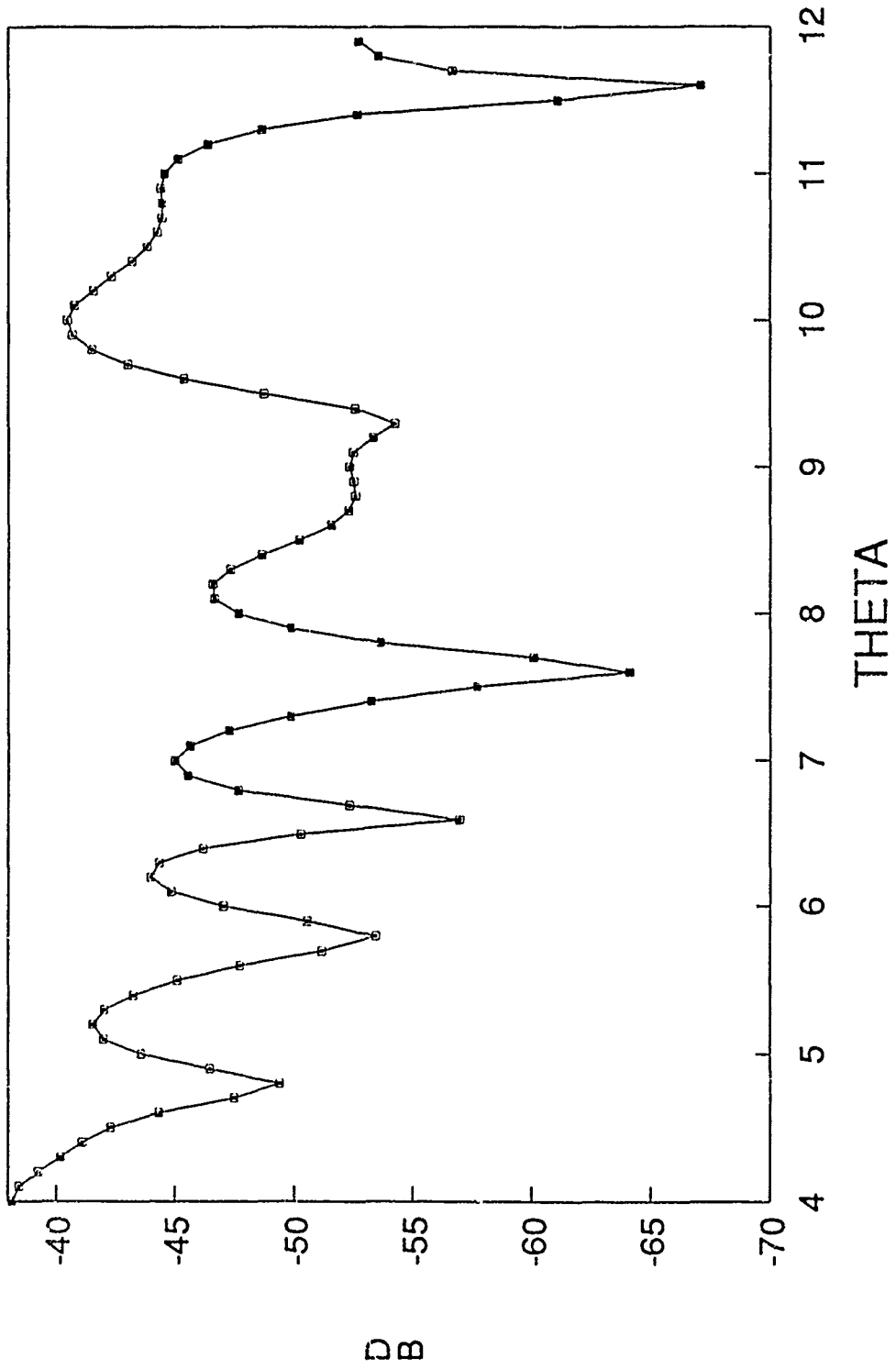

FIG.6 PATTERN WITH CORRECTION 4-12(DEG)

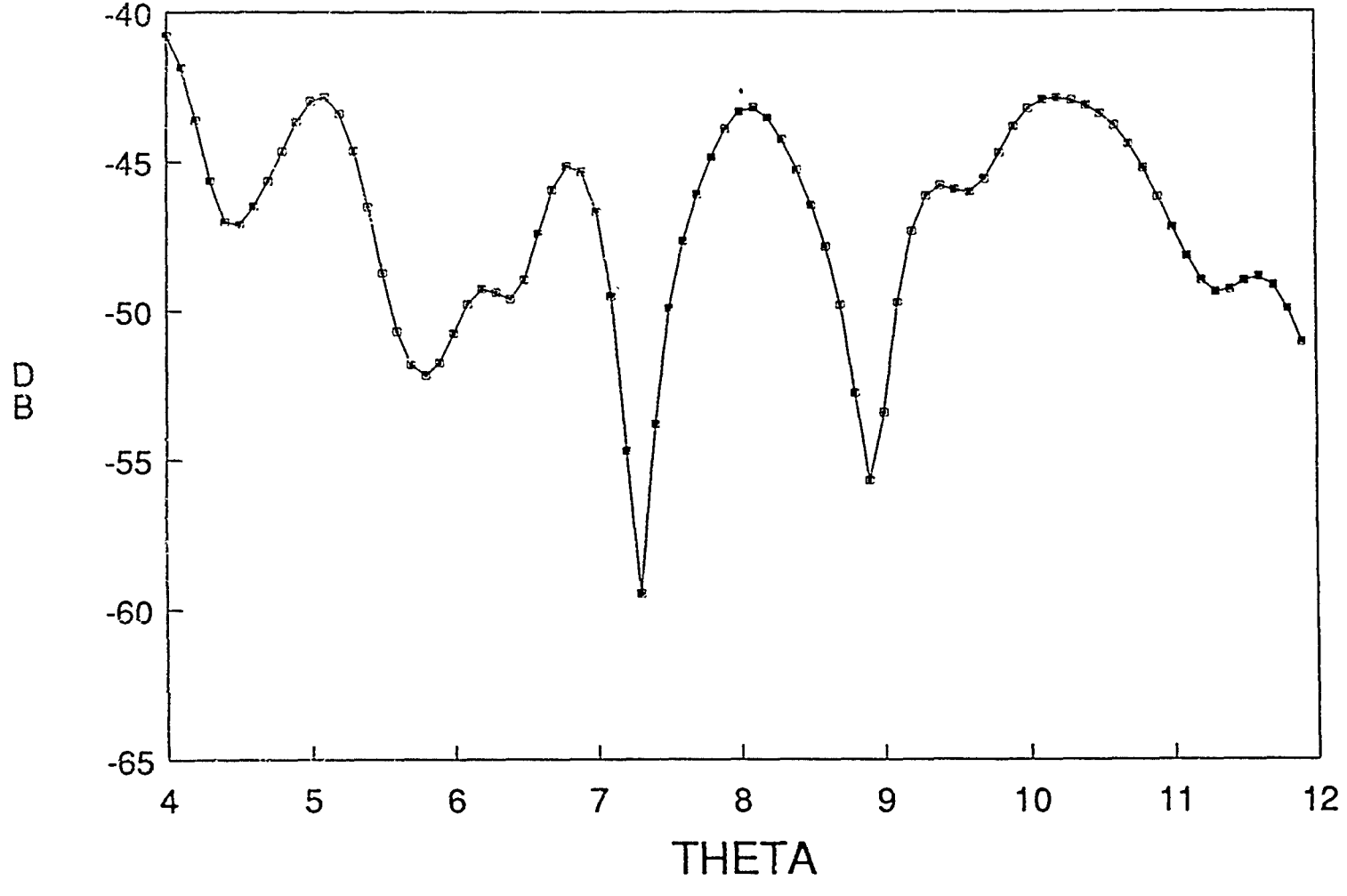

FIG.7 F.FIELD AVERAGE SLL 4-12(DEG)

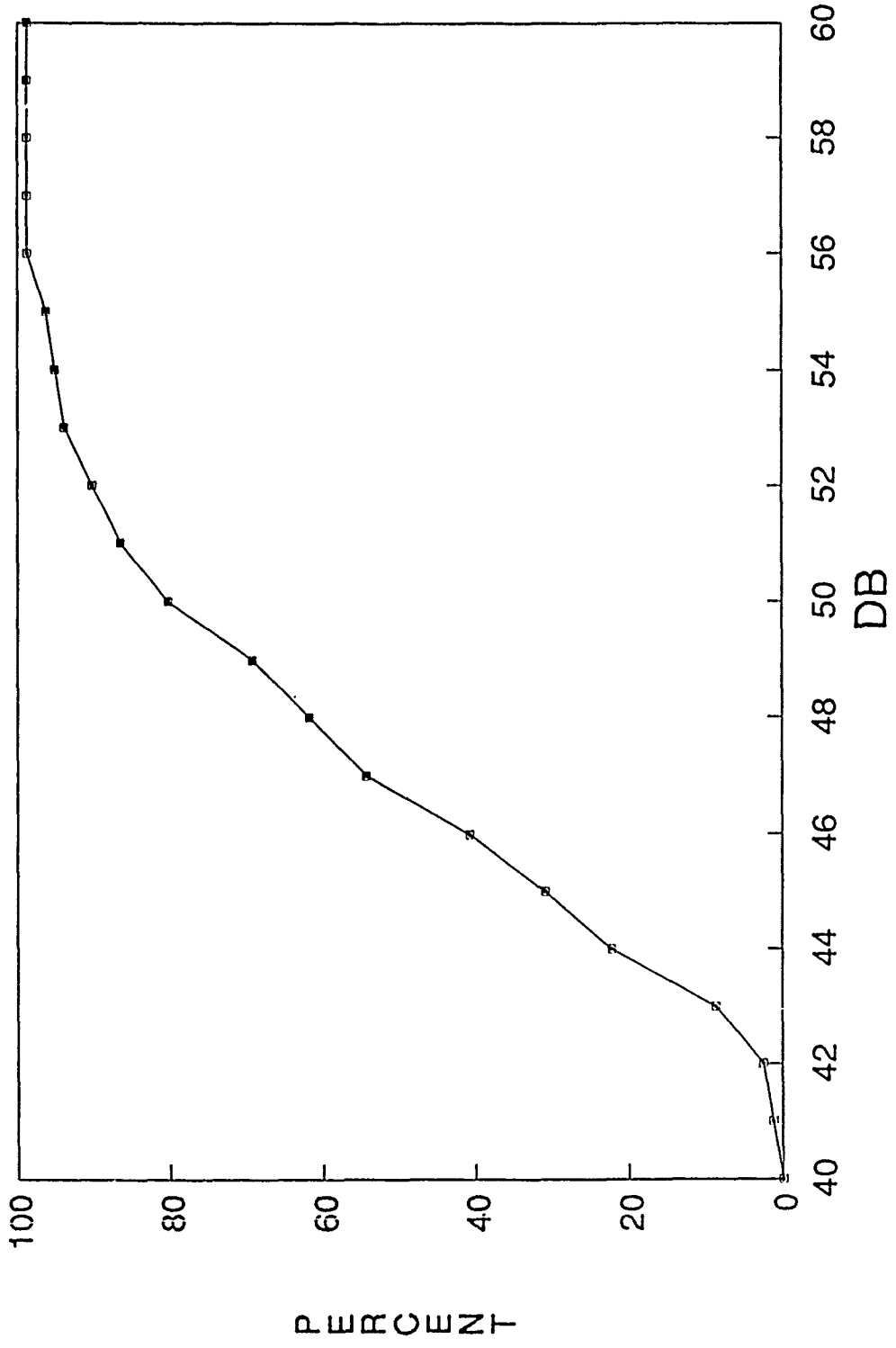

FIG.8 W.OUT CORRECTION SLL 4-12(DEG)

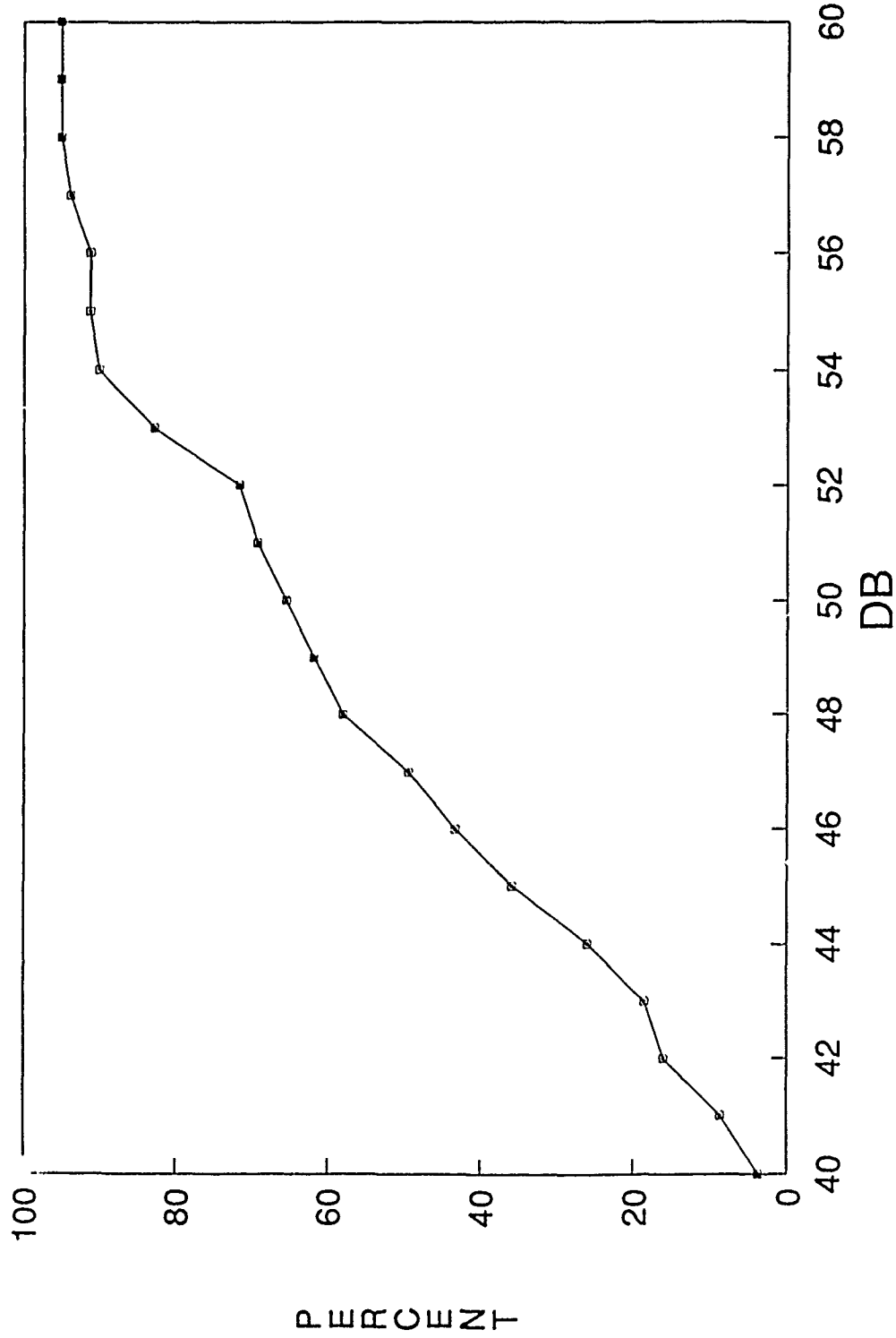

FIG.9 W.CORRECTION AVERAGE SLL 4-12(DEG)

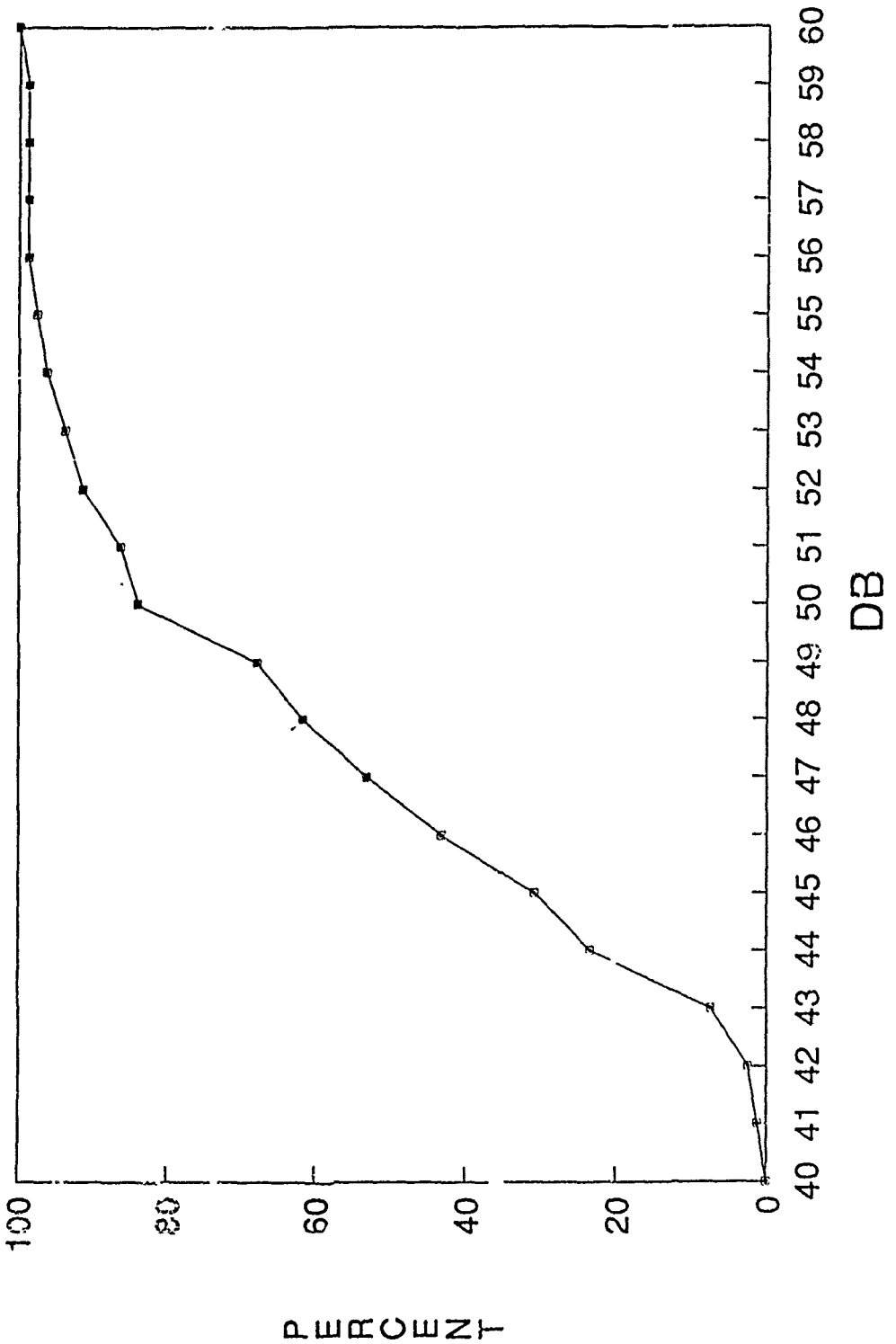

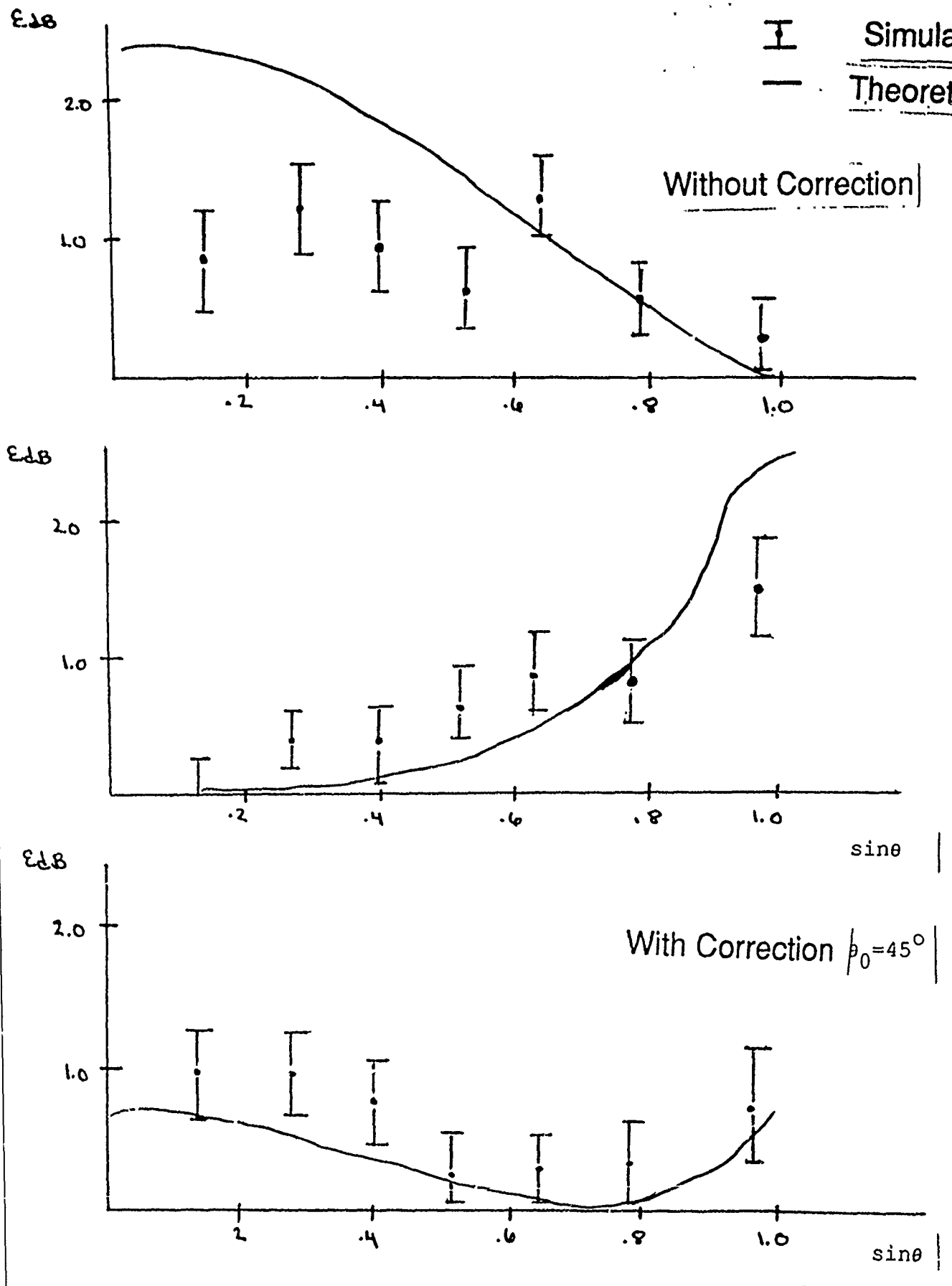

Fig. 10 Theoretical and Simulation Results

AN INCIDENT FIELD SENSOR FOR EMP MEASUREMENTS

Everett G. Farr and Joseph S. Hofstra

The BDM Corporation

Abstract

When making field measurements at EMP simulators, one needs broadband antennas that are flat to above 100 MHz. In additional, it would be helpful if these antennas were directional, in order to reject reflections from directly behind the sensor. This becomes important in extrapolation procedures that correct for differences between the field generated by the simulator and an actual threat field. Currently available antennas, however, are short dipoles and small loops, which are omnidirectional in one plane. The purpose of this paper is to report on the development of an antenna that solves this problem with a $1 + \cos\theta$ antenna pattern in both the E- and H-planes. We call this antenna the Balanced Transmission-line Wave (BTW) sensor.

The design of the sensor is based on the idea that if one could sum the antenna patterns of a short dipole and a small loop, one could achieve a directional sensor. Although a technique for combining these patterns in a single sensor has been known for some time, to our knowledge, a working model has never been built and tested.

In this presentation, a simple theory of operation is discussed. Furthermore, experimental results are presented for a prototype sensor. A Front/Back ratio somewhere between 20 and 29 dB was achieved. These results confirm the principal of operation of the sensor, and encourage further engineering development.

1. INTRODUCTION

This paper describes the development of a novel antenna that is both electrically small and directional. It was developed to meet the need for a directional antenna when making EMP field measurements whose response would be flat to 100 MHz [1]. The antennas that are typically used in EMP field measurements are small dipoles and loops, but these are not directional. The antenna we have developed is called the Balanced Transmission-line Wave (BTW) sensor.

The design of the sensor is based on an idea developed for a unidirectional EMP transmitter to be used in a simulator [2]. Although the original device was proposed some time ago, it has not to our knowledge been built or tested.

In this note a simplified theory of operation is discussed. Furthermore, experimental results are presented for two prototype sensors in a number of different types of tests. These results confirm the principle of operation of the sensor and encourage further engineering development of the BTW.

2. APPROACH

A simple view of a BTW is shown in Figure 1(a). It consists of a 100-Ω transmission line that tapers to a 100-Ω load on either end. This load can be either a 100-Ω resistor or a 100-Ω twinax cable. For structural reasons, an extra ground plane is normally inserted at the symmetry plane. In doing so, the 100-Ω resistors become two 50-Ω resistors, and the 100-Ω twinax terminations become two 50-Ω coax transmission lines.

The structure of Figure 1(a) has been analyzed in detail by Jiunn Yu et al in Sensor and Simulation Note (SSN) 243. The treatment in SSN 243, however, is more complicated than what is required for a simple understanding of the BTW. Therefore we begin with a simplified low-frequency explanation of how and why the device operates.

The BTW can be described most simply in terms of a parallel plate transmission line. This is later generalized to an arbitrary transmission-line configuration. We begin with the parallel plate model.

2.1 Parallel Plate Transmission Line Model

Consider the diagram of Figure 1(b). It consists simply of two closely spaced parallel plates that form a transmission line. Each end of the line is assumed to be terminated in the characteristic impedance of the line. We can describe the characteristics of the device in terms of a simple equivalent circuit, shown in Figure 1(c). This is a current and voltage source feeding into two matched loads. The voltage and current sources are derived from inductive and capacitive coupling, respectively.

First, we derive the voltage source due to inductive coupling. If a plane wave is incident upon the sensor as shown in Figure 1(b), then the induced voltage through the loop in the y-z plane is

$$\mathcal{V}(t) = -\bar{A} \cdot \frac{d\bar{B}}{dt} \tag{1}$$

where $\bar{A} = lh\hat{x}$. Since $\bar{B} = \mu_o H_x \hat{x}$, we can express the above as

$$\mathcal{V}(t) = -\mu_o lh \frac{dH_x}{dt} \tag{2}$$

where $\mu_o = 4\pi \times 10^{-7}$ H/m. This behavior is directly analogous to a B-dot sensor.

Next, we derive the current source due to capacitive coupling. For the configuration of Figure 1(b), the current induced between the plates is

$$\mathcal{I}(t) = C \frac{dV}{dt} \tag{3}$$

If we assume a uniform electric field between the plates, then the voltage between the plates is

$$V(t) = -h\,\hat{y} \cdot \bar{E}(t) \tag{4}$$

where $\bar{E}(t)$ is the electric field due to the incident field. If we also assume that fringing is negligible at the edge of the plates, then

$$C = \frac{\epsilon_o lw}{h} \tag{5}$$

where $\epsilon_o = 8.85 \times 10^{-12}$ F/m. Combining the above three equations, we find the current source as

$$\mathcal{I}(t) = -\epsilon_o lw \frac{dE_y}{dt} \tag{6}$$

It turns out that this current source can be simply expressed in terms of the voltage source, $\mathcal{V}(t)$. This is accomplished by assuming $E_y/H_x = \eta = \sqrt{\mu_o/\epsilon_o}$, where $\eta = 377\ \Omega$ is the impedance of free space. By doing this, we have

$$\mathcal{I}(t) = -\epsilon_o \eta lw \frac{dH_x}{dt} = -\frac{\mu_o lh \dfrac{dH_x}{dt}}{\dfrac{h}{w}} \tag{7}$$

Since the characteristic impedance of a parallel plate transmission line is $Z_o = \eta h/w$ we have, by combining Equations (2) and (7)

$$\mathcal{I}(t) = \frac{\mathcal{V}(t)}{Z_o} \tag{8}$$

This is the desired result.

It is clear from Figure 1(c) that if Equation (8) is true, then the voltage at Port 1 of the sensor is

$$V_1(t) = \mathcal{V}(t) \tag{9}$$

whereas the voltage at Port 2 is

$$V_2(t) = 0 \tag{10}$$

This is the behavior required for a directional sensor. If the wave is incident from the $-\hat{z}$-direction, it is simple to show with symmetry that Port 2 is excited and Port 1 has no response.

2.2 Arbitrary Transmission Line Model

It is not necessary to have a parallel plate transmission line to observe the effect described in the previous section. We now demonstrate that the phenomenon remains valid with an arbitrary transmission line.

The critical result that needs to be proven is Equation (8). We need a more general expression for $\mathcal{I}(t)$. In general,

$$\mathcal{I}(t) = C_l l \frac{dV(t)}{dt} \tag{11}$$

where C_l is the capacitance per unit length of the transmission line, l is the length of the line, and $V(t)$ is as defined in Equation (4). Using Equation (4), we get

$$\mathcal{I}(t) = -h\, C_l\, l\, \hat{y} \cdot \frac{d\bar{E}(t)}{dt} = -hl\, C_l \frac{dE_y}{dt} = -hl\, C_l \eta \frac{dH_x}{dt} \tag{12}$$

Furthermore, $\mathcal{V}(t)$ is unchanged from Equation (2), since the area of the loop does not change. Thus, combining Equations (2) and (12), we find

$$\frac{\mathcal{V}(t)}{\mathcal{I}(t)} = \frac{\mu_o}{\eta C_l} = \frac{\sqrt{\mu_o \epsilon_o}}{C_l} = Z_o \tag{13}$$

The last equation follows from a definition of characteristic impedance that holds for transmission lines with air dielectric. This confirms that Equation (8) is valid for a transmission line of arbitrary cross section provided that its phase velocity equal to the speed of light. This allows us flexibility in the final design of the sensor.

2.3 Sensor Bandwidth

The frequency bandwidth is of concern when attempting to use the BTW at higher frequencies. It is, however, a somewhat difficult number to define. For our purposes, a reasonable definition would be the frequency band over which a minimum Front/Back ratio is maintained. This turns out to be somewhat difficult to measure, since our measurements of Front/Back ratio are taken in pulse mode and not in CW mode.

With this in mind, our best definition of bandwidth is probably given by Carl Baum in Sensor and Simulation Note 8 [3]. This was developed originally for a Multi-Gap Loop (MGL) sensor, and since there is an analogy between the performance of a BTW and MGL, this definition may be reasonable. According to SSN 8, the maximum frequency of operation is

$$f_{max} = \frac{1}{\pi \mathcal{T}_t} \tag{14}$$

where $\mathcal{T}_t$ is the round trip transit time of a signal on the sensor. If there is no dielectric in the transmission line, then $\mathcal{T}_t = 2l/c$, and

$$f_{max} = \frac{c}{2\pi l} \tag{15}$$

As an example, the BTW we designed could be built to have a length about 0.35 m if some extra lengths of transmission line were removed. For this length, the bandwidth would be about 135 MHz. Of course, the bandwidth could always be increased by decreasing the size of the BTW, which in turn would decrease the effective area of the BTW.

2.4 Design Considerations

A diagram of the BTW is shown in Figure 2. The effective area was designed to be close to that of an MGL-2, 0.01 m^2. This is the same as the area of the loop one sees when looking at the side view of the sensor. The ground plane acts as a structural support, and does not affect the fields due to symmetry. The characteristic impedance of each side of the parallel plate transmission line is 50-Ω, and it was calculated using reference [4].

The output of the BTW is two SMA connectors at Port 1, which are each connected by cable to one of the inputs of a differential mode fiber optic transmitter. In fact, it is possible to measure fields from both directions concurrently. This can be done by replacing the two 50-Ω loads at Port 2 with cables that are connected to a second fiber optic transmitter.

An incident field excites the end of the transmission line structure port closest to the direction of incidence. The cables from Port 1 are routed to the back end of the sensor in order to keep instrumentation behind the incident field.

3. LABORATORY MEASUREMENTS

Two experiments were performed in the laboratory to check the performance of the BTW. First, a Time Domain Reflectometry (TDR) measurement was performed to check the impedance matching between different sections of the sensor. We connected the TDR input to one side of Port 1, leaving the remaining connector of Port 1 and both connectors of Port 2 matched to 50-Ω loads.

Results for the TDR are shown in Figure 3. One can relate bumps in the TDR measurements to physical features of the structure. The maximum deviation from the zero

line is about 50 mρ, or about 5 percent of the maximum possible reflection coefficient, which is 1.

Next, TEM cell measurements were performed. In derivative sensors, one expects to see the measured response increase proportionally with frequency, or 20 dB/decade. TEM cell measurements were made in order to confirm this.

A diagram of the experimental setup is shown in Figure 4. The BTW was placed in a 3-ft TEM cell and the output was fed through a balun into a network analyzer. The output of the sensor was referenced to the total throughput of the TEM cell. The BTW was placed in a manner that would maximize the coupling into it.

Results are shown in Figure 5. The response increases at 20 dB/decade, exactly as it should. There are a few small bumps in the data in the decade between 10 and 100 MHz, but these are limitations of the TEM cell technique that normally occur at higher frequencies. This is simply demonstrated by replacing the cables with ones of a slightly different length and watching the bumps move to a different frequency.

4. EXPERIMENTS AT HPD

A number of tests were performed at HPD to verify the performance of the BTW. HPD is an EMP test facilty and it is shown in Figure 6. It consists of a pulser 30 m above the ground that is connected to an elliptical loop antenna that connects to the ground at either end. This was the facility that spurred the development of the BTW sensor; we wanted to measure the incident field by itself, while rejecting the reflected field.

Two tests were performed at HPD. First, measurements were made comparing a BTW to an MGL when used under the pulser in a normal mode of operation. Since the MGL is a loop sensor, one would expect to see both incident and reflected fields with the MGL, and only the incident field with the BTW. Next, the BTW was pointed down in order to observe how well it rejected the incident field.

In the first experiment, the response of the BTW was compared to that of an MGL-2 on the same shot, while both were positioned 5 m above the ground, directly under the HPD pulser. This is the normal mode of operation for the BTW. We expected to see the BTW reject the reflected field while the MGL would measure it The BTW was directly under the pulser, while the MGL was 2 m outside the plane of the loop of the HPD antenna. Since the HPD pulser is 30 m above the ground, this is effectively directly under the pulser.

For this experiment, the output of the BTW and MGL-2 were each fed directly into a differential mode Nanofast fiber optic link with 1 μs integrators turned on inside the transmitters. Since the output of the MGL is a twinax connector, a twinax-to-coax tee (TCT) was used to convert the twinax to two coaxial lines. The receivers fed into LeCroy 6880 A/D converters. Noise filters were turned on in the LeCroy digitizers at 150 MHz.

These data were processed using standard signal processing techniques. The zero line was found by averaging the first two hundred points. The effect of the fiber optic links was deconvolved from the output using standard Fourier transform techniques. Although we did not know exactly what the effective area of the BTW would be, we had to assume an effective area in order to get the data through the standard processing algorithms. For this reason, we assumed during our data processing that the effective area of the BTW was 0.01 m^2, as it was designed. Later, during testing at ALECS, we conducted an experiment to measure this quantity (see Section 5.1).

The waveforms measured with the MGL-2 and the BTW are shown in Figure 6. In comparing the two results, it is clear that the second large bump in the response of the MGL is the reflected field. It occurs at about 33 ns after the first peak, which is the two-way transit time between the sensor and the ground. The response of the BTW, however, is missing this second bump at 33 ns.

Next, we placed the BTW pointing down, 5 m above the ground, in order to observe the rejection of the incident field. The same instrumentation and signal processing was used as before, except that a 150 MHz filter was introduced in data processing rather than in data acquisition.

A plot of the measured field is shown in Figure 7. Ideally, we expect to see the first 33 ns of the signal to be noise, with a large signal following that being the reflected field. Our measurment shows essentially this; the first 33 ns of the signal is almost in the noise.

5. EXPERIMENTS AT ALECS

The final set of tests took place at ALECS. This facility was used because it is a transmission-line type simulator. It is shown in Figure 9. It provides a TEM field with almost no reflections. First, we attempted to calibrate the effective area of the BTW by comparing its response to that of an MGL. This was done with both integrated and derivative data. Next, we measured the Front/Back ratio of the BTW, again using both integrated and derivative data. Finally, we made measurements of the antenna pattern of the BTW in the E- and H-planes.

5.1 Effective Area Calibration

The first test was to compare the effective area of the BTW tapered design to that of an MGL-2. To do this, we compare the ratio of peak magnitudes of the MGL-2 and the BTW on the same shot. This technique requires the assumption that the effective area of the MGL-2 is 0.01m^2, and its accuracy is limited by this assumption.

An MGL-2 and the BTW were placed 2 m apart in the center of the testing volume. These sensors were each fed into a differential mode fiber optic link with the 1 μs integrators turned on. The connection to the link for the MGL required a TCT to split the twinax

output into into two coaxial lines. The output of the fiber optic receivers was then fed into an active signal divider, which splits the signal into three parts and sends it on to three Tektronix 7912 digitizers.

Signal processing involved the normal process of finding the zero line by averaging the first 50 points and then deconvolving the effect of the fiber optic transmitter. As before, we assumed an effective area of 0.01 m^2 for the BTW to get the data through processing. We can calculate the correction needed in the effective area if we start with an assumed value for it.

The peak magnitude as measured with the BTW was compared to that measured with the MGL-2 for four shots. The average normalized peak magnitude of the field measured with the BTW was 1.1. This means that the effective area of the BTW is 10 percent larger than that of the MGL-2, or 0.011 m^2. A summary of this data appears in Table 1.

Table 1. Effective Area and Front/Back Ratio at ALECS

Data Type	Effective Area (m^2)	Front/Back (dB)
Integrated	0.0110	20
Derivative	0.0115	29

This process was then repeated with the integrators turned off. The signal processing involved only time tying, finding the baseline, and then linear scaling by a factor of $1/(\mu_o A_e)$. Again, a normalized peak was calculated by comparing the peak of the BTW data to that of the MGL-2 data. The average normalized peak magnitude of the field measured with the BTW was 1.15. This means that the effective area of the BTW is 15 percent larger than that of the MGL-2, or 0.0115 m^2.

There is some question as to which technique is more accurate, since we get a 5 percent difference in effective areas with the two techniques. This is especially true since the data in general do not have a wide scatter about their means. Normally, one would prefer to use the data from the measurment technique with the fewest signal conditioners to be deconvolved out. This suggests that the derivative data are more accurate, since an integrator is not used. This does not explain, however, why there should be a discrepancy between the integrated and derivative data. Perhaps a reasonable compromise would be to take the average of the two techniques, which is 0.012. This is the effective area we used in the Front/Back ratio measurements.

5.2 Front/Back Ratio Measurements

The next experiment involved a measurement of the Front/Back ratio. This was done with both derivative and integrated measurements, using identical test setups and signal processing as in the HPD experiment. The only difference was that the BTW was pointed away from the pulser instead of toward it. By using the peak magnitudes and correcting for the difference in effective areas between the MGL and BTW, one can calculate a Front/Back ratio.

The peak magnitude of a waveform with the BTW pointing backward was compared to the peak magnitude for an MGL over several shots. After taking into account the different effective areas between the MGL and BTW, there was an average 20 dB Front/Back ratio with integrated data.

The same experiment was repeated with derivative data. This time we found a Front/Back ratio of 29 dB. As in the previous experiment, we obtained different results for the integrated and derivative data. This time, however, the difference in results was more significant, 9 dB. One way to resolve the issue might be to assume that the simplest experiment, i.e., the one with derivative data, is the most accurate. It is a little difficult to say this definitively, however, and it will have to be left for future investigation.

5.3 Anterna Pattern Cuts

In the final experiment, we measured the antenna pattern of the BTW. For far field measurements, the BTW should have an antenna pattern that is $1 + \cos\theta$, according to SSN 243 [2]. This behavior should hold both in the E- and H-planes.

The data sets taken were all integrated, with the instrumentation and signal processing the same as that for all previous integrated data taken at ALECS. Plots of the cuts are given in Figures 8 and 9. It is clear that the sensor performs about as we expect, with the exception near 180 degrees. We should remember, however, that the Front/Back ratio with derivative data was 9 dB better than that for integrated data, so if we had made these plots with derivative data we would expect better agreement at 180 degrees. Finally, we note that each of the points on these graphs was generated with a single shot, not an average over several shots. Therefore, one might expect a few points would be slightly different from theory.

6. CONCLUSIONS

A broadband directional antenna has been developed that should simplify and improve the measurent of the incident field at hybrid EMP simulators. This antenna, the Balanced Transmission-line Wave sensor, has the property of being able to measure the incident field while rejecting the reflected field. Preliminary measurements of the Front/Back ratio suggest an isolation of 29 dB with derivative data and 20 dB with integrated data.

There remain two areas where further investigation would be useful. The first is whether or not the Front/Back ratio could be improved with further experimentation. There are a number of design parameters that could be varied while maintaining the same overall response of the sensor. A systematic study of these variables may reveal designs with a larger Front/Back ratio. The second area where further investigation would be useful concerns the discrepancy between integrated and derivative measurements of Front/Back ratio. At some point, it will be necessary to generate a commonly accepted method of measuring this parameter.

An interesting aspect of this work is that it may have applications outside the area of EMP. It would seem there could be a number of uses for a broadband antenna that is both electrically small and directional.

ACKNOWLEDGEMENT

We wish to express our appreciation to Carl Baum for his many helpful discussions on this topic.

REFERENCES

[1] Farr E. G. (1988) *Extrapolation of Ground-Alert Mode Data at Hybrid EMP Simulators*, Sensor and Simulation Note 311, Weapons Laboratory.

[2] Yu, J., et al (1978) *Multipole Radiations: Formulation and Evaluation for Small EMP Simulators*, Sensor and Simulation Note 243, Weapons Laboratory.

[3] Baum, C. E. (1964) *Maximizing Frequency Response of a $\dot{B}$ Loop*, Sensor and Simulation Note 8, Weapons Laboratory.

[4] Baum, C. E. (1966) *Impedances and Field Distributions for Parallel Plate Transmission Line Simulators*, Sensor and Simulation Note 21, Weapons Laboratory, p. 25.

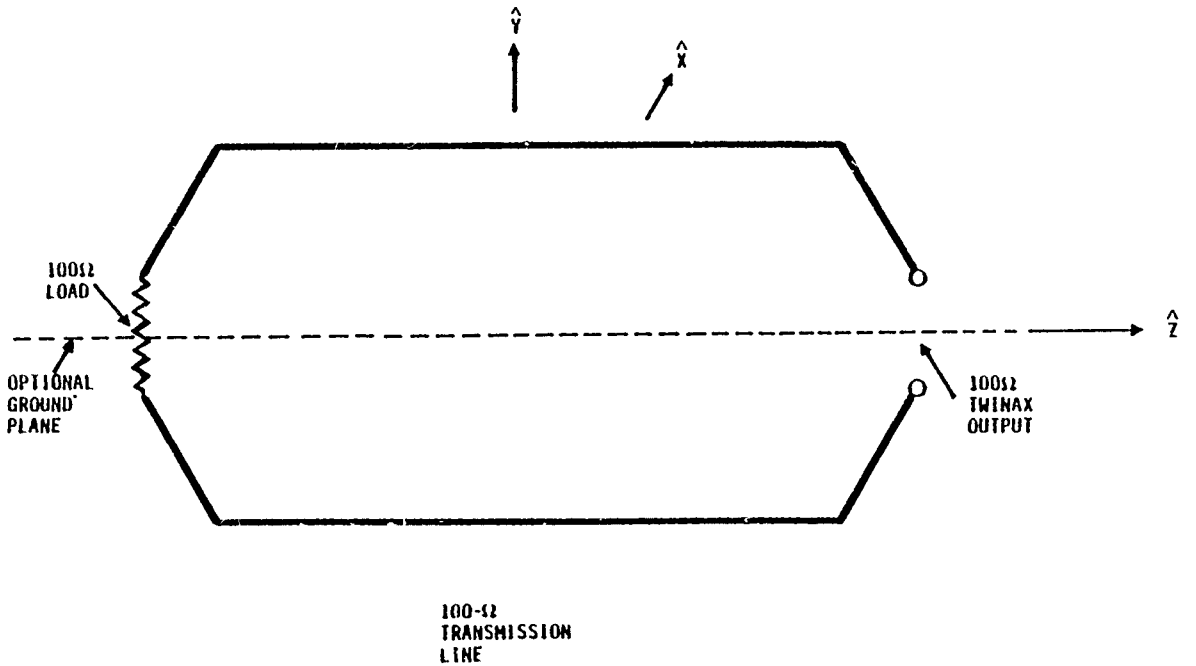

(a) BTW Sensor

Figure 1. Simplified BTW Diagram

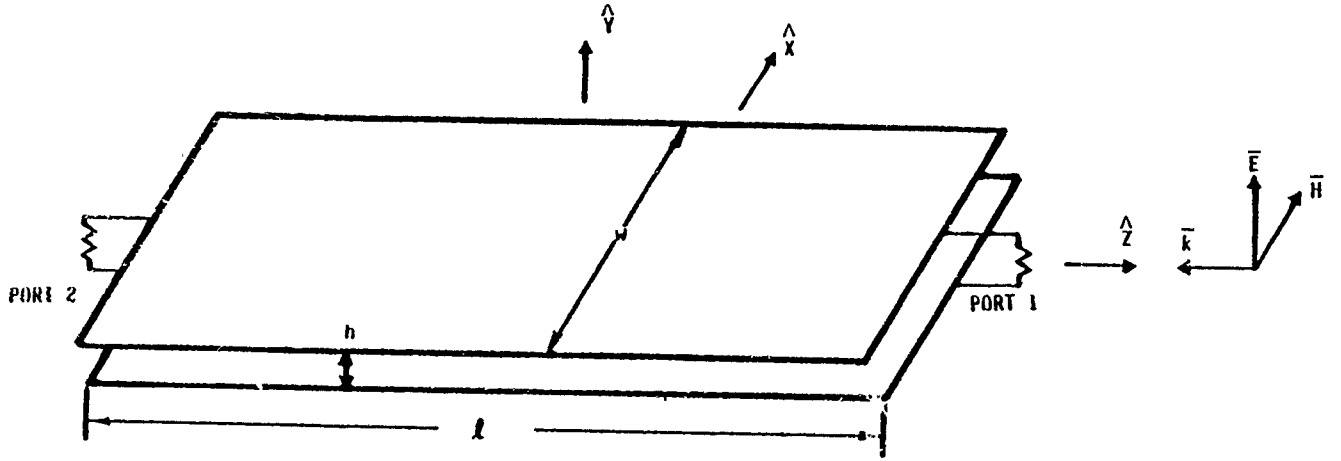

(b) Parallel Plate Model

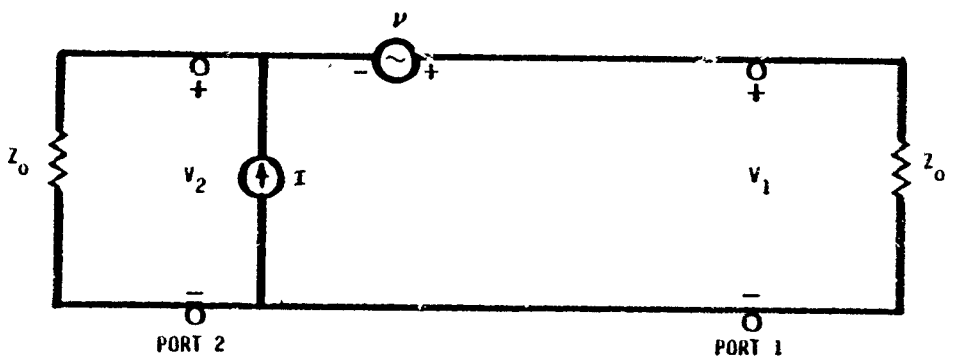

(c) Equivalent Circuit

Figure 1. Simplified BTW Diagram (Concluded)

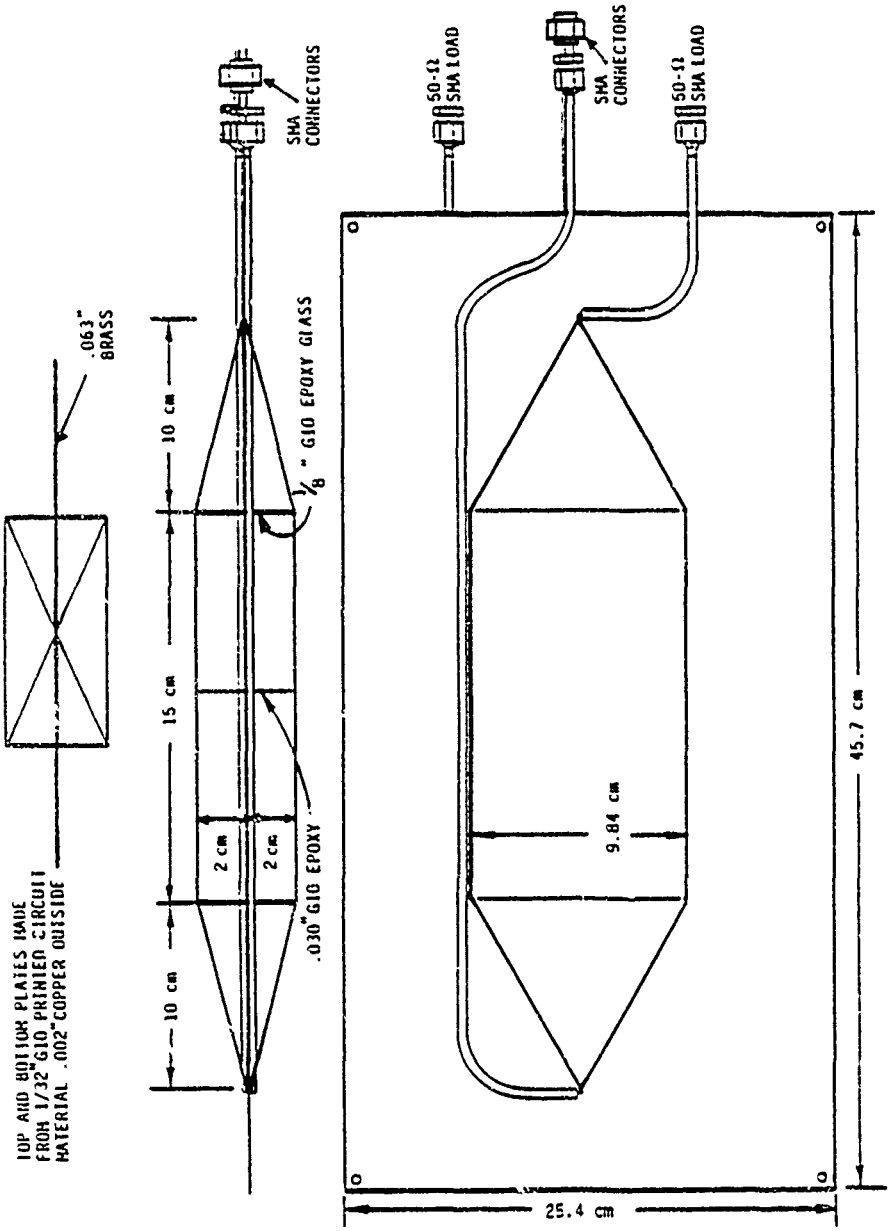

Figure 2. Diagram of the BTW

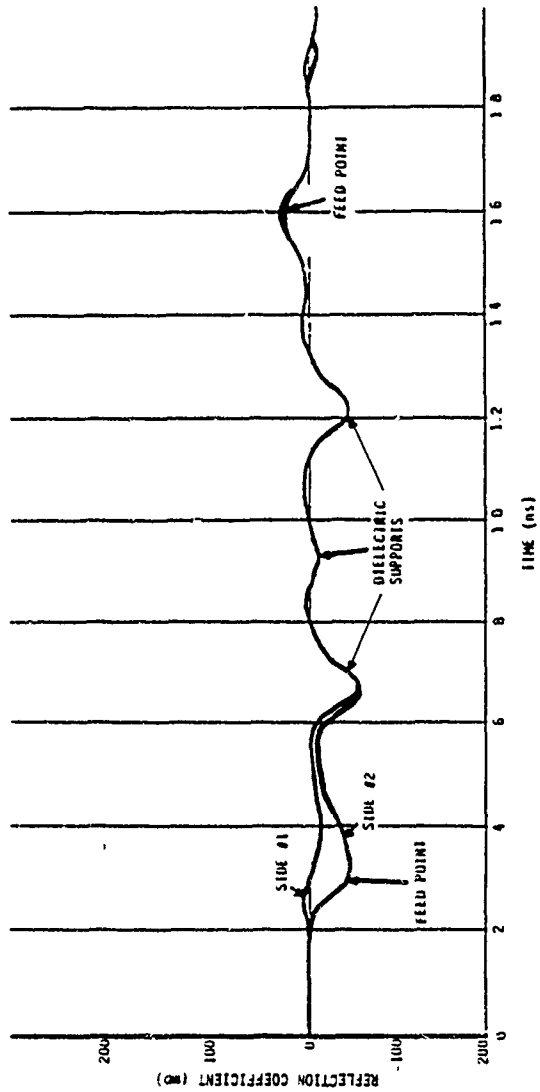

Figure 3. TDR of the BTW

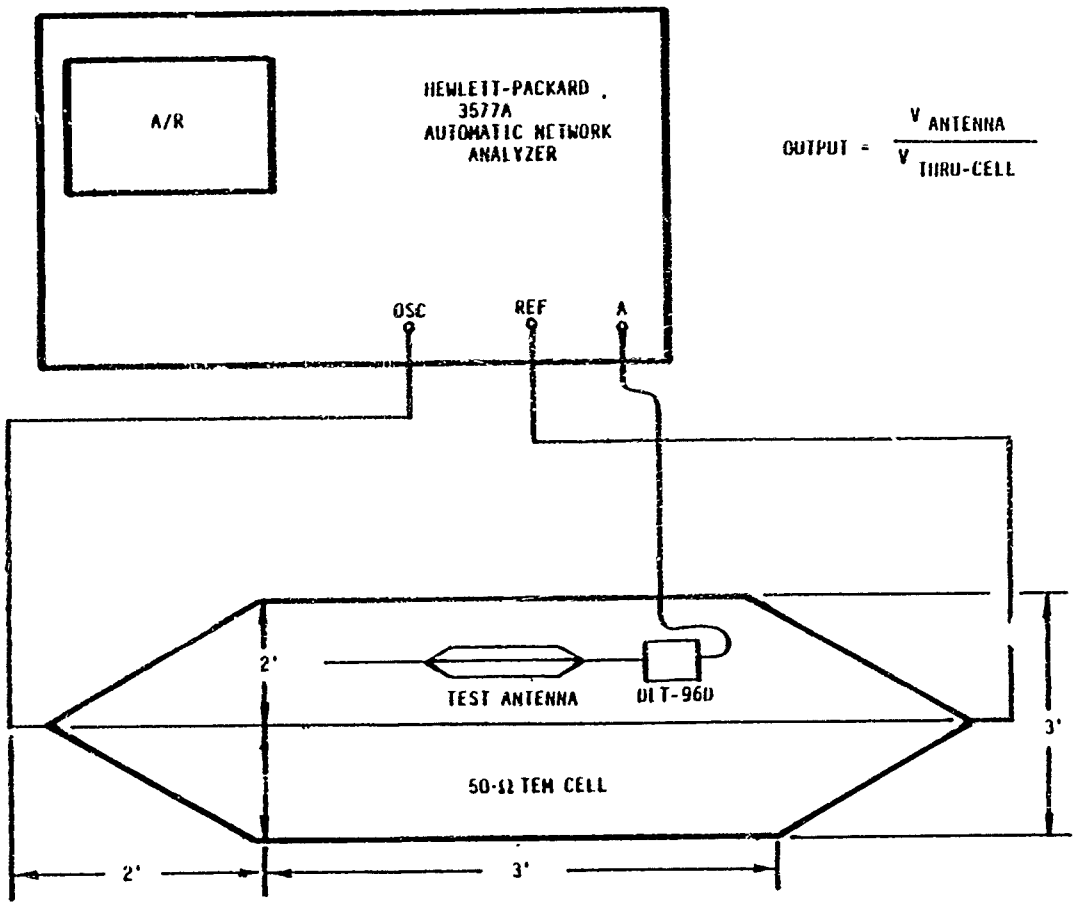

Figure 1. Instrumentation Setup for TEM Cell Measurements

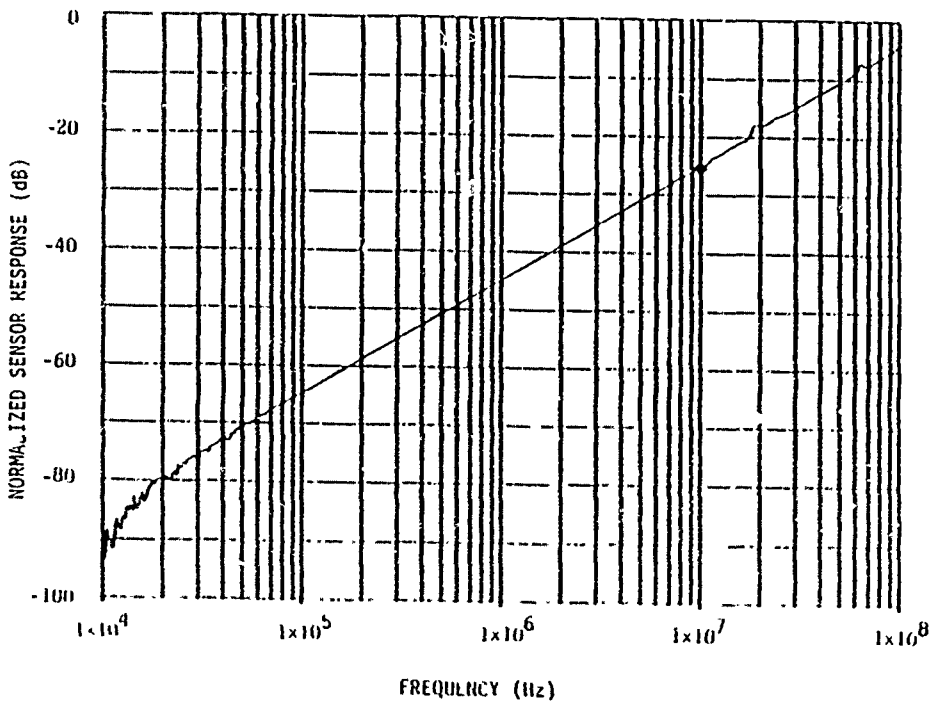

Figure 5. TEM Cell Sweep of the BTW

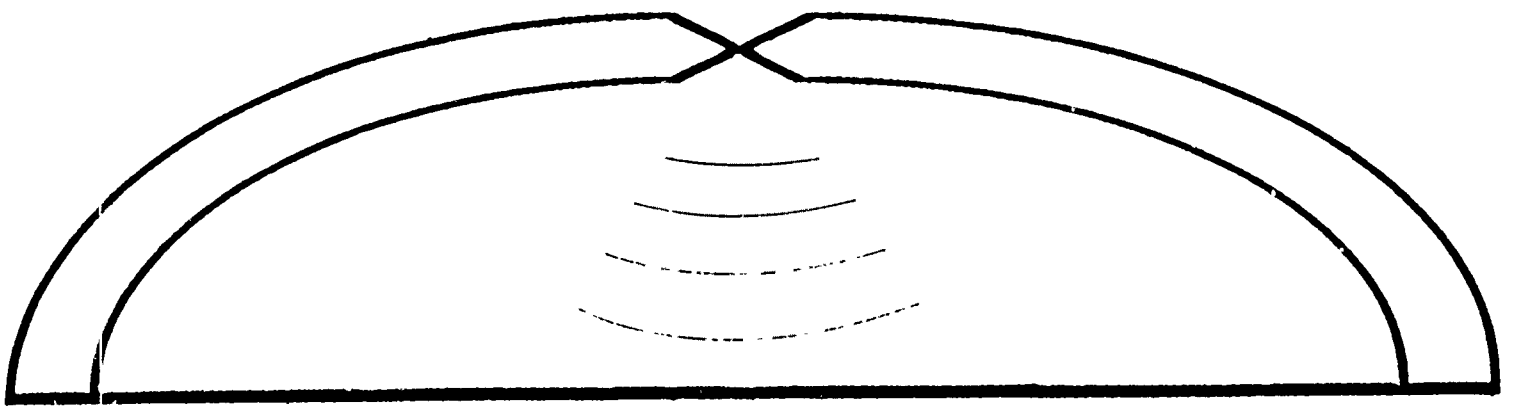

Figure 6. HPD EMP Test Facility

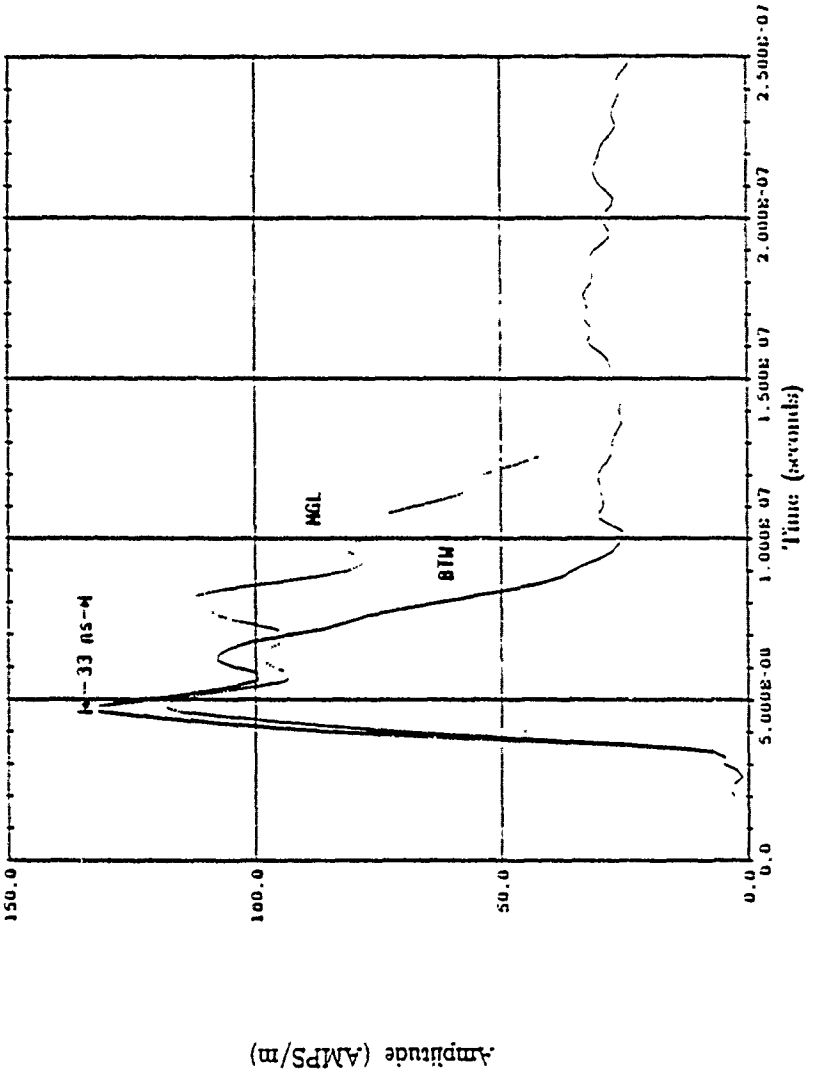

Figure 7. Fields Measured Under the HPD Pulser With an MGL-2 and the BTW

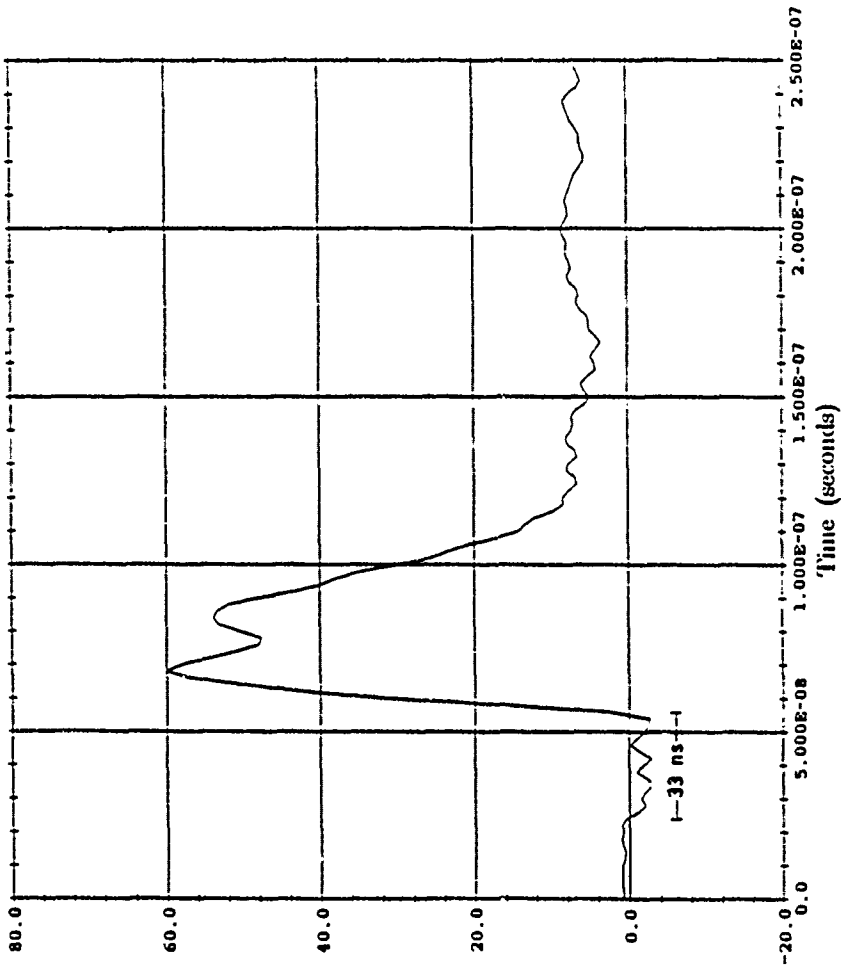

Figure 8. Rejection of the Incident Field at HPD With the BTW

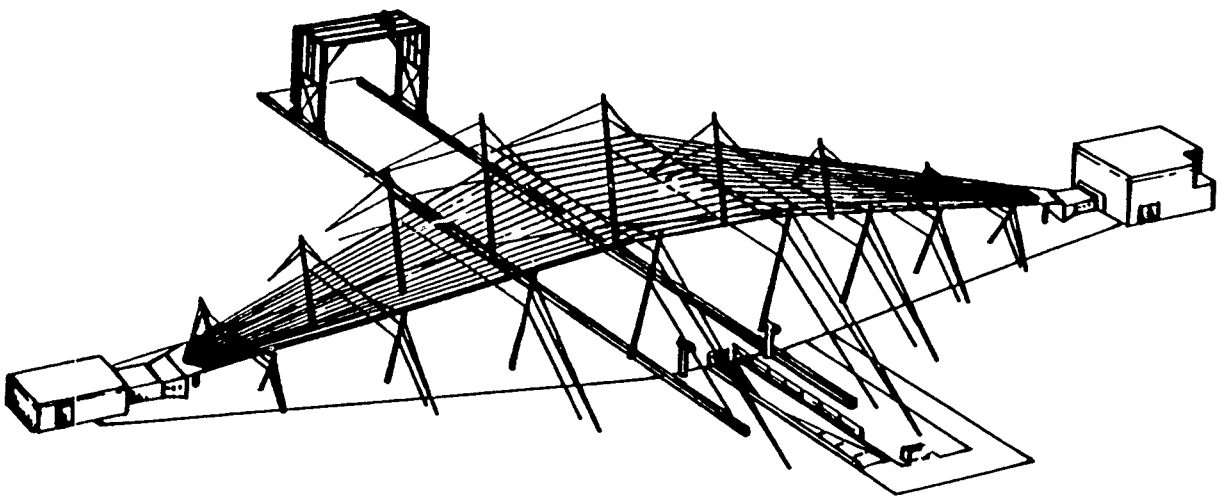

Figure 9. ALECS EMP Test Facility

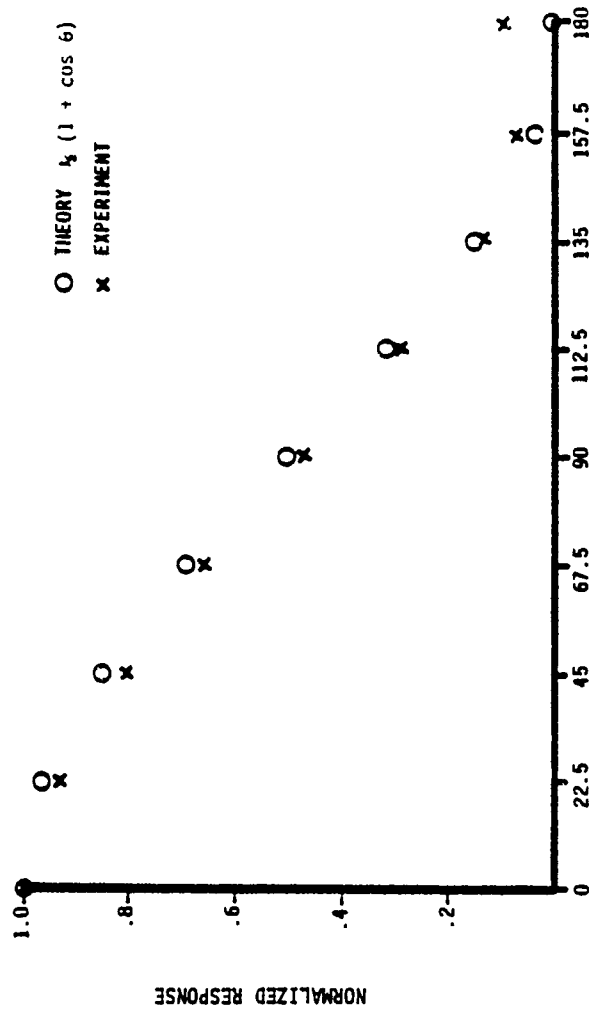

Figure 10. H-Plane Cut of the BTW Measured at AIECS

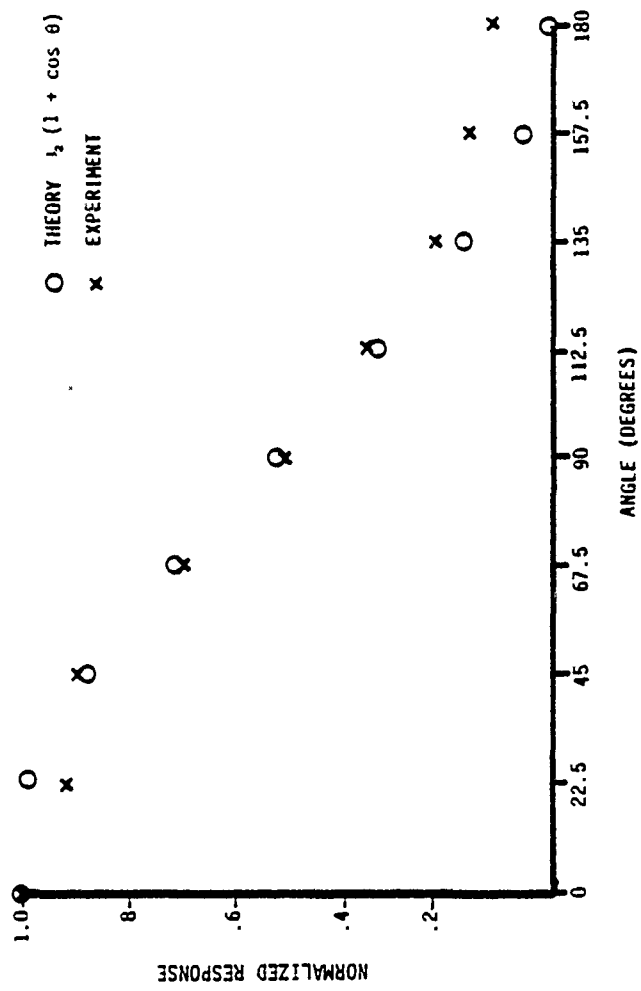

Figure 11. E-Plane Cut of the BTW Measured at AIECS

QUANTIFYING SIMULTANEOUS V AND H COVERAGE FROM AN UNDERSIDE AIRCRAFT LOCATION

George Monser

and

Leonard T. Surette

Raytheon Company
Electromagnetic System Division
6380 Hollister Avenue
Goleta, California 93017

1989

ABSTRACT

Quantifying Simultaneous V and H Coverage from an Underside Aircraft Location

By: George Monser and Leonard T. Surette

This paper presents the results of a measurement program conducted to evaluate antenna coverage from a constrained-space airborne platform.

Two levels of coverage are reported: Level 1 details coverage without the aircraft, but over a small groundplane, while Level 2 includes aircraft effects. Coverage and gain for each polarization was evaluated by quantizing the data and computer processing to obtain a measure of goodness vs frequency. In particular, horizontal polarization showed considerable changes, as expected, compared to Level 1 performance. Vertical polarization showed smaller, but significant changes.

Coverage, Under-Aircraft, Simultaneous

By: George J. Monser and Leonard T. Surette

SUMMARY:

This paper presents the results of a measurement program conducted to evaluate antenna coverage from a constrained-space airborne platform.

Two levels of coverage are reported: Level 1 details coverage without the aircraft, but over a small ground-plane, while Level 2 includes aircraft effects. Coverage and gain for each polarization was evaluated by quantizing the data and computer processing to obtain a measure of goodness vs frequency. In particular, horizontal polarization showed considerable changes, as expected, compared to Level 1 performance. Vertical polarization showed smaller, but significant changes.

1.0 INTRODUCTION

This paper presents the results of a measurement program conducted to evaluate coverage from a under-aircraft platform. In particular, the antenna installation was small, in terms of wavelengths, the bandwidth was greater than 3/1, simultaneous, efficient, dual-polarized radiation was required over 360° in azimuth by 30° in elevation.

2.0 INSTALLATION

The complete antenna system was constrained to fit inside the volume dimensioned in wavelengths shown in Figure 1. In addition, the bottom surface, which was metal, would be positioned under-side the aircraft.

3.0 DESIGN CONSIDERATIONS

The first consideration is how to attain simultaneous, field-of-view, dual-polarization from the volume shown in Figure 1. For vertical polarization (i.e., perpendicular to the aircraft surface underside) the best candidate appears to be some form of conical monopole. This type of antenna can be designed to efficiently cover 3/1 bandwidth and the radiation field-of-view approximates the requirement. In addition, the radiating structure is 1/2-height for the ground-plane image forms the other half. This is an important consideration approaching FLOW where the allowable height (see Figure 1) is only 0.13 wavelengths.

For horizontal polarization (i.e., parallel to the aircraft surface) some form of horizontal turnstile fan-dipoles can be used. Here it is known that the effect of the aircraft surface will result in tilting the radiation downward with the maximum radiation occurring approximately at a depression angle below the aircraft of $\lambda/4H$ where λ is the wavelength and H is the antenna phase-center spacing with respect to the aircraft surface. From these considerations and the space

Figure 1, the arrangement shown in Figure 2 was devised with the fan dipoles placed flat in the upper surface of the installation volume.

Installing both the vertical and horizontal antennas in a common volume leads to antenna shadowing and cross-talk effects both of which were considered unacceptable.

One solution is to integrate the vertical and horizontal radiating structure into a common single-input structure as shown in Figure 3. Here, all elements of the vertical monopole are retained and an asymmetrical top-hat is added to the monopole yielding some degree of horizontal polarization. Thus, omnidirectional coverage is maintained for vertical polarization and a quasi-omni horizontal polarization results.

4.0 PRELIMINARY TESTS

Before installing on the aircraft model an antenna was configured to fit the volume constraints of Figure 1. Figure 4 shows a photograph of one of many antenna assemblies which were tested. Here, the vertical monopole was positioned in the center of the metal base plate. To approximate a conical monopole two triangular plates were used, one with a flare angle of 90° and the second with a flare angle of 65°. Next unbalanced top-loading was added to achieve horizontal polarization.

Tests with a balanced and unbalanced top-hat showed that in the un-balanced configuration that significant horizontal polarization could be provided without affecting the vertical omni coverage.

5.0 MODEL TESTS

Figure 5 shows the 1/10 scale-model aircraft with the antenna system installed on the underside of the aircraft.

Radiation patterns and gain were obtained for a number of test frequencies for four conic cuts and two polarizations. Specifically, the elevation cuts were 0, -10, -20, and -30° in elevation over 360° in azimuth.

6.0 TYPICAL INSTALLED PATTERNS

Figure 6 shows one of many patterns recorded during the tests. In Figure 6(A) the two principal polarizations at F_{LOW} are plotted for 0° in elevation. While the horizontal polarization is not particularly good, it improves as shown in Figure 6(B) as the depression angle approaches -30°. In Figure 6(B) two elevation cuts are displayed, one taken Fore and Aft and the other Broadside.

7.0 INSTALLED PERFORMANCE

Data from plots similar to Figure 6 were used to compile gain vs frequency profiles for each polarization as shown in Figure 7. Each point in Figure 7 represents an average for 360° in azimuth sampled at 10° intervals over four conic cuts.of 0, -10, -20, and -30°.

Figure 8 shows how the average gain over 360° in azimuth varies with elevation for each polarization for three frequencies.

8.0 DISCUSSION

Data in the preceding section illustrates what can be achieved over a wide bandwidth for two polarizations from a constrained space.

At first consideration the gain values given in Figures 7 and 8 may appear low, particularly in Figure 7. The following assessment is offered:

1. Power division between the two polarizations; ideally 3 dB.

2. VSWR loss 1 to 3 dB, based upon measured data.

3. Radiated energy outside the defined field-of-view of 0 to -30° in elevation.

From the above tally only an improvement of gain by improving VSWR appears relevant. At most, about 2 dB is recoverable so that the design for vertical polarization can be made to approach isotropic gain. For horizontal polarization the average gain can be improved to an average value of about -3 to -4 dB. As an alternative the design can be re-configured to enhance horizontal gain (i.e., unequal power split) which should lead to about - 2 dB for each polarization.

9.0 CONCLUDING REMARKS

The paper has shown, by measurements, what level of performance can be expected over a broad bandwidth from a small-volume-installation positioned under an aircraft .

When the installation space is constrained to approximately 0.1 x 0.1 x 0.5 wavelengths balanced average gains on the order of 0 to -3 dB should be realizable over 360° in azimuth by 0 to -30° in elevation.

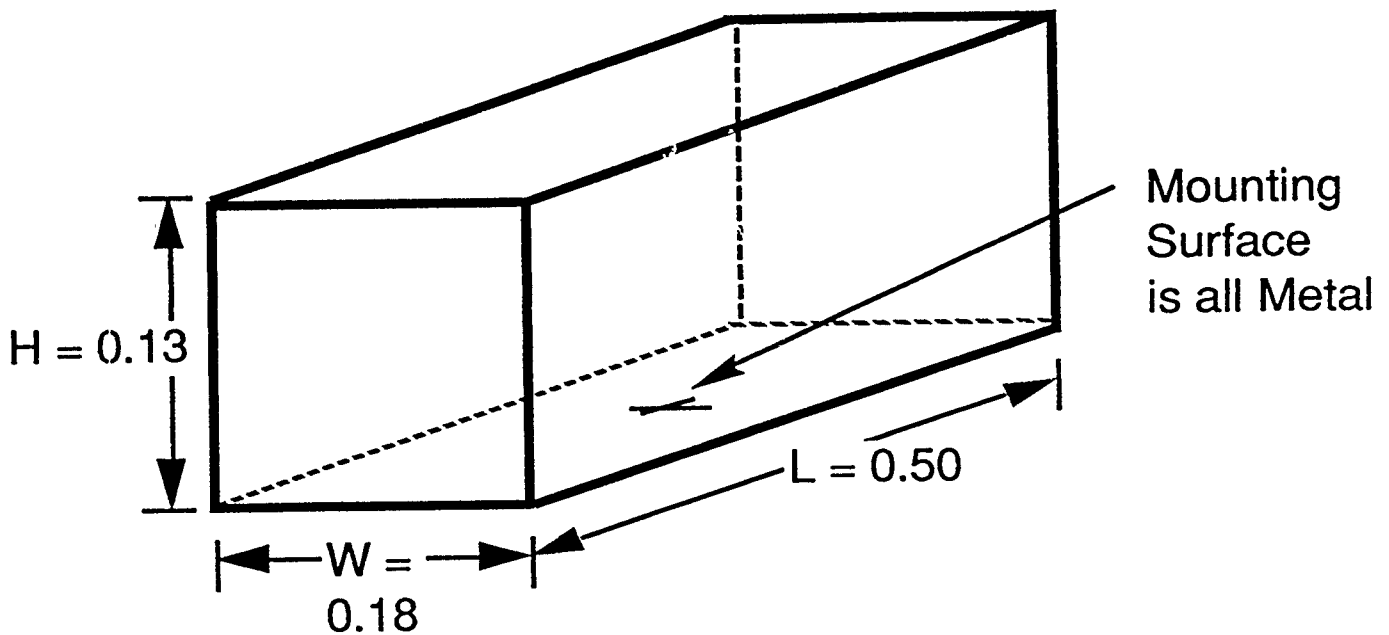

Figure 1. Installation Space in Wavelengths at F_{LOW}

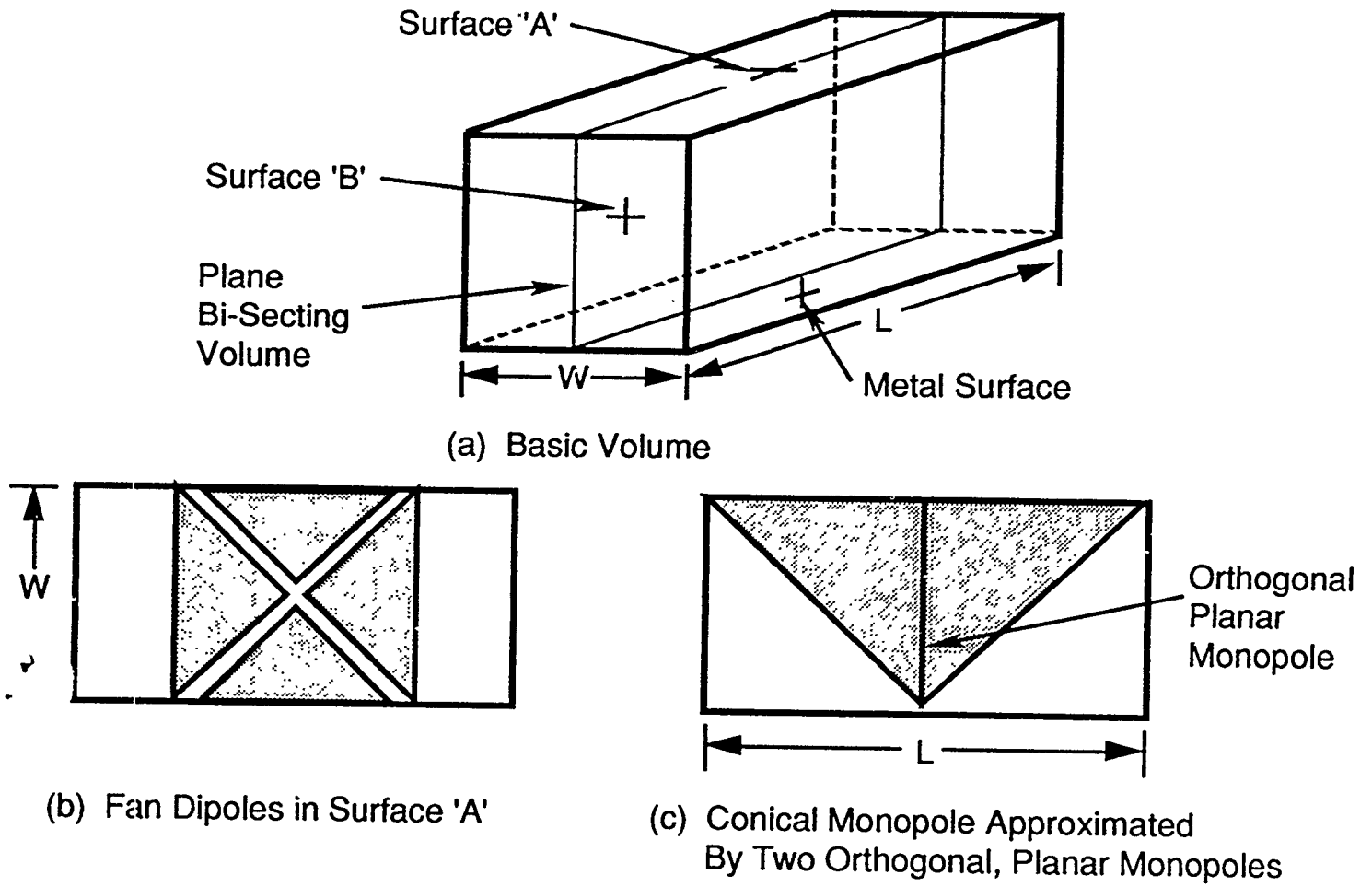

Figure 2. Antenna Concepts

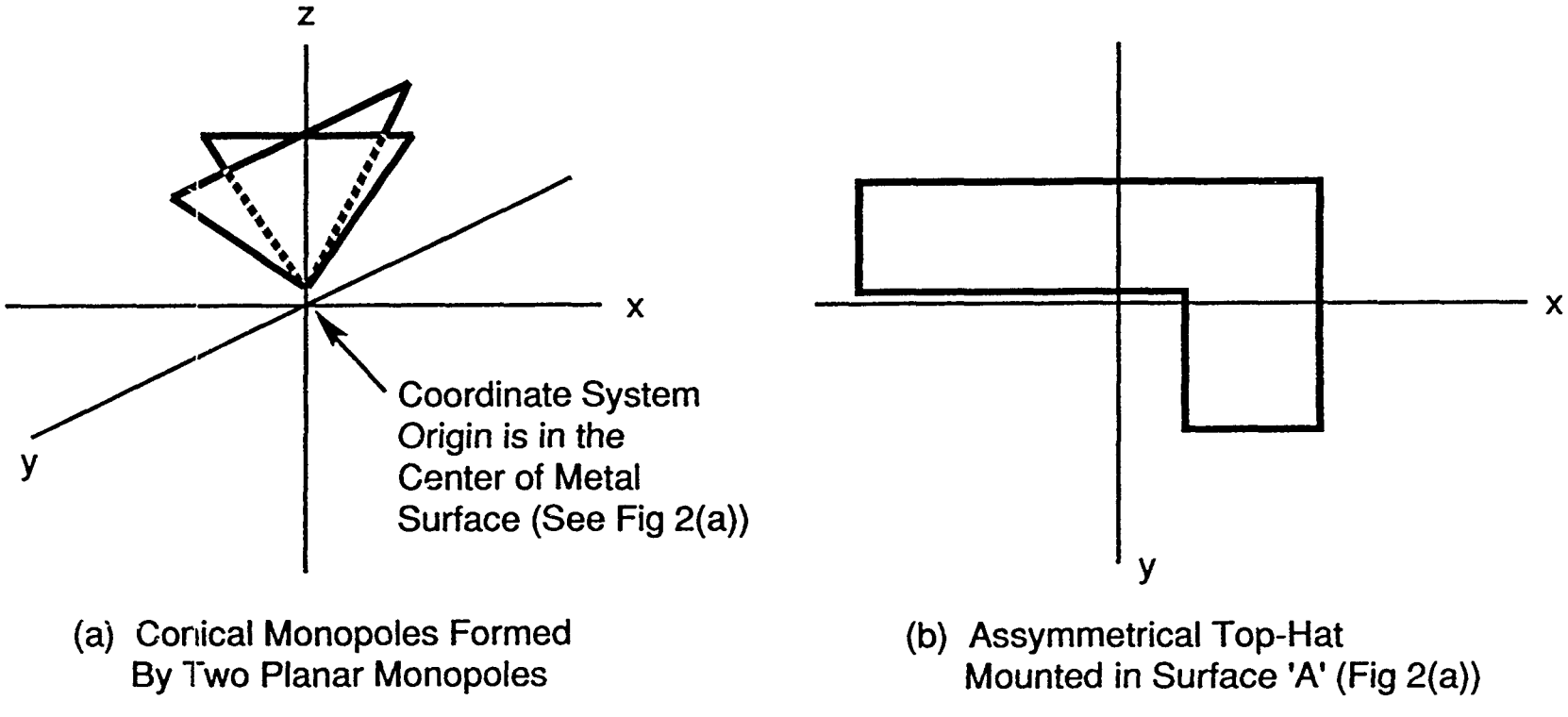

(a) Conical Monopoles Formed By Two Planar Monopoles

(b) Assymmetrical Top-Hat Mounted in Surface 'A' (Fig 2(a))

Figure 3. Conceptual Details of Integrated Antenna

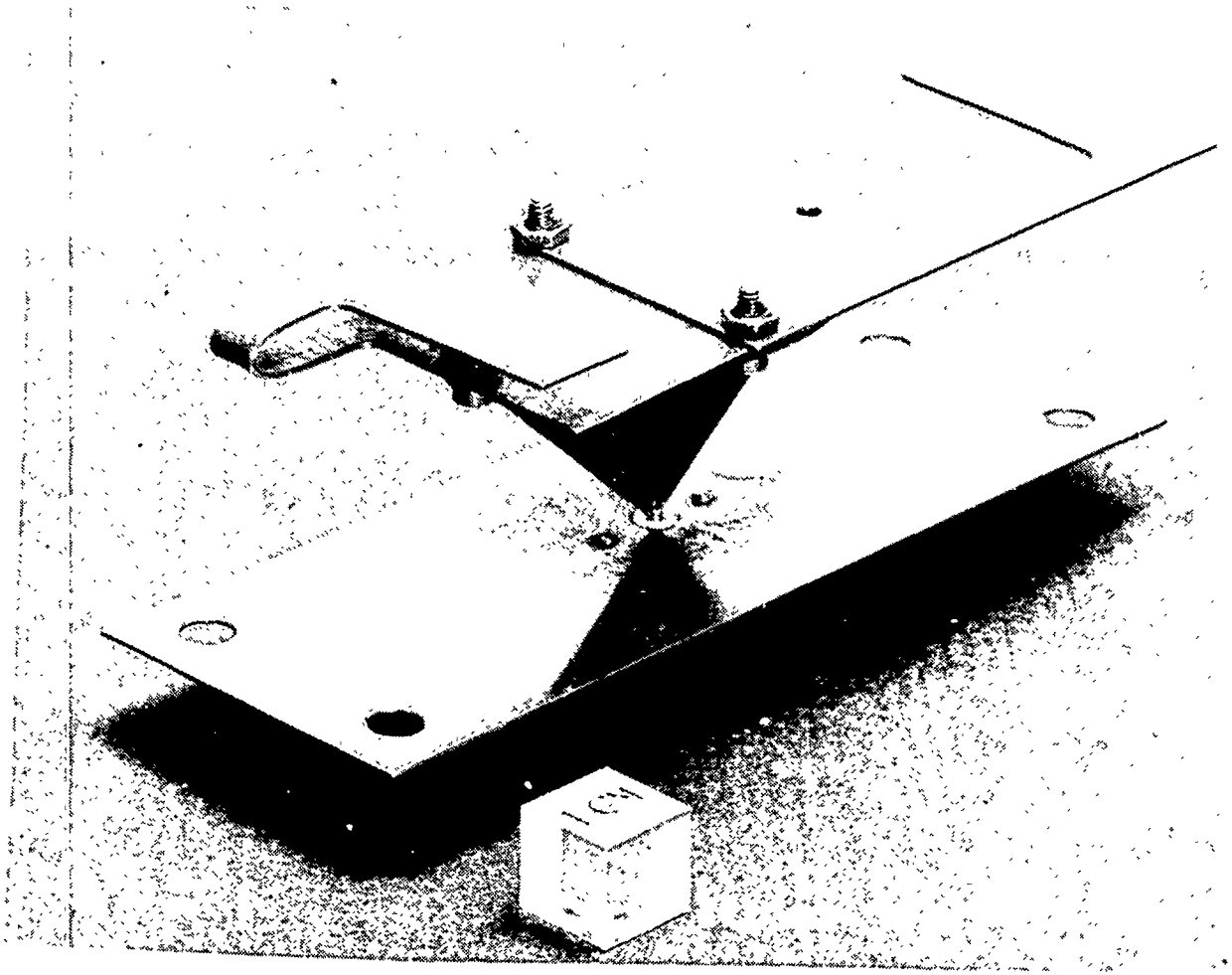

Figure 4. Test Model

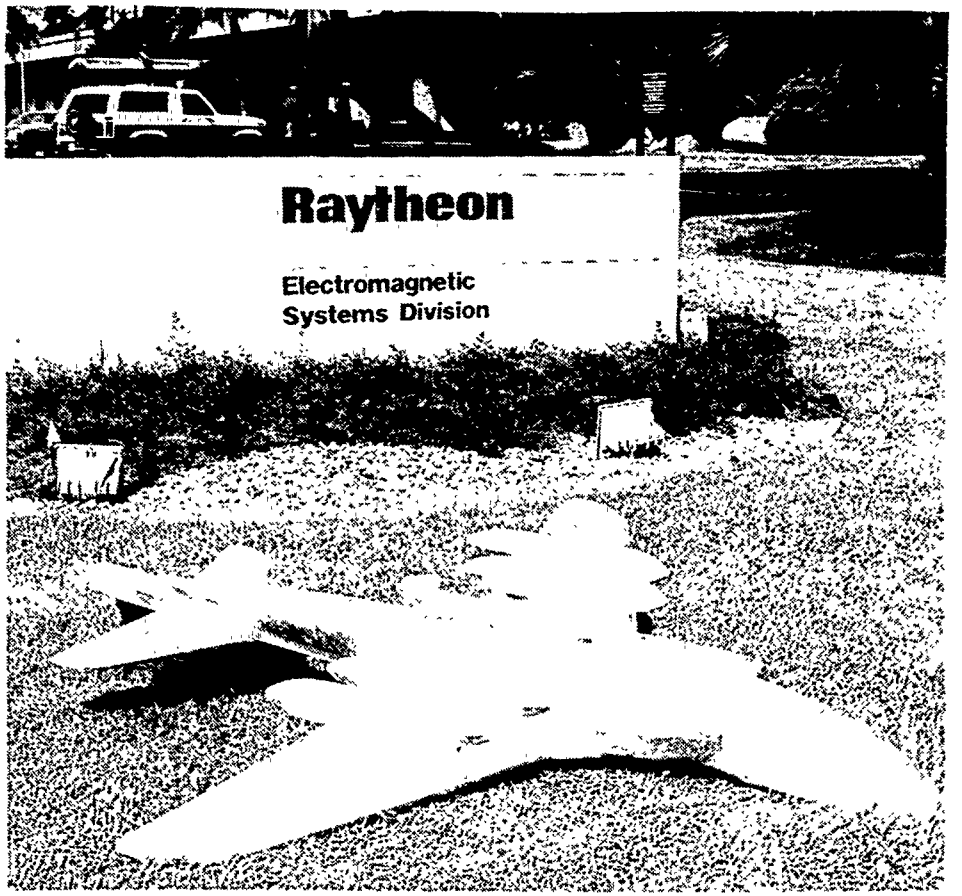

Figure 5. 1/10 Scale Aircraft (Antenna Installed)

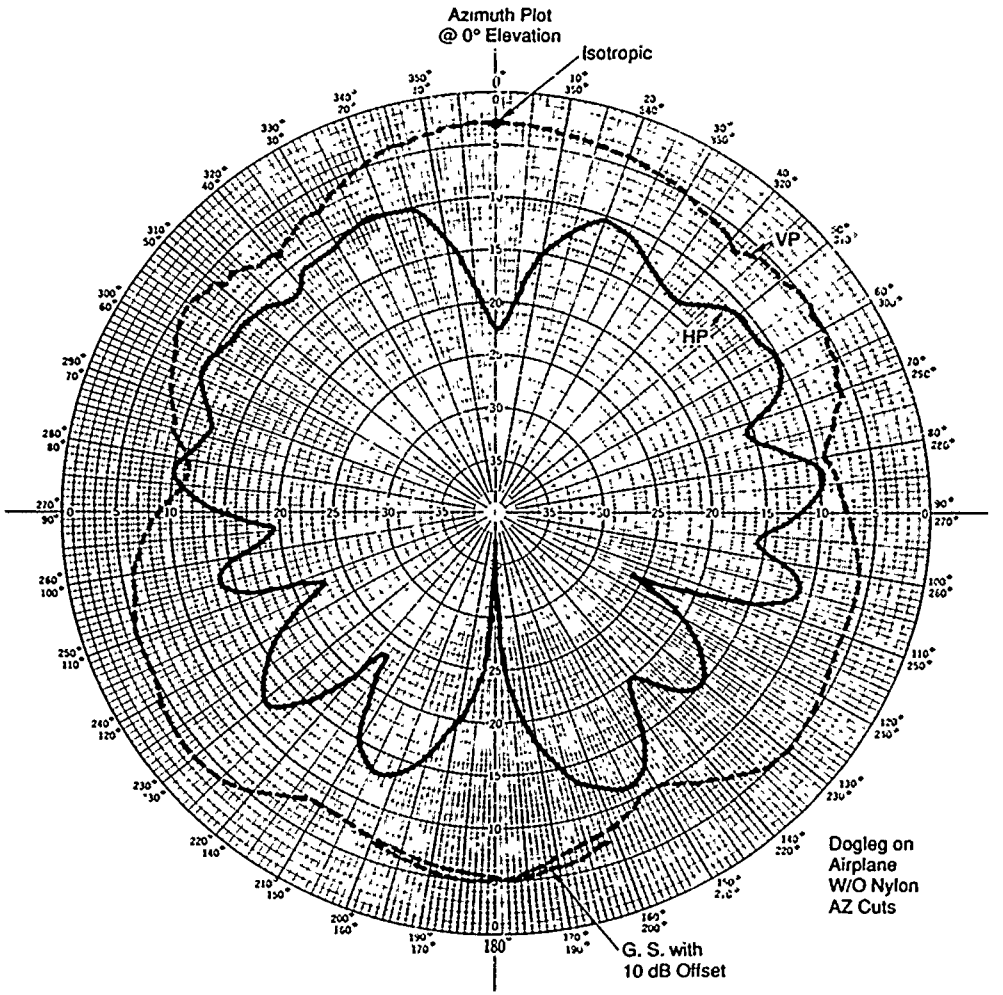

Figure 6(A). Azimuth Pattern, 0^{o} Elevation-plane, Two Polarizations

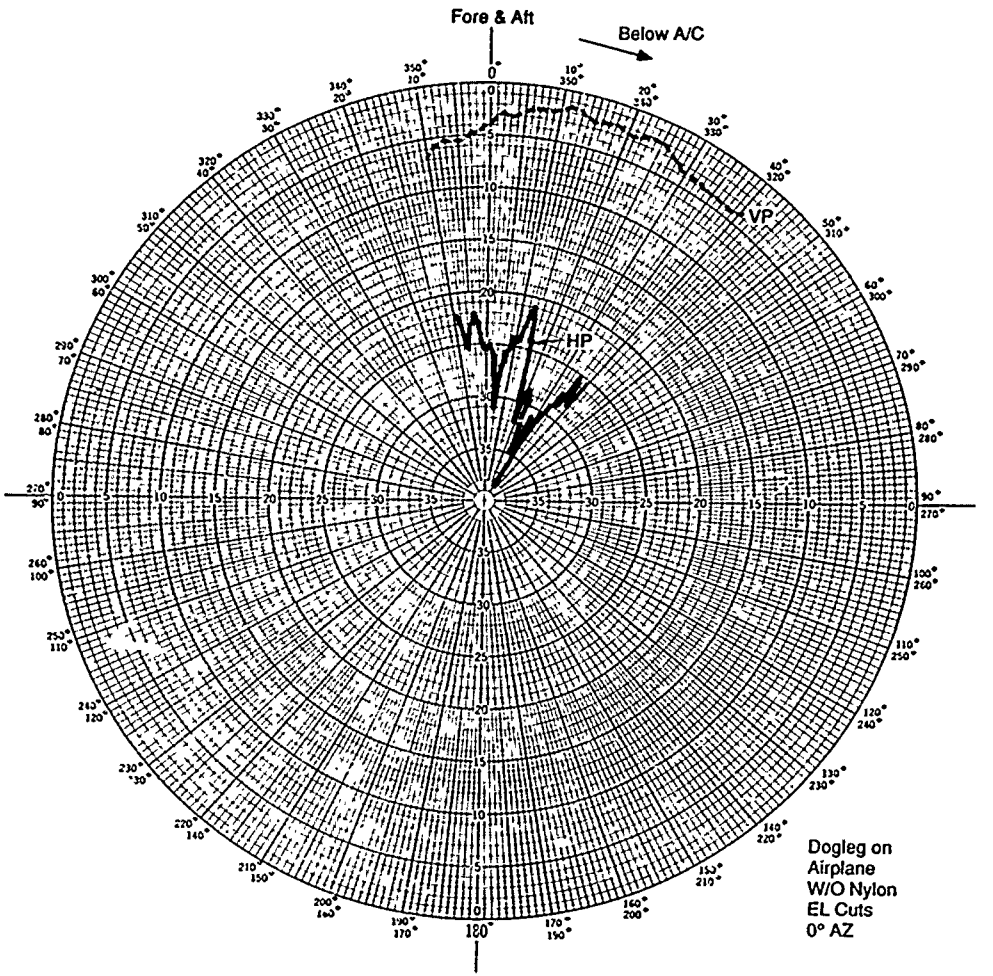

Figure 6(B). Elevation Patterns, Two Polarizations

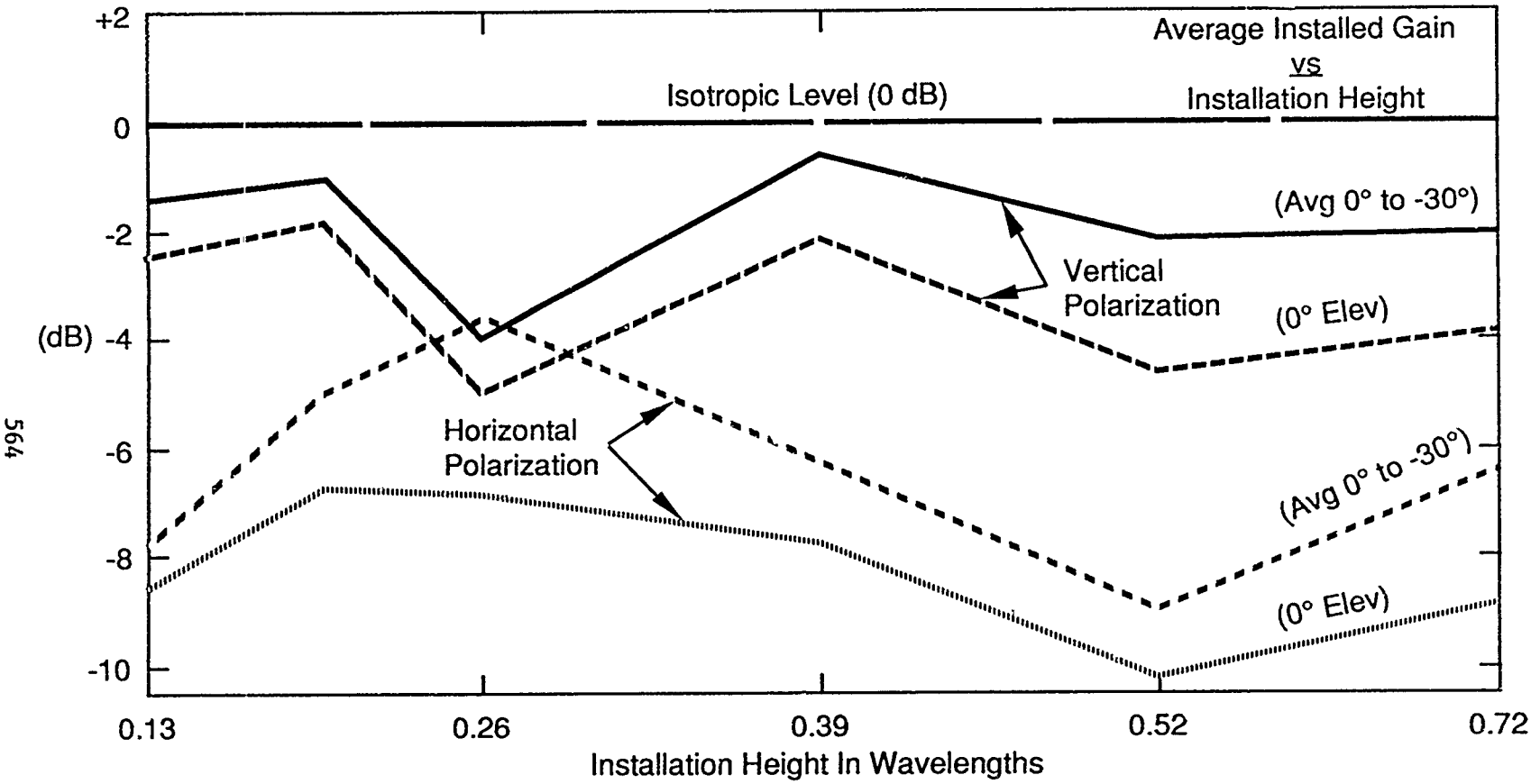

564

Figure 7. Average Installed Gain versus Installation Height

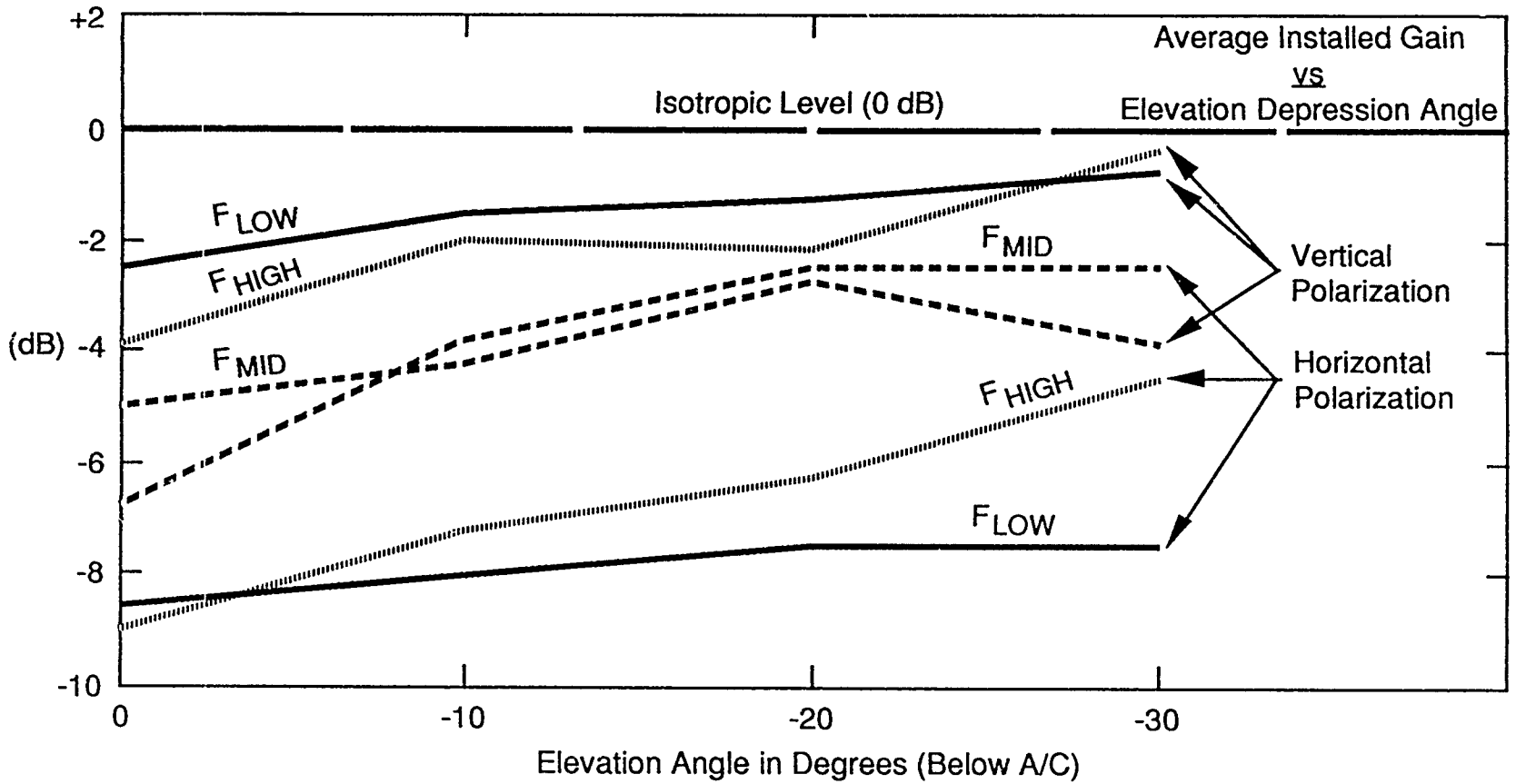

Figure 8. Average Installed Gain versus Elevation Depression Angle

APPENDIX A

LEVEL 1 - UNINSTALLED PERFORMANCE

This appendix presents a brief summary of tests for the dual-polarized antenna before installing on the aircraft.

Figure A1 shows return loss for the dual-polarized antenna. Here, the return loss is typically below -7 dB except at the lower frequencies where the loss approaches -4 dB at F_{LOW}. Thus over most of the band a transmission efficiency of better than 80% results.

Figure A2 shows typical the azimuth coverage for two polarizations. Here, the test frequency corresponds to upper mid-band and the gains for each polarization are referenced to a gain-standard level as indicated.

Figure A3 shows azimuth coverage for two polarizations for a -30° comic taken parallel to the azimuthal plane. Somewhat higher response, as expected, is evident for horizontal polarization than shown in Figure A2.

Figure A4 shows a compendium of gain plots taken to establish expected gain for this type of antenna. All of these models were symmetrical in construction and, as such, represent the achievable gains for vertical polarization. Using the data

from the VSWR plot and estimating the radiation efficiency for the antennas the following gain tally results:

1. For one antenna tested, height equal to 1/12 wavelength the measured gain was -2.9 dB.

2. The theoretical gain was about +3dB.

3. The difference is about 6 dB.

4. The VSWR transmission loss was approximately 3 dB.

5. The radiation efficiency was computed as 50% or -3 dB.

6. Thus the sum of the VSWR and radiation efficiency yield 6 dB which is in good agreement with the difference noted in step 3.

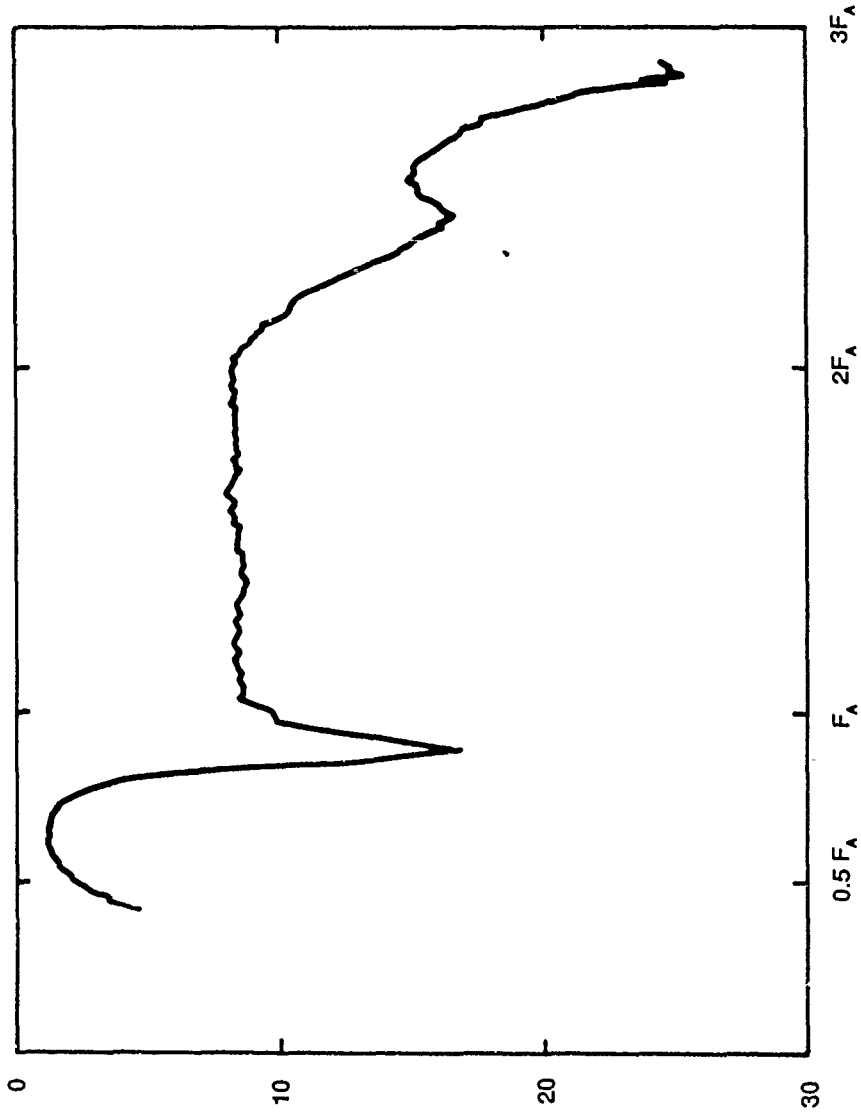

Figure A1. Return Loss 60/90 With 2 Doglegs

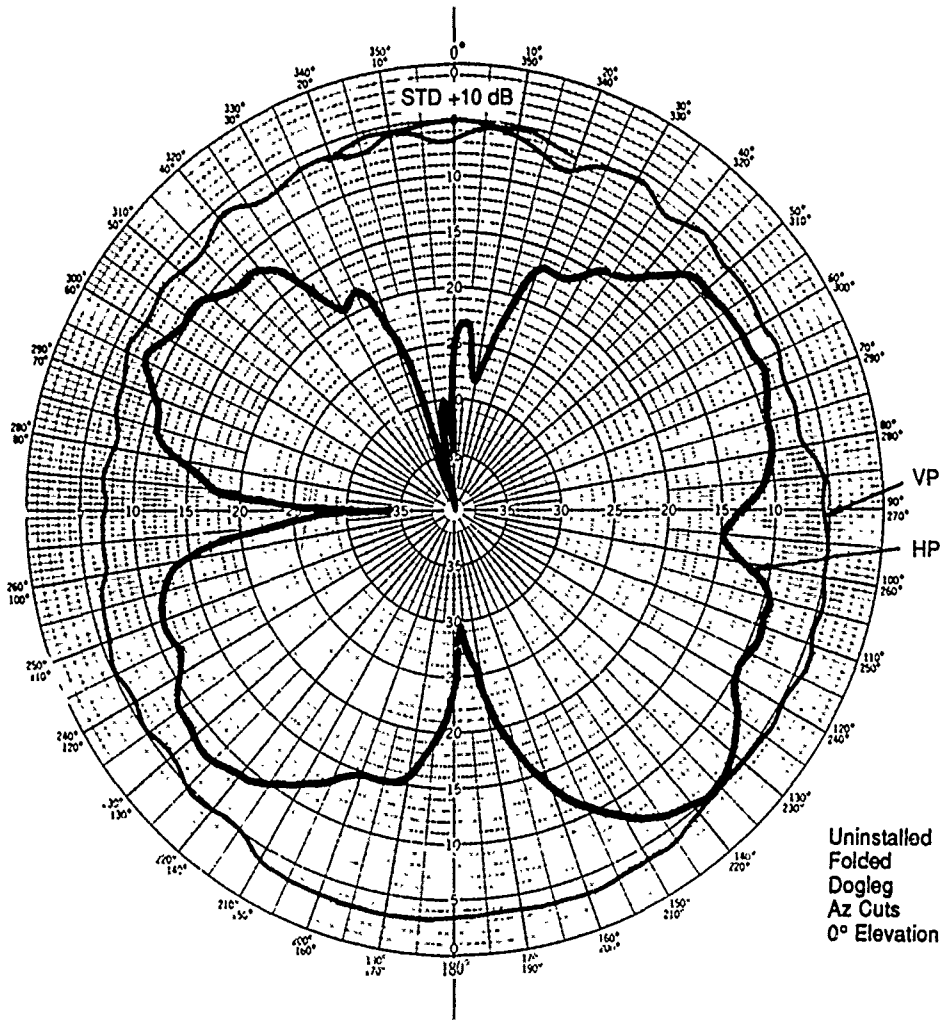

Figure A2. Azimuth Patterns, Two Polarizations (0^{o} Elevation)

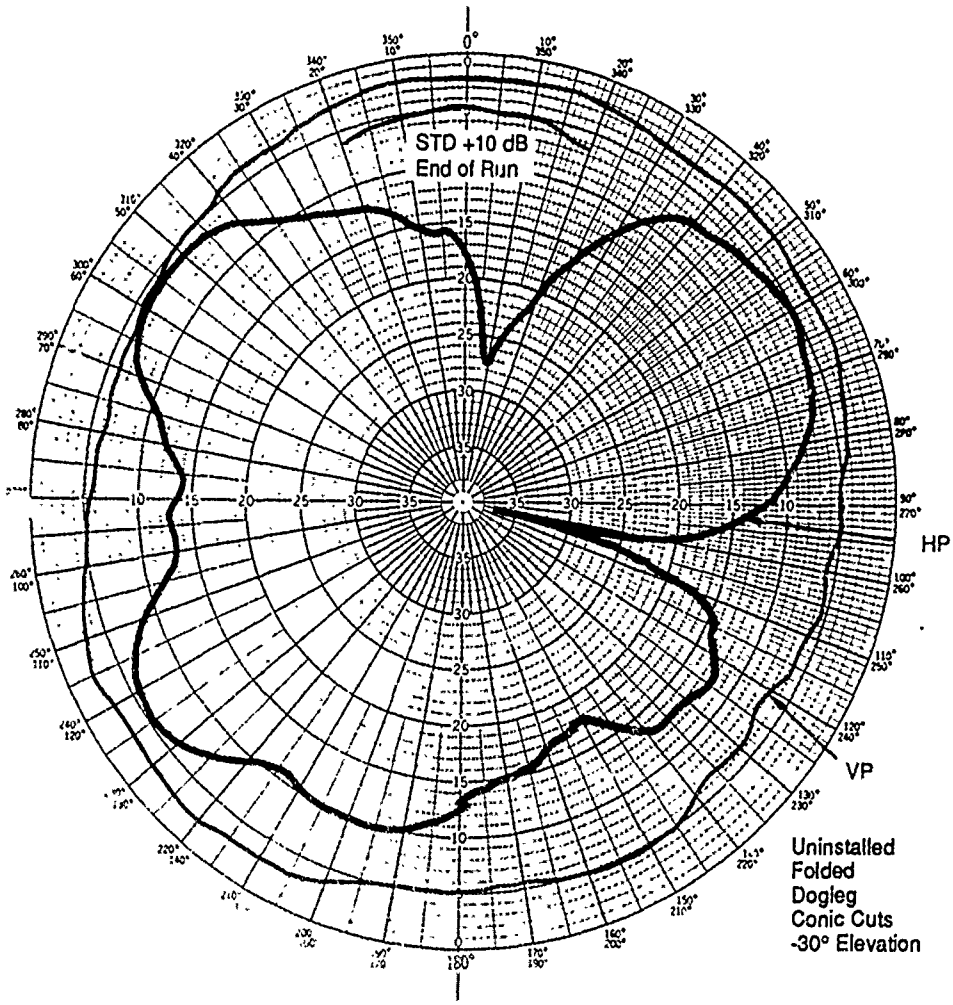

Figure A3. Azimuth Patterns, Two Polarizations (-30^{0} Conic)

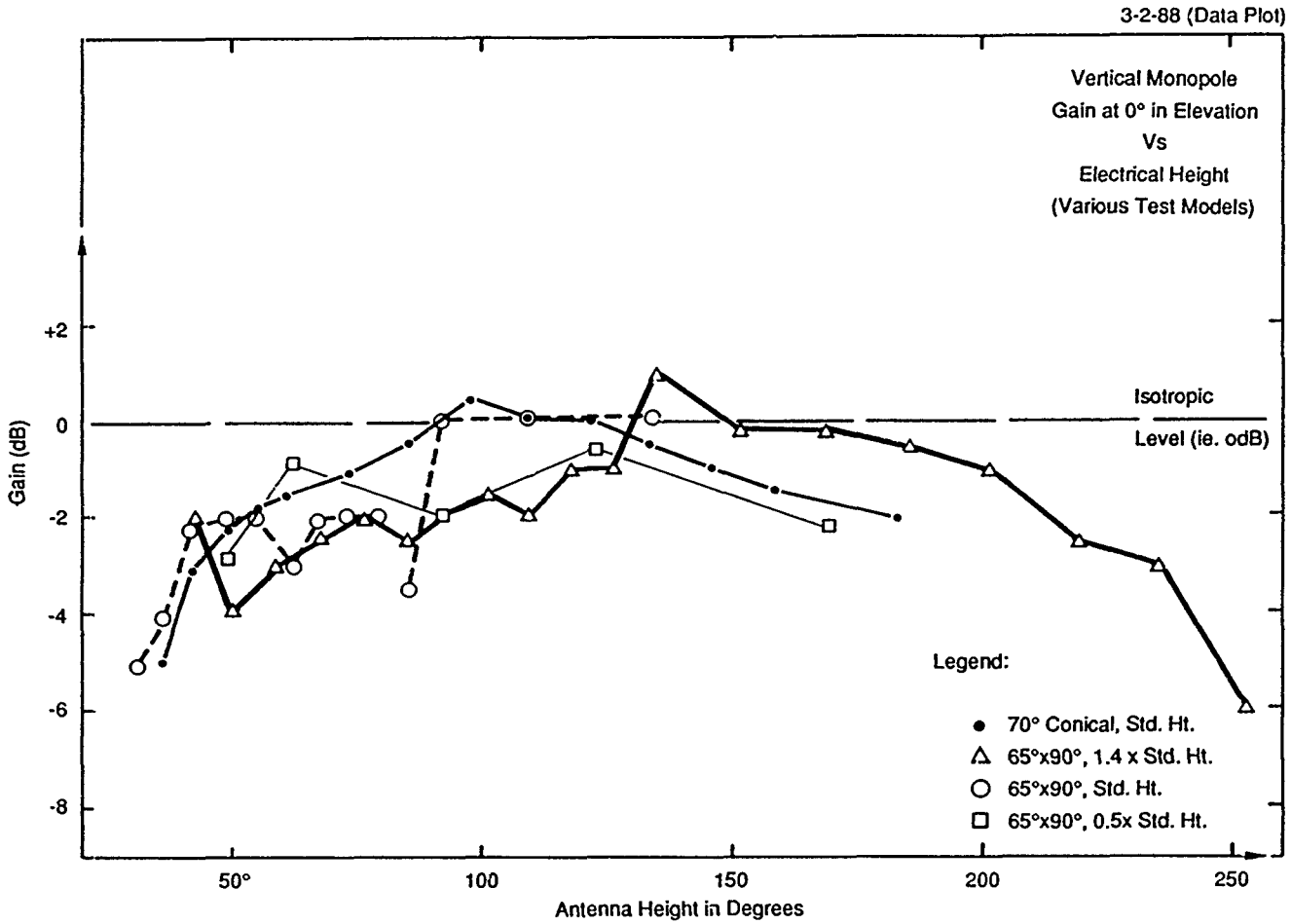

Figure A4. Vertical Monopulse Gain at 0^{o} in Elevation vs Electrical Height (Various Test Models)

POLARIZATION DETERMINATION IN A DF SYSTEM AT MM WAVELENGTHS WITHOUT A ROTARY JOINT

by
Harry B. Sefton Jr.
Director Advanced Programs

PRESENTED AT THE
1989 SYMPOSIUM ON ANTENNA APPLICATIONS

SPONSORED BY THE
ELECTROMAGNETICS DIRECTORATE
ROME AIR DEVELOPMENT CENTER
HANSCOM AIR FORCE SYSTEMS COMMAND
AND
ELECTROMAGNETICS LABORATORY
UNIVERSITY OF ILLINOIS

20-23 September 1989
Robert Allerton Park
Monticello, Illinois

A TECH-SYM COMPANY
9324 Topanga Canyon Boulevard
Chatsworth, California 91311

POLARIZATION DETERMINATION IN A DF SYSTEM AT MM WAVELENGTHS WITHOUT A ROTARY JOINT *

Harry B. Sefton Jr.

ABSTRACT

With wider use of the mm bands 18-26 and 26-40 GHz, it is only natural that the surveillance community would wish to detect, locate, and characterize such emitters. The characteristic which this paper addresses is the determination of the emitted polarization as part of the Direction Finding (DF) process. In response to this challenge, a technique of polarization identification in the mm wave bands was devised by the writer, and implemented by TECOM as part of production of 1-40 GHz spinning direction finding systems. The technique is based on the use of orthogonal grid sets which rotate synchronously with a 45° inclined electromagnetic mirror in such a manner as to act as polarization filters for pairs of receiving horns positioned behind the grids. System test results of actual hardware, taken inside an A-sandwich radome, show identification of the correct emitted polarization with a margin of 12-20 dB across the subject mm wave bands.

1. INTRODUCTION

TECOM Industries has been a leading supplier of wideband direction finding systems, up to 3 GHz, consisting of a shaped ELPAR reflector and feed, a rotator and a controller. (The ELPAR reflector has an ELliptical shape in elevation and a PARabolic shape in azimuth, producing a vertically oriented fan beam.) The elliptical contour results in a defocused elevation beamwidth whose asymtotic value at the high end of the band can be adjusted to any

* The subject of U.S. Patent No. 4,831,384 dated May 16, 1989

convenient values, typically 15° or 35°, to receive signals from both airborne and ground emitters. With a conventional parabolic contour in azimuth, the energy is focused for increased gain and a narrow beamwidth so as to permit precise determination of line-of-bearing to the emitter. Using multi-octave feeds, such as log periodic dipole arrays or cavity backed spirals, having typical bandwidths of 1.0 to 18.0 GHz, the energy from the spinning reflector/feed antenna subsystem is routed through a dc to 18.0 GHz coaxial rotary joint to the base of the pedestal.

To add the mm wave bands of 18-26 and 26-40 GHz to such a spinning DF system we are faced with the non-availability of critical components. Although single channel coaxial rotary joints operating from dc to 40 GHz exist, there are no dual channel joints and no broadband feeds covering 1.0-40 GHz. Any proposed configuration using separate antenna bands, such as 1-18, 18-26, and 26-40 GHz, in order to circumvent the lack of a full range antenna, requires that the outputs either be multiplexed in frequency or sequentially sampled in time due to the restriction of a single channel rotary joint.

For frequency separation, two triplexers are required -- one before and one after the rotary joint. This results in disadvantages which are a 9-11 dB loss at crossover, along with 1-2 dB in-band insertion loss and high cascaded VSWR ripple effects.

If, on the other hand, the outputs from the three bands are time sampled through a single channel rotary joint, many emitters may be lost due to such a time sharing bottle neck. If dual polarized antennas are employed in the mm wave bands the effects of time sharing further reduces the viewing time for 1-18.0 GHz frequencies due to such sharing. The switching configuration also requires that slip rings be added to furnish power to the coaxial or waveguide switches.

What is clearly needed is a configuration that embodies a means of providing the DF function, including polarization determination, in the mm region that does not require the use of rotary joints or multiplexers to separate the 18-26 and 26-40 GHz bands. Use of an all waveguide system, where feasible, would greatly reduce losses and improve the amplitude of signals delivered to the receiver.

2. SYSTEM DESIGN

In 1986 the writer designed and had built such a system for resolving emitter polarization in the mm wave bands of 18-26 and 26-40 GHz by piggy-back of the mm wave system on an ELPAR reflector/feed system operating from 1-18 GHz.

Figure 1 shows the principal components forming the polarization-sensitive microwave radiation receiver. A horizontal, circular filter disk is mounted for rotation in the sense of arrow "R", about a vertical axis of rotation A-A'. The disk comprises a thin membrane material that is substantially transparent to radiation in the microwave frequency band. (It should be noted that the terms "vertical" and "horizontal" in this context need not refer to gravitationally defined directions -- merely to orthogonally oriented axes.)

The filter disk is subdivided into 3 concentric regions. The outer 2 are defined by a plurality of parallel conductors attached to the disk, and the central region is clear. The sets of parallel conductors in the outer region are orthogonal to the array of similar parallel conductors in the inner region. Microwave receiver horns are statically positioned above and close to the surface of the 3 concentric regions of the disc.

Also mounted for rotation on the axis A-A' is a flat mirror so constructed that it acts as an electro-optical reflector. In Figure 1, the mirror is a planar ellipse, mounted at substantially 45° with respect to a horizontal plane orthogonal to the axis of rotation A-A'.

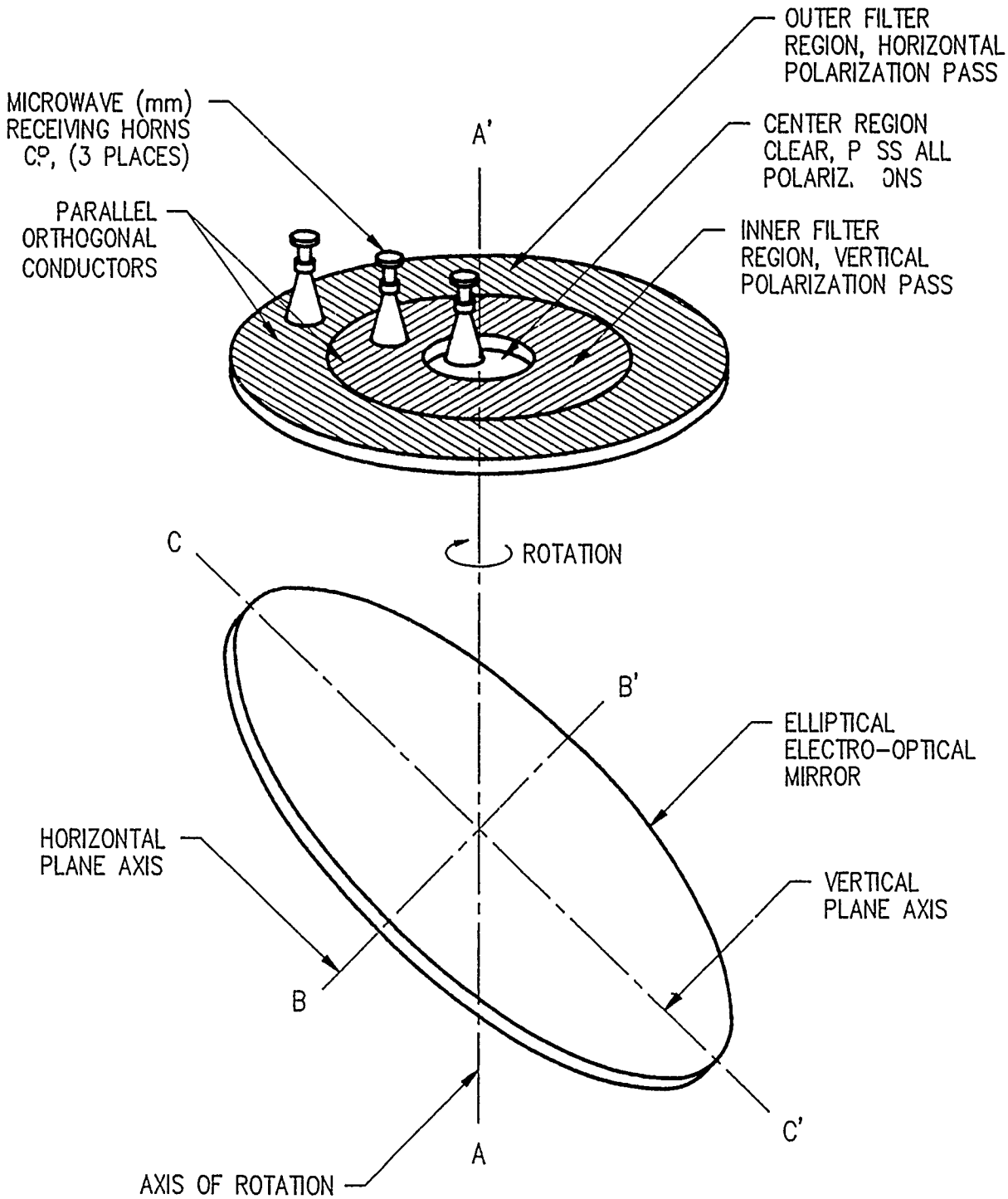

FIGURE 1. CONCENTRIC DISK DESIGN WITH GRIDDED AREAS, RECEIVING HORNS, AND 45° MIRROR

The mirror is synchronously driven with the filter disk, so that a horizontally aligned minor axis B-B' of the mirror remains parallel, at all angular positions of rotation, with the array of parallel conductors defining the inner filter region, and an array of conductors in the outer filter region, aligned with vertical elements in the mirror, including major axis C-C' therein.

The mirror is shown in Figure 1 as lying below the filter disk and being inclined at substantially 45° so as to reflect a horizontally incident beam of radiation on its surface vertically upward through the filter disk.

As radiation originating on the horizon is reflected through the filter disk, vertically polarized components therein will tend to pass through the conductor array of the inner region with little attenuation, and horizontally polarized components of the incident microwave beam will readily pass through the outer region. The converse, in both regions, is not so and radiation with electrical field vectors parallel to the array of conductors will be greatly reflected/attenuated. Consequently, the microwave receiving sensors statically positioned above the filter regions will be exposed to two orthogonally polarized components of the incoming beam.

Measuring the signal strengths collected by these receivers and comparing them will clearly indicate the relative polarization of the received signal. (The ratio of the signal strengths to which the receiver horns are exposed is independent of any angular differential between them.) They are exposed to radiation which, although derived from a signal with a particular polarization plane, varies in direction of polarization as a result of the rotation of the mirror and of the filter disk. Consequently it is important that these sensors be insensitive to such variation, and be selected from the class of microwave receivers (e.g., antennas) having circular polarization and low axial ratios.

The central region of the disk, with no obstacle to the transmission of any component in the signal reflected from the mirror, and the two outer regions, defined by arrays of orthogonal grid lines, along with the third microwave receiver sensor complements the filter, permitting the measurement of the total signal emanating from the source being analyzed.

Figure 2 shows the piggy-back dual range MM wave system, atop a conventional ELPAR antenna reflector, and a planar mirror. The antenna and the mirror are joined by supports and both rotate about vertical axis A-A'. The mirror is secured to the rear of the ELPAR reflector and is exposed to any incoming microwave beam during a complete rotation of the sensor assembly around the axis A A'. Rotational movement for the ELPAR antenna and mirror is derived from an azimuth rotator, which impels the turntable onto which the antenna, mirror, and antenna feed are mounted.

Incident electromagnetic radiation striking the focusing surface of the ELPAR reflector is collected by the feed, located at the focus of the parabolic curve defining the horizontal shape of the surface. The collected electromagnetic signal is transferred to an output port via a coaxial transmission line, with a rotating coaxial joint installed into the bearing supporting the turntable.

Due to the synchronization in the rotational motions of the mirror and of the filter disk, the relative strengths of the three signals derived from the three receiver horns do not vary due to polarization as the rotator impels the mirror and shaped reflector into its circulatory motion. The strength of the signal will be greatest when the mirror axis B-B' is normal to the point of origin of the incoming microwave beam.

The microwave energy captured by the receivers is suitably directed toward analytical instrumentation -- capable of determining the relative strengths of the three signals.

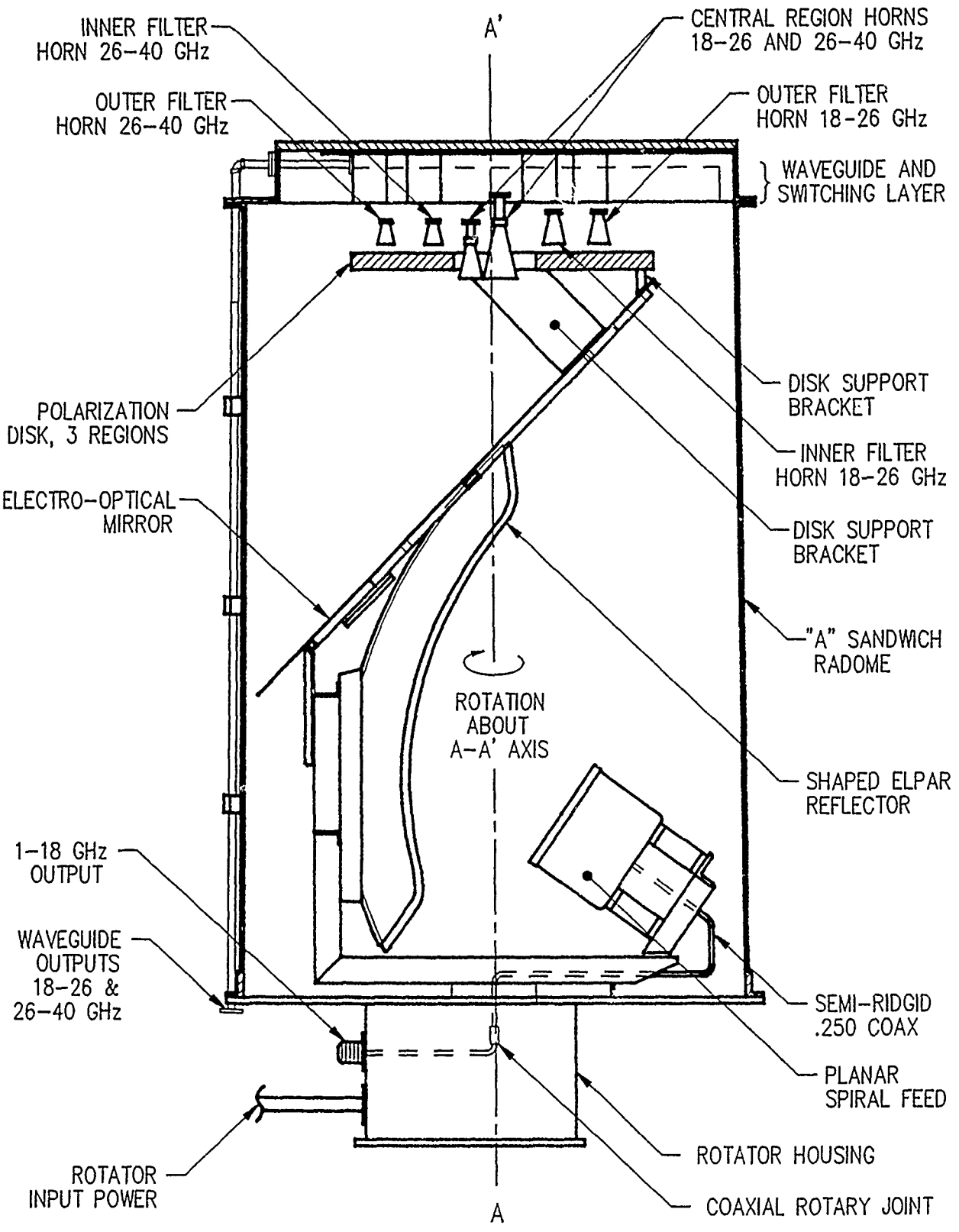

FIGURE 2. ELEVATION VIEW OF POLARIZATION DISK, 2 BAND FEED HORNS, 45° MIRROR AND ELPAR REFLECTOR AND FEED

Figure 3 shows in detail the filter disk, the adjacent, concentric regions formed by parallel conductors printed onto the surface of disk in mutually orthogonal arrays and the 6 receiving horns behind the three zones of the disk. It is enclosed in a stationary housing constructed from a dielectric material that forms the top of the cylindrical radome.

One pair of microwave receiver horns is mounted onto the inner surface of the cover and project downward through the clear center region of the disk and face, the reflecting surface of the mirror. The two microwave horns are circularly polarized and are equally sensitive to microwave radiation in all polarized states, except for opposite-sense circular polarization. Suitably, the smaller horn is sensitive to the 26-40 GHz band, while the second horn is sensitive in the 18-26 GHz band.

The outer region of the filter disk is surmounted by 2 horns (one each for 18 to 26 and 26 to 40 GHz), while the intermediate region is surmounted by an identical pair of horns. These horn pairs are best seen in Figure 3. These horns are also supported by the cover and are positioned with the lips of their sensing horns proximate to, but not touching, the moving surface of the filter disk. The energy derived from an incident microwave beam reflected by the mirror into the horns is conveyed through a network of wave guides and cavity switches to any desired measuring equipment, such as a mm wave receiver subsystem, for further processing.

3. PRODUCTION HARDWARE

A series of over 13 DF sets were fabricated and tested using the polarizing discrimination scheme described, for the mm bands of 18-26 and 26-40 GHz.

Figure 4 is a photo taken looking down on the ELPAR and planar spiral feed to the back of which is mounted the mm wave mirror. Atop the assembly and perpendicular to the axis of rotation is the 3-zoned disk, the outer two zones of which consist of orthogonal sets of copper grids etched on a thin dielectric membrane. (Compare the photo with previous Figures 2 and 3.)

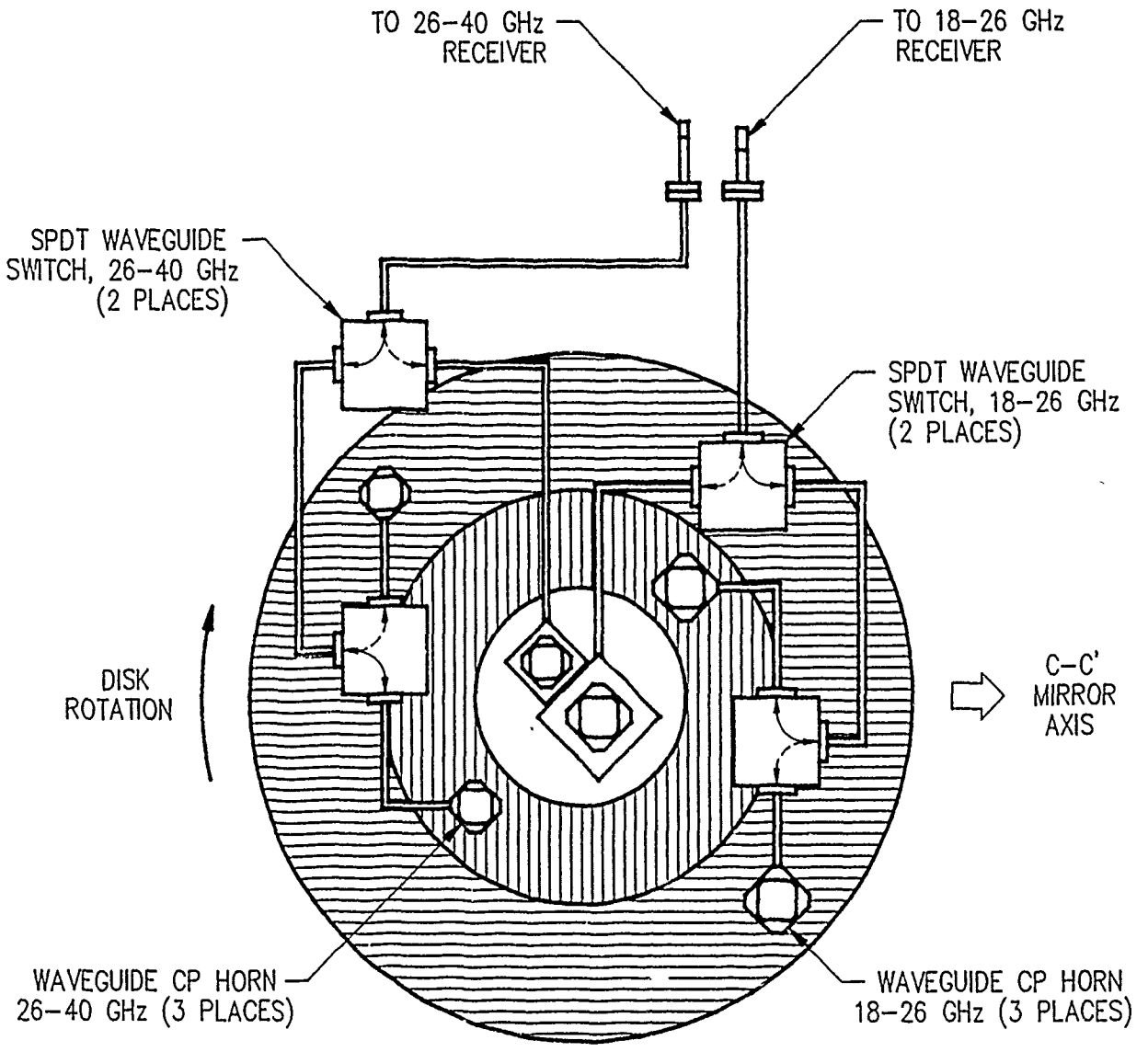

NOTE: WAVEGUIDE SWITCHES ALL SET FOR VERTICAL POLARIZATION BOTH BANDS.

FIGURE 3. PLAN VIEW OF FILTER DISK AND 2 BANDS OF RECEIVING HORNS WITH WAVEGUIDE SWITCHING AMONG 3 ZONES

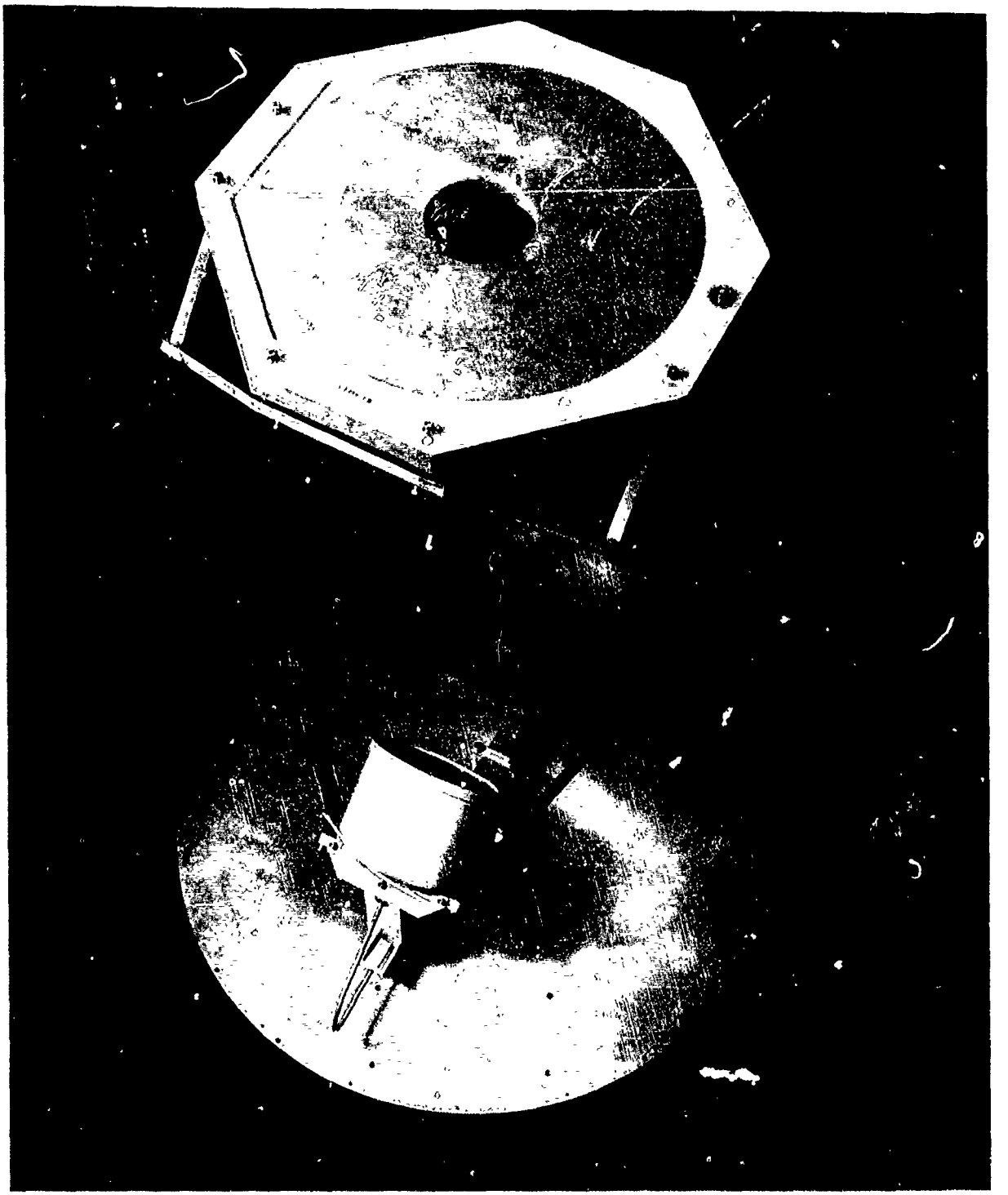

FIGURE 4. TOP VIEW OF 1-18 GHz ELPAR AND FEED SHOWING MM MIRROR AND 3 ZONED MEMBRANE WITH ORTHOGONAL GRIDS

Figure 5 is a photo of the 3 pairs of mm band horns wherein one pair (i.e., 18 to 26 and 26-40 GHz) are located in each of the 3 zones. Also note the waveguide switches and rigid waveguide transmission lines. In the production configuration, the base plate including all the waveguides and switches, less the apertures of the 3 pairs of horns, are covered with microwave absorber to suppress reflections from the mirror to mounting base. Such reflections can be modulated by the spinning mirror and ELPAR structures resulting in DF and processing degradations.

Figure 6 is an exterior view of the radome enclosed DF system operating from 1-40 GHz, with polarization sensing from 18-26 and 26-40 GHz. Note the positioning of the biconical omnidirectional intercept antennas mounted atop the radome. These TECOM standard products cover the same 1-18, 18-26 and 26-40 GHz bands as the DF system.

4. ELPAR PERFORMANCE, 1-18 GHz

The basic antenna subsystem consists of a shaped ELPAR reflector with a planar spiral feed covering the 1-18 GHz frequency range. Table 1 summarizes the performance measured for this 4.1 octave antenna.

Notice that this ELPAR reflector has an elevation beamwidth which converges to about 15° at the top of the band. The fact that the minimum value is 13.5° is accounted for by the original 15° design being based on a slightly reduced reflector height and log periodic dipole array feed.

5. POLARIZATION SENSING PERFORMANCE, 18-26 AND 26-40 GHz

Polarization sensing was measured extensively on the first three systems. Standard testing of VSWR, patterns, and gain were supplemented with swept ratios of co-polarization vs. cross-polarization outputs.

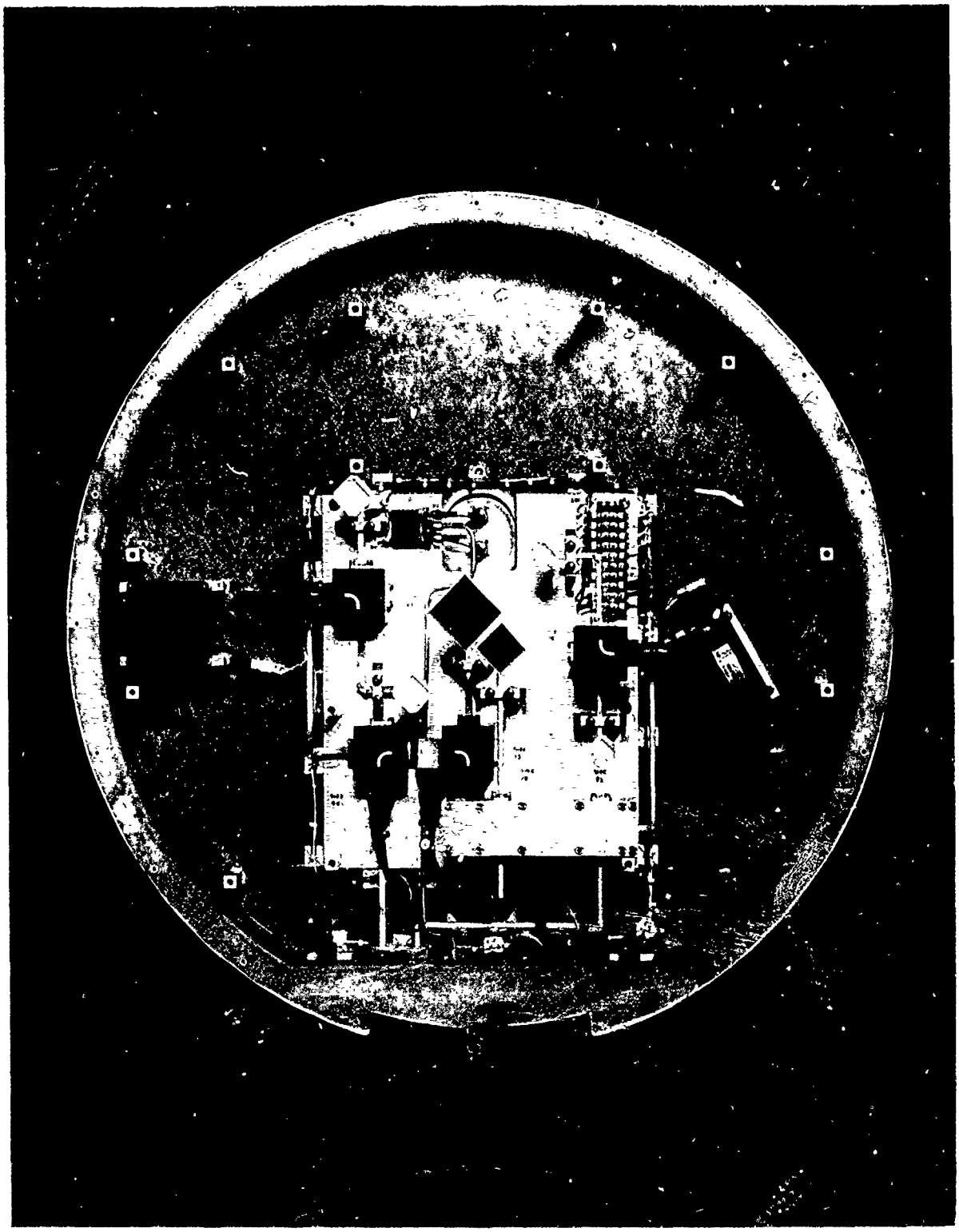

FIGURE 5. VIEW OF 3 PAIRS (18-26 AND 26-40 GHz) OF HORNS, EACH PAIR LOCATED WITHIN ONE OF 3 DISK ZONES

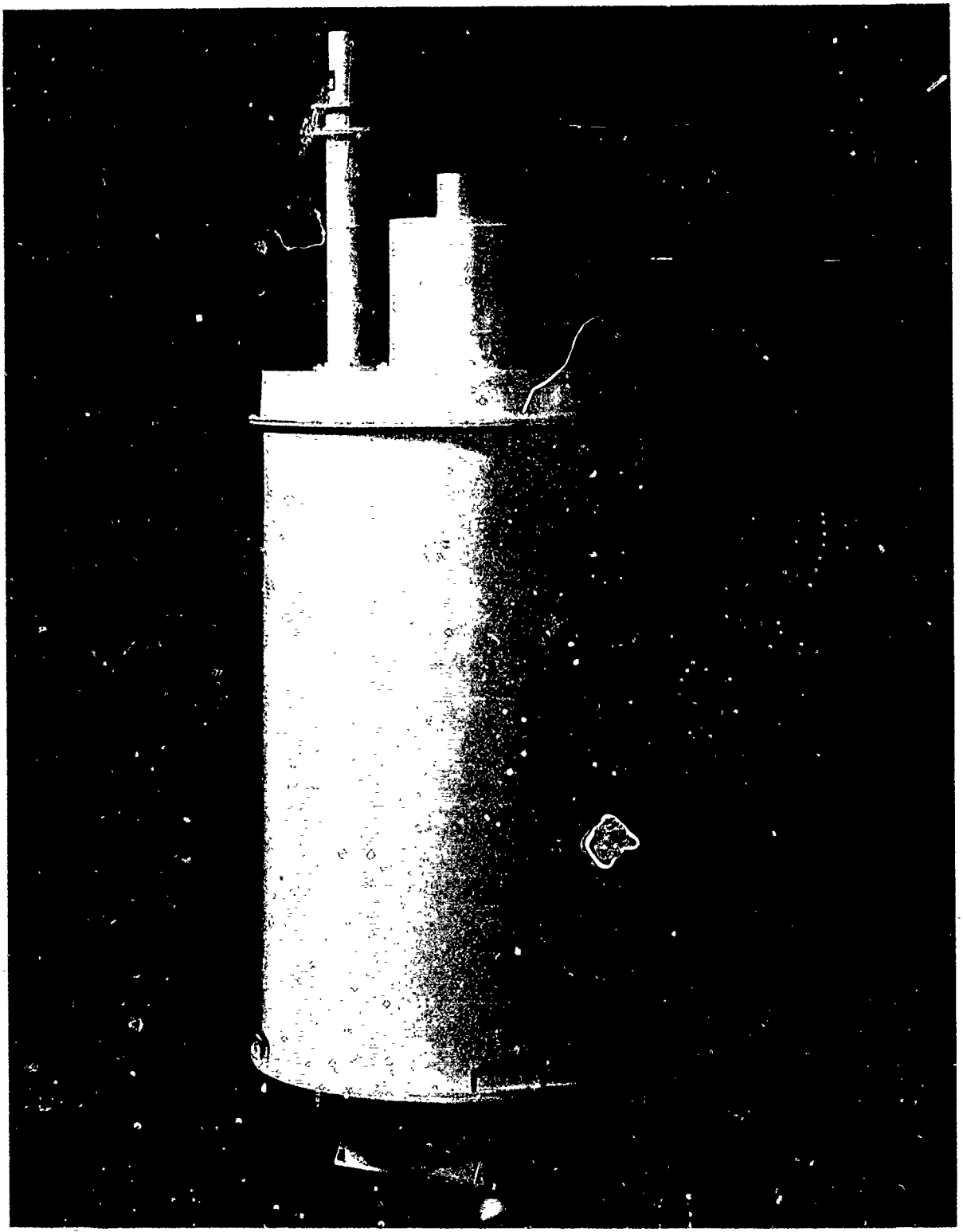

FIGURE 6. EXTERIOR VIEW OF RADOME ENCLOSED ELPAR AND MM DF/POLARIZATION SENSING. NOTE BICONICAL INTERCEPT ANTENNAS ATOP THE RADOME.

TABLE 1

SUMMARY OF 15° ELPAR PERFORMANCE

1 TO 18 GHz

Frequency, GHz:	1.0	2.0	4.0	8.0	12.0	15.0	18.0
Gain, dBic: (1) (2)	10.0	13.0	16.0	19.0	21.0	22.0	23.5
AZ Beamwidth, Deg.:	23.5	12.0	6.1	3.3	2.1	1.6	1.4
EL Beamwidth, Deg.:	24.0	15.7	15.2	15.0	17.0	13.0	13.5
Squint, Deg.:	.4	1.3	.5	.1	.1	.15	.15
Sidelobes:	12	15	16	16	14	13	14

NOTES: (1) Gain measured at feed.

(2) Polarization RHCP

(3) VSWR 2.0:1 maximum

(4) Reflector size 27" wide x 30" high

(5) Weight approximately 20 pounds

Figure 7 is a polar plot taken at 21 GHz, near the center of the lower mm band. On this single figure are plotted three separate patterns, with the radome in place, which are based on the incident polarization being vertical. The three patterns are:

- Patterns generated for DF through the clear zone of the polarization disk.
- Patterns generated from incident vertical polarization and the horizontal gridded annulus.
- Patterns generated from incident horizontal polarization and the vertical gridded annulus.

To avoid confusion between the three separate patterns the measurement of the DF pattern using the ungridded zone is shown oriented at 180° from the other two patterns. Note that the gain of this channel is greater than the gains for the two polarization sensing channels. Since the outputs of the two polarization sensing channels are shown aligned, as in normal operation, the ratio of desired to cross-polarization is easily seen.

Figure 8, similar to Figure 7, is a polar plot taken at 32 GHz, the center of the upper mm band. This plot also includes three separate patterns for no grid, vertical polarization, and horizontal polarization. As previously, the measurements were through the radome.

Figures 9 and 10 are swept plots from 18-26 GHz of the received levels for the two polarization outputs (i.e., vertical and horizontal) when the "mirror" is rotated to peak the beam in the direction of the emitting source. Figure 9 is for a transmitted polarization of vertical while Figure 10 is for a transmitted polarization of horizontal. These figures show the copolar signal to be 12-20 dB greater than the cross-polar signal.

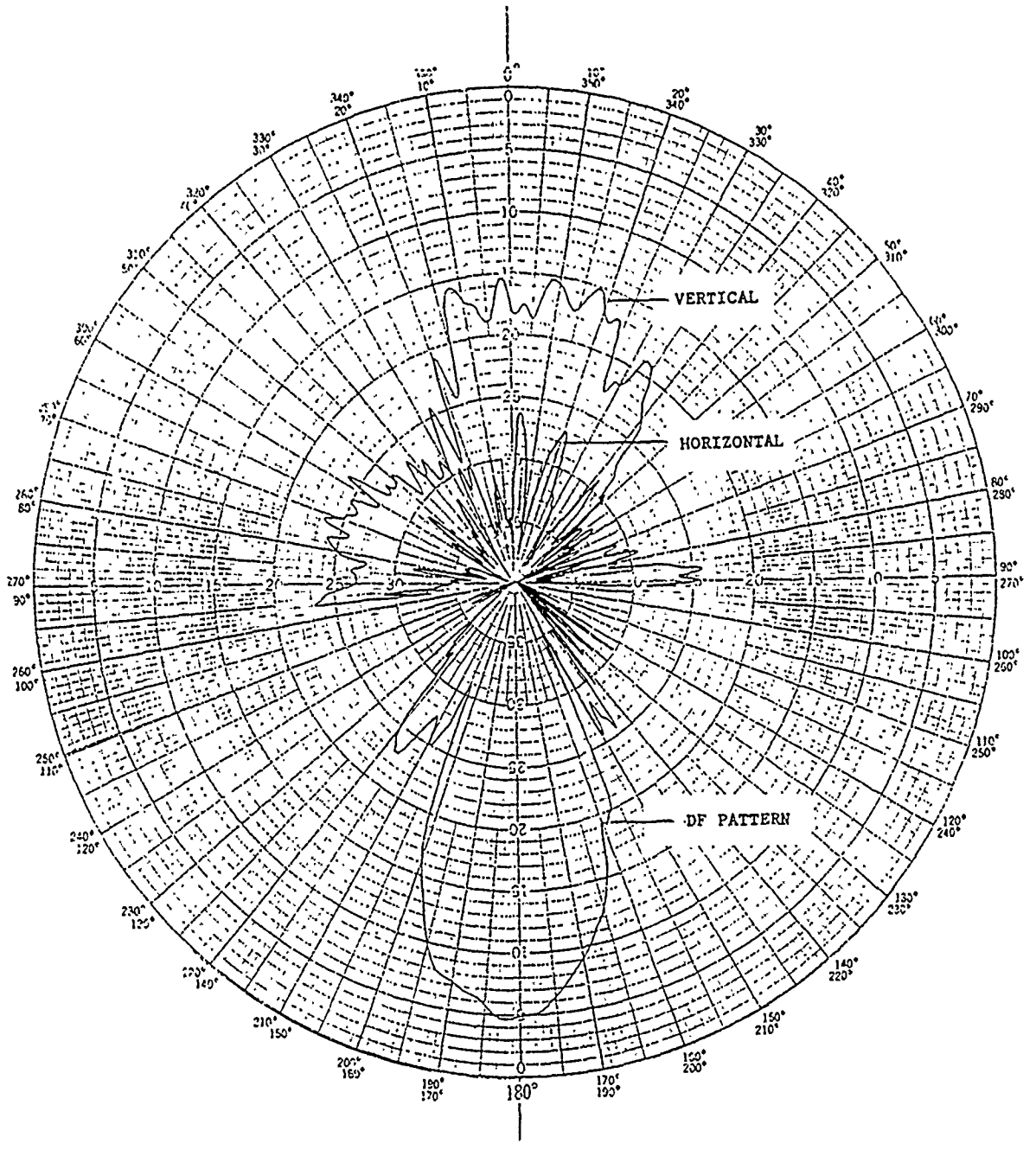

FIGURE 7. PATTERN AT 21 GHz FOR VERTICAL POLARIZATION SHOWING DF VERTICAL AND HORIZONTAL OUTPUTS

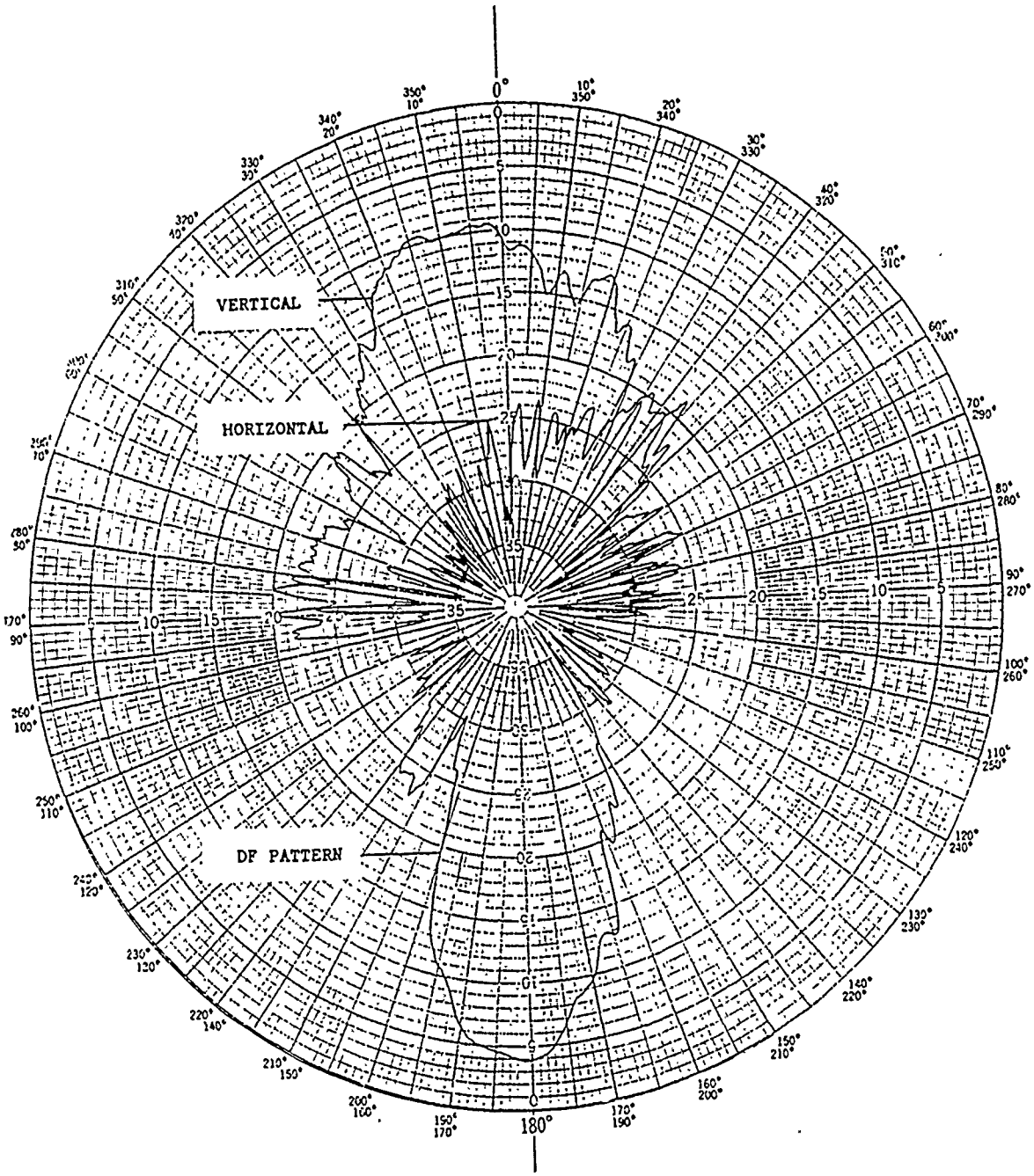

FIGURE 8. PATTERN AT 32 GHz FOR VERTICAL POLARIZATION SHOWING DF VERTICAL AND HORIZONTAL OUTPUTS

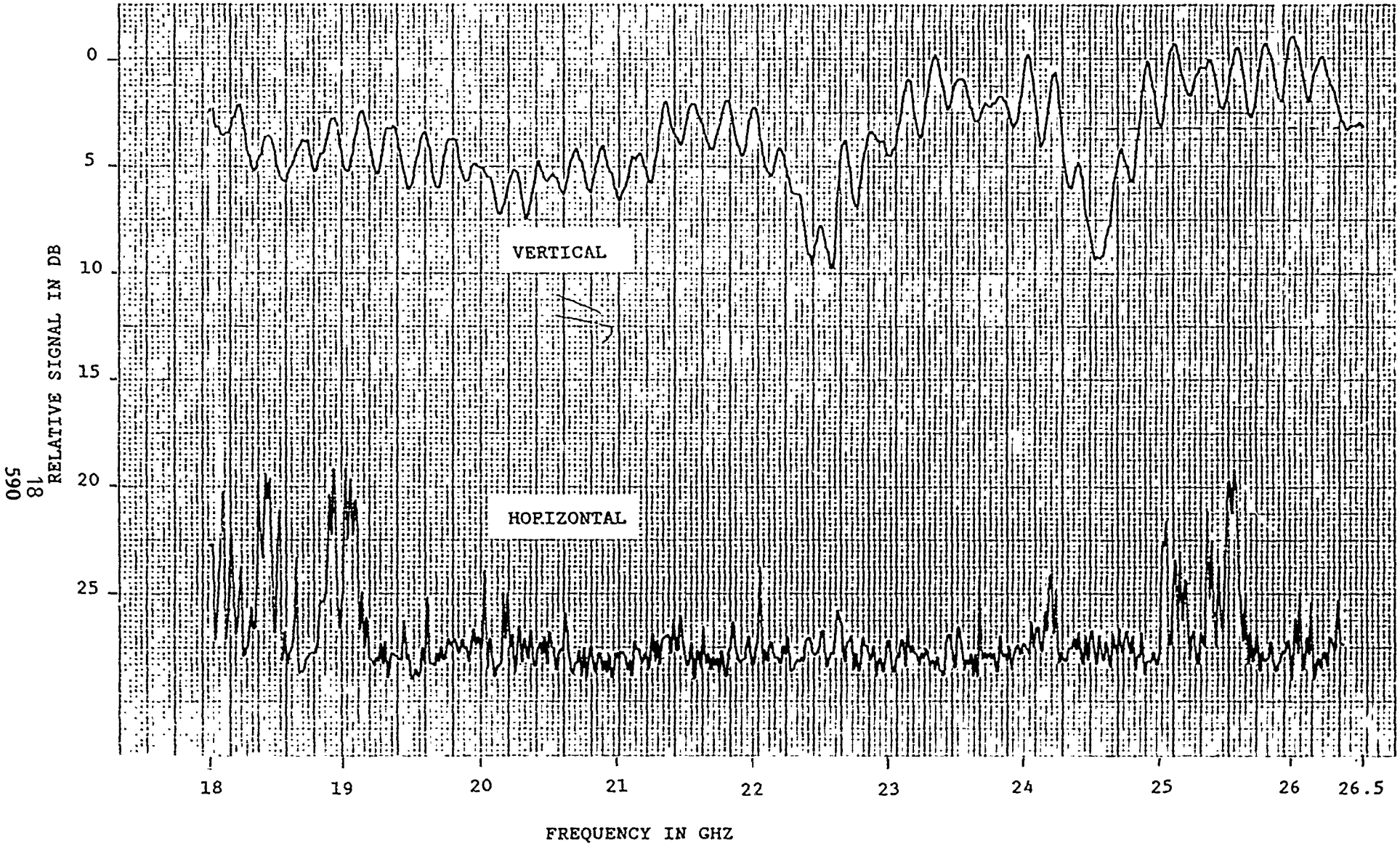

FIGURE 9. SWEEP FROM 18.0 - 26.5 GHz USING VERTICAL POLARIZATION VS. OUTPUTS FOR VERTICAL AND HORIZONTAL

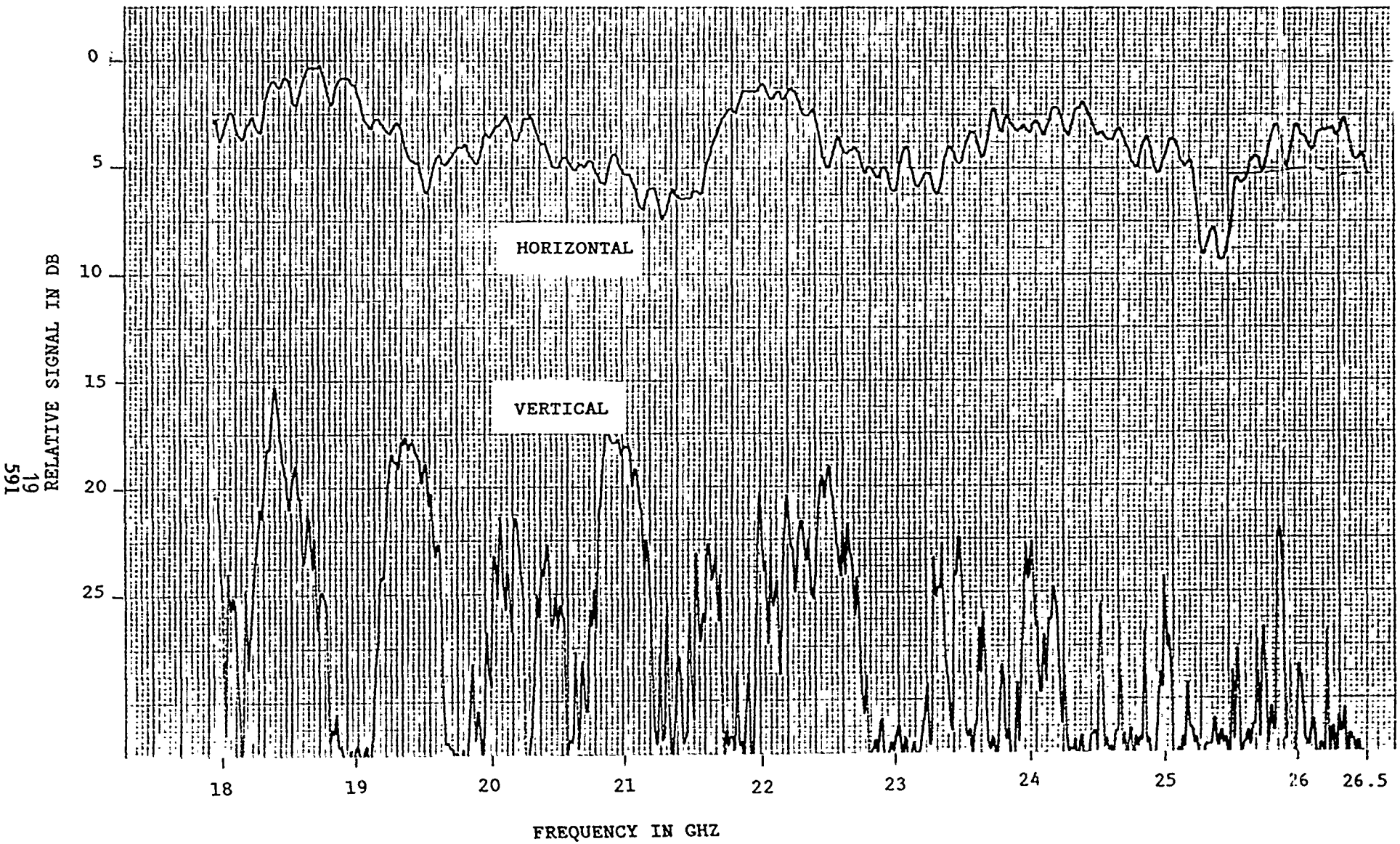

FIGURE 10. SWEEP FROM 18.0 - 26.5 GHz USING HORIZONTAL POLARIZATION VS. OUTPUTS FOR VERTICAL AND HORIZONTAL

Figures 11 and 12 are similar swept plots from 26-40 GHz of the received levels for the signals filtered by the polarization disk to distinguish between vertical and horizontally-polarized emitters. Figure 11 is for a vertically-polarized source while Figure 12 is for a horizontally-polarized source. Clearly, the design objective of discriminating between principally polarized signals sufficiently to identify emitter polarization has been more than adequately met.

6. ACKNOWLEDGEMENTS

The writer wishes to thank Messrs. H. G. Oltman, Jr. and Eli W. Warsaw for their constructive reviews during the writing of this paper.

Thanks also to Mr. Douglas Kough for his assistance with final test data used herein, and to Ms. Linda Swart for preparation of the manuscript.

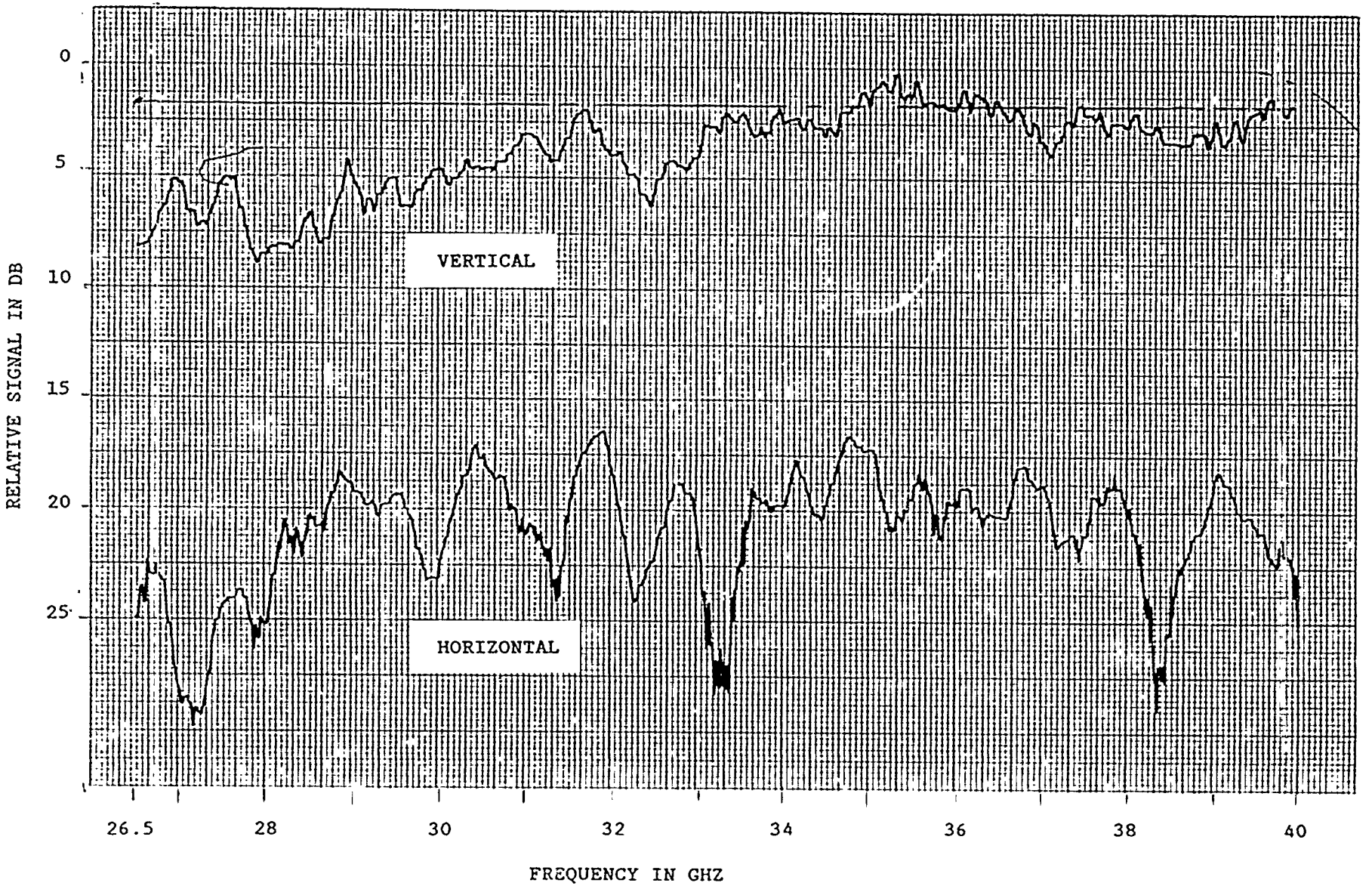

FIGURE 11. SWEEP FROM 26.5 - 40.0 GHz USING VERTICAL POLARIZATION VS. OUTPUTS FOR VERTICAL AND HORIZONTAL

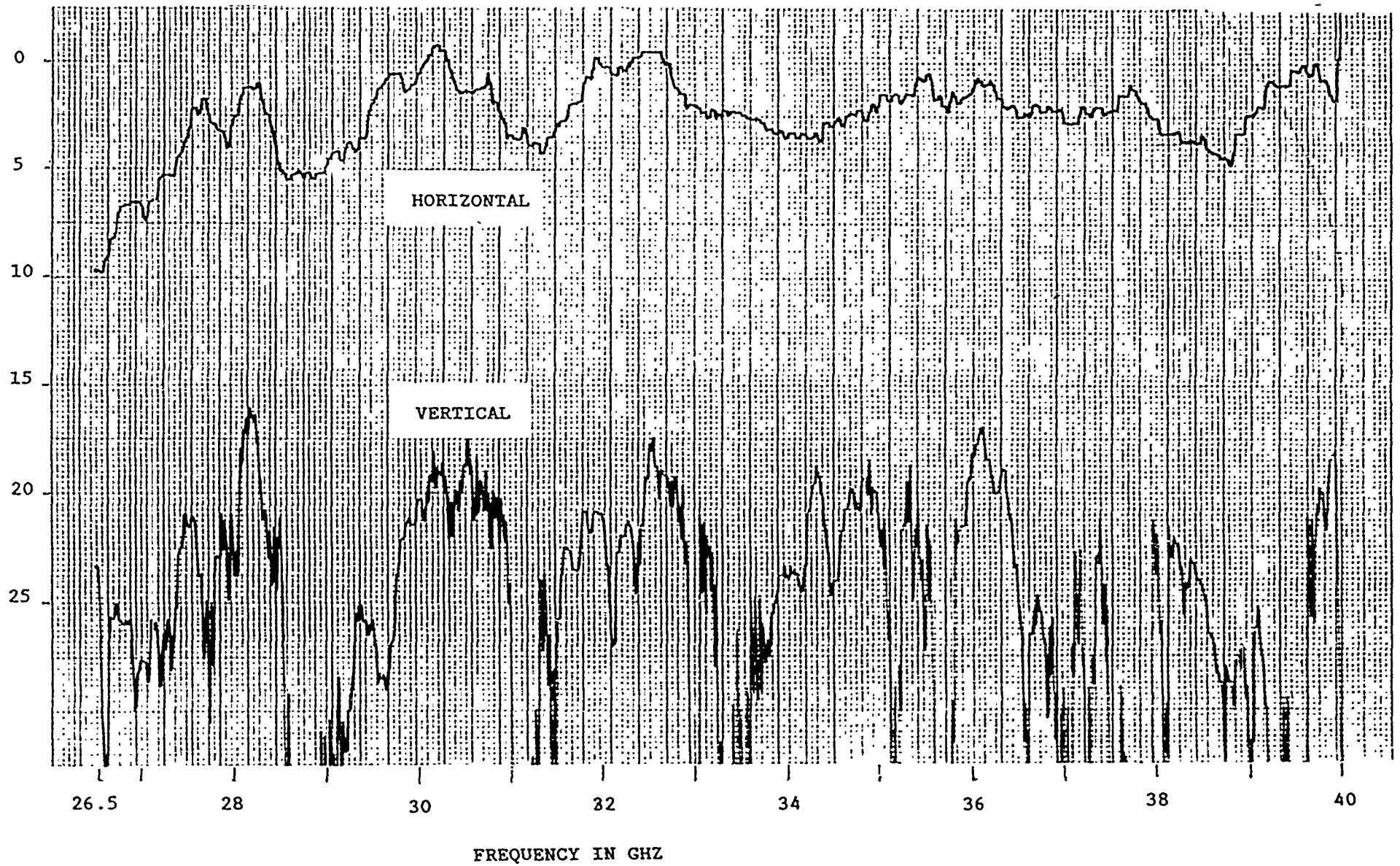

FIGURE 12. SWEEP FROM 26.5 - 40.0 GHz USING HORIZONTAL POLARIZATION VS. OUTPUTS FOR VERTICAL AND HORIZONTAL

AUTOBIOGRAPHY

Harry B. Sefton Jr. was born in Dayton, Ohio in the year of the Dragon and received his BSEE from the Ohio State University in the first 5-year curriculum class. He immediately joined the Martin Company working on antenna systems for aircraft and missiles. He innovated flush VOR, IFF, and TACAN antennas for seaplanes, the latter two ventrally mounted. Other novel designs included retractable/extendable antennas for aircraft/missiles. As the company evolved into Martin-Marietta the writer was responsible for all electrical aspects of the design, instrumentation and flight test of over 45 trainer missiles tested at Eglin AFB, Florida and Nellis AFB, Nevada.

When Bunker-Ramo was spun off to California, he placed into operation there the first large, tapered anechoic chamber for use by the antenna group he was to head. Later he became project engineer for a 4 shelter automatic ground emitter location system using multiple octave band interferometer arrays. A separate spread spectrum link was designed and built to provide timing for the TOA function. Before joining TECOM Industries, he was Engineering Manager, directing the design, production, and testing of state-of-the-art spiral antennas at American Nucleonics.

Mr. Sefton is presently Director of Advanced Programs at TECOM Industries, Chatsworth, California, a Tech-Sym Company.

He was the 1986/7 chairman of the Antenna and Propagation Society at Los Angeles, is a member of the IEEE, and a Fellow of the Institute for Advancement of Engineering.

The Effect of Feed on the Input Impedance of a Microstrip Antenna

W. C. Chew, Z. Nie, and Y. T. Lo
Electromagnetics Laboratory
Department of Electrical and Computer Engineering
University of Illinois
Urbana, IL 61801

Abstract

In this paper, a rigorous analysis is performed to analyze the effect of the feed on the input impedance of a circular and annular-ring-loaded circular microstrip antenna.

The traditional approach to calculating the input impedance of a microstrip antenna is via the reaction formula (also known as the induced EMF formula). However, this formula does not include the effect of feed geometry on the input impedance. For example, for a probe-fed microstrip antenna, the effect of the gap capacitance at the base of the probe is not included in the reaction formula.

A new variational expression for the input impedance of an antenna driven by a voltage across a gap is derived. This formula incorporates the effect of the gap dimension (which affects the gap capacitance) on the input impedance of the antenna. Such a formula is used to derive the input impedance of a probe-fed microstrip antenna.

In addition, the solution of the microstrip antenna driven by a coaxial probe is obtained using the mode-matching method, by matching the modes inside the coaxial line with the modes of the microstrip antenna. The mode matching solution is done with and without a diaphragm at the base of the probe. If a single mode is used in the mode matching approach, the impedance calculated with and without the diaphragm is the same as the input impedance obtained by the varational formula. However, the mode-matching solution is more rigorous than the variational formula, because, in theory, the input impedance of the probe-fed antenna can be calculated to any desire accuracy depending on computational resources.

It is found that the effect of the gap-capacitance on the input impedance is large when the thickness of the substrate is large. This is because the characteristic impedance of the parallel plate "transmission line" is large when the substrate thickness is large. Since the gap capacitance shunts this characteristic impedance, its effect is more pronounced for thick dielectric substrates. Our theory is found to compare very well with experimental measurement.

I. Introduction

In recent years, much progress has been made on the input impedance of the microstrip antennas [1–4]. To have a more general solution, an integral equation, solvable by Galerkin's method, has to be employed to solve the problem [3, 4]. A simple way is to consider a uniform current on the probe to be the exciting source, with which the integral equation is then formulated for the unknown currents on the disk. The currents can then be solved for using standard techniques like Galerkin's method [5]. Having found the current distribution on the disk, the reaction formula† can be used to calculate the input impedance of the antenna. This formula is [6]

$$Z_{in} = -\frac{\langle \mathbf{E}_T, \mathbf{J} \rangle}{I^2} \tag{1}$$

where $\langle \mathbf{E}_T, \mathbf{J} \rangle = \int_V \mathbf{E}_T \cdot \mathbf{J} dV$ is the reaction between $\mathbf{E}_T$ and $\mathbf{J}$. $\mathbf{E}_T$ is the total electric field generated by the probe current and the disk current, and $\mathbf{J}$ is the probe current plus the disk current. When the disk current $\mathbf{J}_D$ is solved for via the Galerkin's method, it can be shown easily that $\langle \mathbf{E}_T, \mathbf{J}_D \rangle = 0$ since Galerkin's method sets this reaction to zero. Therefore, (1) can alternatively be expressed as

$$Z_{in} = -\frac{\langle \mathbf{E}_T, \mathbf{J}_P \rangle}{I^2} = -\frac{\langle \mathbf{E}_D, \mathbf{J}_P \rangle + \langle \mathbf{E}_P, \mathbf{J}_P \rangle}{I^2} \tag{2}$$

where we have written $\mathbf{E}_T = \mathbf{E}_D + \mathbf{E}_P$ and $\mathbf{E}_D$ is the field produced by the disk current while $\mathbf{E}_P$ is the field produced by the probe current. In this decomposition, the physical meaning of (2) is clear: the first term in (2) is the input impedance of due to the disk current, whereas the second term in (2) is due to the self inductance of the probe.

One thing is peculiar about the expression (2): it is independent of the size of the gap at the base of the probe. This gap contributes to a capacitance

† This formula has also been called the induced E.M.F. formula, while the power formula $Z_{in} = -\langle \mathbf{E}_r, \mathbf{J}^s \rangle / |I|^2$ has also been called the induced E.M.F. formula. We call this the reaction formula to avoid confusion.

that shunts the input impedance of the microstrip antenna. Hence, it is exceedingly important when the gap at the base of the probe is small, or when the input impedance of the antenna is large. A small gap gives rise to a large capacitance which shunts the input impedance of the antenna; and the impedance is more sensitive to this shunt when it is large. When the dielectric substrate is thick, the effect of this gap capacitance is more important as we shall show.

In this paper, we shall illustrate three ways of incorporating this gap capacitance into the input impedance calculation of a probe-fed antenna. The three methods, with increasing level of complexity and sophistication, are the variational formula, the mode-matching method, and the mode-matching method with a diaphragm.

II. Variational Formula

When an antenna is fed by a coaxial line as shown in Figure 1a, it could be replaced by an equivalent problem of Figure 1b exterior to the coaxial line. In Figure 1b, $\mathbf{M}_a = \mathbf{E}_a \times \hat{n}$, i.e., the tangential component of the electric field at the aperture of the coaxial line in Figure 1a. Examples of such antennas are probe-fed microstrip antennas and coaxial fed monopoles.

In Figure 1b, $\mathbf{M}_a$ is actually unknown, but when the aperture of the coaxial line is small, its approximate distribution can be ascertained. With this in mind, we shall assume that $\mathbf{M}_a$ in Figure 1b is known which is also the excitation source for the field. Consequently, an electric current $\mathbf{J}_s$ is induced on the antenna structure due to the presence of $\mathbf{M}_a$. A new variational expression for the input admittance of the antenna can be derived such that[†]

$$Y_{in} = \frac{-\langle \mathbf{M}_a, \mathbf{H}_T \rangle + \langle \mathbf{J}_s, \mathbf{E}_T \rangle}{V^2}. \tag{3}$$

In the above, $\mathbf{H}_T$ and $\mathbf{E}_T$ are the total magnetic field and electric field due to $\mathbf{M}_a$ and $\mathbf{J}_s$. V is the voltage across the gap at the aperture of the coaxial line.

[†] It is correctly pointed out to the first author by R. E. Collin [6] that such a formula does not exactly reproduce the input admittance.

Furthermore, $\mathbf{H}_T = \mathbf{H}_s + \mathbf{H}_a$, $\mathbf{E}_T = \mathbf{E}_s + \mathbf{E}_a$, where the subscript s denotes fields due to $\mathbf{J}_s$, and the subscript a denotes fields due to $\mathbf{M}_a$. Taking the first variation of (3) by keeping $\mathbf{M}_a$ and V fixed, we have

$$V^2 \delta Y_{in} = -\langle \mathbf{M}_a, \delta \mathbf{H}_T \rangle + \langle \delta \mathbf{E}_T, \mathbf{J}_{se} \rangle + \langle \mathbf{E}_{Te}, \delta \mathbf{J}_s \rangle, \tag{4}$$

where the extra subscript e denotes exact values. Since $\hat{n} \times \mathbf{E}_{Te} = 0$ on the antenna structure, the last term in (4) vanishes. Furthermore, since only $\mathbf{J}_s$ is allowed to vary but not $\mathbf{M}_a$, $\delta \mathbf{E}_T = \delta \mathbf{E}_s$. Consequently,

$$\langle \delta \mathbf{E}_T, \mathbf{J}_{se} \rangle = \langle \delta \mathbf{J}_s, \mathbf{E}_{se} \rangle = -\langle \delta \mathbf{J}_s, \mathbf{E}_a \rangle = \langle \mathbf{M}_a, \delta \mathbf{H}_s \rangle = \langle \mathbf{M}_a, \delta \mathbf{H}_T \rangle \tag{5}$$

implying the vanishing of the first variation of δY_{in} in (4) and the stationarity of (3) about the exact solution. It can be shown that Equation (3) is also stationary if $\mathbf{M}_a$ and V are allowed to vary.

When the exact current $\mathbf{J}_{se}$ is known on the antenna, then $\langle \mathbf{J}_{se}, \mathbf{E}_{Te} \rangle = 0$ since $\hat{n} \times \mathbf{E}_{Te} = 0$ on the antenna structure and (3) becomes

$$Y_{inc} = -\frac{\langle \mathbf{M}_a, \mathbf{H}_{Te} \rangle}{V^2} = \frac{-\langle \mathbf{M}_a, \mathbf{H}_a \rangle - \langle \mathbf{M}_a, \mathbf{H}_{se} \rangle}{V^2}. \tag{6}$$

The first term on the right-hand side of (6) is identifiable as the contribution to the input admittance due to the gap capacitance, while the second term is the contribution due to the antenna structure.

The numerator of (3) is the reaction between the sources $(\mathbf{M}_a, \mathbf{J}_s)$ with the total field $(\mathbf{H}_T, \mathbf{E}_T)$ generated by the sources. Hence, it falls into the class of variational formulas derivable from reaction [7]. When an antenna is driven by a voltage gap (slice-generator) whose equivalent problem is an antenna driven by a magnetic current, (3) is the variational formula to be used but not (1) as has been erroneously suggested by some authors [8].

Before using (3), the value of $\mathbf{J}_s$ is required. One way of obtaining $\mathbf{J}_s$ is to formulate an integral equation from which $\mathbf{J}_s$ could be solved by Galerkin's or moment method. The integral equation is obtained via the boundary

condition that $\hat{n} \times (\mathbf{E}_a + \mathbf{E}_s) = 0$ on S where S is the surface of the antenna structure. $\mathbf{E}_s$ is generated by $\mathbf{J}_s$ via a dyadic Green's function. Consequently, the integral equation is

$$-\hat{n} \times \mathbf{E}_a(\mathbf{r}) = i\omega \int_V d\mathbf{r}' \hat{n} \times \overline{\mathbf{G}}_e(\mathbf{r}, \mathbf{r}') \cdot \mu(\mathbf{r}') \mathbf{J}_s(\mathbf{r}'), \quad \mathbf{r} \in S \tag{7}$$

where $\overline{\mathbf{G}}_e(\mathbf{r}, \mathbf{r}')$ is the electric-type dyadic Green's function for a general inhomogeneous medium [8]. To solve the above via the Galerkin's method, we let

$$\mathbf{J}_s = \sum_{n=1}^{N} a_n \mathbf{J}_{sn} \tag{8}$$

in (7) and testing the resultant equation with $\hat{n} \times \mathbf{J}_{sm}$, $m = 1, \cdots, N$. As a result, we have

$$-\langle \mathbf{J}_{sm}, \mathbf{E}_a \rangle = i\omega \sum_{n=1}^{N} \langle \mathbf{J}_{sm}, \overline{\mathbf{G}}_e \mu, \mathbf{J}_{sn} \rangle a_n, \quad m = 1, \cdots, N. \tag{9}$$

where $\langle \mathbf{J}_{sm}, \overline{\mathbf{G}}_e \mu, \mathbf{J}_{sm} \rangle = \int d\mathbf{r} \int d\mathbf{r}' \mathbf{J}_{sm}(\mathbf{r}) \cdot \overline{\mathbf{G}}_e(\mathbf{r}, \mathbf{r}') \mu(\mathbf{r}') \cdot \mathbf{J}_{sn}(\mathbf{r}')$. Equation (9) is a matrix equation from which a_n can be solved for yielding $\mathbf{J}_s$ from (8).

Multiplying (9) by a_m and summing over m from 1 to N, we can easily show that $\mathbf{J}_s$ from (8) satisfies

$$-\langle \mathbf{J}_s, \mathbf{E}_a \rangle = i\omega \langle \mathbf{J}_s, \overline{\mathbf{G}}_e \mu, \mathbf{J}_s \rangle = \langle \mathbf{J}_s, \mathbf{E}_s \rangle. \tag{10}$$

Therefore, $\mathbf{J}_s$ obtained from Galerkin's method will make the second term in the numerator of (3) vanish, and

$$Y_{in} = -\frac{\langle \mathbf{M}_a, \mathbf{H}_T \rangle}{V^2} = -\frac{\langle \mathbf{M}_a, \mathbf{H}_a \rangle + \langle \mathbf{M}_a, \mathbf{H}_s \rangle}{V^2}. \tag{11}$$

We have applied the above technique to solve for the input impedance of a probe-fed, annular-ring-loaded (ARL), circular microstrip disk antenna

as shown in Figure 2 with the diaphragm absent. Due to the presence of a dielectric substrate, a stratified medium Green's function has to be used to calculate the field due to the current induced on the probe and the disk. The field distribution $\mathbf{E}_a$ on the coaxial aperture is assumed to be that of the TEM mode of the coaxial cable. The resultant input impedance calculation using (3) is compared with previous calculation using (1) in Figure 3. Better agreement with experiment is noted when Equation (3) is used. We have not used any fudge factor in the theory. The integral equation is solved similar to previous work using vector Hankel transforms [10, 11] and the singularity-subtraction method [3, 12] to accelerate convergence.

III. Mode Matching Method†

In using the variational formula (3), one has to assume knowledge of $\mathbf{M}_a$. The formula itself does not lend much insight as to how $\mathbf{M}_a$ is to be chosen. In order to systematically solve for the value of $\mathbf{M}_a$, the mode-matching method is needed. In th. method, the reflected field inside the coaxial cable is expanded in terms of the modes of the cable. Then, continuity of tangential fields at the aperture is imposed to solve for the reflection coefficients of the reflected modes. For long wavelengths, only the TEM reflected mode will be propagatory while the higher-order modes are evanescent. The reflection coefficient of the TEM mode allows one to unambiguously derive the input impedance of the antenna. We shall consider the case where the diaphragm is absent.

Inside the coaxial region, one assumes that

$$\mathbf{E}(\mathbf{r}) = \mathbf{E}_0(\mathbf{r}_s)e^{ikz} + \sum_{l=0}^{L-1} \Gamma_l \mathbf{E}_l(\mathbf{r}_s)e^{-ik_{lz}z} \tag{12}$$

where $\mathbf{E}_0(\mathbf{r}_s)$ is the field of the TEM mode and $\mathbf{E}_m(\mathbf{r}_s)$, $m > 0$, are the fields

† The mode-matching method has been used previous in conjunction with the cavity-mode model [13].

of the higher-order modes. The corresponding magnetic field is

$$\mathbf{H}(\mathbf{r}) = \mathbf{H}_0(\mathbf{r}_s)e^{ikz} - \sum_{l=0}^{L-1} \Gamma_l \mathbf{H}_l(\mathbf{r}_s)e^{-ik_{lz}z}. \tag{13}$$

Hence, the total electric field at the aperture in accordance with (12) is

$$\mathbf{E}_a = \mathbf{E}_0 + \sum_{l=0}^{L-1} \Gamma_l \mathbf{E}_l. \tag{14}$$

The corresponding magnetic current is

$$\mathbf{M}_a = \mathbf{E}_a \times \hat{n} = \mathbf{M}_0 + \sum_{l=0}^{L-1} \Gamma_l \mathbf{M}_l \tag{15}$$

where $\mathbf{M}_l = \mathbf{E}_l \times \hat{n}$. The electric field in the outer region generated by $\mathbf{M}_a$ can be written as

$$\begin{aligned}\mathbf{E}_a &= \int_V d\mathbf{r}' \epsilon^{-1}(\mathbf{r}) \nabla \times \overline{\mathbf{G}}_m(\mathbf{r}, \mathbf{r}') \epsilon(\mathbf{r}') \cdot \mathbf{M}_a \\ &= \int_V d\mathbf{r}' \epsilon^{-1} \nabla \times \overline{\mathbf{G}}_m(\mathbf{r}, \mathbf{r}') \epsilon \cdot \mathbf{M}_0 + \sum_{l=0}^{L-1} \Gamma_l \int_V d\mathbf{r}' \epsilon^{-1} \nabla \times \overline{\mathbf{G}}_m(\mathbf{r}, \mathbf{r}') \epsilon \cdot \mathbf{M}_l \end{aligned} \tag{16}$$

where $\overline{\mathbf{G}}_m(\mathbf{r}, \mathbf{r}')$ is the magnetic-type dyadic Green's function in an inhomogeneous medium due to a magnetic current source. Using (16) in (9), we have

$$\begin{aligned} -\langle \mathbf{J}_{sm}, \epsilon^{-1} \nabla \times \overline{\mathbf{G}}_m \epsilon, \mathbf{M}_0 \rangle - \sum_{l=0}^{L-1} \langle \mathbf{J}_{sm}, \epsilon^{-1} \nabla \times \overline{\mathbf{G}}_m \epsilon, \mathbf{M}_l \rangle \Gamma_l \\ = i\omega \sum_{n=1}^{N} \langle \mathbf{J}_{sm}, \overline{\mathbf{G}}_e \mu, \mathbf{J}_{sn} \rangle a_n, \quad m = 1, \cdots, N. \end{aligned} \tag{17}$$

The magnetic field outside the aperture is $\mathbf{H}_T = \mathbf{H}_a + \mathbf{H}_s$ where

$$\mathbf{H}_a = i\omega \int_V d\underline{\mathbf{r}}' \overline{\mathbf{G}}_m(\underline{\mathbf{r}}, \underline{\mathbf{r}}') \epsilon(\underline{\mathbf{r}}') \cdot \underline{\mathbf{M}}_a(\underline{\mathbf{r}}'), \tag{18a}$$

$$\mathbf{H}_s = \int_V d\mathbf{r}' \mu^{-1} \nabla \times \overline{\mathbf{G}}_e(\mathbf{r}, \mathbf{r}') \mu \cdot \mathbf{J}_s(\mathbf{r}'). \tag{18b}$$

With $\mathbf{M}_a$ from (15) and $\mathbf{J}_s$ from (18), the above becomes

$$\mathbf{H}_T = i\omega \int_V d\mathbf{r}' \overline{\mathbf{G}}_m(\mathbf{r},\mathbf{r}')\epsilon(\mathbf{r}') \cdot \mathbf{M}_0(\mathbf{r}') + \sum_{l=1}^{L-1} i\omega\Gamma_l \int_V d\mathbf{r}' \overline{\mathbf{G}}_m(\mathbf{r},\mathbf{r}')\epsilon(\mathbf{r}') \cdot \mathbf{M}_l(\mathbf{r}')$$

$$+ \sum_{n=1}^{N} a_n \int_V d\mathbf{r}' \mu^{-1} \nabla \times \overline{\mathbf{G}}_e(\mathbf{r},\mathbf{r}')\mu \cdot \mathbf{J}_{sn}(\mathbf{r}'). \quad (19)$$

Continuity of the tangential components of the magnetic fields requires the equality of the tangential components of (13) and (19). Equating (13) and (19), and testing the result with $\mathbf{M}_p(\mathbf{r}_s)$, $p = 0, \cdots, L-1$, from (15), we have

$$\delta_{0p}\lambda_0 - \sum_{l=0}^{L-1} \Gamma_l \delta_{lp} \lambda_l = i\omega \langle \mathbf{M}_p, \overline{\mathbf{G}}_m \epsilon, \mathbf{M}_0 \rangle + i\omega \sum_{l=0}^{L-1} \Gamma_l \langle \mathbf{M}_p, \overline{\mathbf{G}}_m \epsilon, \mathbf{M}_l \rangle$$

$$+ \sum_{n=1}^{N} a_n \langle \mathbf{M}_p, \mu^{-1} \nabla \times \overline{\mathbf{G}}_e \mu, \mathbf{J}_{sn} \rangle, \quad p = 0, \cdots, L-1, \quad (20)$$

where $\lambda_l = \langle \mathbf{M}_l, \mathbf{H}_l \rangle$ is a normalization constant and mode orthogonality [14] has been used in arriving at (20). Equations (17) and (20) form a set of $N + L$ linear algebraic equations from which Γ_l, $l = 0, \cdots, L-1$, and a_n, $n = 1, \cdots, N$ can be found. Once Γ_0 is known, the input admittance of the antenna is found from

$$Y_{in} = Y_0 \frac{1 - \Gamma_0}{1 + \Gamma_0} \quad (21)$$

where Y_0 is the characteristic admittance of the coaxial line.

If only a single TEM mode is used to approximate the field inside the coaxial cable, one can readily show that the input admittance obtained via (21) is identical to that using the variational formula (3) where a TEM field is assumed for $\mathbf{E}_a$ at the aperture. Hence, the variational formula is a special case of the mode-matching method under the single-mode approximation.

We have implemented the above formulation for the annular-ring-loaded microstrip antenna using a stratified medium Green's function. Figure 4 shows the comparison for the ARL microstrip disk antenna between the mode

matching theory and experiment for different L's ($L = 1$, being the single-mode approximation, is equivalent to the variational formula). It is seen that the need for higher-order mode is not that critical in this case.

IV. Mode Matching with a Diaphragm

Sometimes, a coaxial-fed antenna is made with a diaphragm at the aperture as shown in Figure 2. It will be interesting to study the effect of this diaphragm on the gap capacitance, and hence, the input impedance of an antenna. This method proceeds very much like the mode-matching method except that the aperture field now is expanded in terms of

$$\mathbf{E}_a = \sum_{q=0}^{Q-1} b_q \boldsymbol{\eta}_q \tag{22}$$

where $\boldsymbol{\eta}_q$ is a basis function with support only over the aperture. Hence,

$$\mathbf{M}_a = \mathbf{E}_a \times \hat{n} = \sum_{q=0}^{Q-1} b_q \mathbf{M}_q \tag{23}$$

where $\mathbf{M}_q = \boldsymbol{\eta}_q \times \hat{n}$. The equivalence of (17) is then

$$-\sum_{q=0}^{Q-1} \langle \mathbf{J}_{sm}, \epsilon^{-1} \nabla \times \overline{\mathbf{G}}_m \epsilon, \mathbf{M}_q \rangle b_q = i\omega \sum_{n=1}^{N} \langle \mathbf{J}_{sm}, \overline{\mathbf{G}}_e \mu, \mathbf{J}_{sn} \rangle a_n, \quad m = 1, \cdots, N. \tag{24}$$

Again, the fields inside the coaxial line are expanded as (12) and (13). We equate (15) with (23) to establish the continuity of the electric field, and test the resulting equation with $\mathbf{H}_p$, $p = 0, \cdots, L-1$ to yield

$$\delta_{0p}\lambda_0 + \sum_{l=0}^{L-1} \Gamma_l \delta_{lp} \lambda_l = \sum_{q=0}^{Q-1} b_q \langle \mathbf{H}_p, \boldsymbol{\eta}_q \rangle, \quad p = 0, \cdots, L-1. \tag{25}$$

The equivalence of (19) is

$$\mathbf{H}_T = i\omega \sum_{q=0}^{Q-1} b_q \int_V d\mathbf{r}' \overline{\mathbf{G}}_m(\mathbf{r},\mathbf{r}') \epsilon(\mathbf{r}') \cdot \mathbf{M}_q(\mathbf{r}')$$

$$+ \sum_{n=1}^{N} a_n \int_V d\mathbf{r}' \mu^{-1} \nabla \times \overline{\mathbf{G}}_e(\mathbf{r},\mathbf{r}') \mu \cdot \mathbf{J}_{sn}(\mathbf{r}'). \quad (26)$$

Equating (26) with the magnetic field inside the waveguide given by (13), and testing the resultant equation with $\mathbf{M}_r$, $r = 0, \cdots, Q-1$, we have

$$\langle \mathbf{M}_r, \mathbf{H}_0 \rangle - \sum_{l=0}^{L-1} \Gamma_l \langle \mathbf{M}_r, \mathbf{H}_l \rangle = i\omega \sum_{q=0}^{Q-1} b_q \langle \mathbf{M}_r, \overline{\mathbf{G}}_m \epsilon, \mathbf{M}_l \rangle$$

$$+ \sum_{n=1}^{N} a_n \langle \mathbf{M}_r, \mu^{-1} \nabla \times \overline{\mathbf{G}}_e \mu, \mathbf{J}_{sn} \rangle, \quad r = 0, \cdots, Q-1. \quad (27)$$

Equations (24), (25), and (27) constitute $N+L+Q$ linear algebraic equations from which the unknown a_n, b_q, and Γ_l can be found. Once Γ_0 is known, the input admittance is given by (21).

Strangely enough, if a single mode is used in (12) and (13), and only one basis function is used in (22), the input admittance found this way can again be shown to be identical to that derived using the variational formula. However, the use of a single mode in the coax will not meet the boundary condition on the diaphragm, and the result is inaccurate. In other words, the variational formula is inaccurate for the geometry shown in Figure 2 where a diaphragm exists.

This theory has been used to calculate the input impedance of a probe-fed microstrip antenna with a diaphragm. Figure 5 shows the comparison of the theory with a diaphragm and experiment for an ARL microstrip disk antenna. Excellent agreement is observed. Figure 6a shows the effect of varying the diaphragm size for a thick substrate case, while Figure 6b shows the effect of varying the diaphragm size for the thin substrate case. Varying the diaphragm size alters the gap capacitance. Hence, the effect of the gap

capacitance on the thick substrate case is more pronounced than the effect on the thin substrate case.

The integral equations are solved using the method of reference 12. With the notation of reference 12, in Figure 3, $(M, P, L, Q) = (2, 1, 4, 1)$ in curve 2, and $(M, P, L, Q) = (2, 1, 8, 1)$ in curve 3. In Figures 4, 5, and 6, $(M, P, L, Q) = (1, 0, 2, 0)$ for all curves.

V. Conclusions

Rigorous calculations of a probe-fed, annular-ring-loaded, circular-disk microstrip antenna is presented. The first calculation uses a new variational formula which improves on the input impedance of an antenna driven by a voltage gap. The variational formula is shown to be good for the case when the aperture at the coaxial line does not have a diaphragm.

The second calculation uses a mode-matching method where the field in the coaxial line is expanded in terms of the waveguide modes. It can be shown that if only a single mode is used to expand the field inside the waveguide, the mode matching solution reduces to that of the variational formula. It is found that when the wavelength is long compared to the transverse dimension of the coaxial line, the use of higher order modes is not crucial in improving the input impedance calculation.

The last calculation uses a mode-matching method with a diaphragm. Although the theory under the single mode approximation agrees with the variational formula, the single mode approximation is bad in this case because the boundary condition on the diaphragm cannot be met. Therefore, one concludes that the variational formula cannot be used when the aperture consists of a diaphragm. This is consistent with the fact the variational formula (3) need not exactly represent the input admittance.

By altering the diaphragm size to alter the gap capacitances, we find that the input impedance and the resonant frquency of the microstrip antenna is more sensitive to the influence of this shunting gap capacitance when the dielectric substrate is thick as evidenced by Figure 6. This can be under-

stood from an approximate equivalent circuit of the microstrip antenna close to resonance as shown in Figure 7 (we ignore the probe inductance in this discussion.). When the dielectric substrate is thick, the effective C in the equivalent circuit is smaller due to the larger separation between the top plate and the bottom plate. Since C_g is in parallel with C, its influence on the resonance frequency of the circuit is more pronounced as shown in Figure 6a.

References

[1] Y. T. Lo, D. Soloman, and W. F. Richards, "Theory and experiment on mircrostrip antennas," *IEEE Trans. Antennas Propagat.*, vol. AP-27, pp.137–145, 1979.

[2] W. C. Chew, J. A. Kong, and L. C. Shen, "Radiation characteristics of a circular microstrip antenna," *J. Appl. Phys.*, 51(7), p.3907, 1980.

[3] W. C. Chew and J. A. Kong, "Analysis of cirlular microstrip disk antenna with thick dielectric substrate," *IEEE Trans. Antennas Propagat.*, vol. AP-29, pp.68–69, 1981.

[4] D. M. Pozar, "Input impedance and mutual coupling of rectangular microstrip antennas," *IEEE Trans. Antennas Propagat.*, vol. AP-30, pp. 1191–1196, 1982.

[5] R. G. Harrington, *Field computation by moment methods*, Krieger Publishing Co, Malabar, Forida, 1983.

[6] R. E. Collin, private communication.

[7] R. G. Harrington, *Time-harmonic electromagnetic fields*, McGraw-Hill, New York, 1961.

[8] E. C. Jordan and K. G. Balmain, *Electromagnetic waves and radiating systems*, Prentice-Hall, Englewood Cliff, New Jersey, 1968.

[9] W. C. Chew, *Waves and fields in inhomogeneous media*, published by Depertment of Electrical and Computer Engineering, U. of Illinois, Urbana, Illinois, 1989.

[10] W. C. Chew and J. A. Kong, "Resonance of nonaxial symmetric modes

in circular micorstrip disk antenna," *J. Math. Phys.*, v. 21, no, 10, pp. 2591–2598, 1980.

[11] W. C. Chew and T. M. Habashy, "The use of vector transforms in solving some electromagnetic scattering problems," *IEEE Trans. Antennas Propagat.*, vol. AP-34, pp.871–879, 1986.

[12] Z. Nie, W. C. Chew, and Y. T. Lo, "Analysis of the annular-ring-loaded, circular-disk microstrip antenna," *IEEE Trans. Antennas Propagat.*, scheduled for June 1990.

[13] M. Davidoritz and Y. T. Lo, "Input impedance of a probe-fed circular microstrip antenna with thick substrate," *IEEE Trans. Antennas Propagat.*, vol. AP-34, pp. 905–911, 1986.

[14] R. E. Collin, *Field theory of guided waves*, McGraw-Hill, New York, 1960.

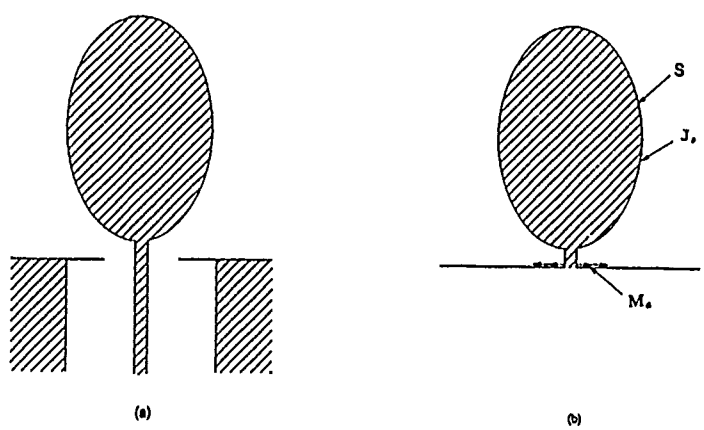

Figure 1. (a) A probe fed antenna. (b) The equivalent problem exterior to the coaxial line where $M_a = E \times n$.

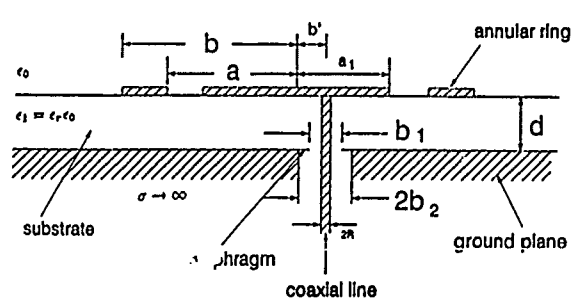

Figure 2. An annular-ring-loaded microstrip antenna fed by a coaxial probe. In Figures 3, 4, 5, and 6a, $a = 1.2$cm, $b = 2.4$cm, $a_1 = 0.815$cm, $\epsilon_r = 2.65$, $b' = 0.6$cm, $R = 0.0635$cm, $b_2 = 0.2$cm, $d = 0.3175$cm.

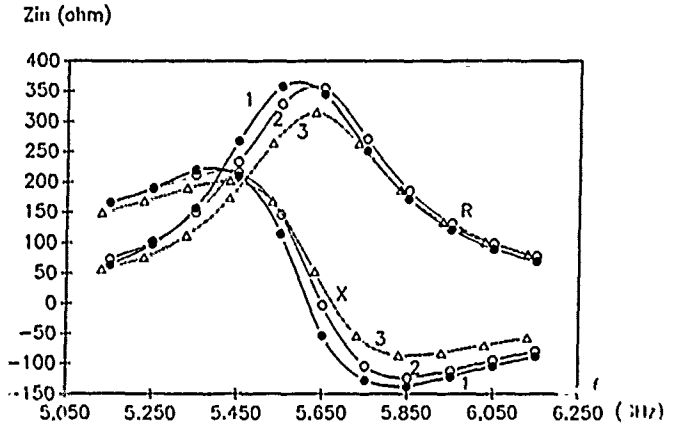

Figure 3. Comparison of theory using (1), (3), and experiment, where curve 1 experiment, curve 2—theory using Equation (3), and curve 3– theory using Equation (1).

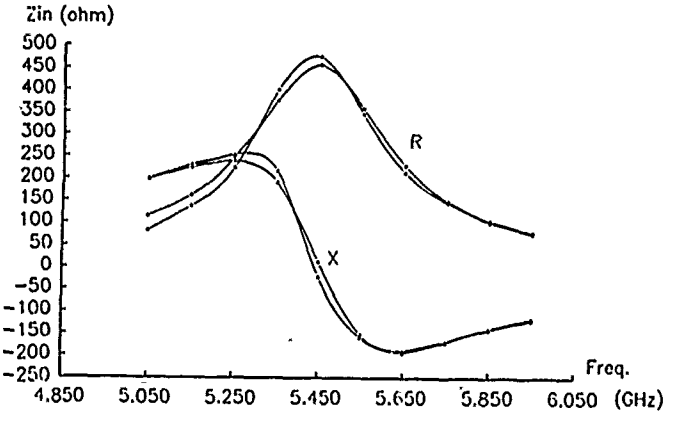

Figure 4. Comparison of theory using mode-matching method and experiment, for an ARL microstrip disk antenna where the curve with full-circle symbols is the experiment, and the curves with open-circle, triangle, and square symbols are mode-matching theory with 1 TEM incident mode, and 1 3 and 5 TM reflected modes, respectively, for the coaxial line.

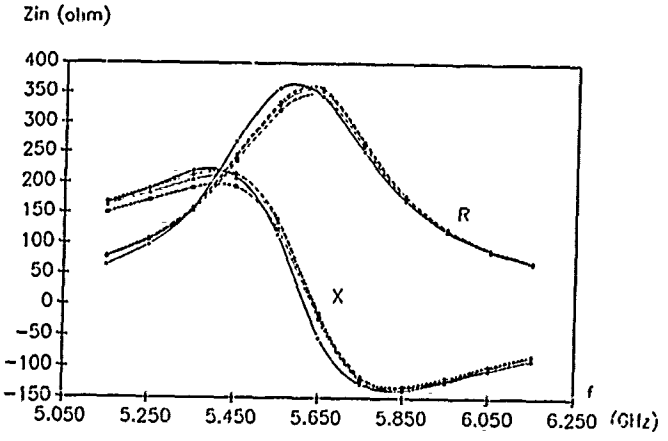

Figure 5. Comparison of theory using mode matching with a diaphragm and experiment for an annular-ring-loaded microstrip antenna, where the curve with full symbols is experiment while the curve with open symbols is the theory. The outer radius of the aperture is $b = 0.12$cm.

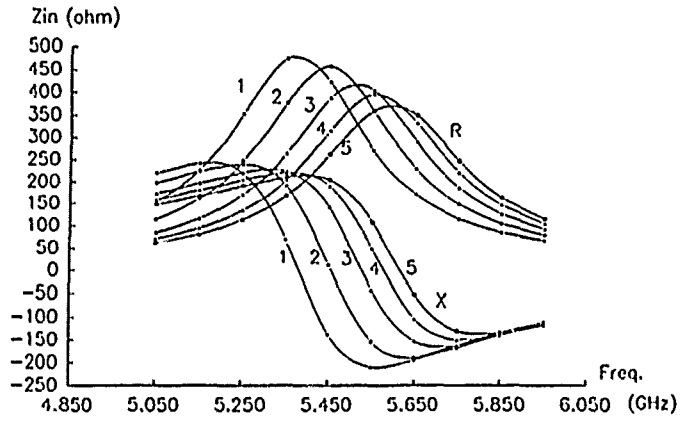

Figure 6a. Effect of diaphragm size on the input impedance of an ARL microstrip disk antenna with a thick substrate, where curves 1, 2, 3, 4, and 5 are theoretical results with substrate thickness $d = 0.1\lambda_\epsilon$ and various diaphragm sizes where the outer radii of the aperture are $b_1 = 0.10, 0.12, 0.14, 0\ 16$, and 0.18cm, respectively.

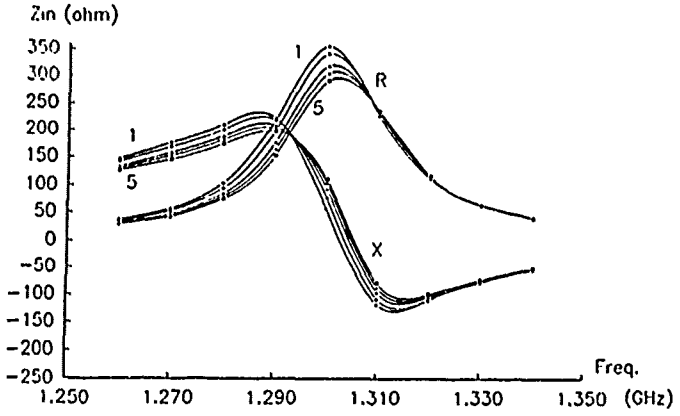

Figure 6b. Effect of diaphragm size on the input impedance of a circular-disk microstrip antenna with thin substrate, where curves 1, 2, 3, 4, and 5 are theoretical results with substrate thickness $d = 0.023\lambda_\epsilon$ and various diophragm sizes where the outer radii of the aperture are $b_1 = 0.10, 0.12, 0.14, 0.16$, and 0.18cm, repectively. $a = 4.0$cm, $b' = 2.5$cm, $R = 0.0635$cm, $b_2 = 0.2$cm, $d = 0.3175$cm in this case.

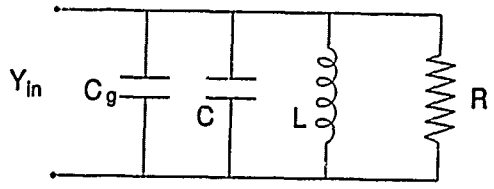

Figure 7 An approximate equivalent circuit of the microstrip antenna to explain the more severe influence of the gap capacitance C_g on the resonant frequency when the substrate is thick or C is small.

* U. S. GOVERNMENT PRINTING OFFICE: 1990--700-000/20009

MISSION
of
Rome Air Development Center

RADC plans and executes research, development, test and selected acquisition programs in support of Command, Control, Communications and Intelligence (C^3I) activities. Technical and engineering support within areas of competence is provided to ESD Program Offices (POs) and other ESD elements to perform effective acquisition of C^3I systems. The areas of technical competence include communications, command and control, battle management, information processing, surveillance sensors, intelligence data collection and handling, solid state sciences, electromagnetics, and propagation, and electronic, maintainability, and compatibility.